MEASUREMENT OF SOIL-GAS RADON CONCENTRATION AND GEOGENIC RADON POTENTIAL MODELLING FOR SOUTHWEST NIGERIA

BY

Joseph Adesoji Ademola FAJEMIROYE
Matric No. 63684

B.Sc. (Ibadan), M.Sc. (Ibadan)

A Thesis in the Department of Physics,
Submitted to the Faculty of Science
in partial fulfilment of the requirements for the degree of

DOCTOR OF PHILOSOPHY

of the

UNIVERSITY OF IBADAN

NOVEMBER, 2023

CERTIFICATION

This is to certify that the research work described in this thesis was carried out under my supervision by Joseph Adesoji Ademola, FAJEMIROYE in the Department of Physics, University of Ibadan, Nigeria

……

Supervisor
I. P. Farai
B.Sc. (Nig.), M.Sc., Ph.D. (Ibadan)
Professor, Radiation and Health Physics
Department of Physics
University of Ibadan, Nigeria

DEDICATION

This work is dedicated to God, the Father, Son and Holy Spirit, who started the programme with me and saw me through; also to my late mother, Mrs. Rebecca Omolade Fajemiroye (a mother in a million) and to my late father-in-law, Hon. Lawrence Oyekunle (a great mentor).

ACKNOWLEDGEMENTS

I give God all the glory for His mercy, grace and loving kindness, for He who began a good work in my life, completed it.

I am most grateful to my supervisor, Professor Idowu Peter Farai (the pioneer researcher on radon in Nigeria) for his painstaking guidance, correction, support and mentoring during the course of the work. Thank you very much sir. My most profound gratitude goes to Professor Olatunde Oni who assisted in giving the work direction and tutelage required to execute the work. God bless you sir.

I cannot but appreciate the helpful contribution of both academic and non-academic staff of the Department of Physics, University of Ibadan, especially members of the Radiation and Health Physics Unit – Prof. F. O. Ogundare, Prof. N. N. Jibiri, Prof. Janet Ademola and Prof. Rachael I. Obed. I also appreciate the Head of Department, Prof. N. N. Jibiri as well as Prof. O. I. Popoola, Prof. J. A. Adegoke, Prof. O. E. Awe and Dr J. A. Adetoyinbo for their support. My sincere appreciation goes to Dr Ogunseye, Dr Ogunsola, Dr Folashade Aderemi, Dr Nympas, Dr Otunla, Dr Oyewande (Postgraduate Coordinator), Dr (Mrs.) Mojisola Adeniyi (former PG Sub-Dean), for their assistance and encouragement.

I appreciate the inestimable contribution of my parents, Barrister and late Mrs. Ade Fajemiroye, my parents-in-law – late Hon. and Mrs. Lawrence Oyekunle (thank you so much), my siblings – Adenike, Adeyinka, Moyofade, Adedoyin and my adopted siblings – Dapo, Niyi, Laide and Laitan. Thanks for being there.

I must register the support and contribution of my friends and team members under Prof. Farai – Dr (Mrs.) Owoade, Dr Bolaji, Dr Efunwole and Mr. Daniel – God bless you.

I am most indebted to the academic and non-academic staff of The Polytechnic, Ibadan, most especially, staff of Department of Physics, who stood by me throughout the years of the programme. Thank you for believing in me. I also want to use this opportunity to acknowledge the contribution of my late friend, Mrs Rachel Adegbola who encouraged me when I was about giving up on the programme. However death denied her the joy of completing her own Ph.D programme. Rest on, in peace!

I acknowledge with thanks the contribution of the following people: Chief (Dr) Olumide Ajani, Rev. Ayo Alo (my childhood friends), Dr and Mrs. L.O.A. Oyinkanola, Bishop (Dr) Adagbada, Dr Ladipo Adejumo, Dr Lekan Taiwo and Mr. Joseph (of Geography dept. UI), Mr. Kazeem (Federal School of Statistics, Ibadan), Dr Abraham Adewale Aremu (Lautech), Dr Bolanle Oseni (Dean, Faculty of Science), staff of the Faculty of Science, Alhaji Isa Momoh, Dr Segun Ogunboyejo, all Abadina college old students association and Golden Estate, Oke-Odo community development association.

Finally and most importantly, I appreciate in no small measure, my heartbeat and heroine, Ajike Olabisi Oluwafunmilayo (thank you dear for the support), my loving sons, Iyinotan and Timileyin for their love, perseverance, understanding and encouragement.

And to others not mentioned, I sincerely say a big thank you.

ABSTRACT

Radon-222 is a radioactive gas in the natural decay series of Uranium-238. It easily emanates from the soil to constitute radiological hazard and is the leading cause of lung cancer apart from smoking. High indoor radon buildup could occur in buildings sited over high radon-bearing bedrocks. Radon hazard, expressed as Geogenic Radon Potential (GRP), is due to a combination of soil-gas radon concentration (C_{Rn}) and soil-air permeability (K_a), both of which depend on bedrocks. Data on these two quantities over different bedrock formations and soil types in Southwest (SW) of Nigeria are very scarce resulting in limited knowledge on radon hazard and lack of requisite radon control guidelines. This study was designed to measure C_{Rn}, determine GRP and model the distribution of GRP over different bedrocks of SW Nigeria.

Measurements of C_{Rn} were made using a calibrated real-time semiconductor radon monitor at a depth of 0.80 – 1.00 m in 150 randomly selected locations across 20 bedrocks in the six states of SW Nigeria. Saturated hydraulic conductivities (K_s) of undisturbed soil samples taken from these locations were measured with a constant-head permeameter in order to determine K_a. The GRP for each location was calculated from C_{Rn} and K_a and categorised using Neznal classification for radon hazard ratings. A Levenberg-Marquardt feed-forward-back-propagation artificial neural network was employed to develop a predictive model for GRP. Data was randomly split in 70:15:15 for training, testing and validation, respectively, for six different architectures and the best was chosen following standard procedure. Goodness-of-Prediction (G), Average Validation Error (AVE), Mean Bias Error (MBE) and Root Mean Square Error (RMSE) were used to determine performance and validation of the model. The C_{Rn} and GRP maps were generated on existing geological map for SW region.

The measured C_{Rn} ranged $0.28 - 47.59\ \mathrm{kBqm^{-3}}$. The K_s ranged $0.02 - 21.54\ \mathrm{m/d}$, while K_a ranged $5.90 \times 10^{-13} - 8.70 \times 10^{-11}\ \mathrm{m^2}$. The GRP ranged $0.15 - 39.19$. Sedimentary formation had highest K_a of $39.84 \pm 53.41 \times 10^{-12}\mathrm{m^2}$, while granitic bedrocks had highest C_{Rn} and GRP of $14.02 \pm 29.02\ \mathrm{kBqm^{-3}}$ and 13.71 ± 13.83, respectively. Radon hazard classification showed that 75.3, 16.0 and 8.7% of the sites were of low, medium and high radon hazard rating, respectively. Out of the 13 sites with high radon hazard rating, granitic and metamorphic bedrocks presented more sites (84.6%). The best performing architecture was 2 x 8 x 1. Performance indices of the model, yielded G of 73.5%, AVE of 0.073, MBE of 0.42 and RMSE of 4.62 $\mathrm{kBqm^{-3}}$. Validation indices yielded G of 86.5%, AVE of 0.17, MBE of 0.61 and RMSE of $1.65\ \mathrm{kBqm^{-3}}$, indicating good model performance. Values of measured C_{Rn} and GRP were used to generate maps which showed spatial distribution of low, medium and high radon hazard ratings.

The values of measured soil-gas radon concentration and determined geogenic radon potential were highest in granitic bedrocks. The performance indices of the developed neural network model showed good reliability in predicting geogenic radon potential for southwest Nigeria.

Keywords: Soil-air permeability, Soil hydraulic conductivity, Bedrock formation, Geogenic radon potential map, Geogenic hazard rating

Word count: 487

TABLE OF CONTENTS

TABLES	LIST OF TABLES	PAGES

FIGURES	LIST OF FIGURES	PAGES

PLATES	LIST OF PLATES	PAGES

CHAPTER ONE

INTRODUCTION

1.1 Research background

Radiation in the environment comes from many sources which can be categorized as mainly from natural and human activities. Radiation from cosmic rays, naturally occurring radioactive materials (NORM) in the earth's crust and radionuclides inhaled or ingested and retained in the body are all sources of radiation from the natural environment (Thomas *et al.*, 2022). Sources of radiation from human activities are mostly derived from medical and industrial activities. One of the major naturally occurring radionuclides is uranium, ubiquitous in bedrocks, soils and groundwater (Farai and Sanni, 1991; Munyaradzi *et al.*, 2016,). Apart from uranium, other primordial (i.e materials present from Earth's formation) radionuclides are potassium and thorium that are widespread in the soils and bedrocks. Thorium, like uranium has a decay series with many decay products while potassium is a non-series natural radionuclide. The three primordial radionuclides are present in different concentrations in soil, water, air, food and in building materials. The concentrations of these radionuclides in these media are determined by local geology and human activities.

Radon gas is one of the decay products of uranium which either stays in the bedrock where it was produced or emanates into the pore space within bedrock particles. Radon gas can be transported by diffusion and advection (Noverques *et al.*, 2023).

Radon is a colourless and oduorless radioactive noble gas. Of all isotopes of radon, the most abundant and longest lived is radon-222 ($T_{1/2}$ = 3.82 days), the immediate daughter of radium-226 in the uranium-238 decay series. When radon gas escapes from the bedrock or soil and enters the atmosphere and buildings, it poses a threat to human health. If the radon gas builds up to high concentrations in indoor air, radon and its decay products can get trapped in the lungs through inhalation.

Radon decays into its progeny, emitting alpha particles, which irradiate the tissues of the lungs and other organs, potentially causing damage. The severity of the damage has been reported to be responsible for the highest number of deaths from lung cancer among non-smokers (UNSCEAR, 2000). The estimate of the fraction of total deaths from lung cancer due to radon inhalation has been put at 9% for Europe, 10 – 15% for USA and 13.6 – 16.5% on a global scale (Petermann *et al.,* 2020). Regulations and mitigation are therefore important in preventing human beings from the harmful effects of radiation from radon gas. Regulation and mitigation from radon hazard require knowledge of the geographical spread of the radon distribution in a region or country in order to delineate areas requiring attention.

Exposure to Ionizing Radiation

Ionizing radiation exists in the natural environment, and everyone is exposed to it. Exposure differs widely. For instance, at high altitudes, cosmic rays provide more intense radiation, while on the ground, bedrocks and soils release primordial radionuclides which can be inhaled or ingested through food and water. Radon gas contributes more to human exposure to ionizing radiation than other sources. Certain types of bedrock and unconsolidated deposits have been discovered to have high radon levels. Some phosphatic rocks, granites and shales rich in organic materials, for example, have been discovered to contain high levels of radon (Appleton, 2013; Rezaie *et al.,* 2022). Likewise, the design, ventilation systems and building materials of houses strongly influence the level of indoor radon gas and its decay products that contribute to human exposure to ionizing radiation through inhalation (UNSCEAR, 2000).

Radon Hazard and Geogenic Radon Potential (GRP)

Uranium, the parent nuclide of radon-222 is found in soils and rocks, with varying proportions in different locations. Geology is the most important factor influencing radon's presence and distribution (Nuhu *et al.,* 2021). The types of minerals (e.g zircon, tyuyamunite) in which uranium occur determine the release of radon from rocks and soils. The transmitting medium for radon migration into the atmosphere is the soil on top of the bedrock and groundwater. The concentration of soil-gas radon in the top residual soil or overburden is therefore a reflection of the radon concentration in the bedrock as long as the radon is yet to escape into the atmosphere. Therefore, knowledge of the soil-gas radon concentration at a location is

required as it serves as the principal source of indoor radon (UNSCEAR, 2000). After radon gas emanates from bedrock minerals, soil-air permeability of the soil, soil gas characteristics, meteorological parameters (such as air pressure, relative humidity, wind and ambient temperature), soil porosity, soil moisture content and rainfall, all influence radon gas transportation to the soil surface (Appleton, 2013).

Radon concentration indoors constitutes a health hazard and should be kept below the acceptable international reference levels. The World Health Organization (WHO) has set the world reference level for indoor radon at 100 Bq/m^3 (WHO 2016). Table 1.1 shows the reference level for indoor radon concentration set by different regulatory bodies or countries.

The geologically related measure of the potential risk or hazard over a region or at a location that indicates the availability of geogenic radon for infiltration into buildings is described by its Geogenic Radon Potential (GRP) (Petermann *et al.,* 2020). The GRP reveals the potential hazard from radon infiltration and is related to the geology or bedrock because, generally, the subsurface rock holds the uranium which decays to release radon. Geology was discovered to have the most significant influence on indoor radon concentration, among other parameters such as building materials, building type, foundation type, year of construction and floor level (Demoury *et al*., 2013; Nuhu *et al.*, 2021).

Measurements of soil-gas radon concentration and soil-air permeability, spatially distributed over diverse geological formations in a region or country, are used to generate geogenic radon potential maps (Banríon *et al.,* 2022). Geogenic radon potential maps have very useful applications, especially in the control and mitigation of radon gas through environmental health and building control legislation.

Although a geogenic radon potential map does not give direct information on the level of radon concentration in a building, it is more probable that higher health risks can be observed or expected at sites or areas of potentially high radon emissions.

Radon potential maps are generated to indicate where the indoor radon levels are expected to exceed a radon reference level (Banríon *et al.,* 2022).

Table 1.1: Indoor Reference Levels set by International Bodies or Countries

Radon Action Levels (Bq/m^3)	Bodies/Countries
100	WHO (2016)
200	UK (Ajrouche *et al.*, 2017)
300	IAEA (2015)
500	Italy (Bochicchio *et al*., 2019)

As radon is the highest contributor to ionizing radiation, each country must develop measures to control public health risks from this gas, using knowledge of indoor radon concentration and soil-gas radon distribution. It implies the need for indoor radon surveys and soil-gas radon mapping. The International Commission on Radiation Protection (ICRP) has recommended that all countries carry out spatial radon measurements to discover regions of high radon concentration. Most developed and developing countries have embarked on national radon mapping programmes since the 1970s, with a view to generating radon concentration maps leading to setting appropriate standards and action levels (Ielsch *et al.*, 2010; Szabo *et al.*, 2014; Lara *et al.*, 2015; Kropat *et al.*, 2017; Pereira *et al.*, 2017; Mostečak *et al.*, 2018; Idriss *et al.*, 2020). However in Nigeria and most other African countries, data on soil-gas radon concentration are scanty or unavailable (UNSCEAR, 2000). There is, therefore an urgent need for radon surveys to obtain useful data for setting national action levels.

Artificial Neural Network Application to Modelling of Soil-gas Radon Concentration

Measuring soil-gas radon using passive and active techniques has been practiced for over three decades. Patterns and correlations have been reported between soil-gas radon concentration and geological parameters such as lithology (Lara *et al*., 2015; Mostečak *et al*., 2018). Several research studies have used mathematical modelling as a follow-up to field measurements when extensive measurement campaigns could not be carried out (Borgoni *et al.*, 2014; Alrabaiah, 2015; Giustini *et al.*, 2019; Silva and Dinis, 2022). Recently, machine learning has been integrated for effective predictive modelling of soil-gas radon (Petermann *et al.*, 2020; Duong *et al.*, 2021). One of the machine learning procedures is Artificial Neural Network (ANN), a computational and modelling tool patterned after the human nervous system and used to extract a function between two or more independent variables. Using artificial neural network, based on knowledge of geological and permeability features, could help estimate soil-gas radon concentration for areas yet to be covered within a region (UNSCEAR, 2000).

1.2 Statement of Problem

Geogenic radon mapping is used to obtain an inventory of the soil-gas radon concentration in a country in order to ascertain areas of high concentration. In most parts of the world, radon levels in the environment are known and are constantly monitored because of its health effects (Szabó *et al*., 2014; Bossew, 2015).

Rn-222 measurement in Southwest (SW) Nigeria is scanty and there is no adequate coverage of the region, leading to no regulatory guidelines and mitigation measures against radon hazard. The scarcity of data on soil- gas radon concentration in the Southwest region of Nigeria (Farai and Sanni, 1992) is due to several problems such as lack of awareness, non-availability of equipments and inadequate funds. This has not made it possible to have a geogenic radon potential map indicating areas of high radon hazard for the region. Consequently, Nigeria, at present, does not have legislation on building construction guidelines targeted at reducing radon hazard to its citizens.

Due to several reasons, such as lack of equipment and inadequate funds for extensive logistics, comprehensive data acquisition of soil-gas radon concentration and geogenic radon potential over different geological formations has not been possible. This has hampered policy formulation and mitigation measures on radon hazard (Bossew and Petermann, 2022). In order to generate estimates for locations yet to be covered or difficult to access, it is desirable, therefore, to have models generated from existing measured data that would be useful in predicting soil-gas radon concentration and geogenic radon potential.

1.3 Justification for research

Health is wealth and measures to reduce health hazard from ubiquitous radon gas is constantly being implemted. Measures can only be adopted when there is adequate knowledge of the spatial variability of radon in the environment. Data is presently scarce in Nigeria on soil-gas radon concentration and geogenic radon potential. Measuring soil-gas radon concentration and mapping of geogenic radon potential of Southwest Nigeria in relation to underlying bedrock will provide urgently required information about its spatial distribution. Data acquired on soil-gas radon will make possible, identification of radon prone areas for land use planning against associated health risk. The data obtained for Southwest will also be useful for generating soil-gas radon and geogenic radon potential (GRP) maps for Nigeria.

A large number of data is needed to generate maps detailing radon-prone areas (RPAs) in a region or country, which could be extremely expensive. Likewise, because of the cost implication, equipment availability, and logistics consideration, a comprehensive measurement is unattainable. However, the field-obtained data can be useful in developing a model to predict radon levels for areas yet to be covered but for which its geological attributes are known. Therefore developing a model based on measured data is desirable to predict values for the region of interest in this study.

1.4 Aim and Objectives

The aim of this work is to measure soil-gas radon concentration and soil-air permeability for the computation of geogenic radon potential over different bedrocks in Southwest Nigeria and model the field data using Artificial Neural Network.

Towards achieving the aim of this work the specific objectives are:

i. To measure soil-gas radon concentration and soil-air permeability for soils on different bedrock formation in Southwest Nigeria.
ii. To compute the geogenic radon potential for soils on different bedrock formation in Southwest Nigeria.
iii. To determine whether bedrocks significantly contribute to soil-gas radon concentration, soil-air permeability and geogenic radon potential variation in Southwest Nigeria.
iv. To generate soil-gas radon concentration and geogenic radon potential maps for the Southwest Nigeria.
v. To generate a predictive model, using artificial neural network, for soil-gas radon concentration and geogenic radon potential for Southwest Nigeria.

1.5 Organization of Thesis

This thesis is partitioned into five chapters. Chapter one provides background information on radon, concept of geogenic radon potential, importance of mitigation against radon harzard**,** modelling of soil radon concentration, justification for the research as well as the aim and intended objectives.

Chapter two gives the literature review on radon release and transport processes, radon detection and measurement techniques, soil-air permeability,

geogenic radon potential and its classifications, artificial neural network modelling of soil-gas radon concentration as well as related works.

Chapter three contains the methodology adopted in achieving the set aim amd objectives, modelling techniques and assessment.

Chapter four first provides the results obtained from the methodology engaged, followed by the discussion and classification of measured parameters, inferential statistical application and articial neural network modelling outcomes.

Chapter five summarizes major findings of this research, the general conclusion, and its contribution to the body of knowledge. It also provides recommendations for further research followed by the references consulted in the course of the research.

CHAPTER TWO
LITERATURE REVIEW

This chapter reviews well established knowledge and information on radon production, its detection, the link between indoor radon concentration and soil-gas radon concentration, measurement of soil-gas radon using RAD7. It also discusses soil-air permeability and its link with soil-saturated hydraulic conductivity, geogenic radon potential, radon concentration and geogenic radon potential maps. Finally it highlights artificial neural network and its application to modelling soil-gas radon concentration as well as results of relevant previous work.

2.1 Sources of ionizing radiation

Human beings are exposed to ionizing radiation from the environment. Ionizing radiation are emitted by decaying radionuclides in the Earth‘s crust, in water, air, food, building materials and in the human body. The level of exposure differs around the world. Exposure to ionizing radiation differs depending on location and altitude. House design, building materials and ventilation systems also strongly influence indoor radon levels, which contribute significantly to internal doses through inhalation (UNSCEAR 2000).

2.2 Radon

A predominant contributor of ionizing radiation to human beings is radon gas produced within bedrocks and from the overburden soil, which then migrates to the living environment with the potential to build up in confined rooms. Over 50% of human beings exposure to ionizing radiation is from radon (Degu Belete and Anteneneh, 2021). Radon has three major isotopes, ^{220}Rn, ^{219}Rn and ^{222}Rn derived from the radioactive decay series of ^{232}Th, ^{235}U and ^{238}U respectively. ^{219}Rn from ^{235}U in the Actinium series and ^{220}Rn or ‘thoron’ from the ^{232}Th series have comparatively shorter half-lives (3.96s and 55.0s, respectively) and do not contribute as much to radon exposure when compared to ^{222}Rn from the ^{238}U series.

^{238}U has a half-life of 4.5 billion years, and two of its intermediate decay products: ^{230}Th and ^{226}Ra, have half-lives of 75,380 years and 1,602 years, respectively (Guiseppe *et. al.*, 2011).

^{222}Rn is the immediate daughter of ^{226}Ra; it is an odourless, colourless noble gas and hence can migrate through the soil without going into chemical reaction. Its half-life of 3.82 days is long enough to make it diffuse into and build up in living spaces, except such houses are designed and constructed in a way that does not allow radon gas to permeate, or measures are put in place to reduce build-up of indoor radon. As radon builds up in a room, it decays into solid progenies with electrostatic charges that make them easily attached to dust particles and readily deposited in the lung alongside their transformation energy upon inhalation.

Progenies of radon isotopes emit alpha particles having energies between 5.49 to 7.69 MeV. Since alpha particles are charged and relatively massive, their energy is delivered directly to the cells of the lungs, thereby causing damage through ionization. Although the body has mechanisms to repair or replace impacted cells, damaged lung tissue cells can undergo mutation while being repaired and cellular defects may consequently lead to lung cancer (Riudavets, *et al.*, 2022).

2.3 Rn-222 Sub-series

Radon undergoes three types of decay series namely ^{219}Rn from ^{235}U in the Actinium series, ^{220}Rn, or 'thoron' from the ^{232}Th series and ^{222}Rn in the ^{238}U series. ^{222}Rn (half-life of 3.82 days) decays through alpha particle emission (α = 5.49 MeV) to ^{218}Po (half-life of 3.1 minutes) which also decays by alpha particle (α = 6.00 MeV) to ^{214}Pb (Guiseppe *et. al.*, 2011). ^{222}Rn decays through successive emission of alpha and beta particles and ends with ^{206}Pb which is stable with a half-life of 138 days as shown in figure 2.1.

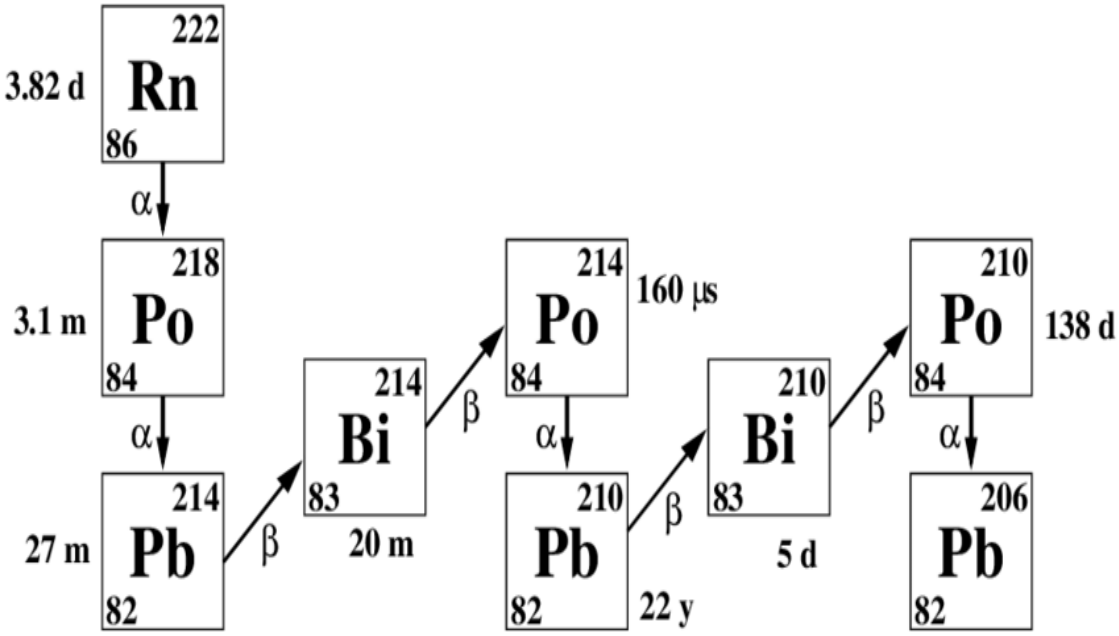

Figure 2.1 Decay Series of Rn-222 (Guiseppe *et. al.*, 2011)

2.4 Health Effects of Alpha Particles from Radon in the Respiratory Tract

In the decay chain of ^{222}Rn, alpha particles are emitted in the 5.49 – 7.69 MeV range. Alpha particles are known to be strongly ionizing because of their charge and mass. They possess very high specific ionization (i.e number of ion pairs formed per unit path length), thereby releasing more than 10,000 ion pairs per cm in air. About 35 eV produces an ion pair (Fourkal *et al.,* 2017). Therefore with the alpha energy range of 5.49 – 7.69 MeV produced in the radon decay series, more than enough lethal doses are released for each radon atom that decays in lung tissues. Compared with electrons, energy from alpha particles is deposited in cells and tissues of the lung in a highly concentrated manner, high enough to destroy the reproductive capability of the cell. In the event the reproductive capability of the cell is not destroyed, the alpha particle energy deposited can cause irreparable damage, which may induce genetic alterations that the cell will pass on to its progeny which could also have a bearing on subsequent events leading to cancer induction (Riudavets, *et al.*, 2022).

As a result of the relatively longer half-life of ^{222}Rn (3.82 days), it can build up in enclosures such as living rooms. When ^{222}Rn builds up in the room, its inhalation can damage lung tissues which can lead to lung cancer. As a result, efforts are always geared towards its measurement and mitigation.

2.5 Radon Emanation from Mineral Grains

The generation of radon depends on the radium concentration and the nature of the host mineral. When radium decays, the alpha particle is ejected and the newly formed radon atom recoils in the opposite direction to the direction of the ejected alpha particle. The position of the radium atom to the mineral grain surface, the direction of the ejected alpha particle and the content of the pores space (whether air or water) between mineral grains determine whether or not the newly formed radon atom enters into the pores space between the mineral grains, becomes embedded in the mineral grain or is transported across to become embedded in another mineral grain. Not all the radon atoms produced by radium, present in a rock or soil grains, are released into intergranular spaces. Between 10 – 50% of the radon produced are released into the pore space (Otton, 1992). When a radon atom is formed after the decay of ^{226}Ra atom, it: (i) may be trapped within the same grain if the grain diameter is large enough to accommodate the recoil distance of the radon atom, (ii) it can shoot across and be trapped in an adjacent grain as it moves across air-filled pore space (iii) it can be

trapped within water molecules present in the pore space or (iv) be released into a pore space if the recoil of the radon atom occurs close to the mineral grain surface. The radon atom that has been released into the pore space moves in the pore space surrounded by adjacent grains. A radon atom released into the pore space can: (i) move in soil-air (usually referred to as soil-gas radon) and be released into the atmosphere, (ii) move and get embedded in water molecules, or (iii) get embedded in other grains lying along its trajectory (Otton, 1992). The speed of the radon in soil depends on the amount of water in the soil pore space, the volume of the pore space in the soil (porosity) and how connected the pore spaces are (soil permeability). The partition of radon between the gas and liquid phases is determined by the relative volume of water in the pore spaces and by temperature because radon solubility decreases in water as temperature increases (Noverques *et al.,* 2020).

The fraction of radon atoms released into soil pore space is referred to as the Radon Emanation Coefficient, and for typical rocks and soils, it has a range of 0.05 - 0.70. The Radon emanation coefficient varies inversely to the radius of the soil grain and depends on the porosity and density of rock or soil particles (Thu *et al.,* 2019). That means radon emanation coefficient depends on the soil grain properties, which are derivable from the bedrock type. Soils derived from the same type of parent bedrock in different regions or locations may, however have contrasting radon emanation coefficients due to the effects of weather on the derivation of soils from their parent geologic material.

2.6 Mechanism of Radon movement through Soil into Buildings

The transport mechanisms of radon atoms released into the intergranular space are by advection and diffusion until the atoms are released through exhalation into the environment. Diffusion of atoms is characterized by random molecular interactions, which result in a net movement of gas molecules from a location of higher concentration to a location of lower concentration. Therefore, the net migration of gas molecules occurs from the soil (having a higher concentration of radon gas) to the atmosphere or to living enclosures where there is a lower concentration. Cracks and holes in the building foundation and walls serve as avenues for radon infiltration into buildings that become trapped in a poorly ventilated indoor environment. Diffusive radon flux density which tends to be constant does not depend on the soil-air to indoor-

air pressure difference or soil-air permeability but on the radioactivity of radon in soil gas and indoor air.

High radon entry rate into buildings also occur through pressure-driven flow processes between the soil, the building substructure and indoor air which is referred to as advection or convection. Advective entry refers to the movement from soil into a building by the bulk flow of soil gas. Small but persistent indoor-outdoor temperature-induced pressure differences are responsible for advective radon entry into buildings. Indoor-outdoor pressure difference, though being a transient phenomenon, may be the reason behind fluctuations observed in indoor radon concentrations. The advective radon flux density can vary over very wide range due to large variation in soil-air permeability. A very important factor that determines the entry of radon is the design and construction of the building foundation, which affects the movement of the air in the soil to the indoor air. The total cross- sectional area of all penetrations through a foundation is known as the open area, which has been found to play an important role in radon entry into houses (Jelle, 2012). The construction of a house tends to compress the soil, distorting the pore size distribution of the soil and changes the spatial distribution of the soil moisture content (as it protects the soil from direct rainfall), thereby affecting the emanation and radon transport parameters.

While advective radon entry involves large volume of radon gas into buildings which require many leakage points, diffusion requires net movement based on differences in radon concentration from higher radon concentration in the soil and lower radon concentration in the indoor air.

2.6.1 Entry of Radon into Houses by Advective Process

Advection is the transport or movement of a substance present in a fluid by the bulk motion of the fluid. Radon gas is present alongside other gases, such as CO_2, in soil gas and the bulk movement of the soil gas determines their transport rate. Entry of soil gas through the advective process into houses is controlled by indoor-soil pressure differences caused by many factors. Indoor air-soil pressure differences can be due to the slow response of the soil-air to outdoor barometric pressure changes compared to the indoor response. These pressure differences are often called transient pressure differences. The ability of soil gas to transmit barometric pressure changes depends mainly on the soil-air permeability (Ka). For a 1m depth, the characteristic time (τ_p) for transmission of pressure disturbance from the soil to the soil surface can range from 0.01s (for a highly permeable soil like gravel) up to 10 days (for a very low permeable

soil as clay). It can be estimated from (Guiteras, 1997):

$$\tau_p = \frac{{L_p}^2}{D_p} \quad (2.1)$$

where L_p is the distance of the propagated pressure disturbance

$$D_p = kP_a(\mu\varepsilon)^{-1} \quad (2.2)$$

where Dp is the "Diffusion coefficient" for pressure disturbance (m^2s^{-1}); k = soil-air permeability (m^2); Pa = atmospheric pressure (Pascal); μ = dynamic soil gas viscosity (P_{as}.s) and ε = soil porosity.

The speed of the radon atom in soil is governed by the soil permeability, soil moisture content and soil porosity. Soil permeability shows the connectedness of one part of the soil to another and controls the ability of the soil to transmit water and air. Equation 2.2 explains why radon experiences more rapid movement in permeable soils, such as coarse sand and gravel than through impermeable soils, like clays, because higher soil permeability results in higher diffusion coefficient.

2.7 Influence of Geology on Indoor Radon Concentration

All rocks contain some amount of uranium, however small. Rocks break down to form soils, which means all soils also contain some uranium, however small. Generally the uranium content in rocks will be about the same content in the derived soil. Radium being the daughter product of uranium is also found in varying proportions in the bedrocks and derived soils and so is radon the immediate progeny of radium. The uranium content of a rock type depends on the mineral content which acts as host to the uranium. Minerals which typically act as hosts to uranium are Uraninite, Zircon, Monazite, Apatite and Plumbogummite (Wu *et al.*, 2021). There are studies establishing a positive correlation between indoor radon and soil-gas radon (Lara *et al*., 2015; Al-Khateeb *et al*., 2017; Pazwash, 2020). Lara *et al.*, (2015) confirmed soil-gas radon concentration and soil-air permeability as good predictive tools for deriving indoor radon as they obtained a good correlation of 0.66. Granites (or Igneous bedrocks) have been found to possess relatively higher soil-gas radon concentrations compared to sedimentary and metamorphic rocks with intermediate radon concentrations. In contrast, basalts and limestone generally possess low soil-gas radon concentrations. There are many exceptions however to this trend.

The soil-air permeability of bedrocks and soils also varies considerably as it is related to the degree of weathering of the bedrock, moisture content, porosity and the presence of faults or cracks. Studies have identified faults in bedrocks as contributing to an anomalous increase of radon concentration over a particular site. In a study conducted by Obed *et al*. (2018), radon concentration was found to be correlated with distances to fault lines and also to the nature of the fault line – whether major fault line or minor fault line. However, values from fault lines cannot be used to determine or model soil-gas radon concentration or geogenic radon potential (Kropat *et al*. 2017).

2.8 Radon Measuremnt and Detector Types

Radon can be detected and measured directly from its α-particle emission or indirectly from its progenies in equilibrium with it (e.g ^{218}Po). Radon detection and measurement are also done by detecting β-radiation from its daughters. Long term measurement of radon is required to determine the average indoor radon concentration under varying weather conditions. This would help determine whether a building or region is radon prone or not. However in order to ascertain the entry or leakage points in a building, continuous but quick measurements are required. The purpose of the radon measurement determines the type of measurement method and equipment to adopt. Methods requiring long term measurement are referred to as passive or time-integrated methods while continuous but quick measurement methods are referred to as spontaneous or active methods. Under active methods we have instruments such as scintillation cells, ionization chambers and electrostatic decay produts collectors e.t.c. Under passive methods we have activated charcoal detectors, electret detectors and etched track detectors, thermoluminiscent detectors e.t.c..

2.8.1 Active Techniques

These are instantaneous measurement techniques that require an external electricity supply that is used to pump air into the detector chamber to function. The technique involves the collection of air for some seconds or minutes, followed by the measurement of radon concentration through its alpha-particle emission. These detector types are briefly described below.

(a) Ionization Chamber detector type

This technique involves filling a chamber with filtered air containing radon. The alpha particle released as radon decays, ionizes the air in the chamber, generating free

electrons. The electrons drift towards the anode while the ions drift towards the cathode, thus generating a pulse. The radon concentration is obtained from the number of pulses produced. The ionization produced is that of radon and its decay products. The total ionization generated can be measured or that of the individual decay products if the associated electronics has the capability to do so.

(b) Continuous Working Level detector type

It involves continuous measurement of the decay product(s) of radon in air in real time. Sampling of radon daughter products is done through continuous pumping of air through a filter. As radon decays to solid daughter products, alpha particles are emitted and counted from the decay of the trapped solid daughters which is used to obtain radon concentration in the sampled air.

(c) Surface Barriers Detector (SBD)

This detector is a p-n junction diode driven in reverse bias condition. Alpha particles ejected during radon decay, go into the depletion region, thus creating electron-hole pairs. Electrons flow towards the anode while the holes flow towards the cathode. An electronic pulse whose amplitude is proportional to the energy deposited by radon is generated from the total number of electrons collected.

(d) Scintillation cells

Scintillation cells were developed by Lucas in 1957. It involves filling a sealed metallic cylinder (containing the Lucas cells) with fresh air through a filter that prevents solid radon daughters from having access into the detector. After the cylinder has been filled, radon decay products, in secular equilibrium with radon, will be formed. The radon decay products release alpha particles. The internal surfaces of the Lucas cells are covered in a scintillator which generates light pulses from the interaction of the alpha particles with the cells. The light pulses generated are counted by a photomultiplier tube.

2.8.2 Time Integrated or Passive Techniques

Time integrated detectors are passive detectors which first acquire information about radon concentration without activation by an external electrical circuit or pumping of air. The information gathered over a long time is processed in a calibrated read-out system to obtain the integrated value of radon concentration within the length

of time. A long-term measurement is required for results that incorporate the effects of environmental and seasonal variations on radon concentration, especially in dwellings. The use of time integrated detectors serves as the most practical means of generating long-term average radon concentration. These detector types are discussed briefly below.

(a) Thermoluminiscent detector type

In this type of detector, radon enters a detection volume where the thermoluminescent dosimeter (TLD) has been placed. A metallic plate (usually previously charged for improved collection efficiency) is positioned a short distance before the TLD. Radon daughters are deposited on the plate, which ultimately decays, releasing energy that is absorbed and stored in the TLD. After adequate exposure, the TLD is retrieved and read in a TLD reader. This TLD reader is a very small oven filled with nitrogen. The temperature of the nitrogen is increased at a well-controlled rate. The amount of light emitted by the TLD which falls on the photomultiplier's photocathode, is translated into an electrical signal and counted as a measure of radon concentration.

(b) Solid State Nuclear Track Detectors (SSNTDs)

Solid State Nuclear Track Detectors (SSNTDs) or etched-track detectors are cellulose esters (nitrate and acetate) or polycarbonates (e.g CR-39) which exhibit different sensitivity. SSNTDs are sensitive to alpha particles which are heavily charged but are, to a large extent, not sensitive to gamma and beta rays as they do not produce etchable tracks. A major advantage of SSNTDs is that they are mostly unaffected by low temperatures and humidity. They offer unique characteristics for long-term radon gas measurement, especially for large-scale surveys (Tommasino, 1990). SSNTDs are of various types, such as CN-85, LR-115, CR-39, etc.

(c) Solid State Alpha detector type

A solid state alpha-particle detector is a semiconductor material, usually of silicon which uses electrostatic collection of alpha particles, thereby converting alpha radiation to electrical signals. Energy deposited by alpha particles ionizes the silicon detector atoms, thereby creating electron-hole pairs swept to opposite electrodes by an applied electric field. The current generated is proportional to the alpha particle energy transferred and generally well distinguished from the electronic noise of the counter as

a result of the high quantum efficiency. The advantages of solid state alpha particle detector in radon measurement are their ruggedness and ability to distinguish between each alpha particle from radon daughters.

(d) Charcoal Canister detector type

Activated charcoal can absorb and retain radon. In this detector type, canisters filled with activated charcoal are left exposed to air for a few days to collect as much radon gas as possible. The radon absorbed and retained by the activated charcoal is counted using liquid scintillation counters or by gamma spectroscopy.

(e) Electret detector type

An Electret Ion Chamber (EIC) is an integrated ionization chamber containing the electrets made of charged Teflon discs. The special procedure used in processing the Teflon requires that the charges be retained and stable even at low/high temperatures and high humidity. The Electret Ion Chamber (EIC) serves as both the sensor and source of the electrostatic field. The ions produced during radon decay inside the EIC chamber are collected by the charged electret which results in reduction of the ions on the electret. The reduction in ions is a measure of the total ionization during the period that the electret is in the volume of the chamber. A portable electret voltage reader measures the charge on the electret before and after the exposure. The EIC is commercially produced as Electret Passive Environmental Radiation Monitors (E-PERMs).

2.9 RAD7 Alpha Detector

The RAD7 is a highly versatile active radon measuring device that uses or incorporates solid state alpha-particle detector that can measure radon concentration in air, soil gas and radon dissolved in water. It is a fast, compact and rugged equipment which measures radon concentration in real time.

Soil gas radon measurement is used to assess the subsurface conditions and potential environmental risks associated with radon emanation from bedrock and groundwater.

RAD7 (Plate 2.1) is a continuous, active radon measuring device produced by Durridge Company Incorporation (USA). RAD7 is a Sniffer gadget that uses the 3.05-minute alpha decay of ^{218}Po and the 0.16s alpha decay of ^{216}Po to determine Rn-222 and Rn-220 concentrations. The RAD7 has a silicon alpha particle detector placed at the

Plate 2.1 RAD7 radon Detector (Mily *et al.*, 2016)

centre of a hemispheric chamber of volume 0.7 litre, coated on the inside with an electrically conducting material charged to a potential of 2000 to 2500V relative to the detector, thus creating an electric field inside the hemisphere. On entering the detector chamber, the ^{222}Rn gas decays by alpha particle emission into ^{218}Po, which also decays to ^{214}Pb. The decay of ^{222}Rn to polonium (^{218}Po) within the hemisphere leaves its transformed nucleus as a positively charged ion. The strong electric field generated within the hemisphere propels the positively charged ions to the silicon detector, to which it sticks.

When the ^{218}Po nucleus decays on the silicon detector's surface, it releases alpha particles, which ionize the silicon detector, thereby generating a pulse of electrical signal proportional to the alpha particle energy. The microprocessor in the system filters, amplifies, sort and stores the electrical signal according to their signal strength in a spectrum of 200 channels. The read-out of the equipment displays the radon concentration in Bqm^{-3}. The microprocessor groups the generated signal into a range between 4 and 750000 Bqm^{-3}.

Generally, soil radon measurements are taken at 80 – 100 cm depth because, at depths shallower than 80 cm, soil gas may be affected by surface processes, e.g temperature and moisture content variation. At depths greater than 100 cm, radon soil gas may be affected by anaerobic conditions or other gases such as methane or carbon dioxide. Therefore 80 – 100 cm is considered the optimal depth for soil radon measurements to minimize interference and to obtain reliable results.

Figure 2.2 presents a schematic diagram of RAD7 for measuring soil gas radon. The probe shaft with an inner diameter of ¼ inch (6.35 mm) is pushed to a depth of 80 – 100 cm. The probe is joined to a air pump through a air filter, and a vacuum pump gauge is attached to a desicant. The inlet air filter prevents solid daughters of ^{222}Rn and dust particles from accessing the detector chamber. Desiccant consists of cobalt chloride, which absorbs moisture from incoming air and keeps relative humidity under 10% because the detection efficiency of RAD7 decreases as humidity increases due to the neutralization of polonium ions by water particles (RAD7 User Manual, 2012).

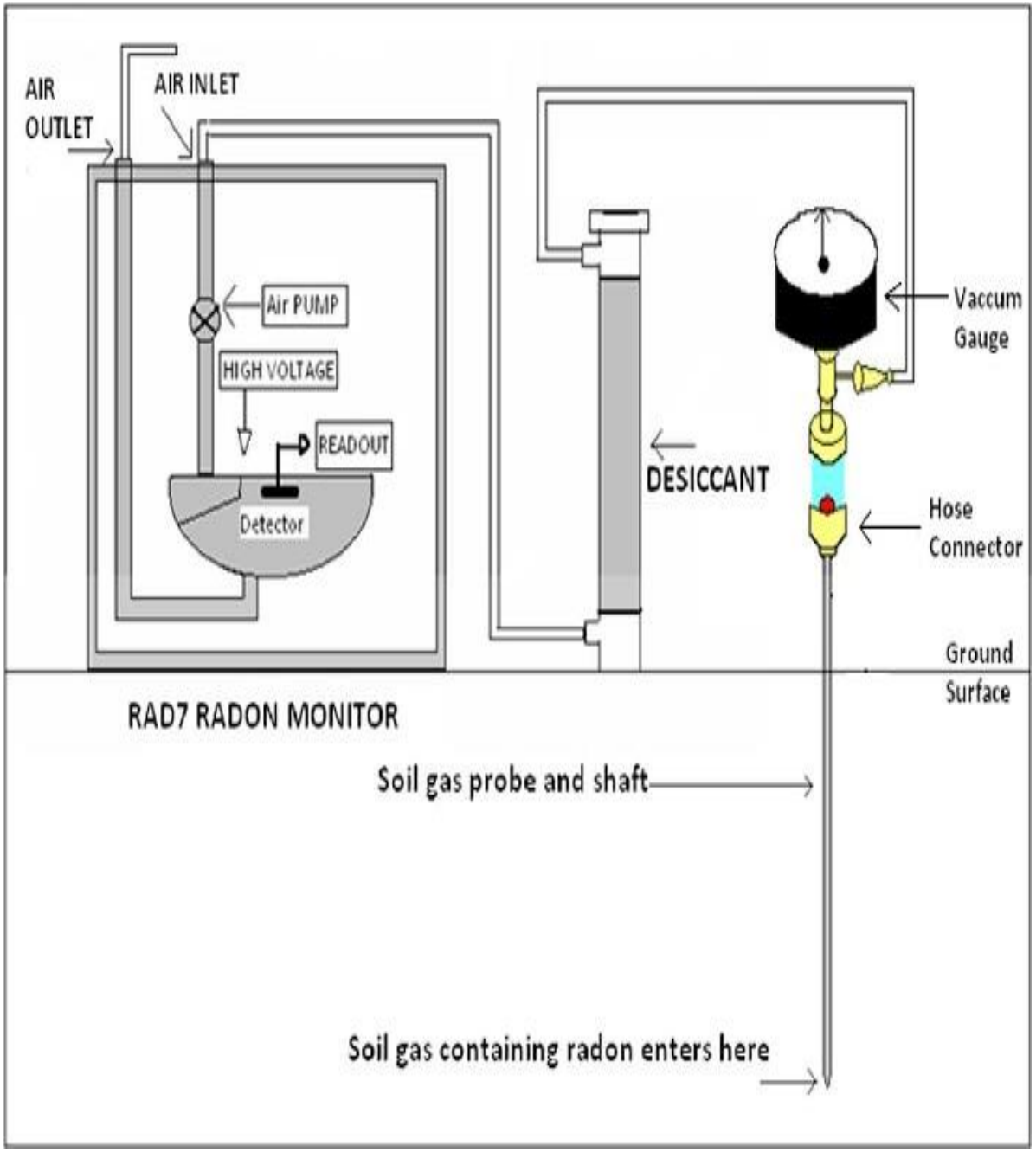

Figure 2.2 Schematic Diagram showing RAD7 Radon Monitor Setup (Ravikumar *et al.*, 2015)

2.10 Soil-air Permeability – Definition, Attributes and Applications

Soil is made up of irregular-shaped solid particles in different sizes arranged in no particular order, which also contain air and water (fluid) in their interstices or voids. The size and arrangement of the soil particles (i.e soil texture) determine the soil pore geometry. The existence and arrangement of interconnected interstices or voids through which water and air can flow determine how permeable the soil body is. Soil permeability, a property of the soil, is a reflection of how soil is able to transmit air or water. The permeability of a porous medium is the quantity of fluid of unit viscosity flowing per unit time under a unit pressure gradient through a unit cross sectional area of a unit length (Hillel, 2004). A soil body is highly permeable when fluid can flow through it easily (e.g gravels), and it can be low in permeability if fluid cannot easily flow through it (e.g clay). There are two main types of soil permeability, namely soil-water permeability (which can be either saturated or unsaturated) and soil-air permeability. Saturated soil water permeability is also referred to as saturated hydraulic conductivity (Ks) while unsaturated soil water permeability is also referred to as unsaturated hydraulic conductivity ($K(\theta)$ which can be measured in m/s, m/day, etc. Soil-air permeability is measured in m^2. The older unit of soil-air permeability is the Darcy where 1 Darcy = 9.87×10^{-12} m^2. The permeability of partially saturated soil (usually referred to as unsaturated hydraulic conductivity ($K(\theta)$) is lower than that of fully saturated soil (K_s) (usually referred to as unsaturated hydraulic conductivity).

When water or air passess through a soil column at a particular water content, water takes liquid-filled pores and air takes gas-filled pores. The increase in soil water content raises soil water permeability and lowers soil-air permeability. Thus it is speculated that a close relation or function must exist between soil water permeability and soil-air permeability. Soil-air permeability (K_a) is very low or negligible in water-saturated soil; thus, soil-air permeability (K_a) and soil water permeability are inversely proportional but non-linear (Petermann *et al.*, 2020).

Permeability application in soil usage is important because it influences the rate at which saturated soils settle under applied load. It is also required in the design of earth dams and retaining structures, as well as in studying the rate of transmission of gases from bedrocks to the soil surface.

Factors that affect the permeability of soils are – grain size, void ratio, properties of pore fluid, adsorbed water, soil stratification, entrapped organic impurities in water, shape of soil particles, degree of saturation and temperature.

Permeability is approximately proportional to the square of the effective diameter of the grain size (D_{10}) (Gupta and Ramanathan, 2019). As the void ratio increases, the available area for fluid flow also increases; hence permeability also increases. Permeability varies proportionally with the temperature of pore fluid, which is inversely proportional to the viscosity of pore fluid. Therefore permeability is also inversely proportional to fluid viscosity. Adsorbed water (or capillary bound water) is the thin microscopic film of water that surrounds individual soil grains, which are not free to move, thereby reducing the effective pore space. This consequently reduces the permeability of the soil. The presence of organic impurities hinders the flow of fluid, thus reducing permeability. Soils are formed or deposited in stratified layers on one another. Flow of water can be parallel or vertical to the stratified soil. If the flow is parallel to the layers of stratification, the permeability will be high, but if flow is perpendicular in direction to the layers, then soil permeability will be low.

2.11 Dependence of Soil-gas Radon on Soil-air Permeability

Radon generation depends on the amount of uranium in the soil and the characteristics of the host mineral. Migration of radon to the atmosphere is, however, to a large extent, independent of the uranium content and the host mineral. As soon as radon is emitted from the host mineral into the interstices, other factors like the fluid transmission characteristics of the bedrock and overlying soil take over. A major factor that determines transmission rate of radon gas into the atmosphere from the production site is soil-air permeability, an intrinsic property of the bedrock or overlying soil. Permeability of radon-bearing soil, apart from geology, is the second most important factor that determines indoor radon concentration enhancement (Yalım *et al.*, 2018). Infiltration of soil-gas radon into living spaces depends on the flow of soil-air from the porous soil media (i.e soil-air permeability) and also on gaps or openings in structures in contact with soil and air-permeable building blocks (Arvela *et al.*, 2016). As observed in equation 2.2, the radon entry rate is determined by the diffusion coefficient (D_p) for radon entry into a building. However, the total radon flux density (the transfer rate of radon per unit area from the earth to the atmosphere measured in $Bqm^{-2}s^{-1}$) is a combination of diffusive flux density ($Ø_d$) and advective flux density (Øa) (Guiteras, 1997):

$$\emptyset = \emptyset_d + \emptyset_a \tag{2.3}$$

$$\emptyset_d = -D_e \nabla C_{Rn} \quad (2.4)$$

where D_e is the effective diffusion coefficient (m^2s^{-1}) and C_{Rn} is the soil-gas radon concentration.

$$\emptyset_a = \frac{C_{Rn}}{\varepsilon}\frac{K_a}{\mu}\nabla P \quad (2.5)$$

where ε = soil porosity, K_a = soil-air permeability, μ = dynamic viscosity of the soil gas phase of the soil pores (P_a.s) and ∇P = the soil-to-air pressure gradient (P_a). From equation 2.4, it can be observed that the radon flux density is proportional to the gradient of the soil-gas radon concentration, and the radon flux density is also proportional to the soil-air permeability in equation 2.5. Consequently, combining equation 2.4 and 2.5, soil-gas radon concentration is dependent on the soil-air permeability. Furthermore, the effective diffusion coefficient of radon in soil gas depends on porosity and soil water content; likewise, the soil-air permeability depends on soil porosity, soil water content and the soil type (i.e shape and size of the pores).

2.12 In-situ measurement of Soil-air Permeability using Radon-JOK

Measurement of soil-air permeability should be done simultaneously with that of the soil-gas radon concentration. The RADON-JOK (a form of a permeameter), as shown in Plate 2.2, is a portable equipment fabricated for in-situ measurements of soil-air permeability.

The determination of soil-air permeability is based on Darcy's equation. The RADON-JOK equipment is set up in the field as shown in Plate 2.3. It operates based on the withdrawal of air under negative pressure (pressure less than atmospheric pressure). A probe is inserted into the same hole where soil-gas radon was measured. Air goes through the probe head that is in close contact with soil at constant pressure. To achieve close contact with soil air, the probe head is pulled back by about 5 cm, thus allowing the special rubber sack attached to the probe head to draw air from the soil. Soil-air permeability (K_a) is determined from a form of Darcy's equation (2.6) using measured airflow through the probe, which is calculated from air volume in the rubber sack and pumping time. The soil is assumed to be incompressible, homogenous and isotropic.

The air flow can be expressed as (Neznal, 2005):

$$Q = \frac{a\,K_a\,\Delta P}{\mu L} \quad (2.6)$$

where Q is the volumetric flow rate in m^3s^{-1}, ΔP is the pressure difference across the sample ($kgm^{-1}s^{-2}$) , a is the cross sectional area (m^2), L is the length of the sample (m) and μ is the dynamic viscosity ($kgm^{-1}s^{-1}$).

Equation 2.6 can be rewritten as (Neznal, 2005):

$$q = \frac{K_a \Delta P F}{\mu} \tag{2.7}$$

where F now represents the shape factor regarded as an estimate of the $\frac{a}{L}$ quotient.

The shape factor F can be calculated from (Neznal, 2005);

$$F = \frac{2\pi l}{\ln(\frac{2l}{d})(\frac{4D-l}{4D+l})} \tag{2.8}$$

where D is the subsurface depth (m), l (m) and d (m) are the length of the probe head and the diameter of the probe head, respectively.

Plate 2.2 **RADON-JOK Equipment for in situ Soil-air Permeability Measurement (Mezon, 2017)**

Plate 2.3 RADON-JOK Equipment set up in the Field (Mezon, 2017)

2.13 Other Indirect Methods of measuring Soil-air Permeability

The soil-air permeability is a function of the soil's porosity, pore shape, pore-size distribution, pore tortuosity and connectivity. As a result, determining soil-air permeability is always difficult because of its relationship with other parameters that can influence its measurement. Soil-air permeability is usually measured using direct in-situ measurement based on soil gas withdrawal under negative pressure or by particle size analyses. The main disadvantages are that, in the case of particle size analyses, other factors influence the permeability, such as soil density, soil moisture and effective porosity, which should be taken into consideration. In the case of soil-gas withdrawal by negative pressure, the results strongly depend on variation at a very small volume of the soil and the limitation of the equipment in measuring soils with extremely low or high permeability (Tuli *et al*., 2005).

Due to the difficulty associated with direct measurement of soil-air permeability, other indirect methods are usually engaged in its estimation. Also, in a situation where the RADON-JOK is not available, an alternative means is to measure a parameter that is directly related to the soil-air permeability. Soil-air permeability is usually determined from other parameters, such as porosity, saturated hydraulic conductivity, e.t.c., using predictive models. Suharyatun *et al.* (2023) and Tang *et al.* (2011) used predictive models to determine soil-air permeability from soil total porosity and soil type. Likewise, Rahmati *et al.* (2019) used modelling to predict saturated hydraulic conductivity from soil-air permeability measurements. These indirect methods can be characterized as fast and cost effective in obtaining the magnitude and spatial variability of soil-air permeability.

An indirect method of obtaining the soil-air permeability is making use of the established relation between the soil-saturated hydraulic conductivity (K_s) and the soil-air permeability (K_a) as developed by Loll *et al.* (1999). In the study, saturated hydraulic conductivity was measured using tension infiltrometers and soil-air permeability was obtained using a portable air permeameter both in the laboratory and on site for small scale and large scale measurements. Different matric potential were used ranging from -10 to -100 cm H_2O to obtain the soil-water characteristics curve. In the calculations, a linear prediction relationship was discovered among the measurements of saturated hydraulic conductivity (Ks) in (m/d) and soil-air permeability (K_a) in (m^2).

A relation of the form:

$$\text{Log}(Ks) = \alpha \text{Log}(K_a) + \beta \quad (2.9)$$

where α is the slope and β is the intercept of the Log(Ks) against Log(K_a) plot.

The Log-Log relationship obtained by Loll *et al*. (1999) was found to be

$$\text{Log}(Ks) = 1.27\text{Log}(K_a) + 14.11 \quad (2.10)$$

The Log-Log relationship had prediction accuracy greater than 0.7 order of magnitude at the 95% confidence level. Although the relation was found to perform best at -100 cm H_2O matric potential, it was recommended for use even at other matric potential.

The Log-Log relation obtained by Loll *et al.* (1999) was used by Iversen *et al*. (2003, 2004) with different soil sample sizes and matric potential. The Log-Log relation obtained by Iversen *et al.* (2003, 2004) fit reasonably well with that obtained by Loll *et al*. (1999). It was confirmed that neither the size of the soil sample nor the different soil water matric potential had a major effect on the Log-Log prediction relationship between soil-air permeability (K_a) and soil-saturated hydraulic conductivity (K_s) (Iversen *et al*., 2003). It therefore means that a general Log-Log prediction relationship as derived by Loll *et al*. (1999) can be used on nearly all soils (Iversen *et al*., 2004).

2.13.1 Hydraulic Conductivity

Hydraulic conductivity is an important parameter used in soil science. It is defined as the rate of flow of water seeping into the soil under a unit hydraulic gradient expressed in units of metres/day (m/d), centimetre/hour (cm/h), metres/seconds (m/s) e.t.c. (Kirkham, 2005). It has a wide range of values depending on the type of porous medium and prevailing conditions. The typical range of hydraulic conductivity is from 10^{-7} to 10^{-3} m/s in most soils.

In saturated soil, hydraulic conductivity is referred to as saturated hydraulic conductivity (K_s). It is defined as the water movement rate through a soil column when all soil pores are filled with water (or are conducting water). When the soil is unsaturated, the hydraulic conductivity is referred to as the unsaturated hydraulic conductivity (K(θ)), which is the rate of movement of water through unsaturated soil pores (Lal and Shukla, 2004). Hydraulic conductivity is sometimes denoted as the coefficient of permeability. In

fully saturated soil, soil-air permeability is almost negligible, and as a result, there is an inverse relationship between the saturated hydraulic conductivity and the soil-air permeability, which is non-linear (Petermann *et al.*, 2020). The hydraulic conductivity depends on the viscosity of soil fluid, soil grain size and the structure of the soil matrix. Generally, the porosity of soil is related to hydraulic conductivity because the more porous a medium is, the higher the hydraulic conductivity and vice versa.

The study of hydraulic conductivity is very useful in agriculture as it relates to soil classification for good crop yield, analysis of irrigation systems for crop production, fertilizer migration through soil, and study of nutrient transport in plants. Hydraulic conductivity is also important in engineering for the design of irrigation projects, drainage systems for roads and erosion control (Moreira *et al.*, 2007).

2.13.2 Methods of measuring Saturated Hydraulic Conductivity

Methods of measuring saturated hydraulic conductivity are grouped into correlation method and hydraulic method. The correlation method is based on applying models between other easily determined soil parameters and saturated hydraulic conductivity. Correlation method uses grain size distribution, pore size distribution, soil texture and soil mapping. The advantage of the correlation method is that an estimate of the saturated hydraulic conductivity value is often quicker and simpler than using the hydraulic method. A cause for concern however, is the inaccuracy of the relationship used in the correlation method, which may introduce random errors. This is due to the saturated hydraulic conductivity being a complex function of packing, soil structure, soil heterogeneity and other factors that may not be accounted for in the empirical relationship or model developed.

The hydraulic method of measuring saturated hydraulic conductivity is based on applying Darcy's law using values of hydraulic head and liquid discharge rate observed under preset flow conditions. Although the hydraulic method is more labour intensive than the correlation method, it is still more reliable and eliminates random errors involved in the correlation method.

Hydraulic method can be in two forms, laboratory and in-situ field methods. The in-situ field method can also be small scale or large scale in nature. The in-situ field

methods normally represent the hydraulic conductivity value of bigger soil volume compared to laboratory methods. Large scale in-situ methods reduce variability in results but are more expensive and time-consuming than other methods. Both large scale and small scale in-situ field methods involve driving instruments into the soil to ensure proper contact with soil but also result in distortion of the soil matrix.

Small scale in-situ method is in two groups, namely those used to determine the hydraulic conductivity above the water table and those used to determine hydraulic conductivity below the water table. To measure the saturated hydraulic conductivity of an unsaturated soil, sufficient water to obtain near-saturation conditions (usually referred to as satiation) must be applied. This method is called infiltration method.

To measure the saturated hydraulic conductivity of a saturated soil, water must be removed from the soil, thus creating a sink. The flow rate is observed together with the hydraulic head induced. This method is called the extraction method. A drawback of the small scale in-situ method is that the imposed flow conditions often do not represent the flow conditions corresponding to the drainage systems in the soil profile.

2.13.3 Use of Darcy's Equation for Saturated Hydraulic Conductivity determination

Most of the different methods used to determine soil hydraulic conductivity, both in the laboratory and on the field, use Darcy's equation or a form of it. In the mid-19th century, Henri Darcy, a French Engineer in the city of Dijon, while using sand filters to conduct an experiment for the best water supply system, discovered a very important physical relationship of fluid-porous media interaction now known as Darcy's equation (Hillel, 2004):

$$q = -K\frac{dh}{dl} \tag{2.11}$$

where q is the flux or the volume discharged (i.e the amount of water collected and measured) through a cross-sectional area perpendicular to the direction of flow per unit time through the soil column; K is the hydraulic conductivity (unit of m/s); and d*h/dl* is the hydraulic head gradient along the flow path. The negative sign in equation 2.11 indicates that the flow is along the direction of the decreasing gradient and, q has a velocity dimension, called the Darcian velocity.

Hydraulic head or hydraulic potential (sometimes called matric potential) is a way of expressing the energy status of water in the soil. Water moves from higher to lower elevation in response to gravitational force. This occurs due to differences in the potential energy of the water at the higher elevation to the lower reference level. The hydraulic head ($h=P/\rho g$) is used to express the potential energy of water. Since the unit of hydraulic head is in metres, it is usually measured by the height of water above a reference (e.g., mean sea level).

Darcy's equation can also be written as (Hillel, 2004):

$$Q = -KA\frac{dh}{dl} \tag{2.12}$$

where Q is the amount of water (θ) discharged per unit time (t); perpendicular to a constant cross-sectional area A of the soil column, and $\frac{dh}{dl}$ is the hydraulic gradient.

Then equation (2.12) can be rewritten as (Moreira *et al*., 2007):

$$\frac{d\theta}{dt} = -K(\theta)A\frac{dh}{dl} \tag{2.13a}$$

Or $$\frac{\partial\theta}{\partial t} = -K(\theta)A\frac{\partial h}{\partial z} \tag{2.13b}$$

Therefore hydraulic conductivity is a function of the soil water content (θ) and the total hydraulic head (h) (Moreira *et al*., 2007).

Measuring change in water content at intervals of time (i.e $\partial\theta/\partial t$) and also the hydraulic head ($\partial h/\partial z$) with a constant head permeameter (figure 2.3) followed by the plotting of $\partial\theta/\partial t$ against $\partial h/\partial z$ will yield the hydraulic conductivity.

A common form of equation 2.12 used in obtaining the saturated hydraulic conductivity (K_s) is given by:

$$K_s = \frac{Q^I \; X \; L}{A \; X \; t \; X \; (h+L)} \tag{2.14}$$

where Q^I, in this case, is the volume of water (in cm^3) collected at preset time intervals (t in minutes), L is the length of the porous medium (in cm); A is the cross-sectional area of the sample (in cm^2) and h is the hydraulic head maintained during the measurement.

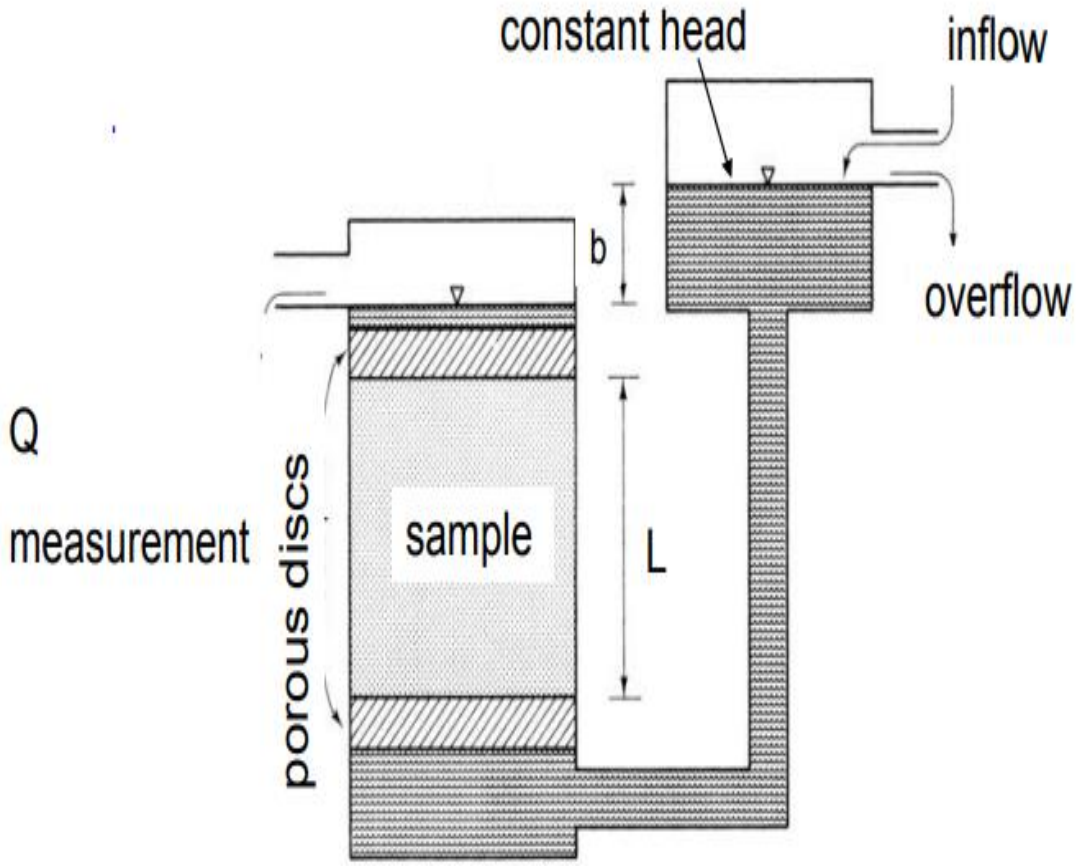

Figure 2.3 Experimental Set-up of Constant Head Permeameter (Brikowski, 2013)

2.14 Geogenic Radon Potential and its Applications

The geogenic radon potential (GRP) is the property of bedrock or soil to release radon gas into soil air and, together with the soil air, make radon available at the ground surface (Bossew, 2015). GRP measures the potential risk due to radon produced from within the earth which becomes an actual risk under certain additional factors. GRP is determined from the quotient of the soil-gas radon concentration and the soil-air permeability. Indoor radon concentration is dependent on a combination of geogenic radon potential and other factors such as living habits, house design and radium concentration in construction materials e.t.c. This implies that indoor radon concentration can be high (e.g if concstruction materials have high radium content) even if the geogenic radon potential is low.

Sites or regions are classified as 'radon prone' based essentially on two concepts. The first concept is based on the measurement of actual indoor radon gas and the second on the geogenic radon potential.

Based on the first concept, a location is classified as Radon Prone Area (RPA) if the indoor radon exceeds a certain national or regional mean value or reference value. However, the status of the RPA in such a location can change if other anthropogenic parameters which control the indoor radon gas also change. When such anthropogenic factors change, the air exchange rate between the building and surrounding air also changes. Based on the indoor radon concept, a more specific definition for RPA has been adopted, which states that "radon prone area is a geographical area or region defined as a result of measurement surveys indicating that the percentage of dwellings expected to exceed the national reference value is significantly higher than in other parts of the country" (Bossew, 2015).

However, there is a problem associated with the RPA definition based on the concept of indoor radon concentration due to the difference in the adoption of the definition by different countries, which introduces inconsistency. For example, an area designated as RPA in, say the Netherlands, where radon concentrations are generally very low, cannot be classified as radon prone across its border in Germany, where mean indoor radon concentration is high even if they have the same geological properties. This

underscores why extensive indoor radon measurement campaigns are encouraged by UNSCEAR for each country to have a national threshold or reference value towards clear demarcation of RPAs in each country or region. Also, such data is required from each country in order to have a standard worldwide mean indoor radon concentration value that is truly representative. The values of 30 Bqm^{-3} and 40 Bqm^{-3} for the geometric and arithmetic means obtained using available data are still in use (Akamba *et al.*, 2022). There is, therefore, an urgent need to generate regional and country-wide data for each country in order to have better global geometric and arithmetic mean values for indoor radon concentration. It is important to note that some countries have adopted the concept of RPAs as defined by the International Commission on Radiological Protection (ICRP). ICRP defined RPAs as a geographic area or administrative region, based on measutrements, having a notably elevated level of radon concentration compared to other areas in the region or country (ICRP, 2012).

The second concept of defining radon prone areas (RPAs) rests on the geogenic factor, the most important contributor to indoor radon, among other controlling factors. The geogenic radon potential quantifies the geogenic factor. According to this concept, a location within several other locations is designated radon prone area if the geogenic radon potential at the location exceeds a threshold or reference value. The geogenic radon potential is a quantity that is independent of anthropogenic factors such as living habits, building patterns, etc. Therefore, the status of an area designated as RPA, under geogenic radon potential, does not change unless the threshold or reference value changes. The threshold or reference value can change if the values of the soil-gas radon concentration or the soil-air permeability change, as these two parameters determine the geogenic radon potential of an area. Defining RPAs in terms of geogenic radon potential is more reliable due to its relative consistency barring any sudden soil excavation event or soil redistribution (Szabo *et al*. 2014).

2.15 Influence of Geology on Soil-gas Radon and Geogenic Radon Potential

Use of geological parameters to generate geogenic radon potential for mitigation purposes is appropriate where indoor radon concentration measurement of only a small number of the total houses in a region or country has been done (Banríon *et al.*, 2022;

Aghdam *et al*., 2022). Studies have established a positive correlation between soil gas radon and geological formations with soil related parameters (Akerblom, 1995; Miles and Appleton, 2005). Studies have also established observable trends of soil-gas radon concentration with geological formations, which may provide a guide to associating certain geological formations with a range of values of soil-gas radon concentration (Korany *et al*., 2013; Szabo *et al*., 2014; Lara *et al*., 2015; Yousef *et al*., 2015; Pereira *et al*., 2017; Esan *et al*., 2020). For example, some studies have observed that granites possess higher radon concentrations when compared with other bedrocks (Pereira *et al*., 2017; Mostečak *et al*., 2018; Cho and Choo, 2019). Gneisses and limestones have also been observed to possess medium to high radon concentration values (Mostečak *et al*., 2018; Siegesmund, 2022). Likewise, some phosphatic rocks and shales of high organic material content have been found to contain high radon concentration (Appleton, 2013; Siegesmund, 2022).

2.15.1 Classification of Soil-gas Radon Concentration

In order to delineate a region as having a high radon concentration, it must be done using a reference value. Different methods or procedures have been used previously for delineation, but recently a new method based on the Swedish or Akerblom criterion has been adopted. The criterion serves as a means of risk assessment and was established by developing a classification based on radon concentration in soil gas (Akerblom, 1987). This criterion states that soil having soil-gas radon concentrations below 10.0 kBq m^{-3} (270 $pCiL^{-1}$) are grouped as "Low"; soil-gas radon concentration between 10.0 and 50.0 kBq m^{-3} (270–1,350 $pCiL^{-1}$) are classified as "Normal" which would require some protective actions for existing houses and new constructions. Soils that present radon concentration above 50.0 kBq m^{-3} (CRn > 1,350 $pCiL^{-1}$) are to be classified as "High" and would require special safety criteria against radon for any building sited on such soils (Lara *et al*., 2015, Nuhu *et al.*, 2021). This classification has gained wide acceptance and has been used in several studies involving country-wide measurement campaigns (O'Brien, 2011; Lara *et al*., 2015, Nuhu *et al.*, 2021).

2.15.2 Determination and Classification of Geogenic Radon Potential (GRP)

The geogenic radon potential (GRP), is conceptually designed to express the hazard posed by the infiltration of geogenic radon from the subsurface towards the soil surface and specifically into buildings (Bossew *et al*., 2015; Nuhu *et al.*, 2021). The GRP reveals the potential risk as it relates to the geology or bedrock because the subsurface rock holds the uranium which decays to release radon. Soil-gas radon concentration and its moderation by soil-air permeability are the required parameters for obtaining the geogenic radon potential.

The GRP is obtained using the equilibrium activity concentration (C_∞) of ^{222}Rn in soil gas (in $kBqm^{-3}$) and the effective soil-air permeability (in m^2) (Neznal *et al*., 2004; Petermann *et al.*, 2020; Nuhu *et al.*, 2021):

$$GRP = \frac{C_\infty}{(-Log(K_a) - 10)} \tag{2.15}$$

In practice, the equilibrium activity concentration (C_∞) is the soil-gas radon concentration (C_{Rn}) between 80 – 100 cm soil depth. As a result of the wide range of soil-air permeability that spans several orders of magnitude, the GRP is adjusted using the logarithm of soil-air permeability. Because GRP represents a relative measure rather than an absolute quantity and was developed semi-empirically and not theoretically, priority is given to its value as a radon hazard indicator rather than its unit (Petermann, *et al*., 2020).

Many research studies have reported the classification of GRP by combining different controlling factors such as geology, topographic features, soil-gas radon concentration and soil-air permeability. The most popular classification is that according to Neznal (table 2.1) which is based on the soil-gas radon concentration and the soil-air permeability (Neznal *et al.*, 2004; Nuhu *et al.*, 2021; Aghdam, 2022).

According to Al-bakhat *et al*. (2017) and Barnet *et al*. (2010), Low GRP (GRP < 10) could lead to < 230 Bqm^{-3}, Medium GRP (10 < GRP < 35) could lead to 230 – 460 Bqm^{-3} while High GRP (GRP > 35) could lead to > 460 Bqm^{-3} in indoor radon concentrations.

Table 2.1 Classification of Geogenic Radon Potential (Neznal *et al.*, 2004)

S/n	Geogenic Radon Potential	Risk Classification
1	GRP < 10	Low
2	10 < GRP < 35	Medium
3	GRP > 35	High

Several studies have determined the geogenic radon potential (GRP) in different regions and countries such as Hungary (Szabó *et al*., 2014); Brazil (Lara *et al*., 2015); a nuclear site in Iraq (Al-bakhat *et al*., 2017); Central Portugal (Pereira *et al*., 2017); Croatia (Mostečak *et al*., 2018); Switzerland (Kropat *et al*., 2017); Germany (Bossew, 2015); France (Ielsch *et al*., 2010) and Central Italy (Giustini *et al*., 2019) to mention a few.
From these studies, areas of low, medium and high GRP were identified and used to generate GRP maps.

GRP maps can be used:

a. as a predictive tool to estimate indoor radon concentration for prospective buildings to be built in newly developing areas.
b. to locate regions where, based on GRP values, a higher number of existing houses would be expected to have enhanced indoor radon values.
c. to determine if radon protective measures would be required in newly opened construction sites or areas.
d. to create public awareness targeted at areas prone to high radon emission.
e. to present a radon potential assessment for property developers and buyers in a particular area.
f. to generate data for epidemiological studies on the relationship between radon and lung cancer.
g. to communicate effectively with developers planning to build new homes in radon prone areas with regards to protocols to follow when building in such areas.
h. to maximize use of limited resources as it helps to focus attention to the right locations where radon mitigation measures are required.

2.16 Role and Application of Inferential Statistics in Radon Studies

Inferential statistics play a major role in radon studies because it helps to analyse and draw cogent inferences from the measured data. Some of the applications of inferential statistics are:

a. It helps to estimate parameters related to radon concentration in air, soil or water. For example, it can be used to identify households with expected radon levels above a given threshold in a region or country. Usually this estimation is derived

from confidence intervals within which the true population is likely to fall (Esan *et al.*, 2020).

b. Inferential statistics can be used to study trends in different structures with regards to indoor radon concentration with the aim of drawing tangible conclusions. For example, a study might be interested in finding out if there is a significant difference in radon levels between houses built with concrete and those built with bricks.

c. Inferential statistics such as regression analysis can be used to determine relationships between radon levels and predictors such as water content, radium content, soil porosity, soil permeability, e.t.c.

2.16.1 Data Distribution pattern in Radon Studies

Radon data obtained from field measurement can vary depending on specific data areas and predictor variables such as geology. Studies have confirmed that radon measurements often do not follow a normal distribution (Cinelli and Tondeur, 2015; Petermann *et al.*, 2020). This is because radon data is usually skewed with a heavy tail either at the lower or higher end.

The distribution pattern of a data set determines how the data would be further treated and the statistical tools to be engaged in analysing it. The first step in applying inferential statistics is to determine whether the data is normally distributed. Statistical tests determine to what extent the data deviate from a normal distribution and if the data can be categorised as non-normally distributed. Tests such as Shapiro-Wilks, Kolmogorov-Smirnov and Anderson-Darling tests are usually used to determine radon values non-normality. These tests calculate test statistics that measure the differences between the dataset and the expected normal distribution. The null hypothesisis rejected if the p-value is less than the chosen significance level (e.g 0.05), suggesting a departure from normality. When performing normality tests on radon data, the practice is to combine two or more of these normality tests in conjunction with a graphical technique such as a Q-Q plot, Frequency plots or density plots to understand the radon dataset comprehensively.

For a normally distributed data, the data can be analysed using tests such as t-test, ANOVA e.t.c. If the deviation from normality is small and the sample size is large, ANOVA can still be used with reasonably accurate results. However, it is recommended that other types of analysis specifically tailored for non-normally distributed data be used to analyse the radon data if it is confirmed to be non-normally distributed. This is because tests such as t-test and ANOVA assume that the data is normally distributed and of equal variance.

It is the usual practice in statistical analysis to fit a non-normally distributed data to a statistical distribution before further analysis. Fitting a distribution is a statistical technique that aims to identify the best-fitting distribution that describes the observed data. Fitting a statistical distribution to observed data does not alter the observed data itself but seeks to mimic the the observed data's variability pattern for better data analysis (Cinelli and Tondeur, 2015). There are several statistical distributions, such as Gaussian distribution (normal distribution), Gamma distribution, Binomial distribution, Exponential distribution, Poisson distribution and Lognormal distribution. Two or more statistical distributions are normally fitted to the non-normally distributed, data and statistical tests are used to determine the best statistical distribution that best mimics the observed data. Such statistical tests are referred to as Goodness-of-fit tests. Examples of such tests are Chi-square tests, Kolmogorov-Smirnov test and Anderson-Darling test.

These tests compare the observed data with the statistical distribution and generate a statistical value indicating the statistical distribution's closeness to the observed data. The lower the statistical value, the better the statistical distribution mimics the observed data.

In general statistical distribution models for non-normally distributed data should be flexible, capable of capturing skewness and kurtosis, mimic the tail behaviour of observed data to extreme values, and offer parameter estimation and goodness-of-fit assessment methods.

Fitting statistical distribution models to non-normally distributed data has several advantages. It provides a descriptive summary of the data by identifying the specific statistical distribution that closely matches the observed data. It enables the estimation of distribution parameters which provide valuable insights into the data's central tendency,

dispersion and shape that can now be used for various purposes, such as making predictions or generating synthetic data. Fitting a statistical distribution facilitates hypothesis testing to determine whether the observed data significantly deviates from the fitted distribution. This is useful for evaluating specific hypothesis about the data distribution. Fitted distribution can be useful for conducting Monte Carlo simulation, sensitivity analysis or generating hypothetical scenarios for decision-making. It is worth reiterating that fitting a statistical distribution model to non-normally distributed data does not alter the observed data but it is only used to mimic the observed data for better statistical analysis, hypothesis testing and better decision making.

Generally, lognormal and gamma distributions are used to model positively skewed data and for positive continuous variables. Such applications of log-normal and gamma distributions are financial modelling for stock prices and asset returns; in natural and social sciences for the size distribution of particles, population dynamics, income distribution e.t.c and in engineering for reliability analysis to model failure times of components and systems. In radon studies, lognormal and gamma distribution are commonly used to analyse radon measurements.

Radon levels are often positively skewed, and the gamma distribution, with its shape and scale parameters, provides a flexible framework for capturing such skewness. The gamma distribution is also used to model the temporal variation of radon levels. Long-term radon measurements taken multiple times can be analysed using the gamma distribution to assess seasonal or yearly variations in radon concentrations. By fitting the gamma distribution to radon data, researchers can conduct radon risk assessment to estimate the probability of radon levels exceeding specific radon threshold levels. Gamma distribution is employed in radon hazard mapping to assess the spatial distribution of radon levels. By fitting the gamma distribution to radon measurements from different locations, researchers can create maps that depict the radon hazard potential in a particular region (Mehmood and Awais, 2021).

The lognormal distribution is also commonly used in radon studies for modelling indoor radon levels. Indoor radon levels tend to be positively skewed, and the lognormal distribution provides the right framework for such data (Makin and Atta, 2018). Using the lognormal distribution, researchers can estimate parameters such as the geometric mean

and geometric standard deviation of radon levels which provide useful insights into the typical radon exposure in a given population or area (USEPA, 2018). Lognormal distribution can also assess the variability of radon levels across different homes or regions. By fitting the lognormal distribution to radon measurements researchers can characterize the spatial and temporal distribution of radon concentration (Rizo *et al.*, 2022).

It is important to note that the choice between gamma distribution and log-normal distribution depends on the specific characteristics of the data and the research objectives. In some cases, both distributions may be compared to determine which provides a better fit to the observed radon concentration measurements.

2.16.2 Application of Non-parametric Tests in Radon Studies

Non-parametric tests are tests conducted on data confirmed to be non-normally distributed. Non-parametric tests are usually used on data with significant skeweness and kurtosis values – indicators of deviations from normal distribution. Non-parametric tests use a test statistic based on ranks or differences in medians. Non-parametric tests start by formulating null and alternative hypothesis that describe the relationship or significant difference being tested in the data. The p-value represents the probability of observing a test statistic as extreme as the one calculated from the actual data assuming the null hypothesis is true. If the p-value is less than the significance level (e.g $\alpha = 0.05$), the null hypothesis is rejected in favour of the alternative hypothesis. Non-parametric tests include Wilcoxon rank-sum test, Kruskal-Wallis test, Man-Whitney U test (or permutation test), Friedman test and Spearman's rank correlation test. Each of these tests is implemented using appropriate software. The type of non-parametric test to adopt depends on the research question and the attributes of the data. However, applying non-parametric tests on a dataset usually follows a general procedure or format. These steps are:

a. Hypothesis formulation: Null and alternative hypothesis are formulated based on the research question.
b. Selection of appropriate non-parametric test: The research question and nature of the data are used to choose the right non-parametric test to adopt.

c. Test statistic determination: Non-parametric tests use test statistic that are based on ranks or differences in ranks. This test statistic is used to assess the significance of the observed effect or difference in the data.
d. Setting of significance level: The significance level (α) represents the threshold below which the null hypothesis is rejected. Commonly used significance levels are 0.05 or 0.01, but the one to adopt depends on the study's requirement and of the research question.
e. Application of the test: The non-parametric test is applied to the dataset using the chosen test statistic and significance level.
f. Result interpretation: The p-value obtained is compared to the significance level. If the p-value is less than the significance level (usually set at 0.05), the null hypothesis is rejected, indicating statistical significance. If the p-value is greater than the significance level, the null hypothesis is accepted, indicating a lack of statistical significance.

2.17 Role of Artificial Intelligence in Radon Studies

Artificial Intelligence (AI) is the domain of science which deals with replicating or imitating human level intelligence, self–awareness, knowledge and thought in computer programming. The quest to process information faster to yield reliable information led to the emergence of artificial intelligence. Another good reason is that handling or processing very large data for the human brain under a very short time frame proves a herculean task. Artificial intelligence therefore involves the engagement of machines e.g robots and computers, to process large information faster than the human brain would. It has to be noted, however that human intelligence far supersedes the highest capabilities of machines and even computers due to the ability of human brain to adjust to different environmental stimuli simultaneously and adapt behavior accordingly through learning.

The target of Artificial Intelligence (AI) is the design of intelligent software or machines for as many tasks as possible. Elaine Rich (Rich, 1983) defined artificial intelligence as the art of making computers perform tasks, which the human brain can perform better. In other words, making computers perform very difficult tasks quickly does not remove the fact that human brains can perform same tasks.

At a conference organized by McCarthy in Dartmouth College in 1956, the name Artificial Intelligence was first coined and used. In 1958, McCarthy invented the high-level language LISP – a computer programme capable of modifying itself. He also founded the first artificial intelligence laboratory at Stanford University in 1963.

In 1997, IBM's chess computer code named 'Deep Blue' defeated the then world chess champion, Gary Kasparov, based on artificial intelligence. In 2006, the use of service robotics became a major artificial intelligence research area and by 2009 the first self-driving car manufactured by Google, drove on a highway in California. As at 2016, deep learning technique had been applied to pattern recognition and Monte Carlo tree search were used by Google to develop the AlphaGo program. Since 1990, data mining has evolved as a sub-discipline of artificial intelligence, specifically in statistical data analysis used for extraction of information from large databases. Although data mining does not bring any new technique to AI, it does introduce the requirement of using large databases to extract explicit knowledge (Ertel, 2017).

Artificial Intelligence is an interdisciplinary science because it uses interesting discoveries from diverse fields such as neurobiology, statistics, operations research, logic, control engineering, linguistics, philosophy and image processing.

2.17.1 Machine learning and learning in Artificial Intelligence

Machine learning is a field under Artificial Intelligence that deals with developing algorithms and techniques that allow computers to learn. Machine learning can also be defined as the application of computer programs that improve automatically on their own through experience (Janiesch *et al.*, 2021). Considering the fact that computer's ability to learn is presently inferior to that of human beings, machine learning algorithms would be one of the cornerstones of artificial intelligence.

Learning to perform a task comes from practising a technique over time, mastering the technique and performing or applying the known technique to new tasks. For instance, having two variables, X and Y, generating X + Y can lead to infinitely many values depending on the range of X and Y. For each combination of X and Y variables, some samples would be used to 'learn' and the results stored. New combinations of X and Y can easily be generated from the stored results of the 'learning' process. For example, in

learning mathematics, the students follow as the teacher explains the process with examples. With practice, the students perfect the process using new examples. After using about 50 examples, the students can apply what has been 'learned' to many new cases. This is a process known as the generalization procedure. The learning agent can be described as a function that is not programmed but rather comes into operation or modifies itself during the learning process. In Artificial Neural Network learning (a form of machine learning), the data is divided into three parts – training data, test data and validation data. The task of the computer algorithm (or learning agent) is to learn a mapping pattern from the training data (i.e the experience). The test data is needed to evaluate whether the computer algorithm used to train can generalize well to new data. The validation data is used as a performance measure to determine how well the algorithm performs the task.

2.17.2 Modelling using Artificial Neural Network (ANN)

Artificial Neural Network (ANN) is a modelling tool under Machine Learning that can learn data patterns and extract a general function or model from several input data training rounds. The basis of artificial neural network is drawn from human nervous system where neurons serve as building blocks for signal transmission. The neurons respond to external stimuli modifications, which are transferred to the brain. Axons and dendrites connect neurons while regions between axons and dendrites are known as synapses. Stimulus (or input) is transferred from one neuron to another until an output is generated. Each stimulus (or input) has an attached weight (or strength) which determines how the information is processed by the neurons (or learning agent). The strength or weights of synaptic connections often change as external stimuli change. The human nervous system can therefore be said to have 'learned' over time how to respond to external stimuli with appropriate modification to the strength or weight associated with each neuron connection.

The biological nervous system mechanism is also replicated in artificial neural network with its basic unit referred to as neurons. The computational units are connected to one another through weights which resembles the weights of synaptic connections in biological organisms. The essence of ANN modelling is the generation of a model, drawn

from the training of existing data for generalization purposes, which leads to prediction of more data.

The neural network modelling provides a feedback which indicates how accurate the weights are in the neural network, depending on how well the predicted output matches the expected output value(s). Where there are differences between the predicted output and the expected output, the difference is fed back into the neural network which instigates the adjustment of the connecting weights between the neurons at the input stage and at output stage. By successfully adjusting the weights between computational neurons, the generated function is refined over time to provide more accurate predictions.

The artificial neural network (ANN) is grouped into Input, Hidden and Output layers. The hidden or processing layer lies between the input and the output layers (figure 2.4). The hidden layer can be single or multiple layers each with two or more neurons. The complexity of the network topology depends on how many hidden layers are chosen and the number of neurons in each hidden layer. No two neurons between the hidden layers have the same connection. The net signal arriving at the end of a connection is the product of the input and its corresponding weight. The ANN assigns arbitrary weight values to the input signal during training until a good match is obtained between the output data and the target or expected output.

A bias must be added after the weights have worked on the input. The bias can be likened to the intercept in a linear equation. After that, a transfer function further works on the sum of the weights and the bias (figure 2.4). The transfer function is applied on the aggregate weighted sum of input values and the bias value for a particular neuron. The transfer function converts or transforms the input signal to output signal. There are four main transfer functions at the hidden layer: Unit step, Sigmoid, Piecewise linear and Gaussian transfer functions. The result of the transfer function operating on the input, weights and biases serves as the input for the next neuron in the next hidden layer or in the output layer. A typical neural network configuration is as shown in figure 2.4.

Embedded in Artificial neural network is an array of networks useful for different applications depending on the required output. The most commonly used neural networks are Hopefield, Perceptron, Radial basis, Exact fitting radial basis, Probabilistic, General Regression self-organising map, Linear network, Feed forward network with back

propagation and Cascade-forward with back propagation network. The typical applications of these networks are in areas of signal processing, function approximation and data classification problems. Multilayer feed-forward network with back propagation is more popular because of its flexibility for both linear and non-linear relations (Salami *et al.*, 2016).

Figure 2.4 represents two inputs, one hidden layer with six neurons, one processing output layer and final output. 'w' represents weights, 'b' represents bias, curved symbol represents hidden layer activation function (e.g Sigmoid function), line symbol at output layer represent output activation function (e.g Purelin transfer function).

The flexibility of feed forward networks comes at the cost of explicit training using the input and output data. Such networks are known as supervised networks. On the other hand, some networks, like Radial Basis network, have rules governing how many hidden layers and neurons can be acceptable. Usually, those ANNs which do not permit alteration or tuning of the number of layers, neurons and transfer functions associated with a layer belong to the Radial Basis family of ANNs. Examples of such networks are generalized regression and probabilistic neural networks. Such networks are therefore referred to as unsupervised neural networks.

Supervised networks assign and adjust values of connection weights and bias so that the error between expected output values and the predicted values becomes a minimum. In Feed-forward neural network, a form of supervised network, successive layers feed the output of one neuron into the input of another neuron in the forward direction. In feed forward back propagation, the error obtained in the previous iteration is fed back into the network for reassigning of weights and bias towards further reduction in the error. Back propagation is a shortened form for 'backward propagation of errors'. The format for back propagation of errors is to calculate the error in the output, then go back from the output layer to the hidden layer to adjust the weights and bias such that the error is further reduced. The process is repeated until a desired high correlation between the predicted output and the expected output is achieved. A typical architecture of a feed-forward multilayer network with five input parameters at the input layer, one hidden layer (having three neurons) and a single output is shown in figure 2.5.

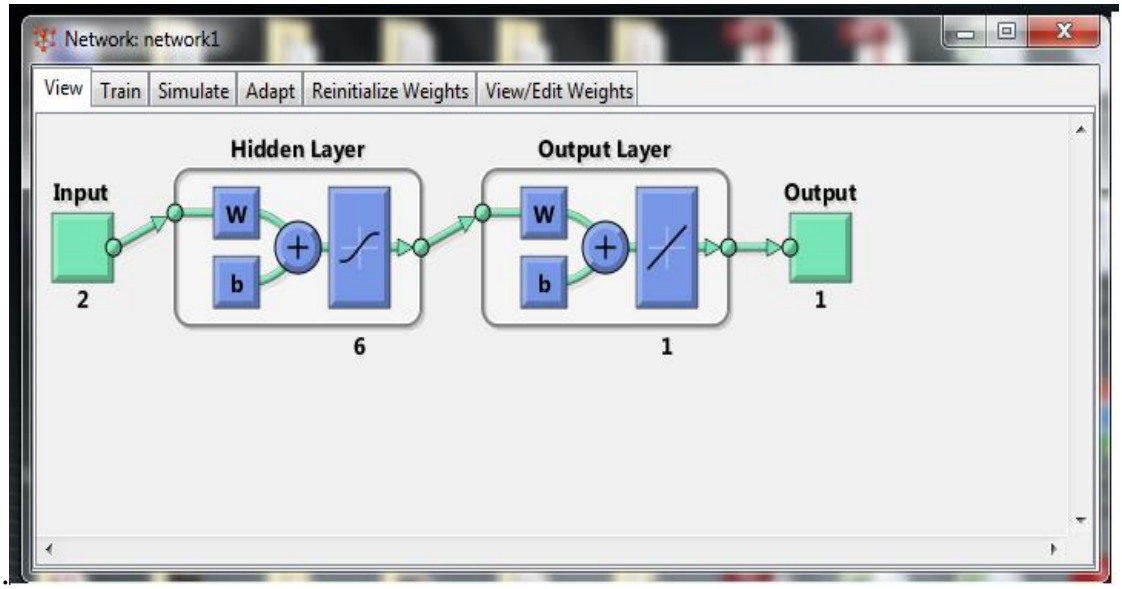

Figure 2.4 A 2 x 6 x 1 Neural Network Configuration

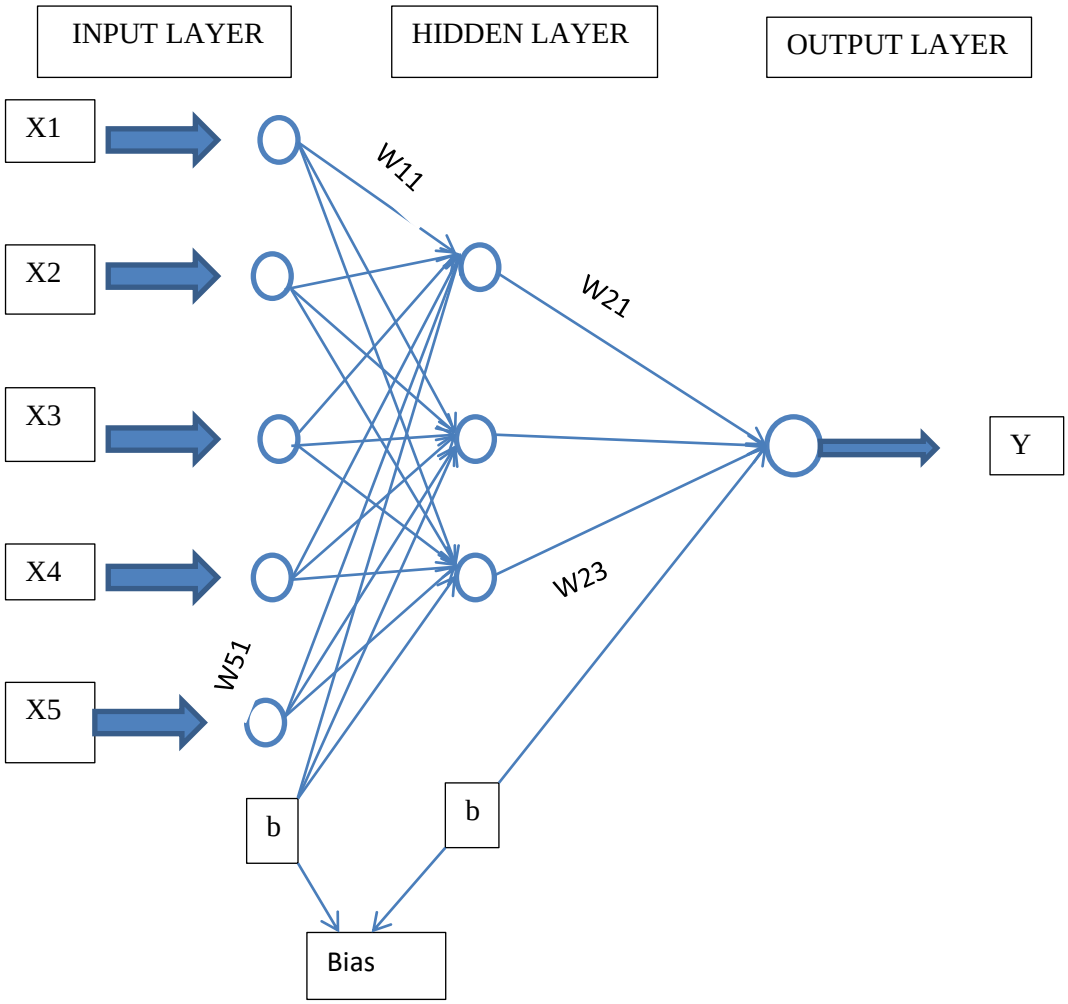

Figure 2.5 Architecture of a Feed-forward Multilayer Network with One Hidden Layer and a Single Output

Predictive-based problems are usually solved in neural network modelling using Levenberg-Marquardt training algorithm. A variant of Levenberg-Marquardt training algorithm is the Levenberg-Marquardt feed forward back propagation algorithm. Levenberg-Marquardt training algorithm, also known as the Damped least square method (DLS), is used to solve non-linear least-square problems. The objective in solving non-linear least-square problems is to obtain a function such that the sum of the squares of the deviations is minimized, and the Levenberg-Marquardt function achieves this easily.

Artificial Neural network is embedded in MATLAB software. MATLAB has a graphic user interface (GUI) that allows the division of the input and target data into three parts – training, testing and validation. The training dataset is used to create the model. The test and validation datasets are used to verify the performance of the developed model. The validation dataset refers to part of the data kept aside and later used to provide an independent measure of network performance during and after the training. It gives an indication of how good the model is. The test dataset is the part of the data, set aside to provide the generalization effectiveness of the trained data and to stop the training when the generalization stops improving. The data is usually divided in the ratio 70:15:15 which is 70 % for training, 15% for testing and 15% for validation. One is at liberty however, to vary the ratio but a greater percentage of the data must be used for training. Another ratio commonly used is 60:20:20.

The model generation using Artificial Neural Network begins with the normalization of the input parameters which are transposed in the range -1 to +1 corresponding to the highest and lowest values, respectively. The function “mapminmax” is used as a pre-processing format to transpose or scale the inputs in the range of -1 to +1. Scaling is done to avoid any of the inputs having a disproportionate influence on the output because of its scale. For instance if we have two inputs with say X being in the range 1 – 10 and another input Y in the range 100 – 100,000, without scaling, input Y will have more influence on the output than input X.

The equation for the mapminmax procedure for normalisation is shown in equation 2.16.

$$y = \frac{(Y_{max} - Y_{min}) * (X_{in} - X_{min})}{(X_{max} - X_{min})} + Y_{min} \tag{2.16}$$

where ‘y’ is the normalised input parameter value for X_{in}, ‘Y_{max}’ is maximum normalized value (1), ‘Y_{min}’ is minimum normalised value (–1), ‘X_{min}’ is the input parameter’s minimum value, and ‘X_{max}’ is its maximum value.

During training process, the epoch (which represents number of iterations) and goals (which also represents error tolerance) are used as the stopping criteria respectively. The training automatically stops once the goal (error tolerance) or the maximum number of iterations (epoch) is reached, depending on which one comes first. For most studies, an epoch of 10,000 and goal of zero are usually set for the data training. To get the best result, the number of neurons is gradually increased either for single or multiple hidden layer configurations. It is not unusual to train different configurations before finally arriving at the best configuration for modelling in artificial neural network. There must, however, be a basis for comparing the results obtained from the different configurations to determine which performs best.

2.17.3 Assignment of Weights at Hidden Layer

After normalisation of input parameters using equation 2.16, the assignment of weights and biases to the normalised input variables are automatically generated by the computer in MATLAB workspace, leading to the generation of the sum of weighted normalised variables using the general equation:

$$E_{1,i,n} = \sum_{i=1}^{j} W_{1,i,\vartheta} * \vartheta_{(norm)_n} + W_{1,i,\varphi} * \varphi_{n_{(norm)_n}} + b_{1,i} \quad (2.17)$$

where ‘$W_{1,i,\theta}$’ and ‘$W_{1,i,\varphi}$’ are the weights assigned to the normalised input values θ and φ, respectively, with neuron (*i*) at the hidden layer (1); ‘$b_{1,i}$’ is the bias at the hidden layer (1) assigned to the neuron (*i*); ‘$\vartheta_{(norm)n}$’ and $\varphi_{n(norm)n}$ are the nth normalised input values. ‘$E_{1,i,n}$’ is the nth sum of the weighted normalised variables based on the weight assignment associated with i^{th} neuron at the particular hidden layer (1…..j) with j being the last neuron in the configuration.

2.17.4 Transfer Function at Hidden Layer

After the computation of $E_{1,i,n}$, a transfer function is made to operate on $E_{1,i,n}$, for example, a Tansigmoid transfer function, which can be mathematically expressed as:

$$Tansig(E_{1,i,n}) = F_{1,i,n} = \frac{2}{(1+\exp(-2E_{1,i,n}))} - 1 \quad (2.18)$$

The mathematical expression in equation 2.18 is limited to that of a single hidden layer. Where double or multiple hidden layers are used, two or multiple levels of the tansigmoid transfer function will be involved and treated separately.

2.17.5 Weight Assignment and Transfer Function at Output Layer

The step after Tansigmoid transfer function computation is assigning weight and bias to the output layer, which is generated automatically by the NNtool software in MATLAB. At the output layer, we have the Tansigmoid, Logsig and Purelin transfer functions. As an example, the Purelin transfer function can act on the $F_{1,i,n}$ computation in equation 2.18 to generate the final function or model. The weight(s) and bias are assigned at the output layer using Purelin transfer function as:

$$a_{nO} = Purelin\,(O_{1,i,j}) = \; Purelin(\sum_{i=1}^{j}(W_{o,i} * F_{1,i,n}) + \; b_0) \qquad (2.19)$$

where '$W_{o,i}$' is the assigned weight at the output layer (O) attributed to neuron (i): '$F_{1.i,n}$' is the Tansigmoid-transformed variable associated with the sum of the nth normalised input variable at the last hidden layer (1); 'b_0' is the bias at the output layer while 'a_{n0}' is the normalised final output.

2.17.6 De-normalisation of Normalised Output

In order to get the predicted output, there is a need to denormalise the output obtained in equation 2.19. To denormalise '$a_{no'}$, the normalisation equation 2.16 is also used, but this time 'X' is made the subject of the formula instead of 'Y'.

In essence, ANN has been used to obtain a model which generates a set of normalised predicted values which must be denormalised to get the predicted values, 'a_{no}'.

2.17.7 Assessment of ANN Configurations

The different ANN configurations generated while developing the ANN model are evaluated with different statistical criteria to determine the best to use in developing the ANN model. Some of the statistical criteria are Correlation coefficient, Sum Square Error (SSE), Mean Bias Error (MBE), Mean Square Error (MSE), Average Absolute Relative Error (AARE) and Nash-Sutcliffe efficiency coefficient (NS).

(a) Sum Square Error (SSE)

This is the sum of the squares of the deviations between the actual output data and the predicted data given by:

$$SSE = \sum_{i=1}^{n}(S_{obs} - S_{cal})^2 \quad (2.20)$$

where N is the total number of data points, S_{obs} is the actual output or target value and S_{cal} is the predicted or calculated value.

(b) Mean Square Error (MSE)

This is the average of the squared differences between the predicted value (S_{cal}) and the actual output value (S_{obs}) of a variable. The MSE is always non-negative because of the square of the deviation of the predicted from the actual value. The lower the value is, the better. For a number of data points N, MSE can be obtained by finding the average of SSE. It can be computed using:

$$MSE = \frac{1}{N}\sum_{n=1}^{N}(S_{obs} - S_{cal})^2 \quad (2.21)$$

(c) Average Absolute Relative Error (AARE)

This is the average of the relative error in prediction of a particular variable expressed as a percentage. The lower the value of AARE, the better the model performance. It can be computed using:

$$AARE = \frac{1}{N}\sum_{n=1}^{N}\left|\frac{S_{cal}-S_{obs}}{S_{obs}}\right| X\ 100 \quad (2.22)$$

(d) Nash-Sutcliffe Efficiency Model Efficiency Coefficient (NS)

Nash-Sutcliffe model efficiency coefficient is used to determine the relative magnitude of the error variance compared to the measured data variance. Nash-Sutcliffe model efficiency coefficient range from -∞ to 1. A value of NS equal to 1 depicts a perfect match between observed data and predicted data. Therefore the closer the NS coefficient is to unity, the more accurate the model developed will be. Nash-Sutcliffe coefficient is computed with (Abidoye *et al.*, 2018):

$$NS = 1 - \frac{\sum(S_{cal}-\acute{S}_{obs})^2}{\sum(S_{obs}-\acute{S}_{obs})^2} \quad (2.23)$$

where $\acute{S}_{obs}$ is the average of the observed output.

2.17.8 Assessment of ANN generated Model

(a) Average Validation Error (E_{avg})

The average validation error is used to evaluate the model's performance generated using ANN. It is used to determine how close the predicted value is to the expected output. Specifically, the model that produces the least value of the average validation error is the target in artificial neural network modeling. The average validation error is computed using following equation:

$$E_{avg} = \frac{1}{N_v}\sum_{i=1}^{N_v}\left|\frac{F_{ann}(x_i,w)-y_i}{y_{max}-y_{min}}\right| \quad (2.24)$$

In equation 2.24, $F_{ann}(x_i,w)$ is the predicted output of the ANN model with input data x_i having associated weight, w while y_i is the desired output. Y_{max} and Y_{min} are the maximum and minimum values of desired output while N_v is the number of training samples. The lower the value of the average validation error, the better the model generated is able to predict the soil gas radon concentration.

(b) Mean Absolute Error (MAE)

Mean Absolute Error is the arithmetic average of the absolute error obtained between paired observations expressing the measured and predicted parameter.

$$MAE = \frac{\sum_{i=1}^{N}|P_m-P_p|}{N} \quad (2.25)$$

where P_m is the measured value, P_p is the predicted value and N is the total number of dataset.

(c) Mean Absolute Percentage Error (MAPE)

Mean absolute percentage error is a measure of a model's prediction accuracy. It is the average of the absolute sum of the deviation of the predicted mean value from the measured mean value divided by the measured mean value.

$$MAPE = \frac{1}{N}\sum_{i=1}^{N}\left|\frac{P_{mt}-P_{pt}}{P_{mt}}\right| \times 100\% \quad (2.26)$$

where P_{mt} is the mean of the measured value, P_{pt} is the mean of the predicted value and N is the total number of dataset. Although there is no standard MAPE value, a MAPE $\leq$ 10% is usually acceptable.

(d) Root Mean Square Error (RMSE)

It is a measure of how a model accurately predicts the measured data. In practice, the root mean square error is the square root of the mean square error (MSE). Lower RMSE is the target in any modelling application, and a value close to zero would indicate a very good fit.

$$RMSE = \sqrt{\frac{\sum(P_m - P_p)^2}{N}} \tag{2.27}$$

where P_m is the measured value, P_p is the predicted value and N is the total number of dataset.

(e) Goodness-of-prediction (G)

The measure of the Goodness-of-prediction provides an indication of the effectiveness of prediction of the model relative to using the mean of the observed parameter of interest.

$$G = \left(1 - \left\{\frac{\sum_{i=1}^{n}[Z(X_i) - Z^*(X_i)]^2}{\sum_{i=1}^{n}[Z(X_i) - Z^-]^2}\right) \times 100 \tag{2.28}$$

where $z(x_i)$ is the observed value, $z^*(x_i)$ is the predicted value and z^- is the mean of the observed values.

Suppose the numerator in equation 2.28 is less than the denominator. In that case, it indicates that the predicted values are more accurate than using the mean of the observed values, and Goodness-of-prediction will be positive. If the numerator, on the other hand, is higher than the denomenator, then Goodness-of-prediction will be negative. The magnitude of Goodness-of-prediction gives the accuracy and a value equal to 100% indicates a perfect prediction.

(f) Mean Bias Error (MBE)

Mean bias error is used to estimate the average bias in the model. Its estimation helps to determine if the model underestimates or overestimates the expected data. A value closer to zero indicates that the model predicts accurately. A positive bias indicates overestimation, while negative bias value indicates underestimation.

$$MBE = \frac{1}{n}\sum_{i=1}^{n}(P_p - P_m) \tag{2.29}$$

where P_p is the predicted value, P_m is the measured value and n is the total data values.

2.18 Some Related Works in Artificial Neural Network Modelling of Soil-gas Radon Concentration

Measuring soil-gas radon concentration for a region or country towards estimating geogenic radon risk is a costly and labour-intensive exercise that requires adequate logistics and acquisition of state-of the art equipments. Consequently, modelling tools are engaged as a follow up to measurement campaigns, where adequate measurements could not be achieved, to predict soil-gas radon concentration and geogenic radon potential for yet to be assessed locations within the region or country. Some models developed based on soil characteristics and bedrock type to predict soil-gas radon have met with limited success and recent efforts have demonstrated that models which encompass measured radon, radiation levels in soils and relevant geophysical and geological parameters are likely to be the most effective (UNSCEAR, 2000).

Borgoni *et al.* (2014) used the mixed effect model to investigate the effect of some factors such as bedrock type, soil type and building characteristics on indoor radon concentration with particular attention to indoor changes in relation to the floor levels. Kojima and Nagano (1999) used time-dependent radon transport model to predict radon exhalaration rate from pressure difference and soil water content profile in the soil. Pasini *et al.* (2003) adopted ANN for predicting atmospheric radon concentration and stable layer depth using residual series of radon data and meteorological data. Sakoda *et al.* (2010) used Monte Carlo simulation to model the significance of soil moisture and grain size on radon emanation fraction. The study concluded that the radon emanation fraction is a factor of pore size between a radon-bearing grain and a neighboring grain while a sharp increase was observed at grain sizes of smaller diameter with increasing soil moisture content.

In the study conducted by Negarestani *et al.* (2003), ANN was employed in modelling the temporal variation of soil-gas radon with environmental parameters of atmospheric pressure, temperature and rainfall. The ANN model was found to compare favourably with that obtained mathematically. ANN was used by Zhu *et al.* (2009) to predict radon concentration based on back propagation neural network in a uranium mining company. Radon anomalies in soil gas preceding earthquakes have been observed, especially at geological faults (Ghosh *et al.*, 2009). Kulahci *et al.* (2009) used ANN to

model the relationship between earthquake magnitude and input variables of location, concentration of soil-gas radon, earthquake depth, barometric pressure and soil temperature at the time of the earthquake for 147 past earthquake occurrences. They used a feed forward back propagation learning algorithm (Levenberg-Marquardt algorithm) with a tansigmoid transfer function. They also used a linear transfer function (Purelin function) at the output layer. The relative error between the magnitudes of the earthquake data acquired by ANN and the measured data was about 2.3%. Torkar *et al.* (2010) also used environmental parameters of air and soil temperature, barometric and soil air pressure and rainfall as inputs to predict anormalous radon concentration in Oleca fault in Slovenia using ANN and were able to predict 10 out of 13 seismic events within a two-year period.

In a study conducted by Atik *et al.* (2013), ANN was used to develop a model between indoor radon and seven input parameters of air temperature, air pressure, relative humidity, local time, location, floor level and aspect direction in six faculty buildings of a university campus in Turkey. Out of the 27 configurations trained, two performed better with the best at 87.2%. The study concluded that variation in indoor radon appeared to be closely correlated with aspect direction and floor level.

Aghdam *et al.* (2022) used ordinary least squared regression (OLS) to model geogenic radon potential using soil-gas radon concentration as the response variable with radionuclide concentrations obtained fron airborne radiometric surveys, distance from major faults, and soil-air permeability as predictor variables. ArcGIS and Empirical Bayesian Krigging were used to interpolate and map the spatial distribution of the predicted GRP. They established the fact that, in modelling, since the GRP is not directly measured, using measured soil-gas radon concentration as an indicator of the GRP is the best approach.

Oni *et al.* (2022) measured indoor radon concentration in 132 offices and 60 classrooms in tertiary institutions within the Southwest region of Nigeria alongside meteorological parameters and used ANN to model the relationship. The obtained ANN model yielded a Nash-Sutcliffe efficieincy coefficient of 0.997 and 83.7% Goodness-of-fit value.

CHAPTER THREE
MATERIALS AND METHODS

3.1 Materials Utilised in the Study

Materials used in the measurement of the soil-gas radon concentration and the soil-air permeability were: a Garmin 76 global positioning system (GPS) instrument, RAD7 solid state radon monitor manufactured by Durridge Incorporation, USA, a desiccant (containing cobalt chloride), constant head permeameter set up, connecting tubes, soil probe with tiny holes at the base, sledge hammer and a long steel rod (4.5 cm thick, 1.5 m long). Also used for the work were shovel, a cutlass, a conical flask, two measuring cylinders, open-end cylindrical soil core samplers (4.9 - 5.5cm length, 2.75cm radius), two retort stands, water reservoir, a funnel, cotton cloth, paper adhesive tape, rubber band, long nose plier, cylindrical plastic containers, water basin, and a tape rule.

3.2 Study Area

The Southwest region of Nigeria has a landmass of 79,665 km^2 comprising six states of Ogun, Ondo, Osun, Oyo, Ekiti and Lagos (Figure 3.1). The entire area is located in Nigeria's equatorial rain forest zone, between latitudes $6^0 – 10^0$ N and longitudes $3^o – 6^o$ E (Oni and Odekunle, 2016). Climate of Southwest region of Nigeria is marked by a range of fairly high to moderate temperatures, high relative humidity, moderate to heavy seasonal rainfall and an intense cloud cover.

The basement complex covers most part of Nigeria's landmass and is made up of Precambrian-age rocks and volcanics (Farai and Sanni, 1991). The other part is made up of sediments dating from the Cretaceous to Quatenary periods (Rahaman, 1988). The bedrocks in the Southwest region of Nigeria can be divided into two which are the sedimentary basin and basement complex. The division between the basement complex and sedimentary basin can be seen along Ogun and Ondo states.

The basement complex in Southwest Nigeria consists of amphibolites, granites, pegmatites, migmatites and gneisses. Other important bedrock units present are the schists belts such as biotite schist, quartzite schist, talc schist and muscovite schist (Oyinloye, 2011). These bedrocks show great variation in grain size and mineral composition. The sedimentary basin consists of shale, limestone, siltstone, sandstone and clay sand (Okeke *et al.*, 2019). The lithological units found in Southwest region of Nigeria are shown in the geological map of Southwest Nigeria in figure 3.2.

3.3 Measurement Considerations

The following were considered before choosing the location for measurement:

a. Avoidance of low-lying areas: valleys were avoided during the soil-gas radon concentration measurement campaign. The value of the soil-gas radon concentration obtained in such a location cannot be relied on as water in soil inhibits the movement of gas in soil.

b. Distance from buildings/roads: Distance was maintained away from roads or buildings during the measurement procedure. This is because during road or building construction, a lot of excavation must have been done and soil beside them would have been disturbed. Therefore the soils beside such structures will not represent the true nature of the soil before excavation.

c. Proximity to trees and vegetation: root fissures create preferential pathway for soil gas movement and this was avoided by taking measurement not too close to trees or thick vegetation.

d. Avoidance of disturbed locations: Locations where there had been minima disturbance due to human activities such as farming (especially mechanized farming), drilling etc. were chosen based on the need to take undisturbed soil samples from the same location for measurement of saturated hydraulic conductivity (which was used to obtain soil-air permeability).

Figure 3.1 Map of Southwest Nigeria showing the States and Sampling Locations

(Department of Geography, University of Ibadan, 2022)

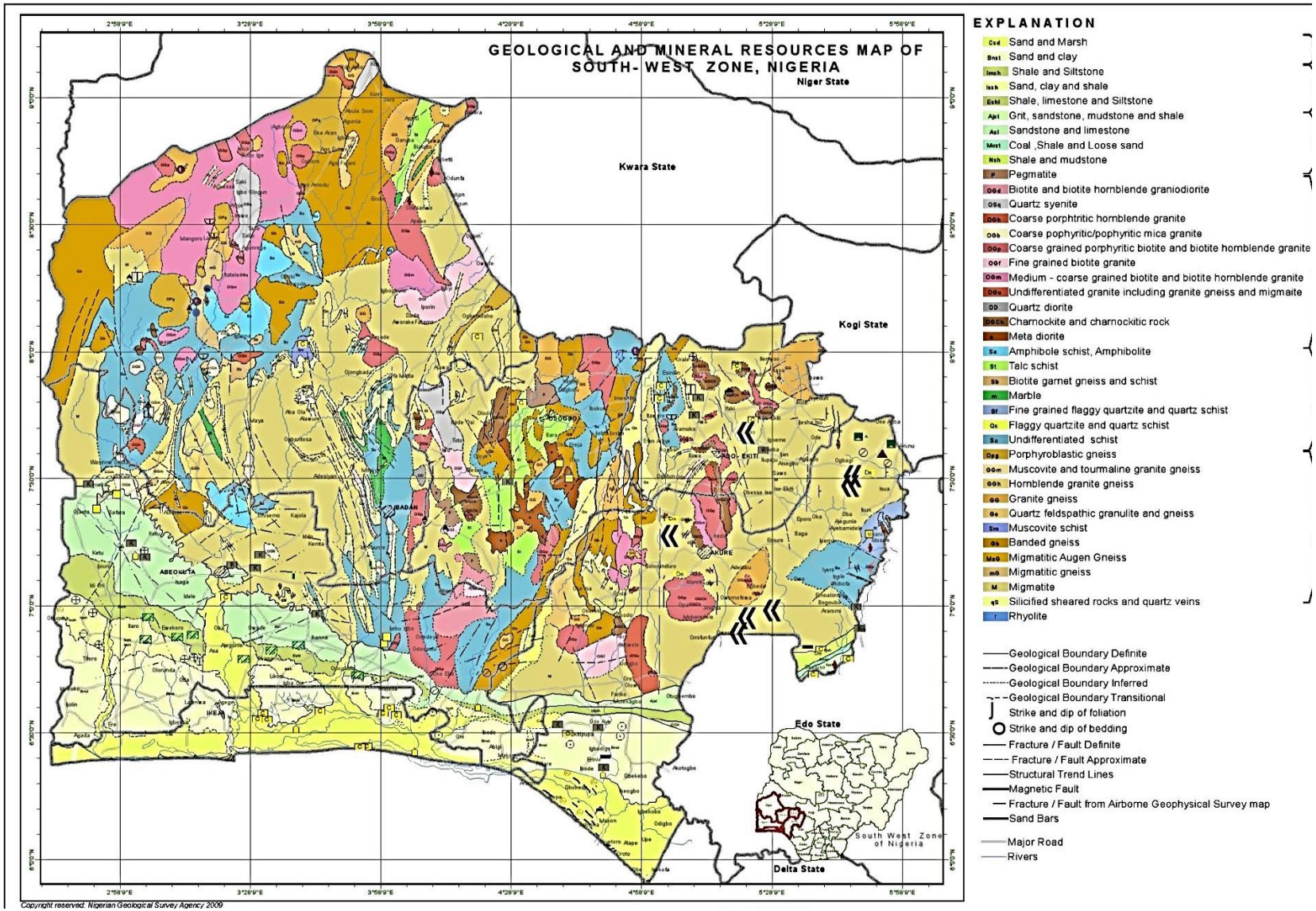

Figure 3.2 Geological Map of Southwest Nigeria (Nigerian Geological Survey Agency (NGSA, 2009)

3.4 Measurement Campaign and Sample Collection

The site coordinates were obtained using a Garmin GPS instrument in conjunction with the geological map of the region obtained from the Nigerian Geological Survey Agency (NGSA), which had identified forty types of bedrocks present in the Southwest region. Depicted in figure 3.2 is the breakdown of the forty lithological formations present in the study area. The measurement of soil-gas radon concentration and soil-saturated hydraulic conductivity (from which soil-air permeability was derived) in the Southwest region of Nigeria was carried out between November, 2018 to July, 2019 using RAD7 and constant head permeameter respectively. A total of twenty bedrocks were considered in the study due to their prevalence and accessibility, and were classified (with the assistance of a seasoned geologist using the Nigerian geological map bedrock classifications) under major bedrocks of Metamorphic, Granitic, Sedimentary and Sediments (table 3.1). One hundred and fifty locations underlain by the twenty bedrocks that cuts across the six states that make up the Southwest region of Nigeria were surveyed (table 3.2). The Southwest region was partitioned into thirty-three grids, with each grid having a dimension of 55km x 55km in line with the grid pattern used by Nigerian Geological Survey Agency (NGSA) for Southwest Nigerian geological map. An average of four measurement points per grid was considered based on the dominating bedrock(s) within the grid in a particular state in the region.

Another set of twenty measurements of soil-gas radon concentration and soil-saturated hydraulic conductivity (from which soil-air permeability was derived) was done, and was used to validate the developed artificial neural network model.

Table 3.1 Classification of Bedrocks considered into Major Bedrocks (NGSA, 2009)

Major Bedrock	Bedrocks
Granitic	Charnokite & Charnokitic Rock Quartz Syenite CG Porphyritic biotite and biotite hornblende granite Pegmatite Fine-grained biotite granite M-CG Biotite and biotite hornblende granite
Metamorphic	Granite Gneiss Flaggy quartzite and quartzite schist Migmatite Banded Gneiss Phorphiroblastic Gneiss Undifferentiated Schist Talc Schist Amphibole Schist and Amphibolite Muscovite tourmaline granite gneiss
Sedimentary	Shale, limestone and Siltstone Sandstone and Limestone Sand, Clay and Shale
Sediments	Sand and Clay Sand and Mash

Table 3.2 Distribution of Sites with underlying Bedrocks in the Six States of Southwest Nigeria

BEDROCKS	SITES	PERCENTAGE	PRESENCE IN STATE(S)
1. Migmatite	23	15.33	(OYO, OSUN, OGUN, ONDO, EKITI)
2. Granite Gneiss	12	8.00	(OYO, OSUN, ONDO, EKITI)
3. Quartz Syenite	03	2.00	(OYO)
4. Banded Gneiss	11	7.33	(OYO, OSUN, ONDO, EKITI)
5. Undifferentiated Schist	14	9.33	(OYO, OSUN, OGUN, ONDO, EKITI)
6. Amphibole Schist & Amphibolite	04	2.67	(OYO)
7. Fine-grained Biotite granite	08	5.33	(OYO, OSUN, OGUN, ONDO)
8. M-CG Biotite & biotite hornblende granite	05	3.33	(OYO, ONDO)
9. CG Porphyritic biotite & biotite hornblende Granite	17	11.33	(OYO, OSUN, OGUN, ONDO, EKITI)
10. Pegmatite	04	2.67	(OSUN)
11. Flaggy quartzite & Quartzite Schist	04	2.67	(OSUN, EKITI)
12. Talc Schist	07	4.67	(OSUN)
13. Shale, Limestone & Siltstone	08	5.33	(OGUN)
14. Sandstone and Limestone	07	4.67	(OGUN)
15. Chanokite and chanokitic rock	02	1.33	(OSUN)
16. Sand and Clay	09	6.00	(OGUN, LAGOS, ONDO)
17. Sand and Mash	05	3.33	(LAGOS)
18. Sand, Clay and Shale	04	2.67	(LAGOS)
19. Phorphiroblastic Gneiss	02	1.33	(OYO)
20. Muscovite & tourmaline granite gneiss	01	0.67	(OGUN)
TOTAL NUMBER OF SITES --- 150			

3.5 Soil-gas Radon Concentration Measurement

Radon can be measured directly or indirectly through its progeny (^{218}Po) using active or passive techniques. In this work, soil-gas radon concentration was measured in-situ using a calibrated RAD7 active radon detector.

3.5.1 RAD7 Measurement Technique

A RAD7 radon measuring equipment (a solid-state detector) manufactured by Durridge Incorporation in the United States of America has been described in section 2.9. RAD7 is used to measure the alpha particles emitted by ^{218}Po in secular equilibrium with ^{222}Rn.

The RAD7 detector came with accessories such as the soil probe, desiccant unit, rubber pipes, filter and charging cable. The steel rod used in getting the soil probe to the desired depth of 80 – 100 cm was locally manufactured. The RAD7 radon detector can measure radon using several modes. A regular mode of measuring the soil-gas radon is the "GRAB" sampling protocol and this was used in this study. Table 3 summarizes the RAD7 protocol utilized for the soil-gas radon measurement.

At the desired location, a sledge hammer was used to drive the steel rod into the ground up to at least 80 cm depth (Szabo *et al*., 2013; Liu *et al.*, 2016). As steel rod is extracted, the soil probe of the RAD7 set up was quickly inserted and the soil surface was quickly covered in order for the soil gas to be in contact with the soil probe rather than escaping into the atmosphere. The soil probe (1.3 m long with inner diameter of 0.634 cm) has very tiny holes at the tip through which soil gas is pumped into the RAD7 equipment (Figure 2.4). The soil gas goes through the soil probe and passes through an air-filter chamber into the RAD7 via a rubber pipe (plate 3.1). The pump inside the RAD7 equipment pumps the soil gas at the rate of 1 $Lmin^{-1}$ into the detector chamber for 5 minutes. After pumping, the RAD7 waits for another 5 minutes in order for ^{218}Po (with half-life of 3.05 minutes and in secular equilibrium with ^{222}Rn) to completely decay which takes about 3 half – lives (between 9 – 10 minutes). The RAD7 then counts the ^{218}Po for four 5 minutes cycles. The total time for measurement amounts to 30 minutes. The RAD7 measures the soil gas radon concentration in Bqm^{-3} with a range of between 4 and 750,000

Bqm^{-3}. The RAD7 readout shows the average of the four-cycle measurement of the soil-gas radon concentration.

In calibration, the RAD7 is exposed to a known concentration of radon (or Thoron) and the count rates are measured. Two main sensitivities are targeted in calibration which are the Sniff Sensitivity (counting only ^{218}Po for fast response) and Normal Sensitivity (counting both ^{218}Po and ^{214}Po decays for higher precision). The RAD7 used for this work was calibrated by the manufacturer on the 6^{th} of May, 2016 and the calibration achieved ±2% reproducibility which, according to the manufacturer specification, makes it highly stable (Durridge Radon Instrumentation, 2012).

As stated earlier, the measurements of soil-gas radon concentration and the soil-air permeability were carried out between November, 2018 and July, 2019. No radon measurement was done when it was raining. Measurements were carried out between 9:00 am to 6:00 pm and under operating atmospheric temperature and pressure as according to Szabo *et al.*, (2013) variation in soil-gas radon concentration is lower in the daytime compared to the night time both for the summer and rainy season.

The RAD7 has the capacity to store up to 1000 radon concentration data in its memory which can later be printed out with an attached Hewlett-Packard model 82240B printer.

An alarm is set on immediately after every cycle of measurement. The RAD7 operates with a 5 AH, 6V battery which is usually pre-charged before field measurement. A major drawback for field measurement is the need to keep the batteries charged or have a backup power supply. The best operating temperature for the equipment is between 0^0C – 40^0C (0^0F – 105^0F) and relative humidity of between 0 to 10%.

Table 3.3 RAD7 Protocol used in measurement of Radon Concentration (Durridge Radon Instrumentation, 2012)

Protocol	Mode	Cycle	Recycle	Thoron	Pump
Grab	Sniff	00.05	04	Off	Auto

3.5.2 Purging of RAD7 Equipment

The process of removing old radon and air moisture from the chamber of the RAD7 detector to allow for fresh measurement of soil gas radon is known as purging. This was achieved by using the pump in the equipment to introduce fresh air into the detector chamber through the desiccant. The pump also removes the air from the chamber through the outlet. The initial relative humidity (which must be less than 10% before use) determines how long the purging exercise takes and this usually takes between 5 to 10 minutes (Durridge, 2012). For this study, a minimum of 10 minutes was maintained for purging of the RAD7 equipment before the start of a new measurement.

3.6 Soil-air Permeability Measurement

To compute the geogenic radon potential (GRP), soil-air permeability, a property of the soil that determines the rate at which soil gas is transported to the soil surface, is required. Soil-air permeability was derived from measured saturated hydraulic conductivity performed in the laboratory on each soil sample collected at a depth of 80 – 100 cm where the soil-gas radon concentration measurement was carried out. At the 80 cm depth, open-end cylindrical metal (usually called soil core sampler) of length 5.0 – 5.5 cm and radius 2.75 cm was placed on the soil surface. A small wooden plank was placed on the cylindrical metal and a hammer head was used to hit the set up until the cylindrical metal was fully driven into the soil. After that a long nose plier was used to carefully extract the soil-filled cylindrical core sampler to have undisturbed soil. The excess soil on the two sides of the soil core sampler was scraped off. The soil-filled core samplers were then carefully placed inside similar cylindrical plastic containers and sealed. The cylindrical plastic containers were then placed inside a rectangular wooden box for onward transfer to the laboratory.

The saturated hydraulic conductivity (Ks) needed to be obtained before soil-air permeability (Ka), was determined. Equation (2.10) given by Loll *et al*. (1999) which relates the soil-air permeability (Ka) to the soil-saturated hydraulic conductivity (Ks) was used to determine soil-air permeability.

3.6.1 Measurement of Soil-Saturated Hydraulic Conductivity

(i) Soil Sample Preparation

The soil-saturated hydraulic conductivity was measured with a constant head permeameter. Soil samples are required to be fully saturated before measurement. This was achieved by placing cotton clothes at one end of the soil-filled core samplers, using a rubber band to hold it in place and placing the soil core samplers in a basin filled with water gradually up to the middle of the soil core samplers. Water moves gradually through the cotton cloth into the soil volume to displace air in soil interstices. Full saturation was achieved in twenty four hours (Hillel, 1998).

(ii) Measurement of Saturated Hydraulic Conductivity with Constant Head Permeameter

An empty core sampler was attached to the soil-filled core sampler with a paper adhesive tape. The soil-filled sampler and the attached core sampler were placed inside the funnel with the cotton cloth end at the base (Plate 3.1). Running water was slowly applied into the setup until it reached a height in the empty core sampler. A calibrated beaker was placed beneath the funnel to collect the water as it drained through the soil sample. The sustained height of water in the attached soil core sampler, known as the hydraulic head (in cm) was measured with a metre rule. The volume of water that flowed through the soil sample was collected and measured using a measuring cylinder after a preset time until a constant volume was attained at least three times successively. The saturated hydraulic conductivity was obtained from the set up using equation 2.14.

Plate 3.1 Constant head permeameter set-up for measurement of saturated hydraulic conductivity

3.7 Computation of Geogenic Radon Potential

The geogenic radon potential was determined from a combination of soil-gas radon concentration and soil-air permeability of soil according to the relation expressed in equation 3.1 (Neznal *et al.*, 2004; Petermann *et al.*, 2020; Nuhu, *et al.*, 2021):

$$GRP = \frac{C_{Rn}}{-LogK_a - 10} \quad (3.1)$$

where C_{Rn} is the soil-gas radon concentration and Ka the soil-air permeability.

3.8 Application of Geographic Information System (GIS) for generation of Maps

Geographic coordinates of sampled locations for soil-gas radon concentration and soil-air permeability measurement were obtained using a hand-held Garmin 76 global positioning system (GPS) instrument. The coordinates were plotted using ArcGIS 10.5 software. Soil-gas radon concentration and geogenic radon potential data were linked to their respective coordinates within the ArcGIS 10.5 software. A soft copy of the existing geological map covering the area of study was provided by Nigerian Geological Survey Agency (NGSA) which served as basemap. The associated field measurements were georeferenced and were overlaid on the geological basemap.

The measured soil-gas radon concentration values and geogenic radon potential values were subsequently manually classified (based on the Akerblom and Neznal classifications) using the data quantification tool in the GIS platform over the study area. The resultant maps showed the distributional pattern of soil-gas radon concentration and geogenic radon potential overlaid on the geological map of the study area. The derived maps enabled the visual representation of the spatial distribution of soil-gas radon concentration and geogenic radon potential.

3.9 Statistical Analysis of Data Set

Measures of central tendency and variability used include minimum, maximum, range, median, arithmetic mean, standard deviation and mean absolute deviation (MAD). Frequency distribution plot for soil-gas radon concentration, soil-air permeability and geogenic radon potential was done. Shapiro-Wilk and Kolmogorov-Smirnov test of normality were used to determine if the data was normally distributed. On confirmation that the dataset was not normally distributed, the dataset was fitted to Lognormal

distribution (using EasyFit and Minitab) after which Kruskal–Wallis test of significance (using SPSS) was used to determine if bedrocks play significant role in determining the values of soil-gas radon concentration, soil-air permeability and geogenic radon potential in the Southwest region of Nigeria. Kruskal-Wallis ranking and Means plot were used to determine which bedrocks had the highest significance on the parameters.

3.10 Artificial Neural Network Modelling of Soil-gas Radon Concentration

Artificial neural network modelling was carried out on the soil-air permeability and soil-gas radon concentration data. A simple neural network configuration was employed to avoid artificial over-fitting, which comes with complex neural network configurations (Abidoye *et al.*, 2018).

The Artificial Neural Network (ANN) using Levenberg-Marquardt feed forward back propagation training algorithm was implemented on the data of bedrock type and measured soil-air permeability of the study locations, which served as the input, while the soil-gas radon concentration served as the target.

Following the mapminmax normalisation formula discussed in section 2.16.2, the input data of the bedrock type and the soil-air permeability were respectively normalised by the expressions:

$$T_{norm} = 0.105T - 1.105 \quad (3.2a)$$

$$P_{norm} = 0.032P - 1.022 \quad (3.2b)$$

The output data of soil-gas radon concentration was normalised by the expression:

$$CRn_{(norm)} = 0.044CRn - 1.012 \quad (3.2c)$$

The training of different configurations was done using neural network application tool of MATLAB R2013b version with 70% of the randomly selected dataset while 15% was used to test and 15% was used to validate. The 2 x 8 x 1 ANN configuration, having the highest correlation value, was chosen for the modelling. The schematic diagram of the 2 x 8 x 1 ANN configuration is shown in figure 3.3. The input, hidden and output connections of the ANN configuration is presented in figure 3.4.

The normalised input variables were imported to the input interface of the NNtool App for the chosen ANN configuration comprising two neurons at the input layer, eight neurons at the hidden layer and one neuron at the output layer. The connection weights and biasis of the 2 x 8 x 1 configuration for the Input–Hidden layer neurons were recorded after the training. The sum of the weighted normalised function $E_{I,i,n}$ for each neuron in the hidden layer was computed by substituting T_{norm} and P_{norm} in equation 2.17 and using equation 2.18 to obtain the tansigmoid function $F_{1,i,n}$.

The weights which connect a neuron of the hidden layer to a neuron of the output layer auto-generated by NNtool App as well as the bias of the neuron in the output layer translated $F_{I,i,j}$ to Purelin $O_{I,i,j}$ or a_{no} using equation 2.19.

The de-normalised value of a_{nO} gives the ANN predicted soil-gas radon concentration corresponding to bedrock type and soil-air permeability in the study area. The flowchart used for training the data is shown in appendix 2. The mathlab codes used in training the data to obtain the output and measures of performance for the model are shown in appendix 3.

3.11 Assessment of ANN Configurations

The correlation coefficient (R), mean square error (MSE), sum square error (SSE), Average Absolute Relative Error (AARE) and the Nash-Sutcliffe (NS) model efficiency coefficient were used in determining best performing ANN configuration. The 2 x 8 x 1 configuration performed best among the other configurations and was used to generate the ANN model. The performance of the ANN model derived was assessed by various statistical approaches detailed in section 2.16.8.

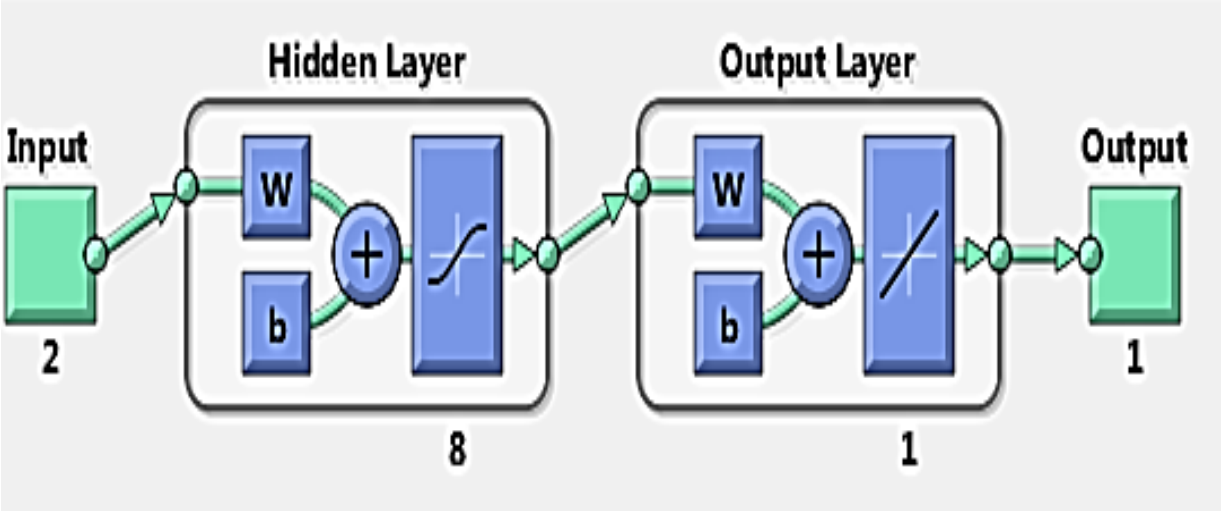

Figure 3.3 Schematic of 2 x 8 x 1 ANN Configuration

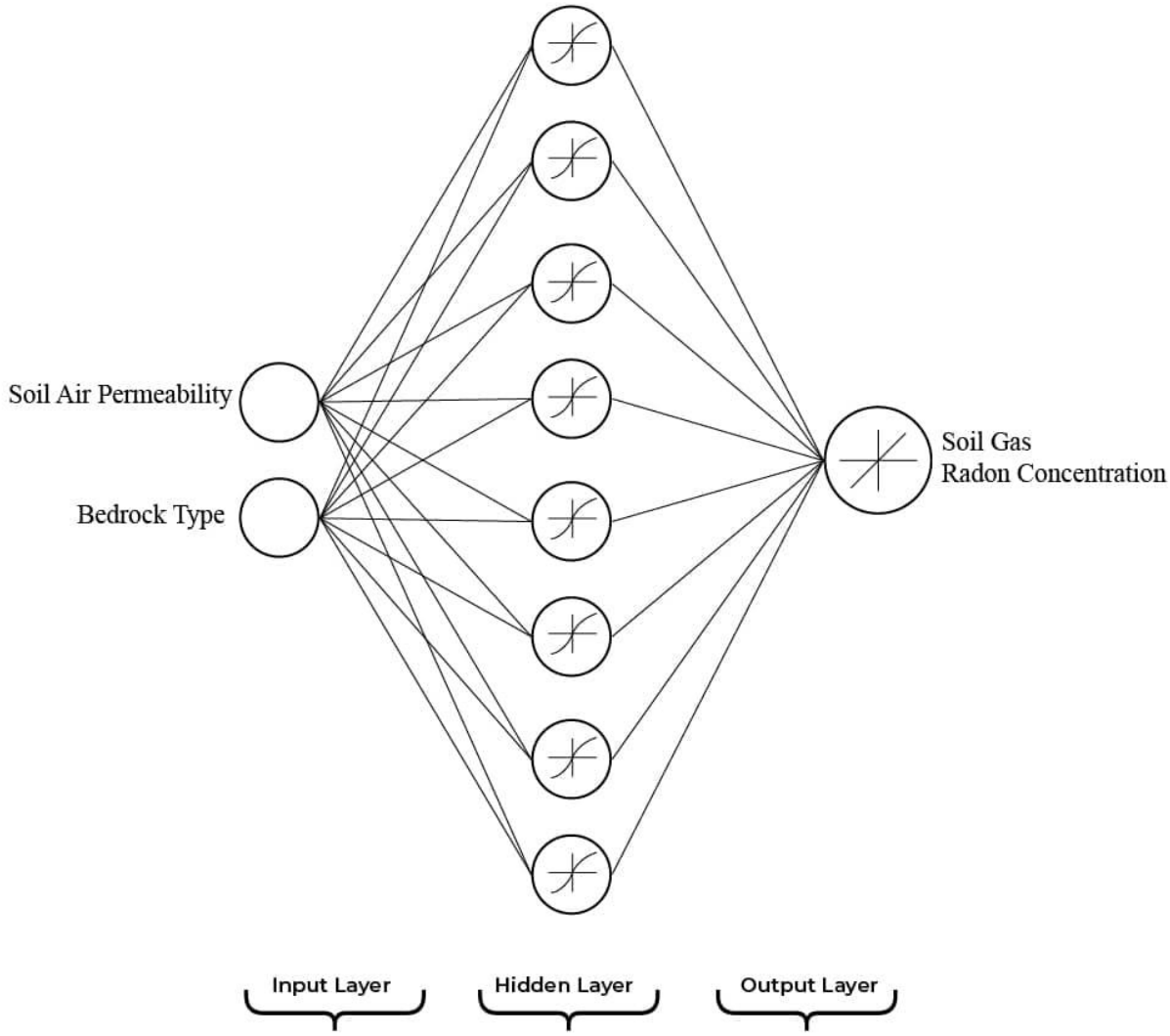

Figure 3.4 Input, Hidden and Output connections for the 2 x 8 x 1 ANN Configuration

CHAPTER FOUR
RESULTS AND DISCUSSION

4.1. Outline of Result Presentation and Discussion

The results of soil-gas radon concentration measured at 150 sites covering 20 bedrock types in Southwest Nigeria are presented and discussed. The distribution pattern of the soil-air permeability and that of the derived geogenic radon potential (GRP) across the bedrock types are also highlighted.

Results and discussion are also presented on the artificial neural network equation generated to predict the soil-gas radon concentration and geogenic radon potential from the obtained soil-air permeability and the bedrocks types. The distribution of measured and predicted data leading to soil-gas radon concentration and geogenic radon potential map generation are also discussed.

4.2 Analysis of measured Soil-gas Radon Concentration

Results of soil-gas radon concentration measured from study locations are presented in Appendix 1 (Table 1A1). The soil-gas radon concentration results were analysed using descriptive statistics, and a summary of the analysis is shown in table 4.1. Variation in mean values of soil-gas radon concentration indicates dependence on the lithology of the area under consideration (figure 4.1). The dependence of soil-gas radon concentration on geology is also observed from the boxplot in figure 4.2.

The mean soil-gas radon concentration obtained for the 150 measurements was 10.39 ± 12.59 kBqm^{-3} .The bedrocks in Southwest region of Nigeria can be divided into two main types which are Basement complex and Sedimentary terrain (section 3.2). The mean soil-gas radon concentration value for the Basement complex was 11.39 kBqm^{-3} while that of Sedimentary terrain was 7.06 kBqm^{-3} (table 4.2) showing that Basement complex has preponderance for higher soil-gas radon concentration than Sedimentary terrain.

Table 4.1 Statistical summary of Soil-gas Radon Concentration ($kBqm^{-3}$) on the Bedrocks

	Sites	Min.	Median	Max.	Mean	STDEV	Range	MAD
Migmatite	23	2.16	3.53	35.02	9.72	17.35	32.86	8.92
Granite Gneiss	12	8.49	29.24	44.89	26.93	22.58	35.90	15.13
Quartz Syenite	03	16.87	34.54	35.73	29.05	13.33	18.85	8.12
Banded Gneiss	11	2.76	6.44	10.37	6.76	0.06	7.62	1.76
Undifferentiated Schist	14	1.87	3.15	13.76	3.83	1.21	11.89	1.68
Amph. Schist & Ampibolite	04	8.92	10.45	13.56	10.85	3.28	11.52	1.36
FG Biotite Granite	08	2.31	3.52	7.79	3.91	1.40	5.47	1.07
M-CG Biotite & Biotite Hornblende Granite	05	1.14	3.12	5.93	3.17	0.88	4.79	1.58
CG Porphyritic Biotite & Biotite Hornblende Granite	17	2.11	7.15	47.59	18.09	1.03	45.47	14.87
Pegmatite	04	2.86	4.77	6.14	4.63	1.43	3.28	1.14
Flaggy Quartzite & Quartz Schist	04	6.37	7.21	0.81	7.15	1.06	1.43	0.44
Talc Schist	07	0.28	4.74	7.83	3.73	5.06	7.55	2.81
Shale, Limestone &Siltstone	08	7.42	14.60	46.77	19.92	24.04	39.35	12.84
Sandstone & Limestone	07	1.89	3.37	4.89	3.29	0.05	2.99	0.79
Sand and Mash	05	0.29	0.34	1.55	0.69	0.86	1.26	0.45
Sand and Clay	09	0.33	0.94	12.78	4.64	0.06	12.46	4.76
Sand, Clay and Shale	04	0.69	1.40	1.73	1.30	0.74	1.05	0.41
Phorphiroblastic Gneiss	02	2.90	4.57	6.25	4.57	2.37	3.35	1.68
Charnokite & Charnokitic Rock	02	42.14	43.15	44.15	43.15	1.42	2.01	1.01
Muscovite tourmaline granite gneiss	01	3.64	3.64	3.64	3.64	0.00	0.00	0.00

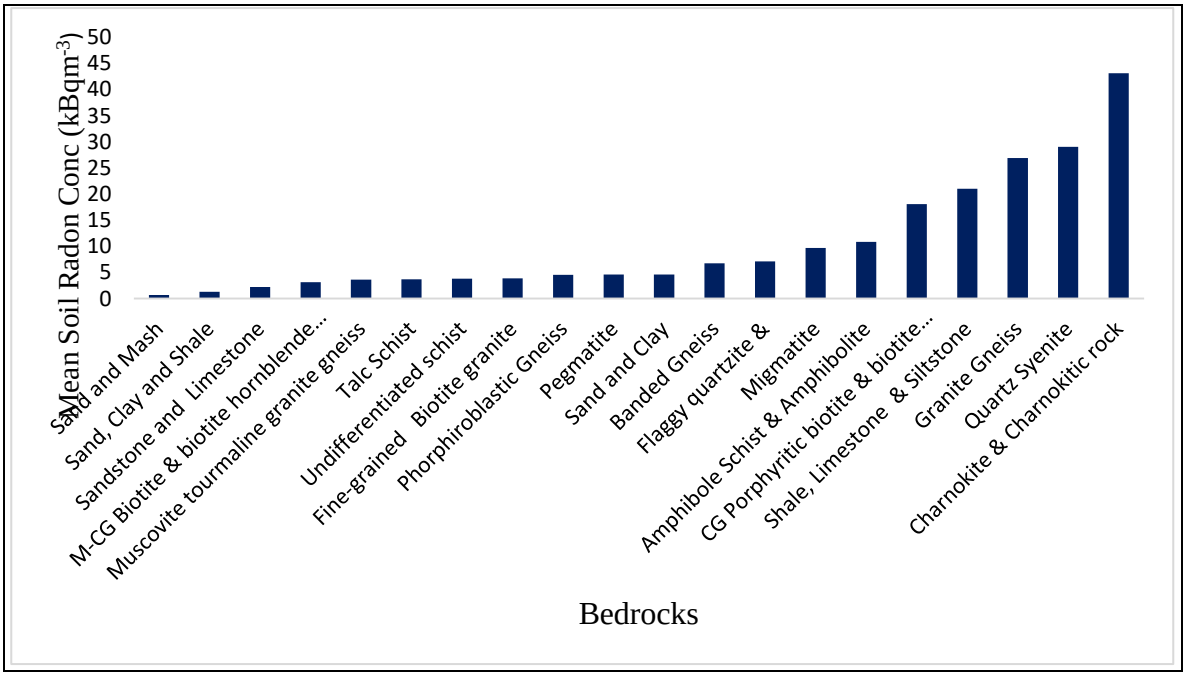

Figure 4.1 Variation of Soil-gas Radon Concentration according to bedrock types

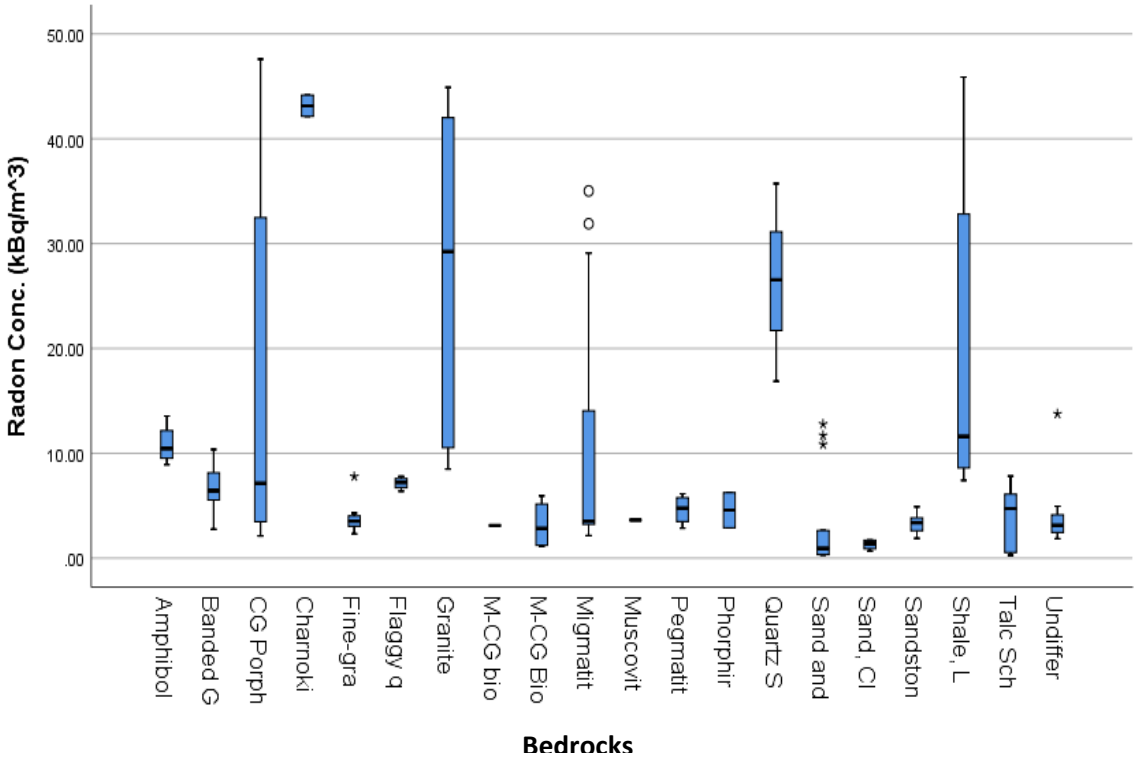

Figure 4.2 Box and Whiskers Plot of the Soil-gas Radon Concentration

Classification of obtained soil-gas radon concentration into major bedrocks of Granitic, Sedimentary, Metamorphic rocks and Sediments formation shows that the mean soil-gas radon concentration for soils on granitic bedrocks is 14.02 ± 29.02 $kBqm^{-3}$, for sedimentary rocks is 9.87 ± 29.72 $kBqm^{-3}$, for metamorphic rock is 10.07 ± 26.01 $kBqm^{-3}$, and for sediments is 3.23 ± 0.56 $kBqm^{-3}$, respectively (table 4.2). The highest soil-gas radon concentration was observed above a granitic bedrock, specifically in the soil above coarse-grained porphyritic biotite and biotite hornblende granite (47.59 $kBqm^{-3}$), while the lowest was found at a site over Talc schist with 0.28 $kBqm^{-3}$. Soils above Charnokites and charnokitic rocks (usually referred to as orthopyroxene granite) were found to have the highest average value of soil-gas radon concentration with a value of 43.15 ± 1.42 $kBqm^{-3}$. From table 4.1, the granitic bedrock that also gave a higher soil-gas radon concentration after Charnokite and chanokitic rock is Quartz Syenite (another granitic bedrock) with a mean value of 29.05 ± 13.33 $kBqm^{-3}$. It can therefore be inferred that granitic bedrocks tend to have higher soil-gas radon concentration than other bedrocks of Southwest Nigeria. Studies have confirmed that soils above granite-based bedrocks present higher mean soil-gas radon concentration than other bedrock types (Liu *et al.*, 2016; Mostečak *et al*., 2018; Cho and Choo, 2019; Nuhu, 2021).

Granitic rock has been discovered to contain the highest uranium and thorium content with a thorium to uranium (Th/U) ratio of 3/5. The average uranium content in granite generally is 3.5 – 4 ppm and for most uranium deposits, granitoids play the role of either "host" or more commonly as source (Ielsch *et al.*, 2010). This could explain why granitic bedrock had the highest mean soil-gas radon concentration in this work.

Uranium and thorium concentrations in metamorphic rocks depend on the mobilization and redistribution of elements during metamorphism (transformation due to high temperatures and pressure) and metasomatism (change in composition due to addition or removal of minerals) as well as by the grade of metamorphism suffered by the parent rock. This makes the uranium and thorium contents in metamorphic rocks to vary extensively. However among the metamorphic rocks, amphibolites, gneisses and migmatites have high tendencies for uranium, often acting as host to uranium-bearing minerals (Yassaghi and Masoodi, 2011). In the present study, granite gneiss rock

Table 4.2 Classification of Mean Soil-gas Radon Concentration over Twenty Bedrocks into Major Bedrocks

Major Bedrock	Bedrocks	Mean C_{Rn} ($kBqm^{-3}$)	STDEV
Granitic	Charnokite & Charnokitic Rock	43.15	
(39 Sites)	Quartz Syenite	29.05	
	CG Porphyritic biotite and biotite hornblende granite	18.09	
	Pegmatite	4.63	
	Fine-grained biotite granite	3.91	
	M-CG Biotite and biotite hornblende granite	3.17	
	Mean	14.02	29.02
Metamorphic	Granite Gneiss	26.93	
(78 Sites)	Flaggy quartzite and quartzite schist	7.15	
	Migmatite	9.72	
	Banded Gneiss	6.76	
	Phorphiroblastic Gneiss	4.57	
	Undifferentiated Schist	3.83	
	Talc Schist	3.73	
	Amphibole Schist and Amphibolite	10.85	
	Muscovite tourmaline granite gneiss	3.64	
	Mean	10.07	26.01
Basement Complex	Mean C_{Rn}	11.39	
Sedimentary	Shale, limestone and Siltstone	19.92	
(19 Sites)	Sandstone and Limestone	2.21	
	Sand, Clay and Shale	1.30	
	Mean	9.87	29.72
Sediments	Sand and Clay	4.64	
(14 Sites)	Sand and Mash	0.69	
	Mean	3.23	0.56
Sedimentary terrain	Mean CRn	7.07	

presented highest mean soil-gas radon concentration among metamorphic rocks followed by amphibole schist and amphibolite.

Shales, siltstone, sandstone, bauxite, bentonites and alum shales are types of sedimentary rocks. Thorium, uranium, and Th/U ratio in shales are nearer to those of granites. The high affinity of shales for uranium could explain why sedimentary bedrock follows after metamorphic bedrocks with regards to the mean soil-gas radon concentration observed in in this work.

Sand and mash sediments had the lowest soil-gas radon concentration with a mean value of 0.69 ± 0.86 $kBqm^{-3}$. Sediments are known to possess high soil-air permeability due to the interconnectedness of its pores resulting in high porosity and this explains its soil-gas radon concentration high standard deviation. This, in effect, means that radon gas can easily move from the site of production to the soil surface thereby leading to low value of soil-gas radon concentration at the 0.8 – 1.0m depth of measurement. This agrees with the results of studies showing that sediments present low soil-gas radon concentration (Szabo *et al.*, 2013).

Esan *et al.* (2020) found the mean soil-gas radon concentration measured above three bedrocks (granite gneiss, mica schist and grey gneiss – all metamorphic bedrocks) for OAU campus, Ile Ife, Nigeria, to be 14.1 $kBqm^{-3}$ which is in the same range with the mean value of 10.07 $kBqm^{-3}$ obtained for metamorphic bedrocks in this study. However, the mean soil-gas radon concentration value in this work (10.39 $kBqm^{-3}$) is lower when compared with 38.9 $kBqm^{-3}$ obtained by Ajiboye *et al.* (2018) in Ekiti state, Nigeria. The remarkable difference could be due to the predominance of granitic bedrocks in Ekiti state. The range of 0.53 – 9.70 $kBqm^{-3}$ reported for Ibadan, Nigeria in Obed *et al*. (2018) could be as a result of passive radon detector used and the shallow depth of measurement.

The mean soil-gas radon concentration obtained from the 150 locations in Southwest Nigeria is comparable to the mean soil-gas radon concentration obtained from studies in other parts of the world (table 4.3).

Table 4.3 Mean Soil-gas Radon Concentration in other parts of the World compared with this study

Country/Region	Mean soil-gas radon conc. ($kBqm^{-3}$)	Reference
Sudan	8.20	Elzain (2015)
Part of Iraq	5.74	Shafik. and Mohammed (2013)
Jeddah, Saudi Arabia	6.71	Farid (2016)
China	85.81	Liu, *et al.*, (2016)
Perak state, Malaysia	18.96	Nuhu *et al.* (2021)
SW Nigeria	10.39	This study

4.3 Classification of measured Soil-gas Radon Concentration based on Akerblom/Swedish Criteria

Several criteria have been suggested for classification of soil-gas radon concentration into Low, Medium and High levels (Lara *et al.*, 2015; Liu *et al.*, 2016). However the criteria that has gained wider acceptance is that based on Swedish or Akerblom criteria (Lara *et al.*, 2015) and this was adopted in this study. Based on the Swedish or Akerblom criteria (as discussed in section 2.15.1), 41 sites (representing 27.33% of the total number of sites) underlain by different bedrocks were found to have soil-gas radon concentration above 10 $kBqm^{-3}$ (figure 4.3) while 109 sites (representing 72.67%) were found to be below 10 $kBqm^{-3}$. This result compared favourably with that obtained by Esan *et al.* (2020) for Obafemi Awolowo University (OAU), Ile-Ife, Nigeria, where 65.9% of the sites fall under 10 $kBqm^{-3}$, 29.7% fall under 10 – 50 $kBqm^{-3}$ while 4.3% were above 50 $kBqm^{-3}$. It then suggests that Southwest Nigeria can be classified as mainly under 'Low' level of soil-gas radon infiltration. The sites above 10 $kBqm^{-3}$ classified under 'Normal' would require some protective measures which include but are not limited to ensuring no cracks in existing buildings, designing natural and extra ventilation channels in new buildings and use of low radon content materials for construction. None of the sites, in this study, had soil-gas radon concentration value above 50 $kBqm^{-3}$ that can be classified as 'High' level (figure 4.3).

The soils on bedrocks that had mean soil-gas radon concentration above 10 $kBqm^{-3}$ indicating 'Normal' level are Amphibole Schist and Amphibolite (10.85 $kBqm^{-3}$), Coarse - grain Porphyritic biotite and biotite hornblende granite (18.09 $kBqm^{-3}$), Shale, limestone and siltstone (19.92 $kBqm^{-3}$), Granite gneiss (26.93 $kBqm^{-3}$), Quartz syenite (29.05 $kBqm^{-3}$) and Charnokite and charnokitic bedrock (43.15 $kBqm^{-3}$), respectively.

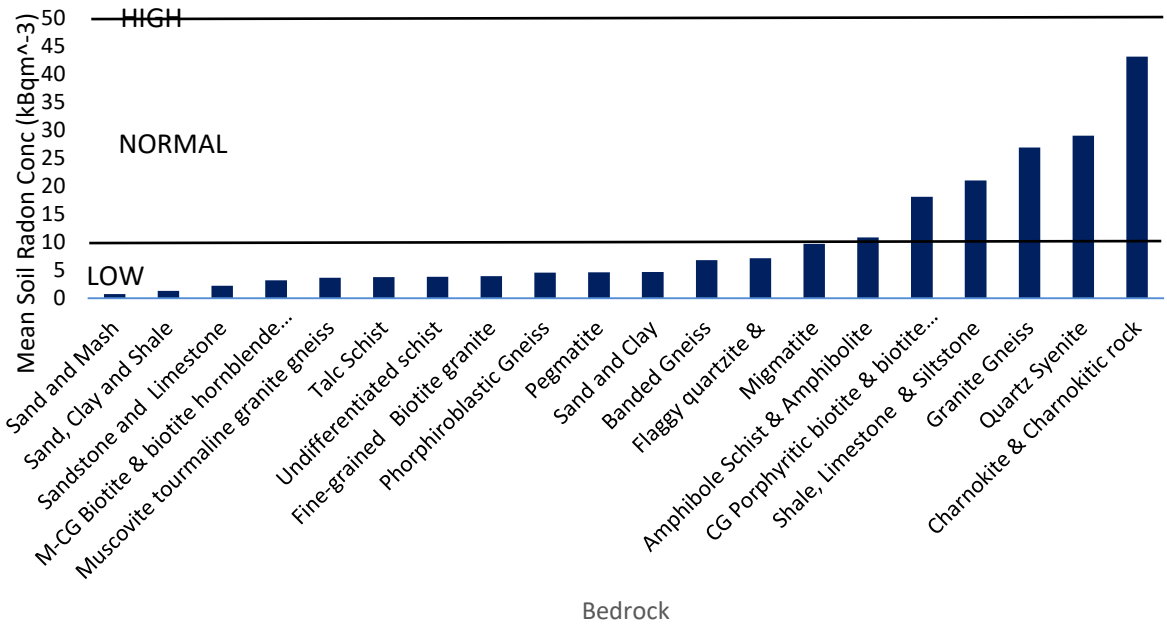

Figure 4.3 Classification of Mean Soil-gas Radon Concentration on the Bedrocks based on Akerblom/Swedish Criteria

4.4 Analysis of measured Soil-Saturated Hydraulic Conductivity and Soil-air Permeability

The result of the soil saturated hydraulic conductivity obtained for the 150 sites as well as the derived soil-air permeability is presented in Appendix 1 (Table 1A2). The statistical summary of the saturated hydraulic conductivity and derived soil-air permeability is as presented in table 4.4.

Soil-air permeability had a range between 5.90 x 10^{-13} m^2 and 8.70 x 10^{-11} m^2, a mean value of 8.87 x 10^{-12} m^2 and standard deviation of 17.4 x 10^{-12} m^2. The variation in the values of the soil-air permeability indicates its dependence on the lithology of the area under consideration. The dependence of soil-air permeability on geology is further observed in the boxplot in figure 4.4.

Further classification of the obtained soil-air permeability into major bedrocks of Granitic, Metamorphic, Sedimentary bedrocks and Sediments formation shows that the soil-air permeability values for soils on granitic bedrocks is 4.56 (± 1.18) x 10^{-12} m^2, for metamorphic bedrock is 4.06 (± 1.36) x 10^{-12} m^2, for sedimentary bedrock is 35.65 (± 42.43) x 10^{-12} m^2 and for sediments is 39.84 (± 53.41) x 10^{-12} m^2, respectively (table 4.5). It can be observed from table 4.5 that soils on sediments had the highest soil-air permeability followed by soils on sedimentary bedrocks, granitic bedrocks and metamorphic bedrocks respectively. This could be due to the fact that sediments and sedimentary bedrocks have bigger pores and interconnectedness compared with granitic and metamorphic bedrocks.

The bedrocks in Southwest region of Nigeria can be further divided into two main stypes which are basement complex and sedimentary terrain (section 3.2). The mean soil-air permeability value for soils that fall on the basement complex was 4.22 (± 2.38) x 10^{-12} m^2 while that of sedimentary terrain was 25.07 (± 50.08) x 10^{-12} m^2 showing that sedimentary terrain has preponderance for higher soil-air permmeability than basement complex.

Table 4.4 Statistical summary of Soil-air Permeability (x 10^{-12} m^2) on the Bedrocks in Southwest Nigeria

	Sites	Minimum	Median	Maximum	Mean	STDEV	Range	MAD
Migmatite	23	1.54	3.96	12.45	4.45	2.39	10.91	1.35
Granite Gneiss	12	2.31	3.34	7.23	4.58	1.75	4.91	1.57
Quartz Syenite	03	3.05	4.09	1.03	5.82	3.93	7.27	3.00
Banded Gneiss	11	3.22	3.93	7.04	4.51	1.22	3.82	1.00
Undifferentiated Schist	14	1.17	4.23	10.04	3.34	1.93	8.87	1.11
Amph. Schist & Ampibolite	04	0.68	1.25	1.67	1.21	0.43	0.99	0.33
Biotite Granite	08	2.56	3.24	9.91	4.61	2.93	7.34	2.33
M-CG Biotite & Biotite Hornblende Granite	05	0.83	4.11	5.36	3.64	1.74	4.52	1.27
CG Porphyritic Biotite & Biotite Hornblende Granite	17	2.39	3.68	9.36	4.16	1.75	6.97	1.18
Pegmatite	04	4.30	5.07	7.05	5.38	1.22	2.74	0.90
Flaggy Quartzite & Quartz Schist	04	2.74	3.85	4.59	3.76	0.79	1.86	0.59
Talc Schist	07	0.59	1.51	6.11	2.04	1.84	5.52	1.16
Shale, Limestone & Siltstone	08	2.41	4.27	6.65	4.29	1.50	4.24	1.17
Sandstone & Limestone	07	1.44	4.31	4.95	3.94	1.16	3.50	7.25
Sand and Mash	05	0.81	76.47	87.00	64.00	35.60	86.19	25.28
Sand and Clay	09	0.70	12.99	82.63	26.41	30.97	81.93	26.35
Sand, Clay and Shale	04	0.72	63.89	79.06	51.89	34.88	78.34	25.58
Phorphiroblastic Gneiss	02	2.58	2.60	2.62	2.59	0.03	0.05	0.02
Charnokite & Charnokitic Rock	02	5.78	6.45	7.12	6.45	0.95	0.03	0.67
Muscovite tourmaline granite gneiss	01	9.14	9.14	9.14	9.14	0.00	0.00	0.00

*STDEV = Standard deviation; *MAD = Mean absolute deviation

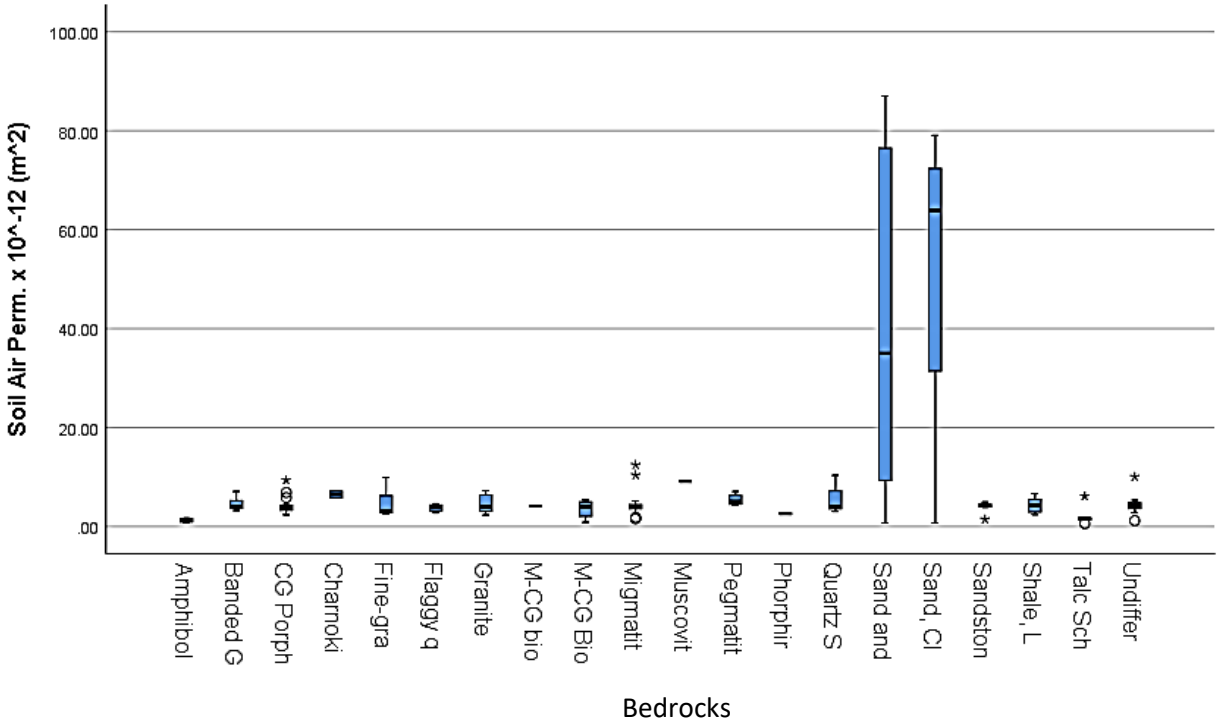

Figure 4.4 Box and Whiskers Plot of Soil-air Permeability (m^2)

Table 4.5 Classification of measured Soil-air Permeability on Twenty Bedrocks into Major Bedrocks

Major Bedrock	Bedrocks	Mean Soil-air Permeability ($x10^2$ m^2)	STDEV
Granitic	Charnokite & Charnokitic Rock	6.45	
(39 Sites)	Quartz Syenite	5.82	
	CG Porphyritic biotite and biotite hornblende granite	4.16	
	Pegmatite	5.38	
	Fine-grained biotite granite	4.61	
	M-CG Biotite and biotite hornblende granite	3.64	
	Mean	4.55	1.18
Metamorphic	Granite Gneiss	4.45	
(78 Sites)	Flaggy quartzite and quartzite schist	3.76	
	Migmatite	4.45	
	Banded Gneiss	4.51	
	Phorphiroblastic Gneiss	2.59	
	Undifferentiated Schist	3.34	
	Talc Schist	2.04	
	Amphibole Schist and Amphibolite	1.21	
	Muscovite tourmaline granite gneiss	9.14	
	Mean	4.06	1.36
Sedimentary	Shale, limestone and Siltstone	4.29	
	Sandstone and Limestone	3.94	
	Sand, Clay and Shale	51.89	
	Mean	35.65	42.43
Sediments	Sand and Clay	26.41	
(14 Sites)	Sand and Mash	64.01	
	Mean	39.84	53.41

4.5 Classification of Computed Geogenic Radon Potential

Parameters of soil-gas radon concentration and soil-air permeability were translated to the geogenic radon potential (GRP) with equation 3.2. The GRP obtained for each of the 150 sites is presented in Appendix 1 (Table 1A3). The statistical summary of the GRP obtained over the 20 bedrocks considered are as shown in table 4.6. The variation of the GRP with regard to bedrock types is shown in the box plot presented in figure 4.5.

The obtained GRP ranged between 0.15 to 39.19, with the lowest value found in soil over Talc schist bedrock and the highest value found in soil over CG Porphyritic biotite and biotite hornblende granite. The mean GRP obtained for the 150 sites was 8.46 ± 10.29. It is seen from table 4.6 that soils above Charnokite and charnokitic bedrock had highest average GRP of 36.19 while soils above M-CG biotite and biotite hornblende granite gave the lowest mean GRP of 2.22. Interestingly the two bedrocks with the highest and lowest mean GRP are granitic bedrocks showing that granitic bedrocks have a varied affinity for radon-bearing minerals based on its formation process. The Neznal classification (section 2.15.2) was used to classify the GRP obtained in soils over the twenty bedrocks considered (figure 4.6). It was observed that 113 sites (75.33%) were having GRP < 10 while 24 sites (16.00 %) had GRP between 10 and 35. Thirteen (13) sites (8.67%) had GRP values above 35.

Among the 13 sites with GRP > 35, metamorphic bedrocks (Migmatite and Granite gneiss) had six sites compared to granitic bedrocks with five sites implying that granitic and metamorphic bedrocks may have elevated soil-gas radon concentration and consequently elevated GRP. It should be noted, however that sedimentary bedrocks such as Shale, limestone and siltstone have elevated GRP as observed at Ewekoro, Sagamu and Ilaro axis in Ogun state. Studies by Obed *et al*. (2005), Jibiri and Famodimu (2013) and Samuel *et al.* (2022) have confirmed Abeokuta and adjourning areas in Ogun state as having high background radiation which is traceable to the predominant Shale, limestone and siltstone underlying bedrocks. Medium GRP (10 – 35) was found at Ijero – Aramoko Ekiti axis with values 13.78 and 23.31 having undifferentiated schist and migmatite bedrocks. This aligns with the study conducted on radioactivity in streams, wells and borehole water in the same area by Olise *et al*. (2016) which reported elevated radon in the

water samples. The mean GRP obtained in this study for the 150 sites (8.46) shows that the Southwest of Nigeria can generally be regarded as under GRP < 10 based on the Neznal classification. The locations where geogenic radon potential above 35 were found are Abeokuta – Sagamu – Ewekoro axis (situated over Shale, limestone and siltstone) in Ogun state; Idanre – Akure axis (situated over CG Porphyritic biotite and biotite hornblende granite) in Ondo state; Igbeti – Oke-ogun axis (situated over Quartz syenite and granite gneiss) in Oyo state and Ede axis (situated over Charnokite and chanokitic granite) in Osun state.

This study being novel for the southwestern region can serve as a baseline for further work.

The range of geogenic radon potential values according to the groups of major bedrocks and their mean values are presented in table 4.7 which shows that granitic bedrocks had the highest mean GRP with 13.71 ± 13.83 while metamorphic bedrocks had the lowest mean GRP of 6.19.

The summary statistics of the ungrouped radon concentration, soil-air permeability and geogenic radon potential for all 150 sites is as presented in table 4.8.

Table 4.6 Statistical summary of Geogenic Radon Potential on the Bedrocks in Southwest Nigeria

	Sites	Minimum	Median	Maximum	Mean	STDEV	Range	MAD
Migmatite	23	1.63	2.82	35.64	7.26	9.02	34.01	6.75
Granite Gneiss	12	5.60	20.11	35.42	20.96	14.02	29.82	13.24
Quartz Syenite	03	12.16	22.79	36.23	23.73	12.06	24.07	8.34
Banded Gneiss	11	1.89	4.58	8.99	5.11	2.08	7.10	1.64
Undifferentiated Schist	14	1.41	2.16	13.78	2.97	3.17	12.37	1.62
Amph. Schist & Ampibolite	04	4.12	5.49	7.64	5.68	1.47	3.51	1.04
Biotite Granite	08	1.92	2.34	7.32	2.95	1.79	5.41	1.11
M-CG Biotite & Biotite Hornblende Granite	05	0.55	2.25	3.99	2.22	1.45	3.45	1.14
CG Porphyritic Biotite & Biotite Hornblende Granite	17	1.56	4.97	39.19	13.62	13.40	37.68	11.46
Pegmatite	04	2.27	3.82	4.49	3.59	0.96	2.22	0.68
Flaggy Quartzite &Quartz Schist	04	4.41	4.91	5.84	5.02	0.68	1.43	0.56
Talc Schist	07	0.15	2.12	6.45	2.30	2.32	6.24	1.82
Shale, Limestone & Siltstone	08	5.06	9.92	35.07	15.73	12.93	30.01	10.56
Sandstone & Limestone	07	1.39	2.09	3.58	2.32	0.75	2.19	0.59
Sand and Mash	05	0.16	5.52	13.28	6.28	5.38	13.12	4.29
Sand and Clay	09	0.17	10.13	15.44	7.17	5.96	15.27	5.25
Sand, Clay and Shale	04	0.32	7.39	16.65	7.94	6.91	16.33	5.12
Phorphiroblastic Gneiss	02	1.83	2.88	3.93	2.88	1.49	2.11	1.05
Charnokite & Charnokitic Rock	02	35.67	36.19	36.73	36.19	0.75	1.07	0.53
Muscovite tourmaline granite gneiss	01	3.50	3.50	3.50	3.50	0.00	0.00	0.00

Note: STDEV = Standard deviation; MAD = Mean absolute deviation

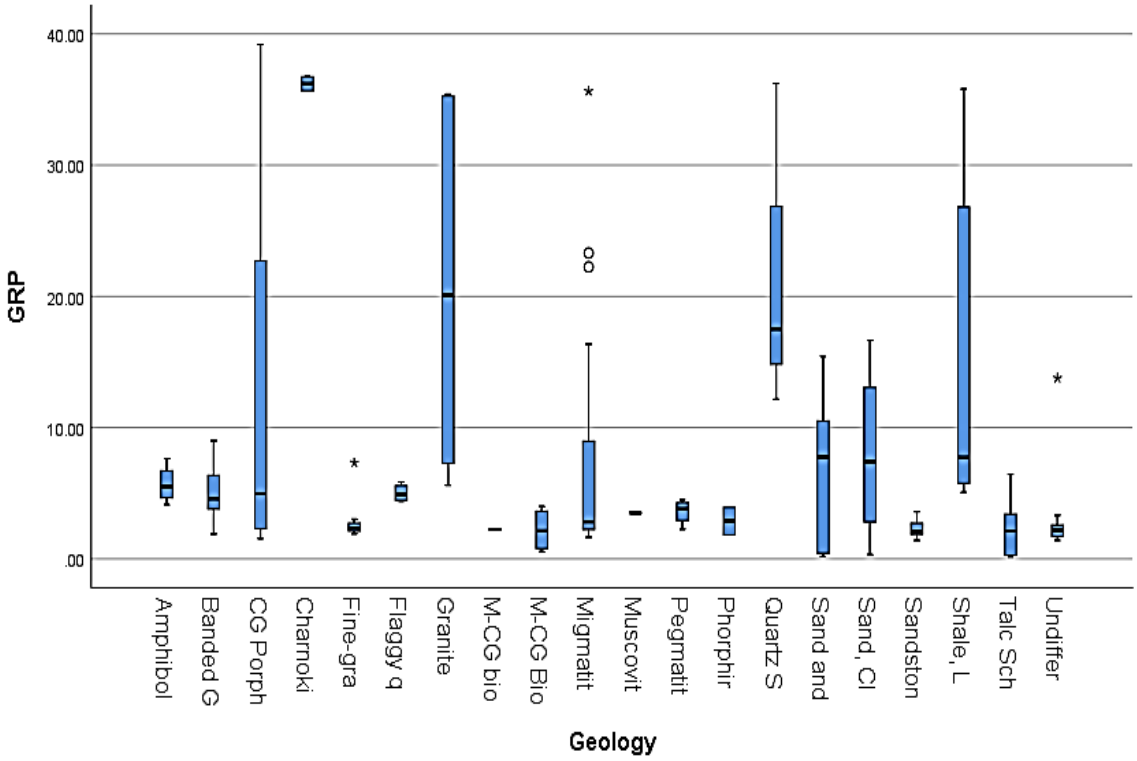

Figure 4.5 Box and Whiskers Plot of Geogenic Radon Potential

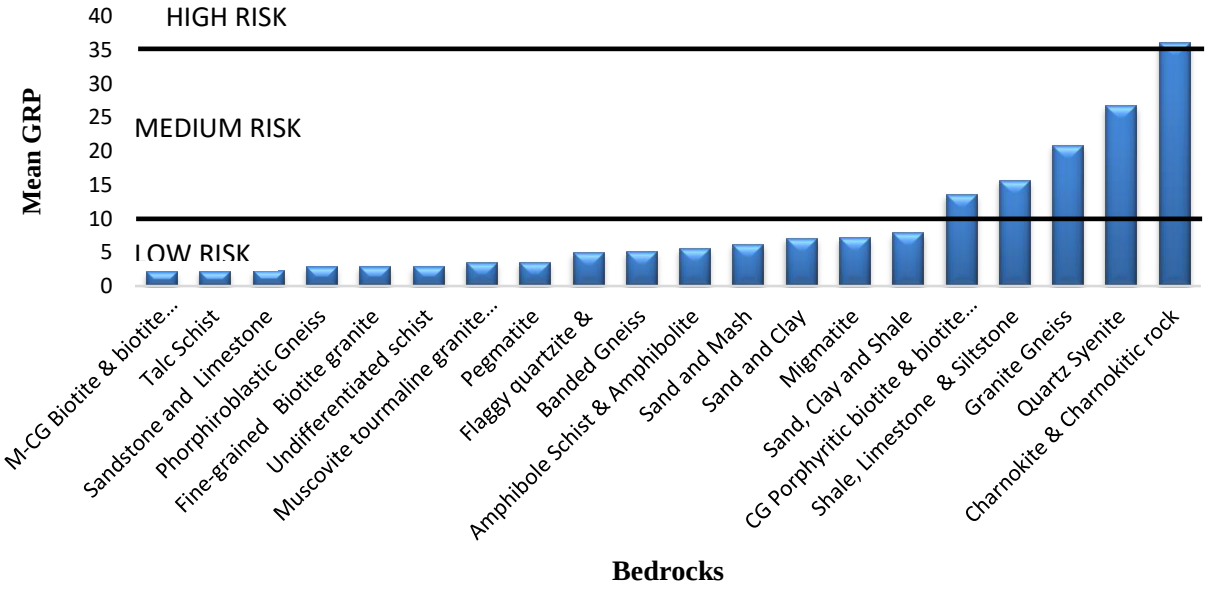

Figure 4.6 Sorting of Mean Geogenic Radon Potential of Bedrocks based on Neznal Classification

Table 4.7 Classification of computed Geogenic Radon Potential over Twenty Bedrocks into Major Bedrocks

Major Bedrock	Bedrocks	Range	GRP (Mean)
Granitic (39 Sites)	Charnokite & Charnokitic Rock	35.67 - 36.73	36.19
	Quartz Syenite	12.16 - 36.23	23.73
	CG Porphyritic biotite and biotite hornblende granite	1.56 - 39.19	13.62
	Pegmatite	2.27 - 4.49	3.59
	Fine-grained biotite granite	1.92 - 7.32	2.95
	M-CG Biotite and biotite hornblende granite	0.55 - 3.99	2.22
		Mean	13.71
Metamorphic (78 Sites)	Granite Gneiss	5.60 - 35.42	20.96
	Flaggy quartzite and quartzite schist	4.41 - 5.84	5.02
	Migmatite	1.63 - 35.64	7.26
	Banded Gneiss	1.89 - 8.99	5.11
	Phorphiroblastic Gneiss	1.83 - 3.93	2.88
	Undifferentiated Schist	1.41 - 13.78	2.97
	Talc Schist	0.15 - 6.45	2.30
	Amphibole Schist and Amphibolite	4.12 - 7.64	5.68
	Muscovite tourmaline granite gneiss	3.50 - 3.50	3.50
		Mean	6.19
Sedimentary (19 Sites)	Shale, limestone and Siltstone	5.06 - 35.07	15.73
	Sandstone and Limestone	1.39 - 3.58	2.32
	Sand, Clay and Shale	0.32 - 16.65	7.94
		Mean	8.66
Sediments (14 Sites)	Sand and Clay	0.17 - 15.44	7.17
	Sand and Mash	0.16 - 13.28	6.28
		Mean	6.73

Table 4.8 Statistical summary of Soil-gas Radon Concentration, Soil-air Permeability and GRP of 150 sites

	Maximum	Minimum	Mean	Median	STDEV	Range	MAD
Soil-air permeability (x 10^{-12} m^2)	87.01	0.59	8.87	4.06	17.40	86.42	8.75
Radon Concentration ($kBqm^{-3}$)	47.59	0.28	10.39	4.76	12.59	47.31	9.29
GRP	39.19	0.15	8.46	3.97	10.29	39.04	7.53

4.6 Inferential Statistical Analysis of Data - Test of Significance

Inferential statistics help to compare parameters from a sample population such that deductions can be generalised to the population data. It involves testing the hypothesis that helps to draw conclusions about the population data. Inferential statistics used in this study helped to characterize the bedrocks in terms of the soil-gas radon concentration, soil-air permeability and geogenic radon potential.

4.6.1 Normality Test

The descriptive statistics of soil-gas radon concentration, soil-air permeability and GRP respectively presented earlier (table 4.8), showed that the mean is generally higher than the median – a good indication that the datasets are skewed and not normally distributed. For confirmation, the dataset was subjected to normality test, using Kolmogorov-Smirnov and Shapiro-Wilk tests for normality and this translated to the levels of significance presented in table 4.9. At 95% confidence level ($p < 0.05$), the result presented in table 4.9 depicts the rejection of the null hypothesis (that the dataset is normally distributed) and the acceptance of the alternate hypothesis that the dataset is not normally distributed. The non-normality of the dataset is further confirmed from the frequency plots of the radon concentration, soil-air permeability and the GRP presented in figures 4.7, 4.8 and 4.9, respectively.

Geospatial data such as soil-gas radon concentration measurements are often characterized by non–normality and outliers (Szabo *et al.*, 2013; Szabo *et al.*, 2014), therefore statistical tools such as ANOVA (which assumes data normality) could not be used to analyze the data further.

Table 4.9 Kolmogorov-Smirnov and Shapiro-Wilks test of Normality on the Dataset

	Kolmogorov-Smirnov			Shapiro-Wilk		
	Statistic	Df	Sig.	Statistic	Df	p-values.
Soil-Gas Radon Conc.	0.259	149	0.0001	0.720	149	0.0001
Sat Hydraulic Conductivity	0.424	149	0.0001	0.338	149	0.0001
Soil-Air Permeability	0.396	149	0.0001	0.385	149	0.0001
Geogenic Radon Potential	0.231	149	0.0001	0.742	149	0.0001

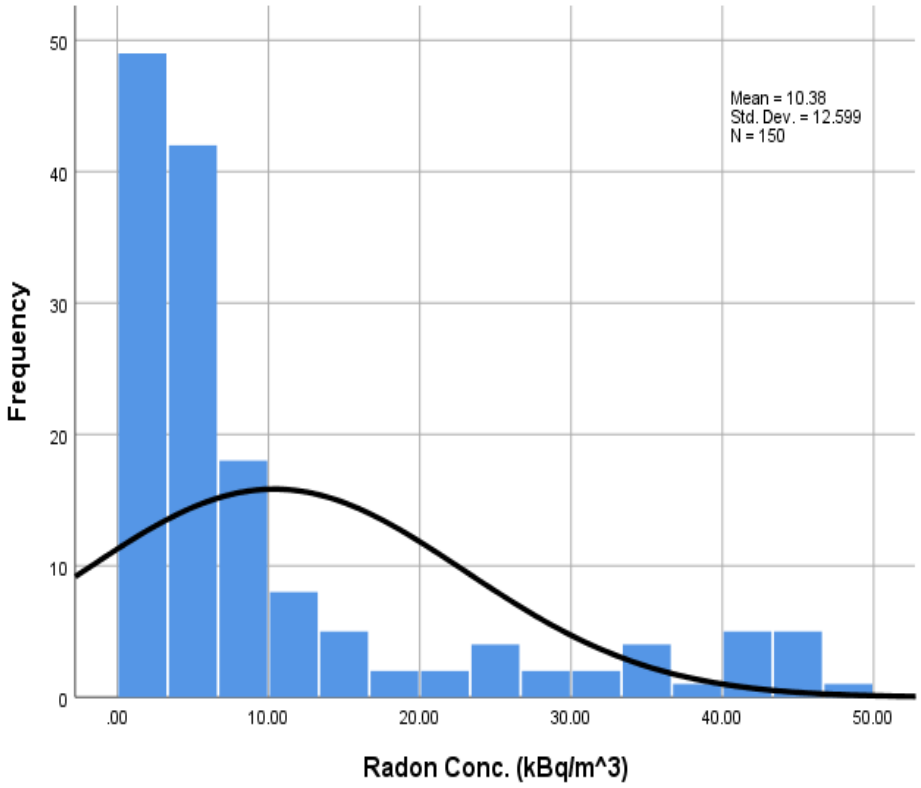

Figure 4.7 Frequency Distribution for Soil-gas Radon Concentration Data

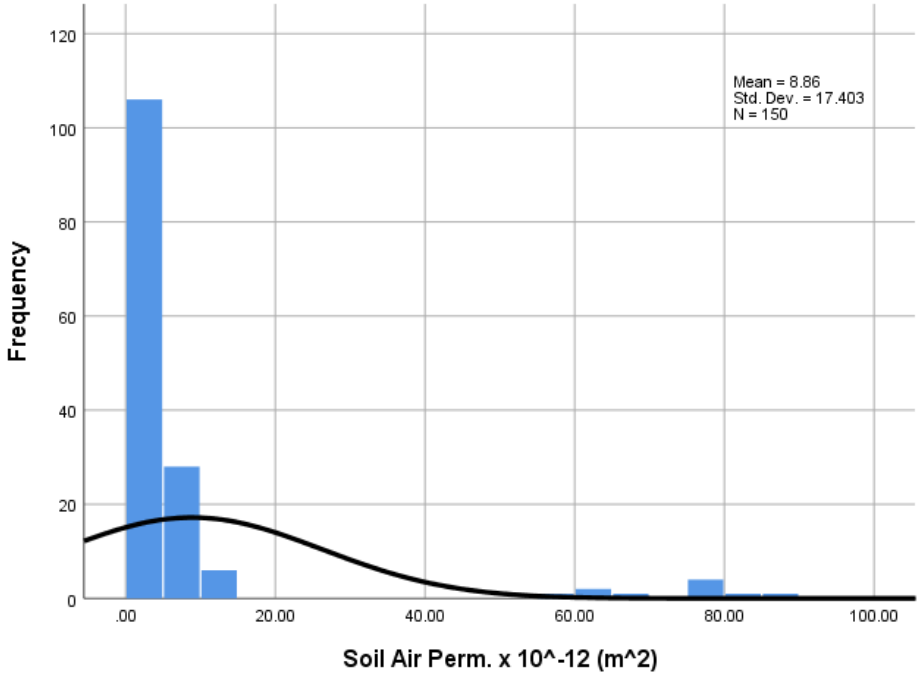

Figure 4.8 Frequency Distribution for Soil-air Permeability Data

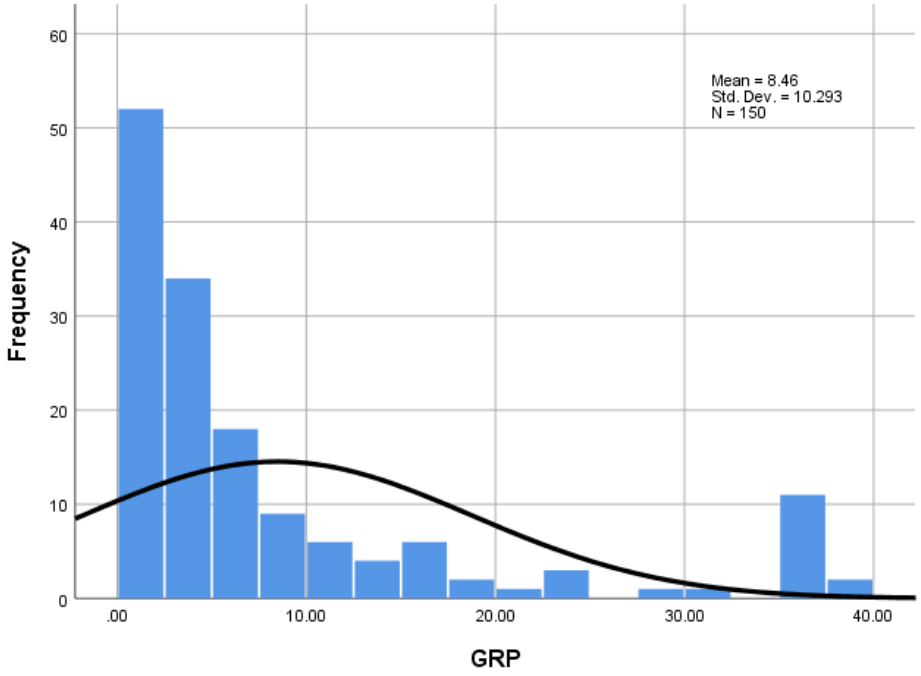

Figure 4.9 Frequency Distribution for Geogenic Radon Potential Data

4.6.2 Fitting of Data and Goodness-of-fit Test

The frequency distribution plots earlier presented revealed that the datasets of soil-gas radon concentration, soil-air permeability and geogenic radon potential are skewed to the right. With the dataset confirmed to be not normally distributed, the data was fitted to a statistical distribution that allows for analysis of not normally distributed data. To determine which type of statistical distribution to engage, goodness-of-fit tests were performed on the proposed distribution models. From the application of the three goodness-of-fit tests (Anderson-Darling, Kolmogorov-Smirnov and Chi-squared) considered in this study, it was observed from the statistic value that lognormal distribution performed better than gamma distribution (tables 4.10 and 4.11). The fact that lognormal distribution best describes spatially distributed GRP data was confirmed by Makin and Atta (2018) and Petermann *et al.*, (2020). The lognormal distribution fitted to the radon concentration and geogenic radon potential data are shown in figure 4.10 and figure 4.11, respectively.

Non-parametric tests, such as Kruskal-Wallis, are usually used to test the significance of a parameter (such as bedrock type) on data. The dataset, having been fitted to a lognormal distribution was subjected to Kruskal-Wallis test under the null hypothesis that bedrock type does not determine the values of radon concentration, soil-air permeability and GRP. The result presented in table 4.12 shows that the p-value is less than 0.05 at the 95% confidence level. This confirmed that the bedrocks have unequal chances of having high or low values of the measured parameters thus affirming the influence of the bedrock type on the parameters of soil-gas radon concentration, soil-air permeability and GRP, respectively. The result confirmed that bedrock types significantly determine the variation in soil-air permeability, soil-gas radon concentration and geogenic radon potential.

Table 4.10 Goodness-of-fit test for Lognormal and Gamma Distributions for Soil-gas Radon Concentration data

#	Distribution	Kolmogorov Smirnov		Anderson Darling		Chi-Squared	
		Statistic	Rank	Statistic	Rank	Statistic	Rank
2	Lognormal	0.17054	1	8.0224	1	68.896	1
1	Gamma	0.48412	2	50.729	2	447.38	2

(Note: the lower or closer to zero the statistic value is, the better the data distribution model)

Table 4.11 Goodness-of-fit test for Lognormal and Gamma Distributions for Geogenic Radon Potential Data

#	Distribution	Kolmogorov Smirnov		Anderson Darling		Chi-Squared	
		Statistic	Rank	Statistic	Rank	Statistic	Rank
2	Lognormal	0.09637	1	1.8615	1	15.581	1
1	Gamma	0.17306	2	4.8829	2	47.937	2

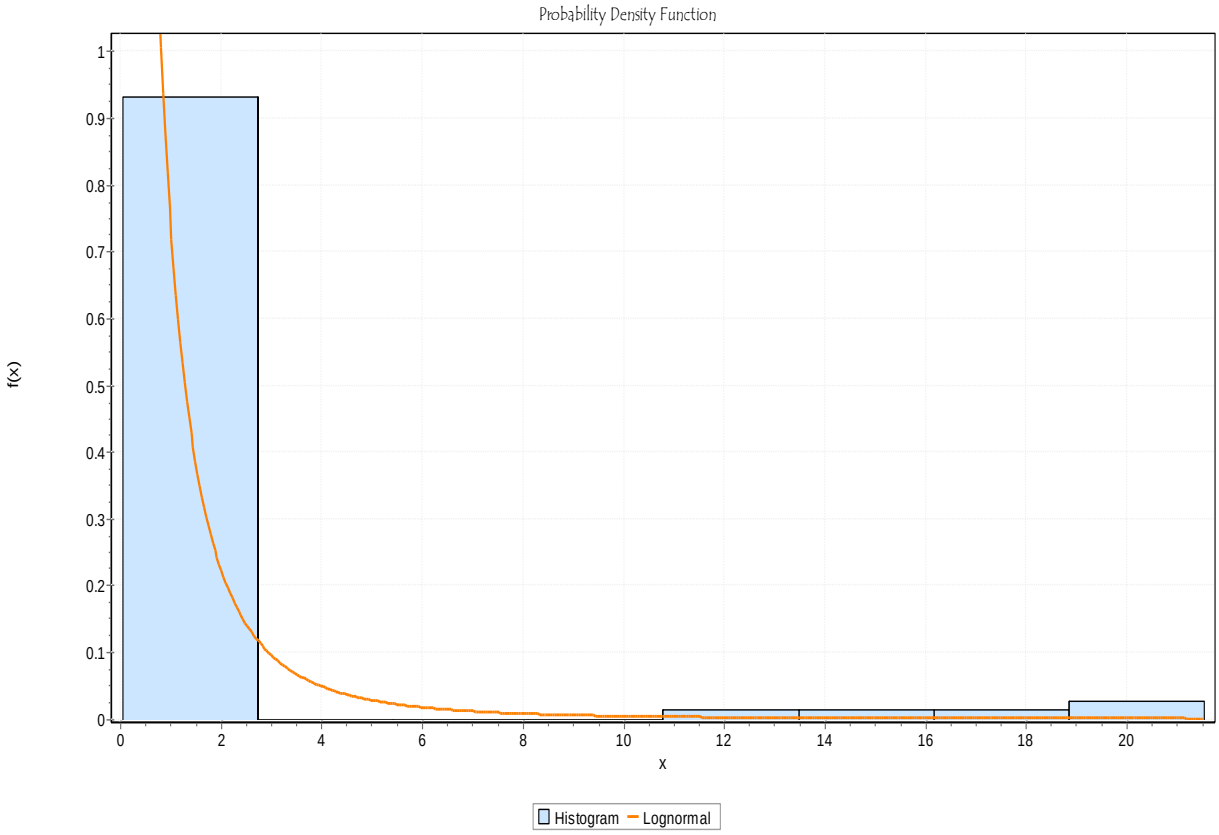

Figure 4.10 Soil-gas Radon Concentration Data Fitted to a Lognormal Distribution

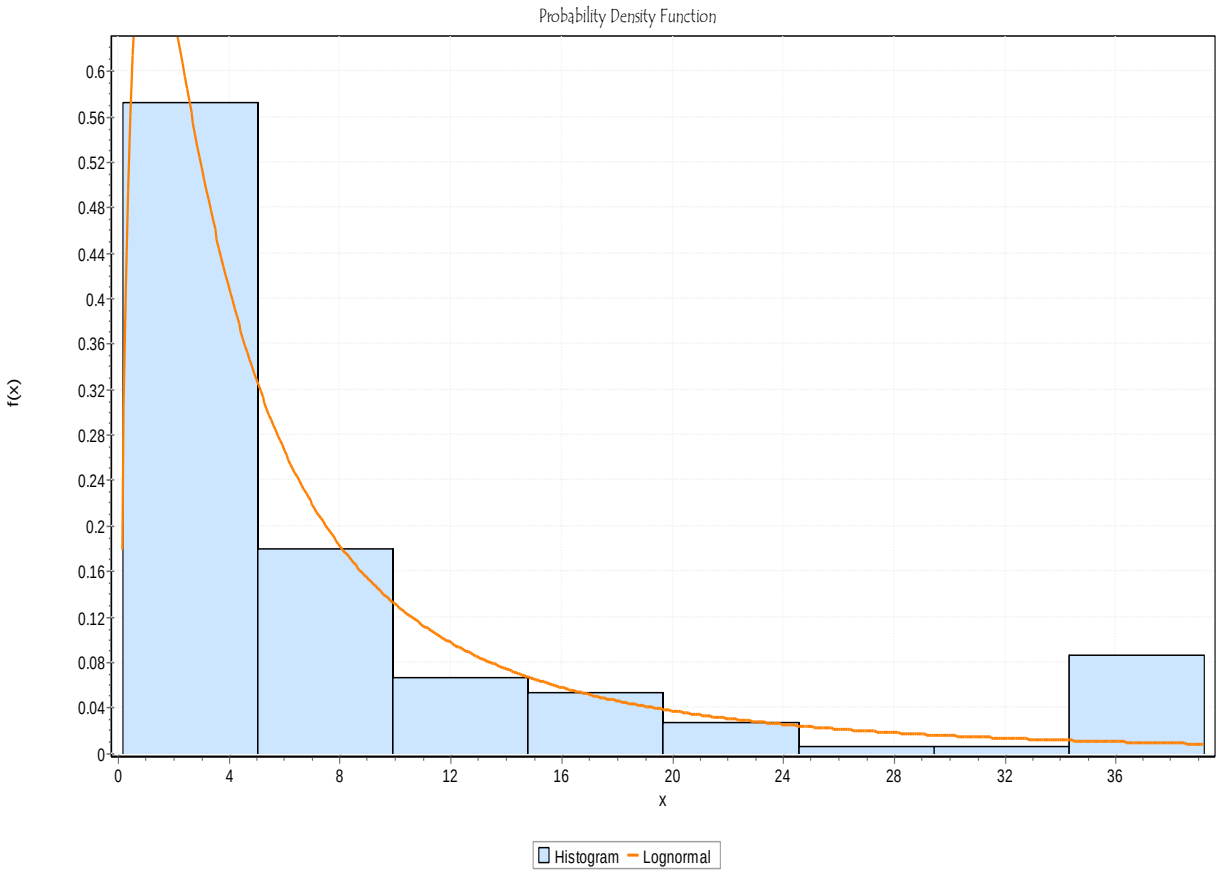

Figure 4.11 Geogenic Radon Potential Data Fitted to a Lognormal Distribution

Table 4.12 Kruskal-Wallis Test of Significance of Bedrocks on the Parameters

Test Statistics[a,b]

	Radon Conc. (kBq/m^3)	Sat. Hyd. Cond. (m/day)	Soil Air Perm. x 10^{-12} (m^2)	GRP
Kruskal-Wallis H	79.584	37.417	41.499	60.259
Df	19	19	19	19
Asymp. Sig.	.000	.007	.002	.000

a. Kruskal Wallis Test

b. Grouping Variable: Geology

To determine the bedrocks with the strongest influence on the parameters of interest, the Kruskal–Wallis ranking was obtained, as shown in table 4.13. The ranking revealed that Charnokite and Charnokitic bedrock, Quartz Syenite, Granite Gneiss, Shale, Limestone and Siltstone as well as CG Porphyritic biotite and biotite hornblende granite respectively, contributed more to the soil-gas radon concentration and GRP than the other bedrocks in southwestern Nigeria. Conversely, Muscovite and tourmaline granite gneiss, Charnokite and charnokitic bedrock, Sand and mash, Sand and clay as well as Sand, clay and shale contributed more to high values of soil-air permeability. This confirms that Sedimentary formation (Sand and mash, Sand and clay, Sand, clay and shale) contributed more to soil-air permeability among the bedrocks in Southwest Nigeria. Among the high contributors to radon concentration and GRP, three bedrocks belong to the granitic family of bedrocks (Charnokite and Charnokitic bedrock, Quartz Syenite and CG Porphyritic biotite and biotite hornblende granite). This confirms that granite-based bedrocks produce and release more radon gas compared to other bedrocks in Southwest Nigeria.

The means plot (figure 4.12) was further used to investigate the variation of the mean radon concentration among the bedrocks. The result further confirmed the Kruskal-Wallis ranking showing that Charnokite and Charnokitic rock has the highest average radon concentration. Most of the bedrocks fall below 10 $kBqm^{-3}$ and five bedrocks which are Charnokite and Charnokitic rock, Quartz Syenite, Granite gneiss, Shale, Limestone and Siltstone as well as CG Porphyritic biotite and biotite hornblende granite are bedrocks with average radon concentration above 10 $kBqm^{-3}$. This implies that these five bedrocks (among which three are granitic bedrocks) contributed more to the high radon concentration and consequently, geogenic radon potential in Southwest Nigeria.

Table 4.13 Kruskal-Wallis ranking of the Parameters across the Bedrocks

Bedrocks	CRn $kBqm^{-3}$	Ks m/day	Ka m^2	GRP
Charnokite & Chanokitic rock	1	2	2	1
Quartz Syenite	2	7	7	2
Granite Gneiss	3	10	10	3
Shale, Limestone & Siltstone	4	12	12	4
CG Porphyritic Biotite & biotite hornblende granite	5	14	14	5
Amph. Schist & Amphibolite	6	20	20	6
Flaggy quartzite & quartzite schist	7	16	16	7
Banded Gneiss	8	8	8	9
Migmatite	9	13	13	13
Pegmatite	10	5	6	14
Phorphyroblastic Gneiss	11	18	18	15
Muscovite and tourmaline granite gneiss	12	1	1	12
Fine-grained Biotite Granite	13	17	17	16
Talc Schist	14	19	19	18
Undifferentiated Schist	15	11	11	17
Sandstone and Limestone	16	9	9	20
Sand and Clay	17	6	4	10
M-CG Biotite & Biotite hornblend granite	18	15	15	19
Sand, Clay and Shale	19	4	5	8
Sand and Mash	20	3	3	11

*C_{Rn}: Soil gas radon concentration; *Ks: Saturated hydraulic conductivity; *Ka: Soil air permeability; *GRP: Geogenic radon potential
(Notation: 1 = highest contributor; 20 = Lowest contributor).

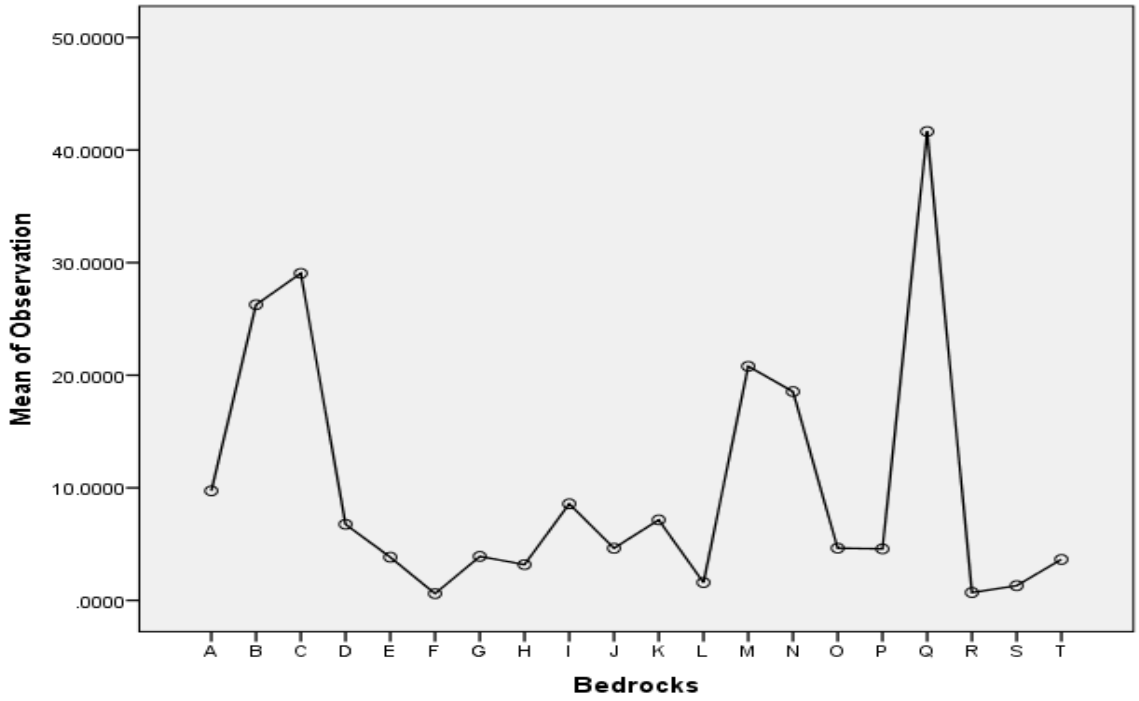

Figure 4.12 Means Plot for the Soil-gas Radon Concentration (Bqm^{-3}) across the Bedrocks

(Note: A- Migmatite; B – Granite Gneiss; C – Quartz Syenite; D – Banded Gneiss; E – Undifferentiated Schist; F - Amphibole Schist and Amphibolite; G - Fine-grained Biotite granite, H - M-CG Biotite and biotite hornblende granite; I - Sandstone and Limestone; J – Pegmatite; K - Flaggy quartzite and quartzite schist; L - Talc Schist; M - Shale, Limestone and Siltstone; N - CG Porphyritic biotite and biotite hornblende granite; O - Sand and Clay; P - Phorphyroblastic Gneiss, Q - Charnokite and Charnokitic rock; R - Muscovite tourmaline granite gneiss; S - Sand and Mash; T - Sand, Clay and Shale).

4.7 Artificial Neural Network Modelling for Soil-gas Radon Concentration and GRP

Several studies have tried to establish a model between indoor radon and soil radon concentration, soil moisture, soil pressure gradient, porosity, relative humidity, atmospheric temperature e.t.c (Kulali *et al.*, 2017; Mancini *et al.*, 2018, Park *et al.*, 2018; Dvorzhak *et al.*, 2021).

In Nigeria, empirical modelling, computational modelling, not to mention artificial neural network modelling of geogenic radon potential, is either non-existent or has not been reported. In generating the ANN model, several configurations were developed and tested using the NNtool app in the Mathlab software.

Among the configurations trained, the 2 x 8 x 1 configuration performed best, based on comparison using statistical indicators such as average absolute relative error, mean square error, sum squared error and correlation coefficient, as shown in table 4.14. The 2 x 8 x 1 configuration produced the highest correlation coefficient, Nash-Sutcliffe model efficiency coefficient and the lowest values of the sum square error, mean square error and average absolute relative error.

4.7.1 Model Generation

Following the training of the 2 x 8 x 1 configuration, the result of the Training, Validation, Test and Overall performance is as shown in figure 4.13. The extracted weights connecting the two input neurons to the 8 neurons in the hidden layer and the bias for each neuron in the hidden layer are shown in table 4.15. For the output layer, the output neuron has a bias value of -0.52312 while connected to each of the 8 hidden layer neurons with weights shown in table 4.16.

The weights and biases generated in table 4.15 operated on the normalised inputs using equation 3.4 which translated to the normalised weighted function, $E_{1,i,j}$. Following the network architecture shown in Fig. 3.4, the Tansigmoid transfer function operated on $E_{I,i,j}$ and yielded $F_{I,i,j}$ as given by equation 3.5. The values obtained for $E_{1,i,j}$ and $F_{1,i,j}$ are shown in Appendix 1 (Table 1A4).

Table 4.14 Comparison of ANN Configurations

ANN Configurations	Correlation coefficient (R)	SSE	MSE	AARE	Nash-Sutcliffe Coeff. (NS)
2 x (4) x 1	0.72	5814	38	121	0.52
2 x (5) x 1	0.75	5262	35	138	0.57
2 x (6) x 1	0.76	5262	35	123	0.57
2 x (7) x 1	0.80	4300	28	114	0.65
2 x (8) x 1	0.86	3209	21	89	0.74
2 x (10) x 1	0.85	3480	23	91	0.71

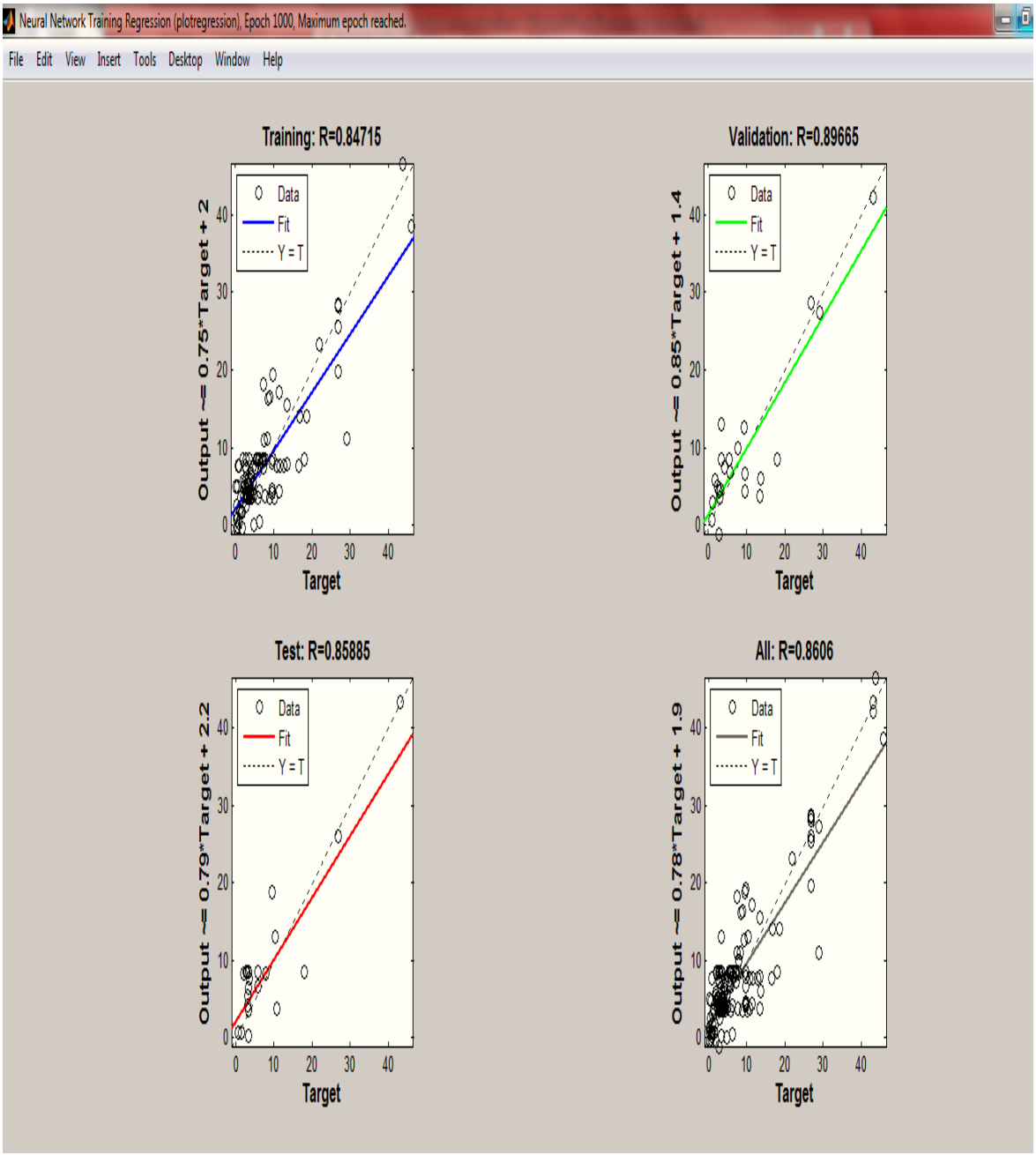

Figure 4.13 Performance of the Training of 2 x 8 x 1 Configuration

Table 4.15 Weights and Biases with Eight Neurons generated at the Hidden Layer

Neurons (i…..j)	Biases, $b_{1,i}$	Weights, $W_{1,i,T}$	Weights, $W_{1,i,P}$
8	3.8306	-22.0874	10.1823
7	0.34117	-4.976	7.014
6	-0.77431	-8.5841	9.2312
5	18.5023	22.1544	29.6913
4	-20.1699	-24.6544	-32.5429
3	64.0703	-2.4232	64.0942
2	-5.3196	0.93981	8.168
1	39.4541	-0.34144	50.798

Table 4.16 Weights and Bias Generated at the Output Layer

Neurons (i…..j)	Bias (b_0)	Weights, $W_{1,i,j}$
8	-0.52312	-0.1117
7	-0.52312	14.2253
6	-0.52312	-6.1301
5	-0.52312	29.6012
4	-0.52312	28.8243
3	-0.52312	0.96792
2	-0.52312	-11.5382
1	-0.52312	-0.82953

Weights connecting each neuron of the hidden layer to the neuron of the output layer auto-generated by the NNtool App as well as the bias of the neuron in the output layer (table 4.16) transformed $F_{I,i,j}$ to $O_{I,i,j}$. The Purelin function, as shown in ANN configuration in figure 3.4 transformed $O_{I,i,j}$ to a_{nO} which is the normalised final output. Having obtained a_{n0} we then denormalise using equation 2.16 but in this case X_{in} becomes

$$X_{in} = \frac{(Y - Y_{min}) * (X_{max} - X_{min})}{(Y_{max} - Y_{min})} + X_{min} \quad (4.1)$$

$$X_{in} = \frac{(Y + 1) * (X_{max} - X_{min})}{2} + X_{min}$$

Inserting the maximum value of the denormalised predicted output a (i.e X_{max}) and the denormalised predicted minimum value (X_{min}) results in:

$$X = X_{in} = 25.15Y + 22.43$$

That is

$$X = a_0 = 25.15\left[\sum_{i=1}^{j}\left(W_{o,i} * F_{1,i,j}\right) + b_o\right] + 22.43 \quad (4.2)$$

The mathematical expression of a_0 (equation 4.2) is the ANN model for soil-gas radon concentration.

Inserting the weights $W_{o,i}$ corresponding to F1 through F8 translated to a simpler form of equation 4.2 as expressed in equation 4.3

$$a_o = 25.15[W_1F_1 + W_2F_2 + W_3F_3 + W_4F_4 + W_5F_5 + W_6F_6 + W_7F_7 + W_8F_8 + b_0] + 22.43 \quad (4.3)$$

When numerical values of the weights W1 to W8 are inserted, equation 4.3 simplifies to equation 4.4 which is the soil-gas radon concentration model:

$$Rn = a_o = -20.86F_1 - 290.19F_2 + 24.34F_3 + 724.93F_4 + 744.47F_5 - 154.17F_6 + 357.77F_7 - 2.81F_8 + 9.27 \quad (4.4)$$

For the GRP model, equation 4.2 becomes

$$GRP = {}^{a_0}/_{\mathrm{K_a}} = \frac{1}{\mathrm{K_a}}[25.15[\sum_{i=1}^{j}(W_{o,i} * F_{1,i,j}) + b_o] + 22.43] \quad (4.5)$$

and equation 4.4 becomes

$$\mathrm{GRP} = \mathrm{R_n/K_a} = (1/\mathrm{K_a})[- 20.86F_1 - 290.19F_2 + 24.34F_3 + 724.93F_4 + 744.47F_5 - 154.17F_6 + 357.77F_7 - 2.81F_8 + 9.27] \quad (4.6)$$

Equations 4.2 and 4.5 are the final ANN models that can now be used to determine the radon concentrations and GRP from the bedrock type and the soil-air permeability.

4.7.2 Model Performance Indices

The overall performance evaluation of the model based on the 150 dataset was done using the average validation error as discussed in section 2.16.8. The average validation error was computed using equation 2.24. Inserting the fixed parameters in equation 2.24 for the soil gas radon concentration, we have:

$$E_{avg} = \frac{1}{150}\sum_{i=1}^{N_v}\left|\frac{F_{ann}(x_i, w) - y_i}{47.59 - 0.276}\right| \quad (4.7)$$

Inserting the fixed parameters for the geogenic radon potential in equation 2.24 gave:

$$E_{avg} = \frac{1}{150}\sum_{i=1}^{N_v}\left|\frac{F_{ann}(x_i, w) - y_i}{39.19 - 0.15}\right| \quad (4.8)$$

Evaluation of equation 4.7 using input parameters of predicted soil-gas radon concentration ($F_{ann}(x_i\ ,\ w)$) and the measured soil-gas radon concentration (y_i) yielded 0.07 as average validation error.

The obtained mean absolute error (MAE) using equation 2.25, root mean square error (RMSE) using equation 2.27 and mean bias error (MBE) using equation 2.29 were MAE = 2.56 kBq m^{-3}, RMSE = 3.59 $kBqm^{-3}$ and MBE = 0.26, respectively. The Goodness-of-prediction (equation 2.28) in section 2.16.8 was used to determine the effectiveness of the model generated and its evaluation gave a value of 76.83%.

Evaluation of equation 4.8 using input parameters of predicted geogenic radon potential ($F_{ann}(x_i\ ,\ w)$) and the measured geogenic radon potential (y_i) yielded 0.073 as average validation error.

The obtained mean absolute error (MAE), root mean square error (RMSE) and mean bias error (MBE) were MAE = 3.33 kBq m^{-3}, RMSE = 4.62 kBqm^{-3} and MBE = 0.42, respectively for the geogenic radon potential. The Goodness-of-prediction evaluation gave a value of 73.53%. Comparison between field obtained geogenic radon potential and the predicted geogenic radon potential showing how the model performs, is presented in figure 4.14. The correlation between the field obtained and predicted geogenic radon potential is also presented in figure 4.15 showing a high correlation. The mathlab code for determining the statistical measures of performance of the model is shown in Appendix 3 (Code 3A2).

4.7.3 Prediction Accuracy of Model

The models generated (equation 4.2 and 4.5) were used to predict the radon concentration and geogenic radon potential for twenty other sites of known bedrock types, where C_{Rn} and Ka were measured. These twenty values were used to validate the model's effectiveness in predicting soil-gas radon concentration and geogenic radon potential.

For the twenty sites, the input of soil-air permeability and bedrock type (after normalisation) were used to generate $E_{1,i,j}$ and $F_{1,i,j}$ using the previously obtained weights and biases. The Purelin function having acted on the $O_{1,i,n}$ generated from $F_{1,i,j}$ led to the output a_{n0} which was denormalised to generate the predicted value of soil-gas radon concentration and geogenic radon potential. The evaluation of goodness-of-prediction (G) gave a value of 86.49%, while the average validation error (AVE) gave a value of 0.17. The MAPE, MBE, MAE and RMSE gave values of 0.35%, 0.61, 1.19 and 1.65, respectively for the GRP. The results of the measured and predicted soil-gas radon concentration as well as for the obtained and predicted GRP for the twenty sites are presented in Appendix 4 (Table 4A1) and Appendix 4 (Table 4A2) respectively.

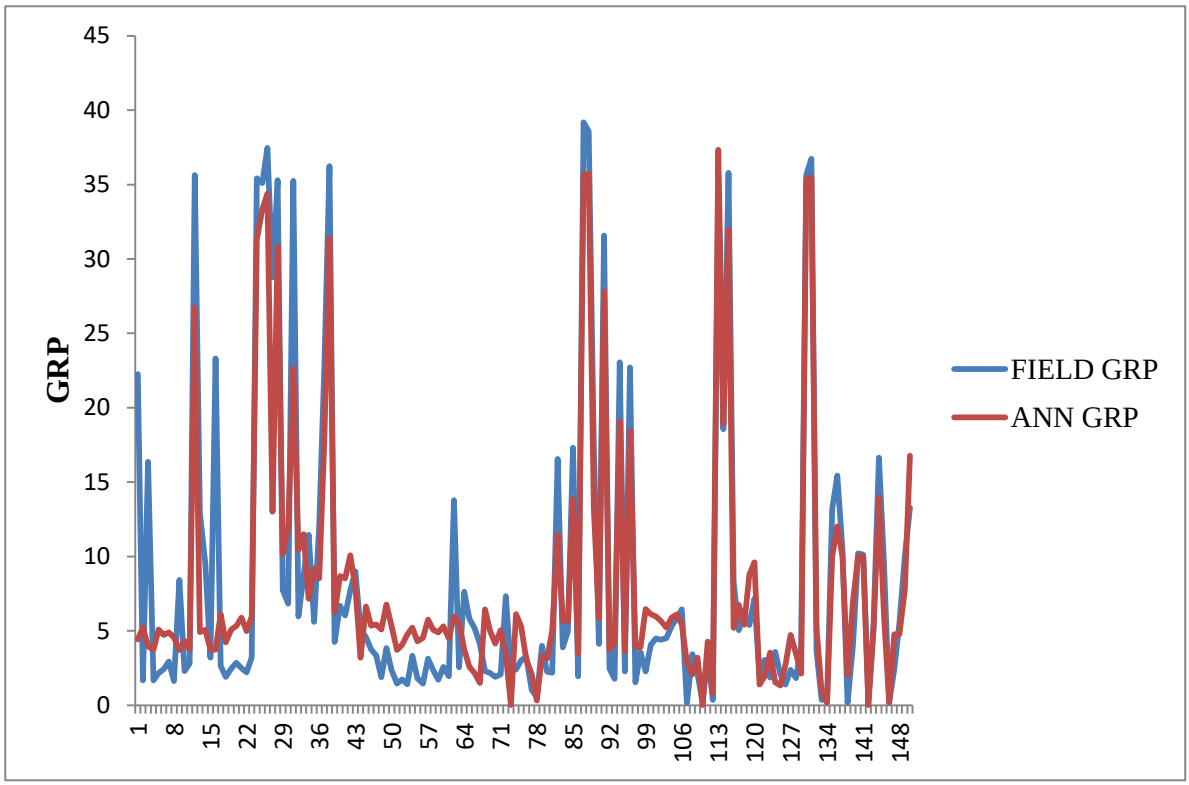

Figure 4.14 Comparison between Field and Predicted Geogenic Radon Potential

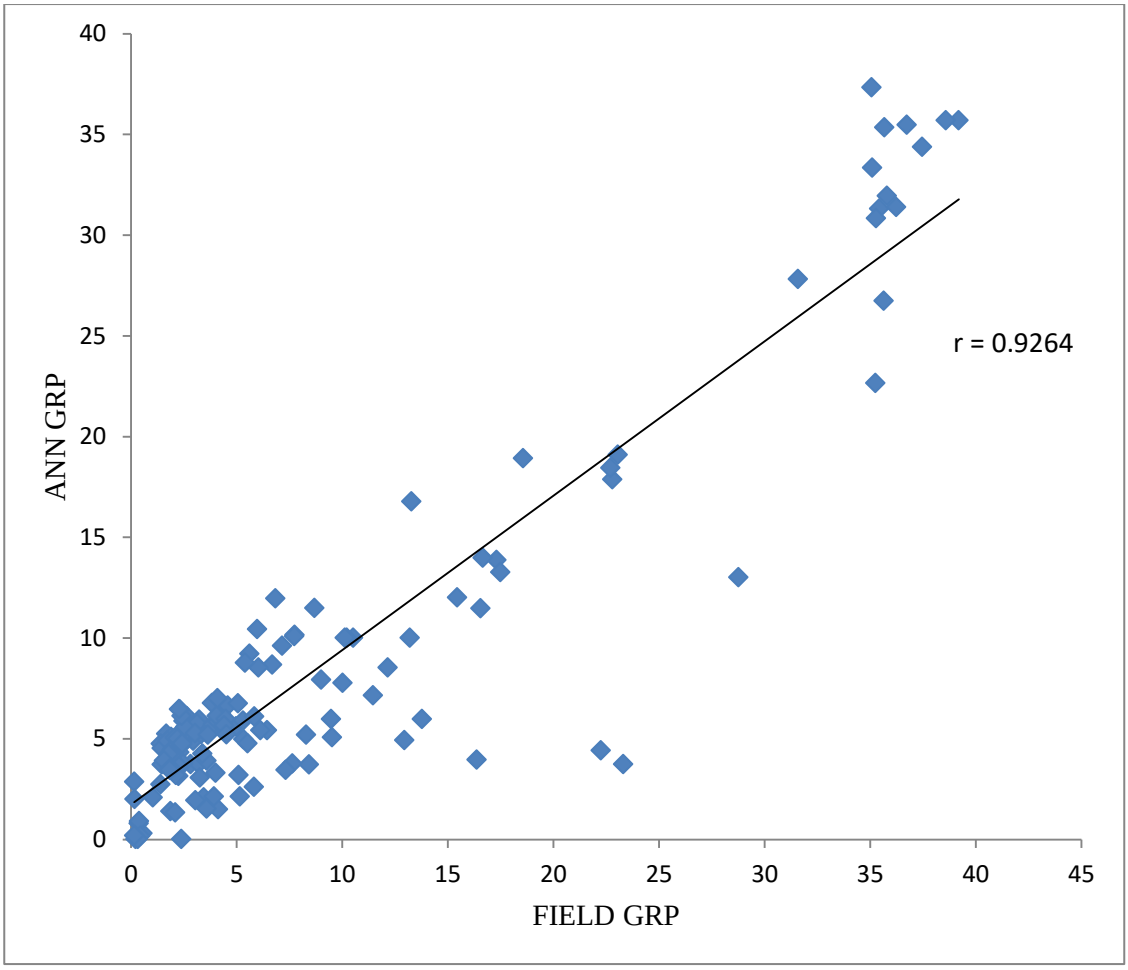

Figure 4.15 Correlation between Field GRP and ANN-predicted GRP

In predicting the radon concentration for yet to be measured locations in Southwest Nigeria, seventy-five (75) other coordinates with different bedrocks but of the same types used in generating the ANN-based model were also picked using the NGSA geological map. Mean values of soil-air permeability of the same bedrocks previously used in generating the model were used as input in the model to obtain radon concentration values. The mean absolute error (MAE) obtained was 1.87 $kBqm^{-3}$, with the root mean square error (RMSE) of 5.61 $kBqm^{-3}$ and average validation error (AVE) obtained was 0.04, respectively. A value of 1.21 was obtained for the mean bias error (MBE) and mean absolute percentage error (MAPE) gave a value of 0.27%.

4.8 Generation of Radon Concentration and GRP Maps

Mapping of the spread or distribution of radon concentration and geogenic radon potential across the 150 locations within Southwest Nigeria using ArcGIS 10.5 was generated and overlaid on the geological map. The derived maps enabled the visual representation of the spread of soil-gas radon concentration and geogenic radon potential based on the Neznal classification. The spread of soil-gas radon concentration and geogenic radon potential generated from the measured data and superimposed on the geological map for Southwest Nigeria are shown in figure 4.16 and figure 4.17, respectively. The spread of the radon concentration in soil and geogenic radon potential in relation to locations in Southwest Nigeria are as expressed in figure 4.18 and figure 4.19, respectively. Maps generated for the 150 measured and 20 validation points (section 4.7.4) for radon concentration in soil and geogenic radon potential are shown in figure 4.20 and figure 4.21, respectively. Furthermore, the predicted 75 radon concentration values and derived geogenic radon potential were added to the previously measured 150 radon concentration and geogenic radon potential values to generate another set of maps as shown in figures 4.21 and 4.22, respectively.

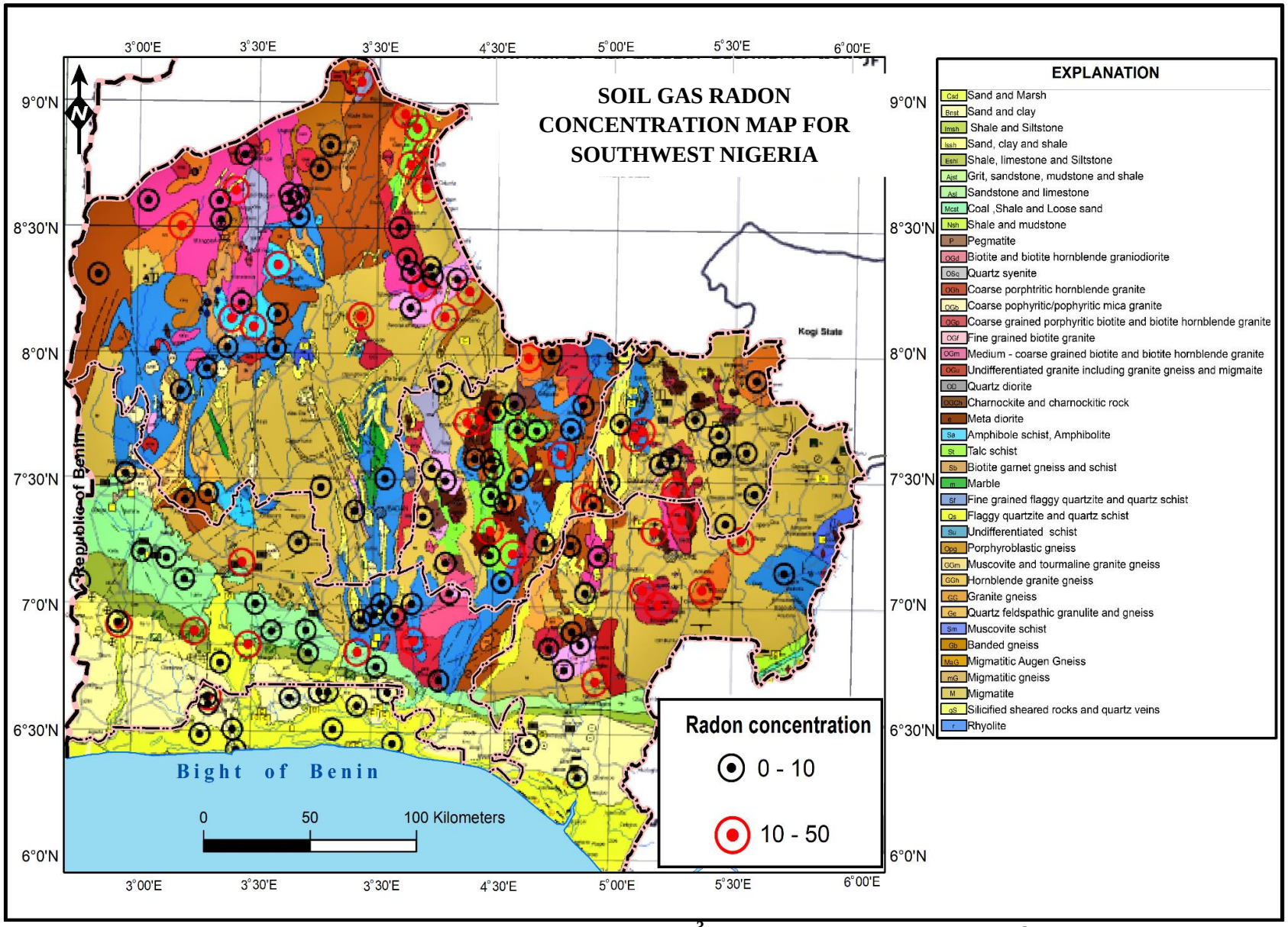

Figure 4.16 Generated Soil-gas Radon Concentration (in kBqm^{-3}) Map in relation to Bedrocks for Southwest Nigeria

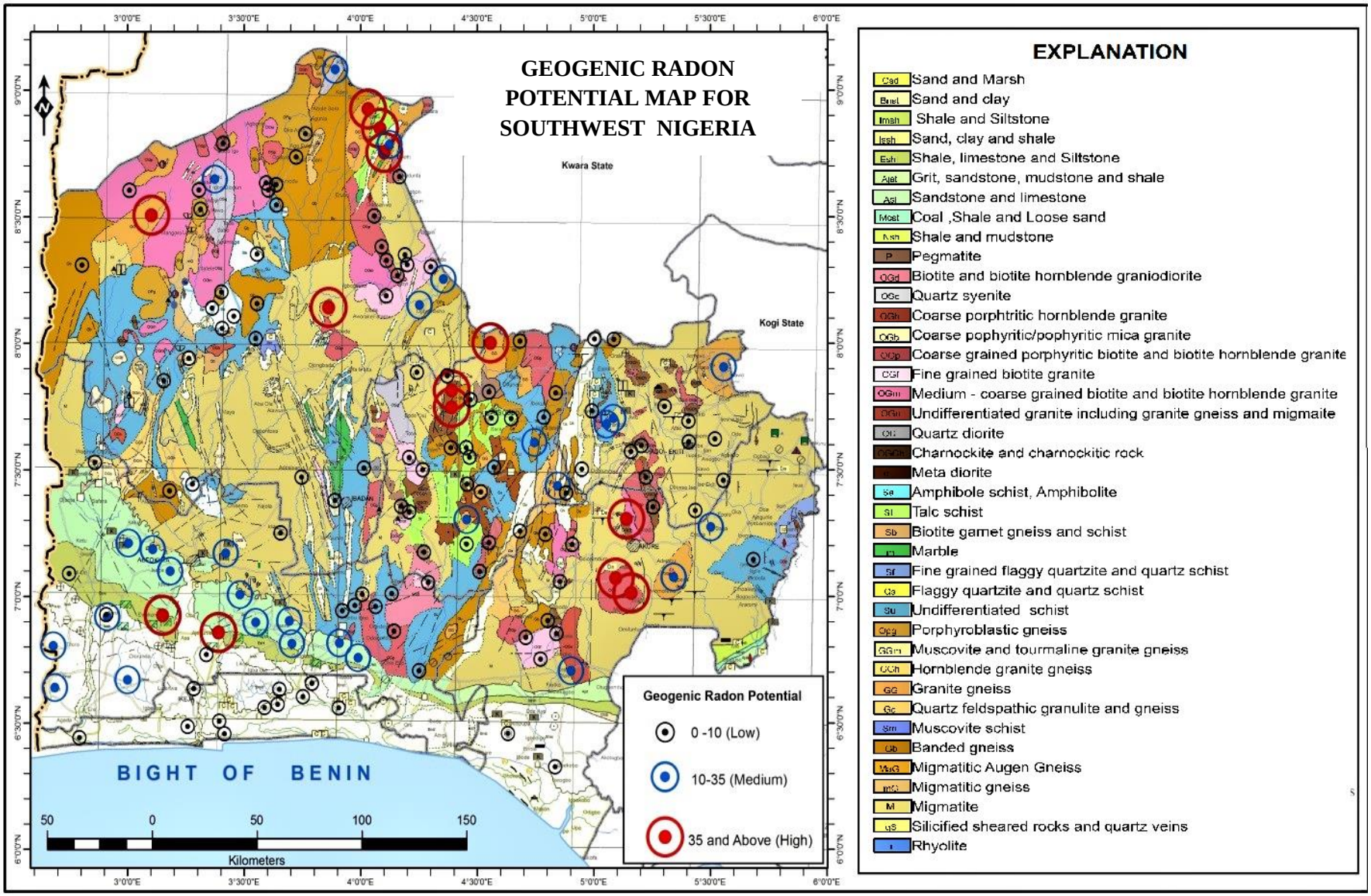

Figure 4.17 Generated Geogenic Radon Potential Map in relation to Bedrocks for Southwest Nigeria

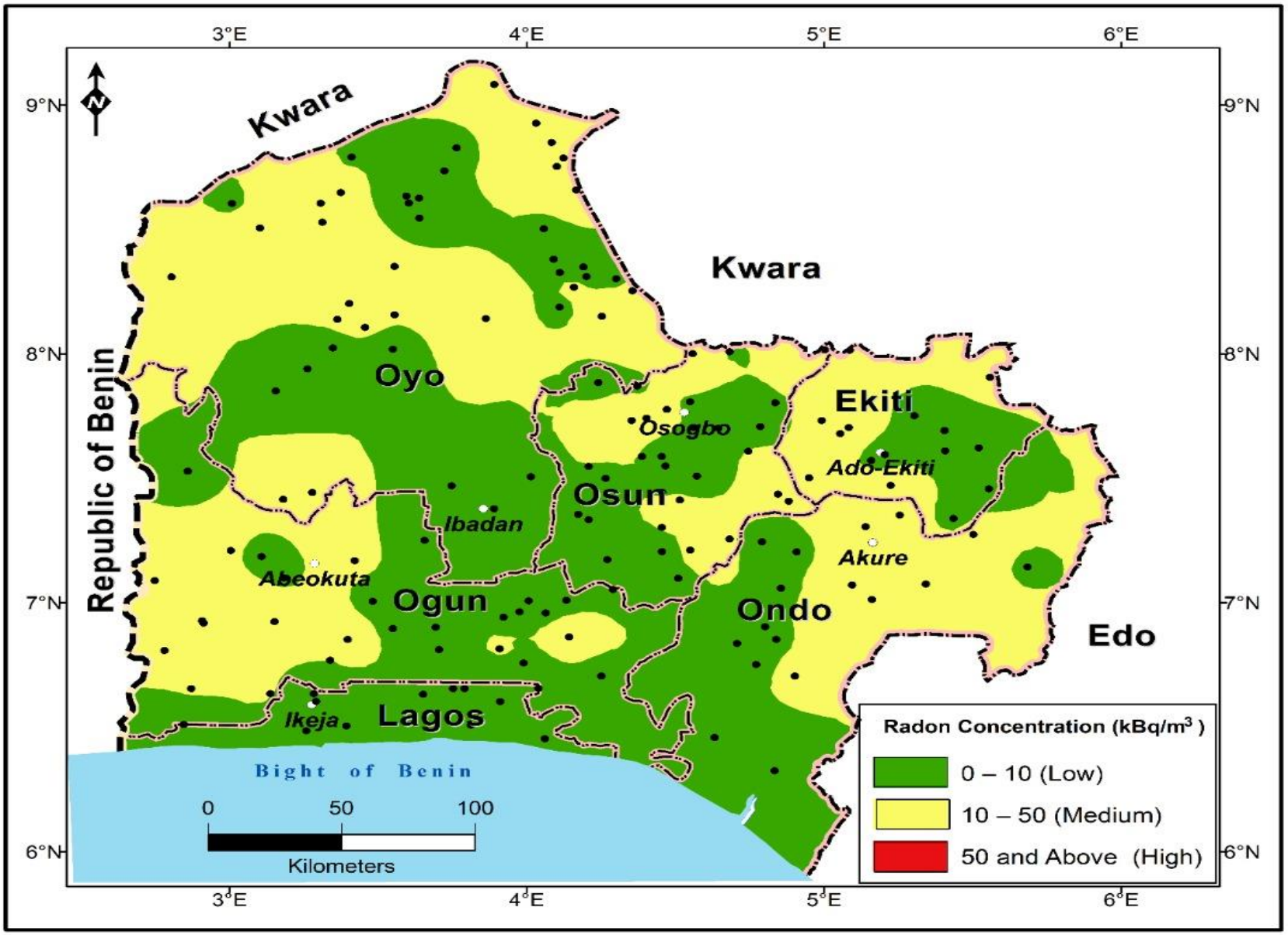

Figure 4.18 Soil-gas Radon Concentration variation across the States in Southwest Nigeria

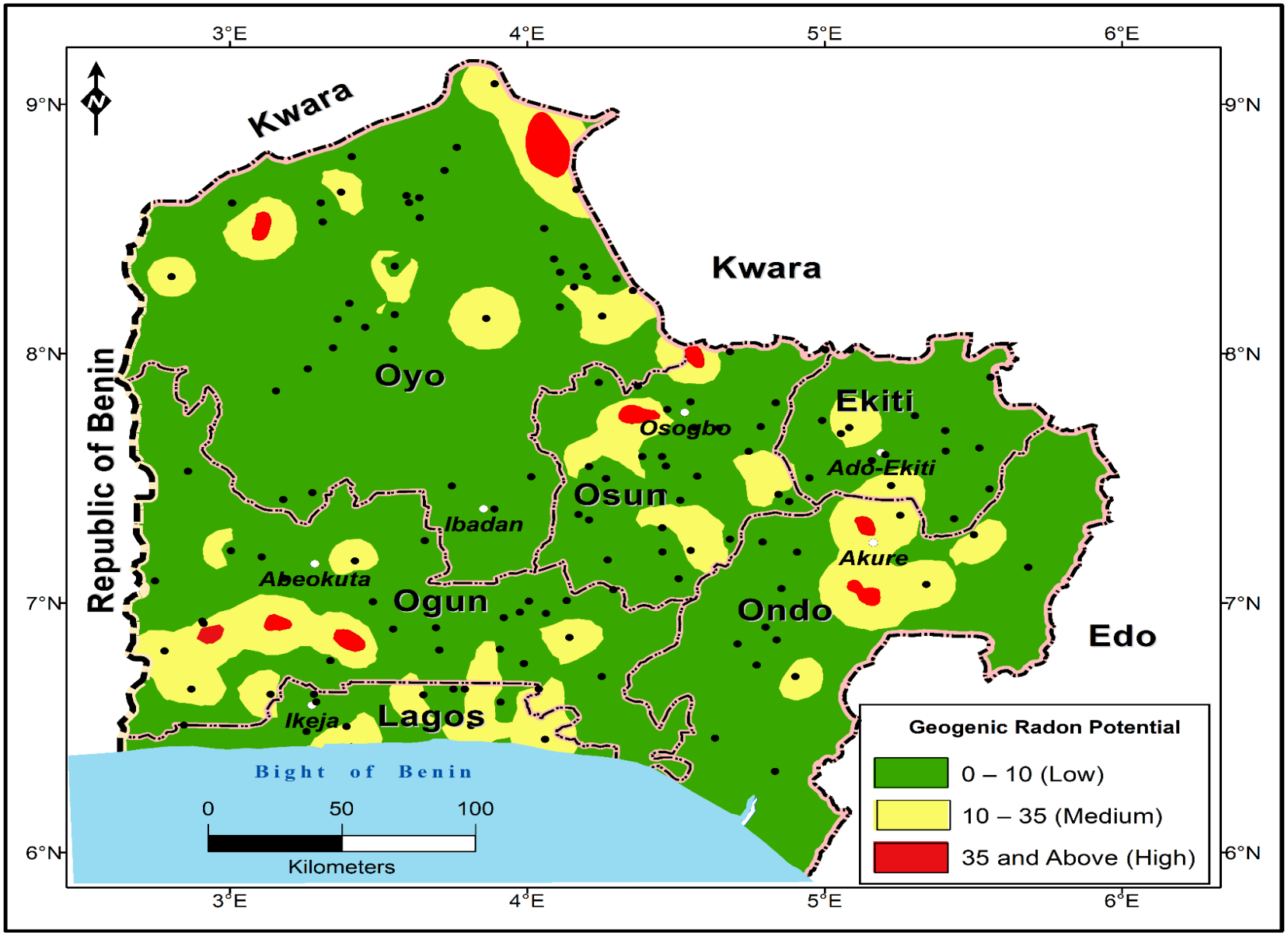

Figure 4.19 **Geogenic radon potential variation across Southwest States in Nigeria**

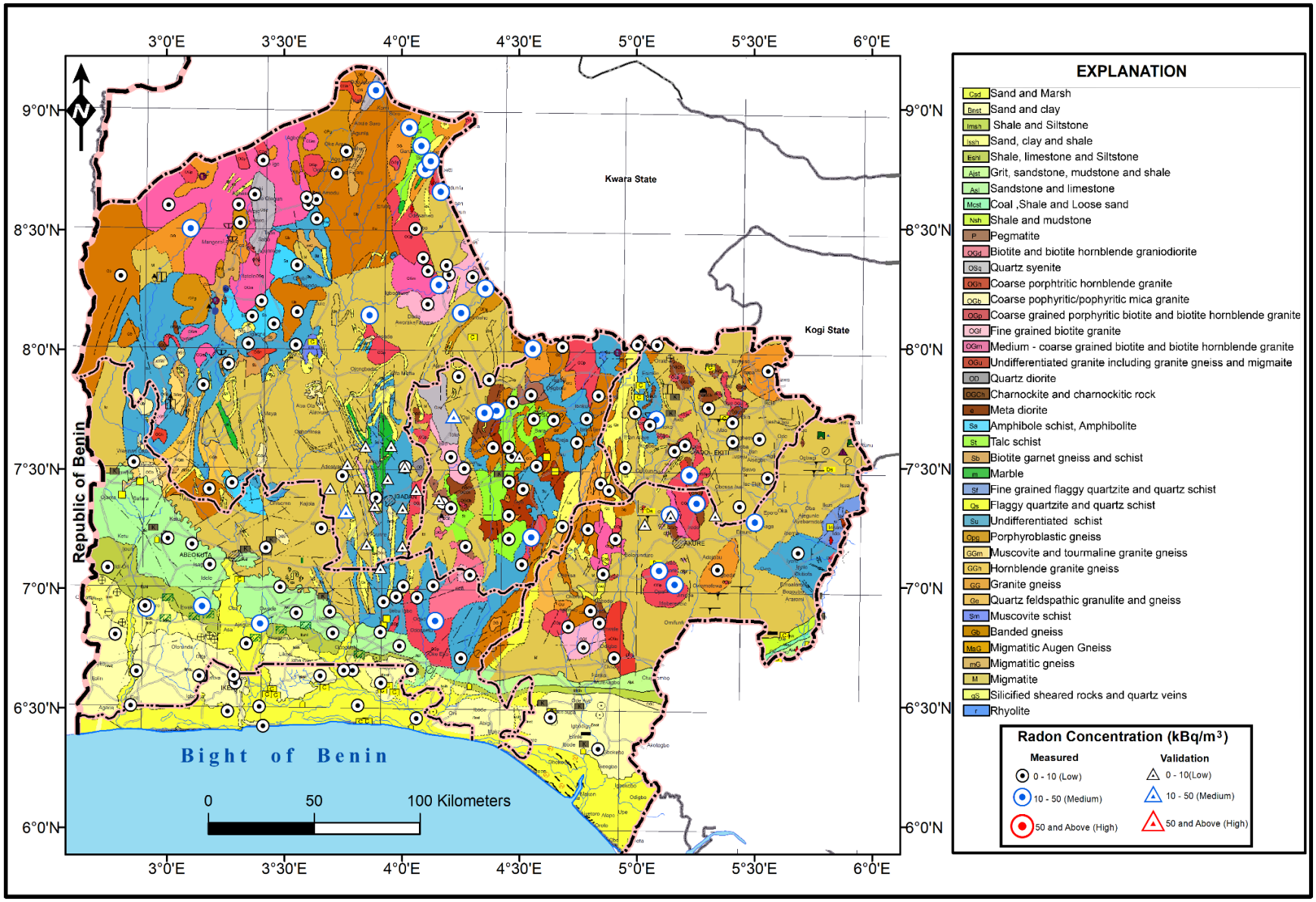

Figure 4.20 Spatial Distribution of Measured and Validation Points for Soil-gas Radon Concentration

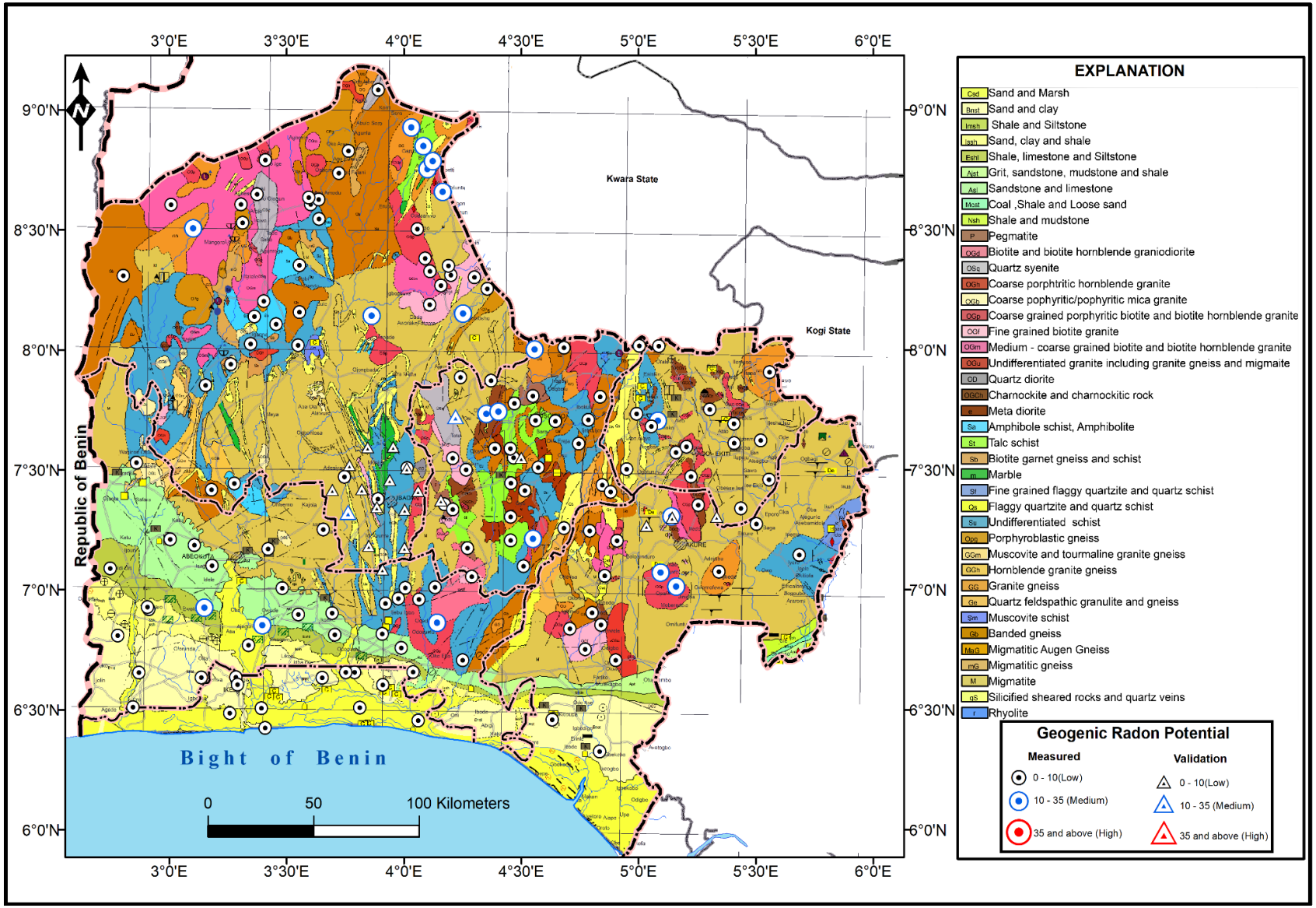

Figure 4.21 Spatial Distribution of Measured and Validation Points for Geogenic Radon Potential

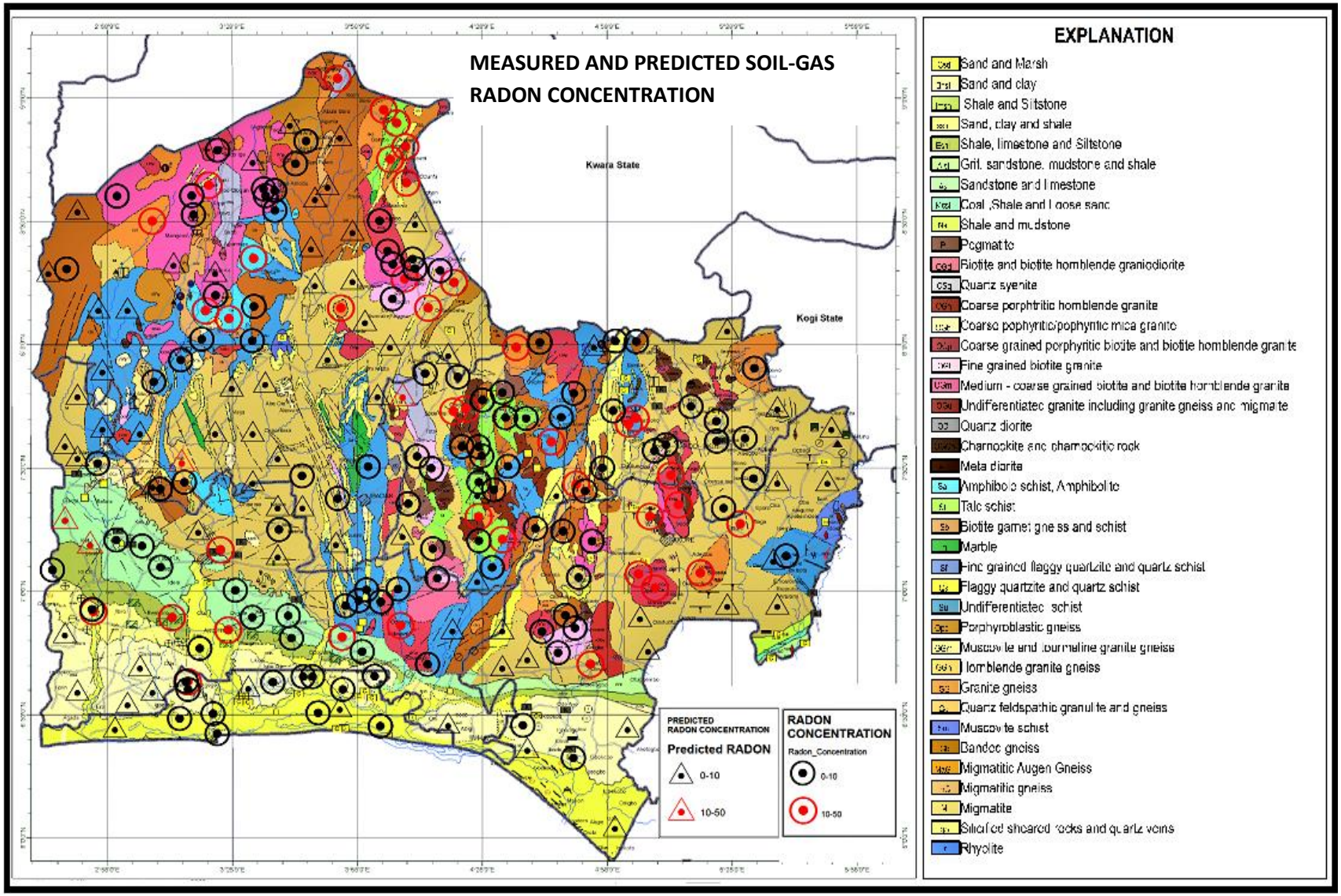

Figure 4.22 Combined Map for Measured and Predicted Soil-gas Radon Concentration in relation to Bedrocks for Southwest Nigeria

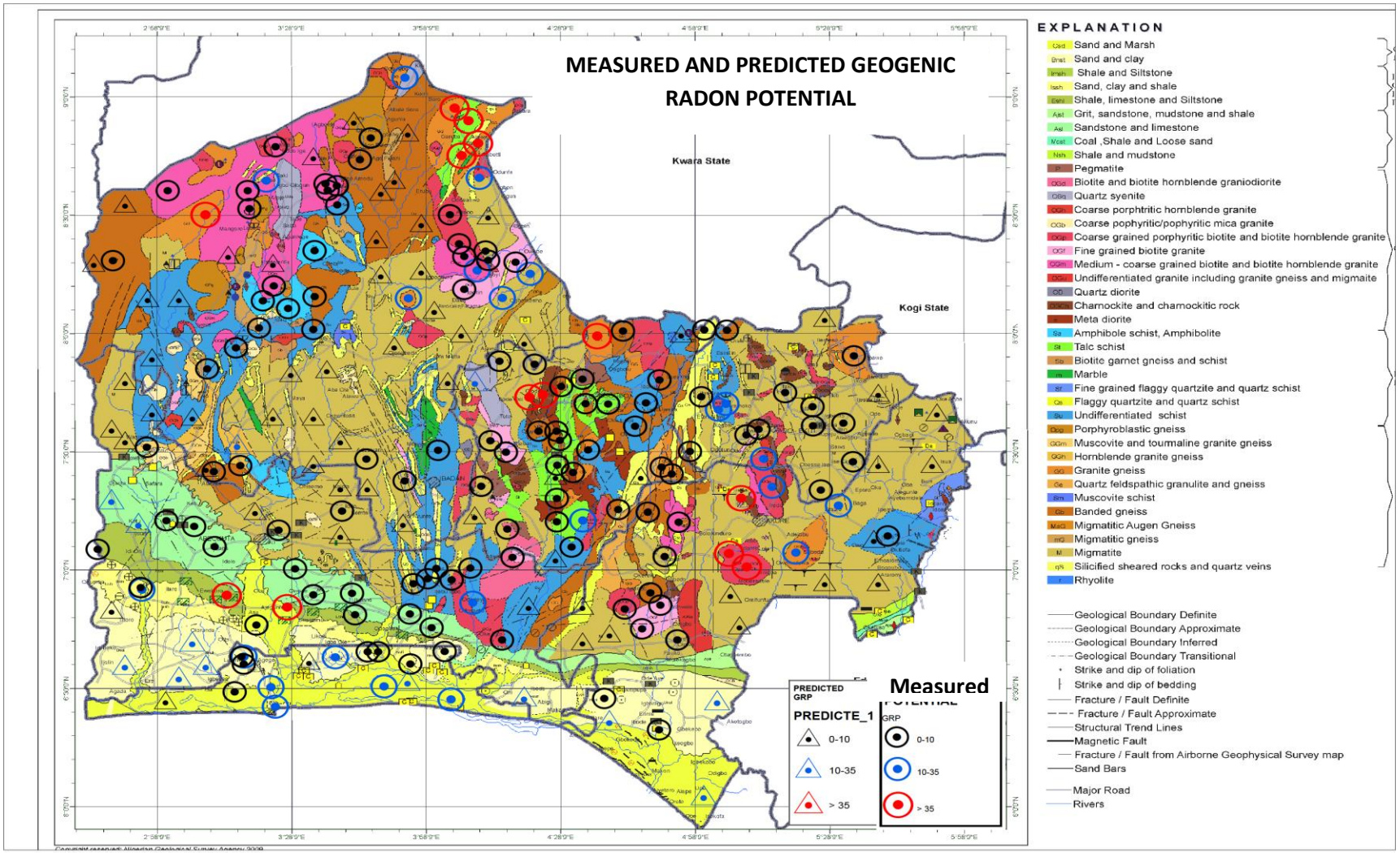

Figure 4.23 Combined Map for Measured and Predicted Geogenic Radon Potential in relation to Bedrocks for Southwest Nigeria

CHAPTER FIVE

SUMMARY, CONCLUSION AND RECOMMENDATIONS

5.1 Summary

The soil-gas radon concentration was measured using RAD7 radon detector and soil-air permeability was obtained from measured soil-saturated hydraulic conductivity at 150 locations covering 20 bedrock types in Southwest Nigeria. The geogenic radon potentials of the locations were also determined. Adopting international classification criteria, the locations radon concentrations and geogenic radon potentials were classified accordingly. The classification revealed the bedrocks with the highest, medium and lowest radon concentration and geogenic radon potential values. A neural network training of the measured data translated to the mathematical expression for the model, which could be utilised to make predictions of the soil-gas radon concentration and, consequently the geogenic radon potential for the southwestern region of Nigeria.

From the results obtained in this work, it was observed that:

1. The soil-gas radon concentration had a range between 0.28 to 47.59 $kBqm^{-3}$ with a mean value of 10.39 ± 12.59 $kBqm^{-3}$. The maximum value was found on CG Porphyritic biotite and biotite hornblende granite bedrock while the lowest was found over Talc schist bedrock. The highest mean radon concentration value was obtained over granitic type bedrock (Charnokite and charnokitic bedrock) with a value of 44.15 $kBqm^{-3}$; the lowest mean radon concentration of 0.69 $kBqm^{-3}$ was from sediments (Sand and mash).
2. Granitic bedrocks were found to have highest mean soil-gas radon concentration (14.02 $kBqm^{-3}$) when compared with metamorphic (10.07 $kBqm^{-3}$), sedimentary (9.87 $kBqm^{-3}$) and sediments (3.23 $kBqm^{-3}$) found in Southwestern Nigeria.
3. The mean soil-gas radon concentration value for bedrocks that fall on the Basement complex was 11.39 $kBqm^{-3}$, while that of sedimentary terrain was 7.06 $kBqm^{-3}$

showing that the basement complex has a preponderance of higher soil gas radon than sedimentary terrain.

4. Soil-air permeability of all the bedrocks considered ranged between 5.90 x 10^{-13} m^2 and 8.70 x 10^{-11} m^2 with a mean of 8.87 x 10^{-12} m^2. Sedimentary formation possessed the highest average soil-air permeability, followed by granitic and metamorphic bedrocks, respectively.
5. The highest GRP was found on CG Porphyritic biotite and biotite hornblende granite (39.19) while the lowest was found on Talc schist (0.15) and the average GRP obtained was 8.46. Charnokite and charnokitic bedrock had the highest mean GRP (36.19) while M-CG biotite and biotite hornblende granite had the lowest mean GRP with 2.22.
6. Based on the Neznal classification, thirteen (13) sites (8.67%) had GRP values above 35 classified as 'High' risk. Bedrocks such as Quartz syenite, Granite gneiss, Shale, Limestone and siltstone as well as CG Porphyritic biotite and biotite hornblende granite fall under 'Medium' risk with 10 < GRP < 35. Granitic bedrocks were observed to have the highest mean GRP with a value of 13.71.
7. Application of inferential statistics (Kruskal-Wallis test), shows that geology influences values of soil-gas radon concentration and geogenic radon potential.
8. A generalised artificial neural network model for geogenic radon potential prediction in southwestern Nigeria was generated and presented as:

$$GRP = \frac{1}{K_a}[25.15[\sum_{i=1}^{j}(W_{o,i} * F_{1,i,j}) + b_o] + 22.43]$$

with '$W_{o,i}$' referring to the weights at the output layer assigned to each neuron (i), '$F_{1.i,n}$' being the value of the Tansigmoid-transformed variable associated with the sum of the nth normalised input variable at the hidden layer; 'b_0' is the bias at the output layer while output is denormalised to obtain the predicted geogenic radon potential in the soil.

9. Soil-gas radon concentration and geogenic radon potential maps were generated for the measured locations. The maps developed also included the predicted soil-gas radon concentrations and geogenic radon potential.

5.2 Conclusions

From the measurement of soil-gas radon concentration, soil-air permeability and geogenic radon potential over twenty bedrocks in Southwest Nigeria, it can be concluded that:

1. Bedrocks determine the variation in soil-gas radon concentration, soil-air permeability and geogenic radon potential.
2. Granitic bedrocks have a preponderance for higher soil-gas radon concentration and geogenic radon potential than other bedrocks.
3. Sedimentary formations present higher soil-air permeability than other bedrocks.
4. Sites with GRP above 35 in Southwest Nigeria are scanty and dispersed as found in Abeokuta – Sagamu – Ewekoro axis in Ogun state, Idanre – Akure axis in Ondo state, Igbeti – Oke-ogun axis in Oyo state and Ede axis in Osun state.
5. Artificial neural network modelling could be applied to estimate soil-gas radon concentration and geogenic radon potential with good prediction capability over different bedrock formations

5.3 Recommendations

From this study, it was discovered that there are radon prone areas that need further study with regads to relating the soil-gas radon concentration with indoor radon. This would help to correlate soil-gas radon to indoor radon in such radon-prone areas.

It is highly recommended that soil-gas radon measurement be included in any environmental impact assessment exercise to be carried out at any site. This would help to identify the radon risk expected from such location and also determine radon-protective measures to be included in the building design before approval is granted.

For further studies on this work, it is therefore recommended that the following should be considered:

1. Adoption of this type of study by the federal government to cover the entire country, which would lead to the generation of a national soil-gas radon map. The generation of such dataset and maps will enable the formulation of action levels and policies towards reducing the effect of radon gas on its citizens.

2. Acquisition of recent radon measuring devices and equipment by research centres dealing with radiological studies.

3. The work should be expanded to include indoor, outdoor and groundwater radon studies in relation to bedrocks at the regional and national level. This will help to develop empirical data for generation of models relating the factors influencing radon concentration.

4. The work should cover year-long variability studies of soil-gas radon concentration in relation to different bedrocks in the country.

5. Data on predictor variables such as density, porosity, hydraulic conductivity, void ratio e.t.c. for soil and bedrocks in Southwest Nigeria can also be generated and embedded in the ANN model to improve the model.

6. Data on meteorological parameters such as atmospheric temperature, pressure and humidity over the Southwest region of Nigeria can be obtained for the same period for the soil-gas radon and soil-air permeability measurements and embedded in the generated models.

5.4 Contributions to Knowledge

This study has been able to, for the first time, determine the radon concentration and geogenic radon potential over different bedrocks for Southwest Nigeria. It has also produced the first soil-gas radon concentration and geogenic radon potential maps in Nigeria, specifically for Southwest Nigeria.

Knowledge of the bedrocks with affinity for higher radon concentration was not available previously in Southwest Nigeria but this study has been able to locate such bedrocks as well as identified radon prone areas in Southwest Nigeria.

Due to difficult terrain and inaccessibility for comprehensive in-situ soil-gas radon concentration measurements, a predictive model was developed using artificial neural network to estimate soil-gas radon concentration and geogenic radon potential over twenty bedrocks for Southwest Nigeria. The model could predict measured soil-gas radon concentration and geogenic radon potential to acceptable accuracy.

REFERENCES

Abidoye, L. K., Mahdi, F. M., Idris, M. O., Alabi, O. O. and Wahab, A. A. 2018. ANN derived equation and its application in the prediction of dielectric properties of pure and impure CO_2. *Journal of Cleaner Production* 175: 123-132.

Ajiboye, Y., Isinkaye, M. O. and Khanderkar, M. U. 2018. Spatial distribution mapping and radiological hazard assessment of groundwater and soil gas radon in Ekiti State, Southwest Nigeria. *Environmental earth sciences* 77.14: 1 - 15.

Ajrouche, R., Ielsch, G., Cléro, E., Roudier, C., Gay, D., Guillevic, J., and Le Tertre, A. 2017. Quantitative health risk assessment of indoor radon: A systematic review. *Radiation Protection Dosimetry* 177.1-2: 69-77.

Al-bakhat, Y. M., Al-Ani, N. H., Muhammad Al-Ezawi, B. F., Ameen, N. H., Zahar Jabr, Z. A. and Hammid, S. H. 2017. Measurement of radon activity in soil gas and the geogenic radon potential mapping using RAD7 at al tuwaitha nuclear site and the surrounding areas. *Radiation Science and Technology* 3: 29-34.

Alrabaiah, H. 2015. Modeling Radon Diffusion across Some Areas of Southern Jordan. *Applied Mathematics* 6.08: 1271.

Al-Khateeb, H. M., Aljarrah, K. M., Alzoubi, F. Y., Alqadi, M. K., and Ahmad, A. A. 2017. The correlation between indoor and in soil radon concentrations in a desert climate. *Radiation Physics and Chemistry* 130: 142-147.

Aghdam, M. M., Dentoni, V., Da Pelo, S. and Crowley, Q. 2022. Detailed geogenic radon potential mapping using geospatial analysis of multiple geo-variables—a case study from a high-risk area in SE Ireland. *International Journal of Environmental Research and Public Health* 19.23: 15910.

Akamba Mbembe, B., Manga, A., Mbida Mbembe, S., Ele Abiama, P., Saidou, Ondo Meye, P. and Ben–Bolie, G. H. 2022. Indoor Radon (222Rn) Measurements and Estimation of Annual Effective Dose in Mvangan Locality, South Cameroon. *Radiation Protection Dosimetry* 198.20: 1565-1574.

Akerblom, G. 1987. Investigations and mapping of radon risk areas. *Geography and . Environmental Planning*. 2: 96-106.

Akerblom, G. 1995. The use of airborne radiometric and exploration survey data and techniques in radon risk mapping in Sweden. *Application of uranium exploration data and techniques in environmental studies* IAEA-TECDOC-827, IAEA, Vienna. 159-180.

Appleton, J.D. (2013). Radon in Air and Water. In: Selinus, O. (eds) Essentials of Medical Geology. Springer, Dordrecht. https://doi.org/10.1007/978-94-007-4375-5_11, ISBN 978-94-007-4375-5. pages 239–277.

Arvela, H., Holmgren, O. and Hänninen, P. 2016. Effect of soil moisture on seasonal variation in indoor radon concentration: modelling and measurements in 326 Finnish houses. *Radiation protection dosimetry* 168.2: 277-290.

Atik, S., Yetis, H., Denizli, H. and Evrendilek, F. 2013. How do different locations, floors and aspects influence indoor radon concentrations? An empirical study using neural networks for a university campus in northwestern Turkey. *Indoor and Built Environment* 22.4: 650-658.

Banríon, M. H., Elío, J., and Crowley, Q. G. 2022. Using geogenic radon potential to assess radon priority area designation, a case study around Castleisland, Co. Kerry, Ireland. *Journal of Environmental Radioactivity* 251: 106956.

Barnet, I., Pacherová, P. 2010. In: Barnet, I., Neznal, M., Pacherova, P. (Eds.) Proc. 10th international workshop on the geological aspects of radon risk mapping. Czech geological survey. Radon v.o.s, Prague ISBN 978-80-7075-754-3: 35-41.

Bochicchio, F., Ampollini, M., Antignani, S., Carpentieri, C., Caprio, M., Caccia, B. and Venoso, G. 2019. Protection from radon in Italy: past, present and perspectives. *Romanian Journal of Physics* 64: 817.

Borgoni, R., De Francesco, D., De Bartolo, D. and Tzavidis, N. 2014. Hierarchical modeling of indoor radon concentration: how much do geology and building factors matter?. *Journal of environmental radioactivity* 138: 227-237.

Bossew, P. 2015. Mapping the geogenic radon potential and estimation of radon prone areas in Germany. *Radiation Emergency Medicine* 4.2: 13-20.

Bossew, P., and Petermann, E. 2022. From data to decisions–Quality assurance in radon policy. *Journal of the European Radon Association* 1-6.

Brikowski, T., 2013. GEOS 4430 Lecture Notes: Darcy's Law (http://www.utdallas.edu/~brikowi/Teaching/Geohydrology/LectureNotes/Darcy_Law/Permeameters.html) accessed 13th November, 2023.

Cho, B. W., and Choo, C. O. 2019. Geochemical behavior of uranium and radon in groundwater of Jurassic granite area, Icheon, Middle Korea *Water* 11.6: 1278.

Cinelli, G., and Tondeur, F. 2015. Log-normality of indoor radon data in the Walloon region of Belgium. *Journal of Environmental Radioactivity* 143:100-109.

Samuel, D. T., Farai, I.P., Oni, O. M., Aremu A. and Fajemiroye, J.A. 2022. Correlation Between Soil-gas Radon and Soil-surface Radon Concentration and Estimation of Annual Effective Dose From Outdoor Concentration in Abeokuta, Southwestern Nigeria. DOI: https://doi.org/10.21203/rs.3.rs-1875391/v1.

Degu Belete, G., and Alemu Anteneh, Y. 2021. General overview of radon studies in health hazard perspectives. *Journal of Oncology*, 2021: 1-7, Article ID 6659795. https://doi.org/10.1155/2021/6659795.

Demoury, C., Ielsch, G., Hemon, D., Laurent, O., Laurier, D., Clavel, J. and Guillevic, J. 2013. A statistical evaluation of the influence of housing characteristics and geogenic radon potential on indoor radon concentrations in France. *Journal of environmental radioactivity* 126: 216-225.

Duong, V. H., Ly, H. B., Trinh, D. H., Nguyen, T. S., and Pham, B. T. 2021. Development of Artificial Neural Network for prediction of radon dispersion released from Sinquyen Mine, Vietnam. *Environmental Pollution* 282:116973.

Durridge Radon Instrumentation. 2012. RAD7 user manual, Durridge Company Inc. Billerica, USA.

Dvorzhak, A., Mora, J. C., Real, A., Sainz, C. and Fuente, I. 2021. General model for estimation of indoor radon concentration dynamics. *Environmental Science and Pollution Research* 28.38: 54085-54095.

Elzain, A. E. A. 2015. Radon exhalation rates from some building materials used in Sudan. *Indoor and Built Environment* 24.6: 852-860.

Esan, D. T., Sridhar, M. K. C., Obed, R., Ajiboye, Y., Afolabi, O., Olubodun, B., and Oni, O. M. 2020. Determination of Residential Soil Gas Radon Risk Indices Over the Lithological Units of a Southwestern Nigeria University. *Scientific Reports* 10.1: 1-10.

Ertel, W. 2017. *Introduction to artificial intelligence*. 2nd ed. Springer International Publishing AG.

Farai, I.P. and Sanni, A. O. 1991. ^{222}Rn in groundwater in Nigeria: A survey. *Health Physics* 62(1): 96 – 98.

Farai, I.P. and Sanni, A. O. 1992. Year-long variability of Rn-222 in a groundwater system in Nigeria. *Journal of African Earth Sciences* 15(3/4): 399 – 403.

Farid, S. M. 2016. Indoor radon in dwellings of Jeddah city, Saudi Arabia and its correlations with the radium and radon exhalation rates from soil. *Indoor and Built Environment* 25.1: 269-278.

Fourkal, E., Nahum, A., Ma, C., and Paskalev, K. 2017. Average energy required to produce an ion pair, revisited. *arXiv preprint arXiv:*1703.10032.

Ghosh, D., Deb, A. and Sengupta, R. 2009. Anomalous radon emission as precursor of earthquake. *Journal of Applied Geophysics* 69.2: 67-81.

Giustini, F., Ciotoli, G., Rinaldini, A., Ruggiero, L. and Voltaggio, M. 2019. Mapping the geogenic radon potential and radon risk by using Empirical Bayesian Kriging regression: A case study from a volcanic area of central Italy. *Science of the Total Environment* 661:449-464.

Guiseppe, V. E., Elliott, S. R., Hime, A., Rielage, K., and Westerdale, S. 2011. A radon progeny deposition model. In *AIP Conference Proceedings* American Institute of Physics 1338.1: 95-100.

Guiteras, F. L. 1997. Radon generation, entry and accumulation indoors. Ph.d thesis, Universitat Autònoma de Barcelona. iii+20pp.

Gupta, A., and Ramanathan, A. L. 2019. Grain texture as a proxy to understand porosity, permeability and density in Chandra Basin, India. *SN Applied Sciences*, 1: 1-9.

Hillel D. 2004. *Environmental Soil Physics*, San Diego, California, USA, Academic Press. 525 B Street, suite 1900, San Diego, Califonia, 92101-4495, USA.

IAEA (International Atomic Energy Agency), 2015. Protection of the Public against Exposure Indoors due to Radon and Other Natural Sources of Radiation, Specific Safety Guide No. SSG-32: 18.

ICRP (International Commission on Radiological Protection), 2012. Radiological Protection Against Radon Exposure. ICRP Publication. Ann. ICRP Ref. 4829-9671-6554.

Idriss, H., Salih, I., and Elzain, A. E. A. 2020. Environmental radon mapping in Sudan, orderly review. *Journal of Taibah University for Science* 14.1: 1059-1066.

Ielsch, G., Cushing, M. E., Combes, P. and Cuney, M. 2010. Mapping of the geogenic radon potential in France to improve radon risk management: methodology and first application to region Bourgogne. *Journal of environmental radioactivity* 101.10: 813-820.

Iversen, B. V., Moldrup, P., Schjønning, P. and Jacobsen, O. H. 2003. Field application of a portable air permeameter to characterize spatial variability in air and water permeability. *Vadose Zone Journal* 2.4: 618-626.

Iversen, B. V., Moldrup, P. and Loll, P. 2004. Runoff modeling at two field slopes: use of in situ measurements of air permeability to characterize spatial variability of saturated hydraulic conductivity. *Hydrological processes* 18.5: 1009-1026.

Janiesch, C., Zschech, P. and Heinrich, K. 2021. Machine learning and deep learning. *Electronic Markets* 31.3: 685-695.

Jelle, B. P. 2012. Development of a model for radon concentration in indoor air. *Science of the total environment* 416: 343-350.

Jibiri, N. N. and Famodimu, J. B. 2013. Natural background radiation dose rate levels and incidences of reproductive abnormalities in high radiation area in Abeokuta, Southwestern Nigeria. *Natural Science* 5.11: 1145.

Kirkham, M.B. 2005. *Principles of Soil and Plant Water Relations*, Burlington, MA. Elsevier Academic Press: 145-172.

Kojima, H. and Nagano, K. 1999. The influence of meteorological and soil parameters on radon exhalation. *Radon in the Living Environment* 71: 627-642.

Korany, K. A., Shata, A. E., Hassan, S. F. and Nagdy, M. S. E. 2013. Depth and seasonal variations for the soil radon-gas concentration levels at Wadi Naseib Area, southwestern Sinai, Egypt. *Journal of Physical Chemistry and Biophysics* 3: 123.

Kropat, G., Bochud, F., Murith, C., Palacios, M. and Baechler, S. 2017. Modeling of geogenic radon in Switzerland based on ordered logistic regression. *Journal of environmental radioactivity* 166: 376-381.

Külahcı, F., İnceöz, M., Doğru, M., Aksoy, E. and Baykara, O. 2009. Artificial neural network model for earthquake prediction with radon monitoring. *Applied Radiation and Isotopes* 67.1: 212-219.

Kulali, F., Akkurt, I. and Özgür, N. 2017. The effect of meteorological parameters on radon concentration in soil gas. *Acta Physica Polonica A* 132.3-II: 999-1001.

Lal, R. and Shukla, M. K. 2004. *Principles of soil physics*. CRC Press, Boca Raton. ISBN 9780367394219. https://doi.org/10.4324/9780203021231.

Lara, E., Rocha, Z., Palmieri, H. E. L., Santos, T. O., Rios, F. J. and Oliveira, A. H. 2015. Radon concentration in soil gas and its correlations with pedologies, permeabilities and ^{226}Ra content in the soil of the Metropolitan Region of Belo Horizonte–RMBH, Brazil. *Radiation Physics and Chemistry* 116: 317-320.

Liu, H., Wang, N., Chu, X., Li, T., Zheng, L., Yan, S. and Li, S. 2016. Mapping radon hazard areas using ^{238} U measurements and geological units: a study in a high background radiation city of China. *Journal of radioanalytical and nuclear chemistry* 309.3: 1209-1215.

Loll, P., Moldrup, P., Schjønning, P. and Riley, H. 1999. Predicting saturated hydraulic conductivity from air permeability: Application in stochastic water infiltration modeling. *Water Resources Research* 35.8: 2387-2400.

Mancini, S., Guida, M., Cuomo, A., Guida, D. and Ismail, A. H. 2018. Modeling of indoor radon activity concentration dynamics and its validation through in-situ measurements on regional scale. In *Mathematical Methods and Computational Techniques in Science and Engineering II AIP Conference Proceedings* . AIP Publishing LLC 1982.1: 02004(3).

Makin, I.A. and Atta, A.A. 2018. Statistical Distributions and Methods for Radon Data Analysis. *Radiation Physics and Chemistry* 144: 190 – 195.

Mehmood, T., and Awais, M. 2021. Tukey control chart for radon monitoring in relation to the seismic activity. *Mathematical Problems in Engineering* 2021: 1-8.

Mezon, C. (2017). Caractérisation des circulations thermo-convectives à l'échelle d'une zone fracturée par méthodes géophysiques et numériques (Doctoral dissertation, La Réunion).

Mily Jashank, Jayalakshmi M. Nair and Rajendra S. Khairnar. 2016. Analysis of Radon Gas Variation as a Precursor of Earthquake Prediction Using RAD7. *International Journal. of Advanced Research.* 4**.** 518-524 (ISSN 2320-5407).

Miles, J.C.H. and Appleton, J.D. 2005. Mapping variation in radon potential both between and within geological units. *Journal of Radiological Protection* 25: 257–276.

Moreira, A. C., Portezan Filho, O., Cavalcante, F. H. M., Coimbra, M. M. and Appoloni, C. R. 2007. Gamma ray transmission for hydraulic conductivity measurement of undisturbed soil columns. *Brazilian Archives of Biology and Technology* 50.2: 321-328.

Mostečak, A., Perković, D., Kapor, F. and Veinović, Ž. 2018. Radon mapping in Croatia and its relation to geology. *Rudarsko-geološko-naftni zbornik* 33.3: 1-11.

Munyaradzi, Z., Anna, K. N. and Victor, T. 2016. Elemental Concentration of Natural Occurring Radioactive Materials in Soils nearby Uranium Mine Sites of Erongo Region, Namibia. *European Journal of Scientific Research* 140.4: 402-410.

Neznal M, Neznal M, Matolin M, Barnet I, Miksova J. 2004. The New Method for Assessing the Radon Risk of Building Sites: The Czech Republic; Czech Geological Survey.Special Papers: 1–94.

Neznal, M. 2005. Permeability as an important parameter for radon risk classification of foundation soils. *Annals of Geophysics* 48.1: 175 - 180.

Negarestani, A., Setayeshi, S., Ghannadi-Maragheh, M. and Akashe, B. 2003. Estimation of the radon concentration in soil related to the environmental parameters by a modified Adaline neural network. *Applied radiation and isotopes* 58.2: 269-273.

Noverques, A., Juste, B., Sancho, M., García-Fayos, B., and Verdú, G. 2020. Study of the influence of radon in water on radon levels in air in a closed location. *Radiation Physics and Chemistry* 171: 108761.

Noverques, A., Juste, B., Sancho, M., Verdú, G. 2023. Determination of the radon transfer velocity coefficient in water under static and turbulent conditions. *Radiation Physics and Chemistry* 210: 111057.

Nuhu, H., Hashim, S., Aziz Saleh, M., Syazwan Mohd Sanusi, M., Hussein Alomari, A., and Jamal, M. H. 2021. Soil gas radon and soil permeability assessment: Mapping radon risk areas in Perak State, Malaysia. *PLoS ONE* 16.7: 0254099.

Obed, R.I., Adesunloro, G.M. and Popoola, O.I. 2018. Soil-Gas Radon Monitoring in Ibadan: Innovative Approach to Estimating Geological Fault Zones. *Journal of Applied Physics* 10.5: 33 – 40.

Obed, R. I., Farai, I. P. and Jibiri, N. N. 2005. Population dose distribution due to soil radioactivity concentration levels in 18 cities across Nigeria. *Journal of Radiological Protection* 25.3: 305.

O'Brien, K. E., Goodwin, T. A. and Risk, D. 2011. Radon soil gas in the Halifax Regional Municipality, Nova Scotia, Canada. *Atlantic Geology* 47: 112–124.

Olise, F. S., Akinnagbe, D. M. and Olasogba, O. S. 2016. Radionuclides and radon levels in soil and ground water from solid minerals-hosted area, south-western Nigeria. *Cogent Environmental Science* 2.1: 1142344.

Okeke, O. C., Abiahu, C. M. G., Anifowose, F. A., and Fagorite, V. I. 2019. A review of the geology and mineral resources of Dahomey Basin, Southwestern Nigeria. *International Journal of Environmental Sciences and Natural Resources*, 21(1): 1-5.

Oni, O. M., Aremu, A. A., Oladapo, O. O., Agboluaje, B. A., and Fajemiroye, J. A. (2022). Artificial neural network modeling of meteorological and geological influences on indoor radon concentration in selected tertiary institutions in Southwestern Nigeria. *Journal of Environmental Radioactivity* 251: 106933.

Oni, F. G. O., and Odekunle, T. O. 2016. An assessment of climate change impacts on maize (Zea Mays) yield in south-western Nigeria. *International Journal of Applied and Natural Sciences*, 5(3): 109-114.

Oyinloye, A. O. 2011. Geology and geotectonic setting of the basement complex rocks in southwestern Nigeria: Implications on provenance and evolution. *Earth and Environmental Sciences* 978-953:307-468.

Otton, J. K. 1992. *The geology of radon*. Washington: Government Printing Office, Washington, USA. ISBN 0-16-037974-1

Park, J. H., Whang, S., Lee, H. Y., Lee, C. M. and Kang, D. R. 2018. Measurement and modeling of indoor radon concentrations in residential buildings. *Environmental Health and Toxicology* 33.1. doi: 10.5620/eht.e2018003

Pasini, A., Ameli, F. and Lorè, M. 2003. Short range forecast of atmospheric radon concentration and stable layer depth by neural network modelling. *The 3rd International Workshop on Scientific Use of Submarine Cables and Related Technologies, 2003.* IEEE. 85-90.

Pazwash, H. 2020. A method of radon reduction for new buildings In *Radon, Radium, and Other Radioactivity in Ground Water*. CRC Press. 491-497.

Pereira, A., Lamas, R., Miranda, M., Domingos, F., Neves, L., Ferreira, N. and Costa, L. 2017. Estimation of the radon production rate in granite rocks and evaluation of the implications for geogenic radon potential maps: A case study in Central Portugal. *Journal of environmental radioactivity* 166: 270-277.

Petermann, E., Meyer, H., Nussbaum, M. and Bossew, P. 2020. Mapping the geogenic radon potential for Germany by machine learning. *Science of the Total Environment* 754.2021: 142291.

RAD7 user manual. Durridge Company, Inc. 2012. http://www.durridge.com/documentation/RAD7%20Manual.pdf. Accessed on 19th May, 2022.

RAD7 User Manual 2012. *Durridge Radon Instrumentation, RAD7 Radon Detector* USA: Durridge Co.

Rahaman, M.A. 1988. Recent advances in the study of the basement complex of Nigeria. *Pre Cambrian geology of Nigeria* Geological Survey of Nigeria, Kaduna South, 11-43.

Rahmati, M., Neyshaboury, M. R., and Mohammadi, P. 2019. Prediction of soil hydraulic conductivity at saturation using air permeability at any individual soil water content. *KSCE Journal of Civil Engineering* 23.12: 5226-5234.

Ravikumar, P., Davis, Deljo Somashekar, R.K. and Prakash, K. l. 2015. Measurement of radon activity in soil gas using RAD7 in the Environs of Chitradurga District, Karnataka, India. *Elixir Earth Science* 80: 31078-31082.

Rezaie, F., Panahi, M., Lee, J., Lee, J., Kim, S., Yoo, J., Lee, S. 2022. Radon potential mapping in Jangsu-gun, South Korea using probabilistic and deep learning algorithms. *Environmental Pollution* 292: 118385.

Rich, E. 1983. *Artificial Intelligence*. New York .McGraw-Hill.

Riudavets, M., Garcia de Herreros, M., Besse, B., and Mezquita, L. 2022. Radon and lung cancer: current trends and future perspectives. *Cancers*, 14(13): 3142.

Rizzo, A., Antonacci, G., Borra, E., Cardellini, F., Ciciani, L., Sperandio, L., and Vilardi, I. 2022. Environmental gamma dose rate monitoring and radon correlations: evidence and potential applications. *Environments* 9.6: 66.

Sakoda, A., Ishimori, Y., Hanamoto, K., Kataoka, T., Kawabe, A. and Yamaoka, K. 2010. Experimental and modeling studies of grain size and moisture content effects on radon emanation. *Radiation Measurements* 45.2: 204-210.

Salami, E. S., Ehetshami, M., Karimi-Jashni, A., Salari, M., Sheibani, S. N. and Ehteshami, A. 2016. A mathematical method and artificial neural network modeling to simulate osmosis membrane's performance. *Modeling Earth Systems and Environment* 2.4: 1-11.

Shafik, S. S. and Mohammed, A. A. 2013. Measurement of radon and uranium concentrations and background gamma rays at the University of Baghdad-Jadiriyah site. *International Journal of Application or Innovation in Engineering and Management (IJAIEM)* 2.5: 455-462.

Siegesmund, S., Pereira, A., Sousa, L., Rucker, S., Kallas, L., Kopka, B. and Seco, S. 2022. Is there any health danger by radioactivity on the use of dimensional stones?. *Environmental Earth Sciences* 81.15: 383.

Silva, A. S. and Dinis, M. D. L. 2022. Assessment of indoor radon concentration and time-series analysis of gamma dose rate in three thermal spas from Portugal. *Environmental Monitoring and Assessment* 194.9: 611.

Suharyatun, S., Telaumbanua, M., Haryanto, A., Wisnu, F. K. and Pratiwi, M. T. 2023. Empirical Model for Estimation of Soil Permeability Based on Soil Texture and Porosity. *Jurnal Teknik Pertanian Lampung (Journal of Agricultural Engineering)* 12.3: 533-544.

Szabó, K. Z., Jordan, G., Horváth, Á. and Szabó, C. 2013. Dynamics of soil gas radon concentration in a highly permeable soil based on a long-term high temporal resolution observation series. *Journal of environmental radioactivity* 124: 74-83.

Szabó, K. Z., Jordan, G., Horváth, Á. and Szabó, C. 2014. Mapping the geogenic radon potential: methodology and spatial analysis for central Hungary. *Journal of environmental radioactivity* 129: 107-120.

Tang, A. M., Cui, Y. J., Richard, G. and Défossez, P. 2011. A study on the air permeability as affected by compression of three French soils. *Geoderma* 162.1-2: 171-181.

Thomas, J. R., Sreejith, M. V., Aravind, U. K., Sahu, S. K., Shetty, P. G., Swarnakar, M. and Aravindakumar, C. T. 2022. Outdoor and indoor natural background Gamma radiation across Kerala, India. *Environmental Science: Atmospheres* 2.1: 65-72.

Thu, H. N. P., Van Thang, N., Loan, T. T. H. and Van Dong, N. 2019. Natural radioactivity and radon emanation coefficient in the soil of Ninh Son region, Vietnam. *Applied geochemistry* 104: 176-183.

Tommasino, L. 1990. Radon monitoring by alpha track detection. *International Journal of Radiation Application and Instrumentation. Part D. Nucear Tracks and Radiation Measurements* 17(1): 43 – 48.

Torkar, D., Zmazek, B., Vaupotič, J. and Kobal, I. 2010. Application of artificial neural networks in simulating radon levels in soil gas. *Chemical Geology* 270.1-4: 1-8.

Tuli, A., Hopmans, J. W., Rolston, D. E. and Moldrup, P. 2005. Comparison of air and water permeability between disturbed and undisturbed soils. *Soil Science Society of America Journal* 69.5: 1361-1371.

UNSCEAR (United Nations Scientific Committee on the Effects of Atomic Radiation). 2000. *Ionizing Radiation: Sources and Biological Effects*. Report to the General Assembly with Annexes, New York. 102.

USEPA (U.S Environmental Protection Agency). 2018. A citizen's Guide to Radon: The Guide to Protecting Yourself and Your Family from Radon. U.S Environmental Protection Agency.

World Health Organization. 2016. Protection of the Public against Exposure Indoors due to Radon and Other Natural Sources of Radiation. Specific Safety Guide.

Wu, B., Bonnetti, C., Liu, Y., Zhang, Z. S., Guo, G. L., Li, G. L., and Yan, Z. Y. 2021. Uraninite from the Guangshigou Pegmatite-Type Uranium Deposit in the North Qinling Orogen, Central China: Its Occurrence, Alteration and Implications for Post-Caledonian Uranium Circulation. *Minerals*, 11(7): 729. doi.org/10.3390/min11070729.

Yalım, H. A., Gümüş, A., Başaran, C., Bağcı, M., Yıldız, A., Açil, D. and Ünal, R. 2018. Comparison of radon concentrations in soil gas and indoor environment of Afyonkarahisar Province. *Arabian Journal of Geosciences* 11.11: 246.

Yassaghi, A. and Masoodi, M. 2011. A metamorphic core complex model for the host of uranium mineralization in the Khoshoumi Mountain, central Iran. *Resource geology* 61.3: 259-269.

Yousef, H. A., El-Farrash, A. H., Ela, A. A. and Merza, Q. 2015. Measurement of radon exhalation rate in some building materials using nuclear track detectors. *World Journal of Nuclear Science and Technology* 5.03:141.

Zhu, Y., Zhou, S. and Zang, D. 2009. Discussion of Radon in Uranium Mining Disaster Model Based on Artificial Neural Network. *Second International Symposium on Computational Intelligence and Design.* IEEE 2: 433-436.

Appendix 1: Details of Geological, Measured and ANN data for the 150 locations

Appendix 1: Table 1A1: Soil-gas Radon Concentration Values Obtained from 150 Locations over Different Bedrocks in Southwest Nigeria

S/N	Coordinates	Notation	Geology	Mean Radon Conc. (kBq/m^3)
1	N8^o 09′ 02″ E4^o 15′ 09 ″	OyM1	Migmatite	29.09 ± 0.48
2	N8^o 20′ 55″ E4^o 11′ 25″	OyM2	Migmatite	2.16 ± 0.31
3	N8^o 15′ 10″ E4^o 21′ 19″	OyM3	Migmatite	23.10 ± 0.12
4	N7^o 28′ 10″ E3^o 44′ 49″	OyM4	Migmatite	2.26 ± 0.16
5	N7^o 22′ 38″ E3^o 53′ 22″	OyM5	Migmatite	3.46 ± 0.16
6	N7^o 53′ 02″ E4^o 14′ 28″	OsM1	Migmatite	3.31 ± 0.05
7	N7^o 52′ 12″ E4^o 22′ 18″	OsM2	Migmatite	4.12 ± 0.19
8	N7^o 15′ 01″ E3^o 39′ 22″	OgM1	Migmatite	2.43 ± 0.07
9	N7^o 10′ 09″ E3^o 25′ 16″	OgM2	Migmatite	11.49 ± 0.15
10	N6^o 56′ 32″ E3^o 55′ 17″	OgM3	Migmatite	3.34 ± 0.13
11	N7^o 03′ 28″ E4^o 51′ 19″	OdM1	Migmatite	3.87 ± 0.12
12	N7^o 18′ 19″ E5^o 08′ 23″	OdM2	Migmatite	35.02 ± 0.13

S/N	Coordinates	Notation	Geology	Mean Radon Conc. (kBq/m^3)
13	N7^o 16′ 25″ E5^o 30′ 07″	OdM3	Migmatite	23.48 ± 0.85
14	N6^o 42′ 21″ E4^o 54′ 07″	OdM4	Migmatite	16.62 ± 1.05
15	N7^o 35′ 42″ E5^o 12′ 15″	Ek M 1	Migmatite	2.89 ± 0.17
16	N7^o 42′ 12″ E5^o 04′ 59″	Ek M 2	Migmatite	31.89 ± 0.60
17	N7^o 36′ 35″ E5^o 24′ 27″	Ek M 3	Migmatite	3.49 ± 0.09
18	N7^o 20′ 18″ E5^o 26′ 07″	Ek M 4	Migmatite	2.77 ± 0.10
19	N7^o 27′ 28″ E5^o 33′ 19″	Ek M 5	Migmatite	3.53 ± 0.07
20	N7^o 45′ 03″ E5^o 18′ 14″	Ek M 6	Migmatite	4.17 ± 0.33
21	N7^o 41′ 29″ E5^o 24′ 21″	Ek M 7	Migmatite	3.49 ± 0.27
22	N7^o 37′ 18″ E5^o 31′ 13″	Ek M 8	Migmatite	3.14 ± 0.28
23	N7^o 34′ 18″ E5^o 09′ 33″	Ek M 9	Migmatite	4.55 ± 0.25
24	N8^o 55′ 33″ E4^o 01′ 54″	Oy gg 1	Granite Gneiss	40.42 ± 0.12

S/N	Coordinates	Notation	Geology	Mean Radon Conc. (kBq/m^3)
25	N8° 30′ 19″ E3° 06′ 08″	Oy gg 2	Granite Gneiss	43.26 ± 0.15
26	N8° 45′ 09″ E4° 06′ 02″	Oy gg 3	Granite Gneiss	44.90 ± 0.21
27	N8° 08′ 28″ E3° 51′ 45″	Oy gg 4	Granite Gneiss	39.74 ± 0.09
28	N8° 47′ 09″ E4° 07′ 23″	Oy gg 5	Granite Gneiss	41.96 ± 0.18
29	N7° 18′ 08″ E4° 27′ 17″	Os gg 1	Granite Gneiss	11.43 ± 0.23
30	N7° 24′ 44″ E4° 30′ 53″	Os gg 2	Granite Gneiss	9.65 ± 0.09
31	N8° 00′ 03″ E4° 33′ 27″	Os gg 3	Granite Gneiss	42.06 ± 0.29
32	N7° 15′ 22″ E4° 40′ 56″	Os gg 4	Granite Gneiss	8.99 ± 0.17
33	N7° 26′ 09″ E4° 50′ 42″	Os gg 5	Granite Gneiss	13.48 ± 0.21
34	N7° 04′ 29″ E5° 20′ 31″	Od gg 1	Granite Gneiss	18.74 ± 0.78
35	N7° 54′ 21″ E5° 33′ 28″	Ek gg 1	Granite Gneiss	8.50 ± 0.15
36	N8° 38′ 50″ E3° 22′ 27″	Oy Sq 1	Quartz Syenite	16.88 ± 0.13

S/N	Coordinates	Notation	Geology	Mean Radon Conc. (kBq/m^3)
37	N9° 04′ 54″ E3° 53′ 24″	Oy Sq 2	Quartz Syenite	34.54 ± 0.07
38	N8° 50′ 55″ E4° 04′ 59″	Oy Qs 1	Quartz Schist	35.73 ± 0.48
39	N8° 44′ 05″ E3° 43′ 21″	Oy Gb 1	Banded Gneiss	5.82 ± 0.17
40	N8° 09′ 24″ E3° 33′ 18″	Oy Gb 2	Banded Gneiss	8.43 ± 0.07
41	N7° 24′ 56″ E3° 10′ 48″	Oy Gb 3	Banded Gneiss	7.84 ± 0.11
42	N8° 18′ 31″ E2° 48′ 16″	Oy Gb 4	Banded Gneiss	9.43 ± 0.15
43	N7° 36′ 28″ E4° 44′ 42″	Os Gb 1	Banded Gneiss	10.37 ± 0.55
44	N7° 35′ 13″ E4° 23′ 12″	Os Gb 2	Banded Gneiss	7.36 ± 0.10
45	N7° 48′ 12″ E4° 50′ 10″	Os Gb 3	Banded Gneiss	6.44 ± 0.09
46	N8° 00′ 29″ E4° 40′ 57″	Os Gb 4	Banded Gneiss	5.37 ± 0.15
47	N6° 54′ 13″ E4° 48′ 07″	Od Gb 1	Banded Gneiss	4.78 ± 0.12
48	N7° 14′ 41″ E4° 47′ 30″	Od Gb 2	Banded Gneiss	2.76 ± 0.17

S/N	Coordinates	Notation	Geology	Mean Radon Conc. (kBq/m^3)
49	N8° 00′ 52″ E5° 05′ 10″	Ek Gb 1	Banded Gneiss	5.73 ± 0.08
50	N8° 01′ 24″ E3° 20′ 49″	Oy Su 1	Undifferentiated schist	3.25 ± 0.09
51	N8° 01′ 04″ E3° 32′ 57″	Oy Su 2	Undifferentiated schist	2.16 ± 0.11
52	N8° 32′ 42″ E3° 38′ 18″	Oy Su 3	Undifferentiated schist	2.45 ± 0.08
53	N7° 30 ′ 22″ E4° 00′ 48″	Oy Su 4	Undifferentiated schist	1.87 ± 0.17
54	N7° 51′ 02″ E3° 09′ 19″	Oy Su 5	Undifferentiated schist	4.25 ± 0.15
55	N7° 42′ 27″ E4° 47′ 08″	Os Su 1	Undifferentiated schist	2.47 ± 0.10
56	N7° 30′ 30″ E4° 34′ 19″	Os Su 2	Undifferentiated schist	1.96 ± 0.12
57	N6° 57′ 32″ E4° 03′ 49″	Og Su 1	Undifferentiated schist	4.13 ± 0.12
58	N7° 00′ 35″ E4° 07′ 58″	Og Su 2	Undifferentiated schist	3.34 ± 0.09
59	N7° 00′ 27″ E4° 00′ 23″	Og Su 3	Undifferentiated schist	2.49 ± 0.12
60	N6° 57′ 47″ E3° 58′ 32″	Og Su 4	Undifferentiated schist	3.54 ± 0.08

S/N	Coordinates	Notation	Geology	Mean Radon Conc. (kBq/m^3)
61	N6° 42′ 19″ E4° 15′ 02″	Og Su 5	Undifferetiated Schist	3.04 ± 0.22
62	N7° 08′ 39″ E5° 41′ 07″	Od Su 1	Undifferentiated schist	4.96 ± 0.10
63	N7° 40′ 45″ E5° 03′ 17″	Ek Su 1	Undifferentiated schist	13.76 ± 1.11
64	N8° 21′ 04″ E3° 33′ 18″	Oy Sa 1	Amphibole Schist & Amphibolite	13.56 ± 0.12
65	N8° 06′ 22″ E3° 27′ 18″	Oy Sa 2	Amphibole Schist & Amphibolite	10.75 ± 0.09
66	N8° 08′ 17″ E3° 21′ 45″	Oy Sa 3	Amphibole Schist & Amphibolite	10.16 ± 0.07
67	N7° 26′ 34″ E3° 16′ 39″	Oy Sa 4	Amphibole Schist & Amphibolite	8.92 ± 0.08
68	N8° 18′ 36″ E4° 12′ 00″	Oy OGf 1	Fine-grained Biotite granite	2.31 ± 0.13
69	N8° 18′ 05″ E4° 18′ 03″	Oy OGf 2	Fine-grained Biotite granite	3.46 ± 0.12
70	N8° 11′ 12″ E4° 06′ 35″	Oy OGf 3	Fine-grained Biotite granite	2.85 ± 0.13
71	N7° 29′ 58″ E4° 15′ 55″	Os OGf 1	Fine-grained Biotite granite	3.22 ± 0.07
72	N7° 32′ 52″ E4° 12′ 29″	Os OGf 2	Fine-grained Biotite granite	7.79 ± 0.19

S/N	Coordinates	Notation	Geology	Mean Radon Conc (kBq/m^3)
73	N7° 03′ 13″ E4° 17′ 22″	Og OGf 1	Fine-grained Biotite granite	3.75 ± 0.09
74	N6° 45′ 06″ E4° 46′ 19″	Od OGf 1	Fine-grained Biotite granite	3.59 ± 0.11
75	N6° 51′ 09″ E4° 50′ 21″	Od OGf 2	Fine-grained Biotite granite	4.29 ± 0.13
76	N8° 36′ 14″ E3° 00′ 29″	Oy OGm 1	M-CG Biotite & biotite hornblende granite	4.36 ± 0.13
77	N8° 37′ 32″ E3° 38′ 15″	Oy OGm 2	M-CG Biotite & biotite hornblende granite	1.32 ± 0.16
78	N8° 38′ 00″ E3° 35′ 40″	Oy OGm 3	M-CG Biotite & biotite hornblende granite	1.14 ± 0.16
79	N8° 36′ 17″ E3° 18′ 21″	Oy OGm 4	M-CG Biotite & biotite hornblende granite	5.94 ± 0.08
80	N7° 12′ 14″ E4° 54′ 28″	Od OGm 1	M-CG biotite & biotite hornblende granite	3.12 ± 0.18
81	N8° 19′ 35″ E4° 06′ 38″	Oy OGp 1	CG Porphyritic biotite & biotite hornblende	3.56 ± 0.12
82	N8° 16′ 03″ E4° 09′ 29″	Oy OGp 2	CG Porphyritic biotite & biotite hornblende	24.46 ± 0.14
83	N8° 12′ 06″ E3° 24′ 09″	Oy OGp 3	CG Porphyritic biotite & biotite hornblende	5.49 ± 0.15
84	N8° 36′ 19″ E3° 36′ 11″	Oy OGp 4	CG Porphyritic biotite & biotite hornblende	7.15 ± 0.14

S/N	Coordinates	Notation	Geology	Mean Radon Conc (kBq/m^3)
85	N7° 21′ 08″ E5° 15′ 16″	Od OGp 1	CG Porphyritic biotite & biotite hornblende	23.67 ± 0.13
86	N6° 50′ 12″ E4° 42′ 27″	Od OGp 2	CG Porphyritic biotite & biotite hornblende	2.88 ± 0.15
87	N7° 04′ 15″ E5° 05′ 41″	Od OGp 3	CG Porphyritic biotite & biotite hornblende	45.62 ± 0.19
88	N7° 00′ 47″ E5° 09′ 39″	Od OGp 4	CG Porphyritic biotite & biotite hornblende	47.59 ± 0.16
89	N7° 28′ 15″ E5° 13′ 25″	Ek OGp 1	CG Porphyritic biotite & biotite hornblende	26.94 ± 0.15
90	N8° 47′ 22″ E3° 24′ 35″	Oy OGp 5	CG Porphyritic biotite & biotite hornblende	5.67 ± 0.12
91	N8° 39′ 28″ E4° 09′ 57″	Oy OGp 6	CG Porphyritic biotite & biotite hornblende	32.49 ± 0.12
92	N8° 30′ 09″ E4° 03′ 27″	Oy OGp 7	CG Porphyritic biotite & biotite hornblende	3.47 ± 0.09
93	N8° 22′ 48″ E4° 05′ 26″	Oy OGp 8	CG Porphyritic biotite & biotite hornblende	2.77 ± 0.12
94	N7° 12′ 40″ E4° 33′ 00″	Os OGp 1	CG Porphyritic biotite & biotite hornblende	36.64 ± 0.08
95	N7° 05′ 52″ E4° 30′ 32″	Os OGp 2	CG Porphyritic biotite & biotite hornblende	3.27 ± 0.15
96	N6° 51′ 45″ E4° 08′ 31″	Og OGp 1	CG Porphyritic biotite & biotite hornblende	33.78 ± 0.12

S/N	Coordinates	Notation	Geology	Mean Radon Conc (kBq/m^3)
97	N7° 56 ′ 23″ E3° 15′ 45″	Oy OGP 9	CG Porphyritic biotite & biotite hornblende	2.11 ± 0.09
98	N7° 21′ 19″ E4° 10′ 23″	Os P 1	Pegmatite	4.12 ± 0.11
99	N7° 20′ 01″ E4° 12′ 27″	Os P 2	Pegmatite	2.86 ± 0.20
100	N7° 10′ 23″ E4° 16′ 15″	Os P 3	Pegmatite	5.42 ± 0.09
101	N7° 48′ 24″ E4° 32′ 57″	Os P 4	Pegmatite	6.14 ± 0.09
102	N7° 31′ 43″ E2° 51′ 35″	Og OGGm 1	Muscovite tourmaline granite gneiss	3.64 ± 0.07
103	N8° 00′ 57″ E5° 00′ 09″	Os Qs 1	Flaggy quartzite & Quartzite Schist	6.37 ± 0.13
104	N7° 24′ 26″ E4° 52′ 52″	Os Qs 2	Flaggy quartzite & Quartzite Schist	7.05 ± 0.23
105	N7° 43′ 56″ E4° 59′ 29″	Ek Qs 1	Flaggy quartzite & Quartzite Schist	7.36 ± 0.11
106	N7° 30′ 06″ E4° 56′ 57″	Ek Qs 2	Flaggy quartzite & Quartzite Schist	7.81 ± 0.07
107	N7° 46′ 34″ E4° 28′ 15″	Os St 1	Talc Schist	7.83 ± 0.09
108	N7° 12′ 19″ E4◦27¹18¹¹	Os St 2	Talc Schist	0.28 ± 0.12

S/N	Coordinates	Notation	Geology	Mean Radon Conc (kBq/m^3)
109	N7° 26′ 35″ E4° 27′ 21″	Os St 3	Talc Schist	6.34 ± 0.04
110	N7° 32′ 57″ E4° 28′ 00″	Os St 4	Talc Schist	4.74 ± 0.11
111	N7° 42′ 05″ E4° 38′ 41″	Os St 5	Talc Schist	0.41 ± 0.15
112	N7° 42′ 16″ E4° 33′ 41″	Os St 6	Talc Schist	5.84 ± 0.13
113	N7° 35′ 13″ E4° 27′ 12″	Os St 7	Talc Schist	0.66 ± 0.16
114	N6° 55′ 28″ E3° 09′ 02″	Og Fshl 1	Shale, Limestone & Siltstone	43.77 ± 0.17
115	N6° 55′ 06″ E2° 54′ 45″	Og Fshl 2	Shale, Limestone & Siltstone	21.85 ± 0.14
116	N6° 51′ 08″ E3° 23′ 48″	Og Fshl 3	Shale, Limestone & Siltstone	45.88 ± 0.11
117	N6° 48′ 54″ E3° 54′ 28″	Og Fshl 4	Shale, Limestone & Siltstone	13.43 ± 0.09
118	N7° 05′ 19″ E2° 44′ 54″	Og Fshl 5	Shale, Limestone & Siltstone	7.49 ± 0.12
119	N6° 55′ 38″ E2° 54′ 27″	Og Fshl 6	Shale, Limestone & Siltstone	9.728 ± 0.11
120	N6° 46′ 08″ E3° 20′ 17″	Og Fshl 7	Shale, Limestone & Siltstone	7.42 ± 0.10

S/N	Coordinates	Notation	Geology	Mean Radon Conc (kBq/m^3)
121	N7° 12′ 34″ E3° 00′ 14″	Og Fshl 8	Shale, Limestone & Siltstone	9.77 ± 0.13
122	N7° 11′ 05″ E3° 06′ 26″	Og Asl 1	Sandstone and Limestone	3.44 ± 0.11
123	N7° 05′ 58″ E3° 10′ 57″	Og Asl 2	Sandstone and Limestone	4.25 ± 0.16
124	N7° 00′ 19″ E3° 28′ 52″	Og Asl 3	Sandstone and Limestone	2.45 ± 0.11
125	N6° 54′ 06″ E3° 41′ 36″	Og Asl 4	Sandstone and Limestone	4.89 ± 0.12
126	N6° 45′ 26″ E3° 59′ 20″	Og Asl 5	Sandstone and Limestone	2.79 ± 0.24
127	N6° 48′ 42″ E3° 42′ 18″	Og Asl 6	Sandstone and Limestone	1.89 ± 0.13
128	N6° 53′ 45″ E3° 32′ 59″	Og Asl 7	Sandstone and Limestone	3.37 ± 0.15
129	N8° 49′ 38″ E3° 45′ 48″	Oy Opg 1	Porphyroblastic gneiss	2.89 ± 0.13
130	N8° 31′ 42″ E3° 18′ 45″	Oy Opg 2	Porphyroblastic gneiss	6.25 ± 0.19
131	N6° 19′ 31″ E4° 50′ 02″	Od Bnst 1	Sand and Clay	0.76 ± 0.11
132	N6° 27′ 29″ E4° 37′ 53″	Od Bnst 2	Sand and Clay	0.94 ± 0.12

S/N	Coordinates	Notation	Geology	Mean Radon Conc (kBq/m^3)
133	N6° 38′ 05″ E3° 17′ 01″	Lag Bnst 1	Sand and Clay	0.33 ± 0.07
134	N6° 38′ 36″ E3° 33′ 23″	Lag Bnst 2	Sand and Clay	0.91 ± 0.10
135	N6° 37′ 56″ E3° 39′ 05″	Lag Bnst 3	Sand and Clay	2.64 ± 0.12
136	N6° 30′ 29″ E3° 48′ 42″	Lag Bnst 4	Sand and Clay	0.84 ± 0.06
137	N6° 45′ 38″ E2° 22′ 52″	Og Bnst 1	Sand and Clay	11.70 ± 0.10
138	N6° 36′ 26″ E2° 28′ 17″	Og Bnst 2	Sand and Clay	12.78 ± 0.09
139	N6° 38′ 03″ E3° 08′ 14″	Og Bnst 3	Sand and Clay	10.84 ± 0.09
140	N7° 44′ 28″ E4° 24′ 10″	Os OGCh 1	Charnokite & Charnokitic rock	44.15 ± 0.14
141	N7° 43′ 54″ E4° 21′ 08″	Os OGCh 2	Charnokite & Charnokitic rock	42.14 ± 0.11
142	N6° 36′ 13″ E3° 45′ 07″	Lag Csd 1	Sand and Mash	0.34 ± 0.04
143	N6° 27′ 47″ E2° 26′ 48[11]	Lag Csd 2	Sand and Mash	0.29 ± 0.06
144	N6° 29′ 06[11] E3° 15′ 28[11]	Lag Csd 3	Sand and Mash	0.33 ± 0.08

S/N	Coordinates	Notation	Geology	Mean Radon Conc (kBq/m^3)
145	N6^o 30′ 19″ E3^o 23′ 34″	Lag Csd 4	Sand and Mash	0.98 ± 0.12
146	N6^o 25′ 24″ E3^o 24′ 32″	Lag Csd 5	Sand and Mash	1.55 ± 0.11
147	N6^o 39′ 19″ E3^o 47′ 24″	Lag Issh 1	Sand, Clay and Shale	0.69 ± 0.06
148	N6^o 36′ 11″ E3^o 54′ 37″	Lag Issh 2	Sand, Clay and Shale	1.10 ± 0.18
149	N6^o 27′ 15″ E4^o 03′ 38″	Lag Issh 3	Sand, Clay and Shale	1.69 ± 0.12
150	N6^o 39′ 22″ E4^o 02′ 19″	Lag Issh 4	Sand, Clay and Shale	1.73 ± 0.11

Appendix 1: Table 1A2: Measured Saturated Hydraulic Conductivity and derived Soil-air Permeability for the 150 Sites on different Bedrocks

S/N	Coordinates	Notation	H (cm)	L (cm)	Q (Vol.) (cm^3)	Sat. Hyd. Cond. (m/day)	Air Perm. (Ka) (x 10^{-12}) m^2
1	N8° 09′ 02″ E4° 15′ 09″	OyM1	4.8	5.1	45.10	0.56	4.93
2	N8° 20′ 55″ E4° 11′ 25″	OyM2	4.7	5.0	47.80	0.59	5.17
3	N8° 15′ 10″ E4° 21′ 19″	OyM3	5.2	4.9	35.20	0.41	3.87
4	N7° 28′ 10″ E3° 44′ 49″	OyM4	4.8	5.2	39.20	0.49	4.45
5	N7° 22′ 38″ E3° 53′ 22″	OyM5	5.1	4.9	20.30	0.24	2.53
6	N7° 53′ 02″ E4° 14′ 28″	OsM1	4.8	5.1	38.70	0.48	4.38
7	N7° 52′ 12″ E4° 22′ 18″	OsM2	4.6	5.2	33.10	0.43	3.96
8	N7° 15′ 01″ E3° 39′ 22″	OgM1	4.8	5.1	26.80	0.33	3.28
9	N7° 10′ 09″ E3° 25′ 16″	OgM2	4.9	4.6	40.50	0.48	4.32
10	N6° 56′ 32″ E3° 55′ 17″	OgM3	4.8	4.9	29.80	0.37	3.51
11	N7° 03′ 28″ E4° 51′ 19″	OdM1	4.7	5.1	36.70	0.46	4.23

S/N	Coordinates	Notation	h (cm)	L (cm)	Q (cm^3)	Sat. Hyd. Cond (m/day)	Air Perm. (Ka) x 10^{-12} (m^2)
12	N7^o 18′ 19″ E5^o 08′ 23″	OdM2	4.9	5.0	118.71	1.45	10.41
13	N7^o 16′ 25″ E5^o 30′ 07″	OdM3	5.1	4.8	10.90	0.13	1.54
14	N6^o 42′ 21″ E4^o 54′ 07″	OdM4	5	4.6	13.40	0.16	1.80
15	N7^o 35′ 42″ E5^o 12′ 15″	Ek M 1	4.8	5.0	147.50	1.82	12.45
16	N7^o 42′ 15″ E5^o 04′ 59″	Ek M 2	4.6	5.2	36.60	0.47	4.28
17	N7^o 36′ 35″ E5^o 24′ 27″	Ek M 3	4.9	4.9	44.90	0.54	4.80
18	N7^o 20′ 18″ E5^o 26′ 07″	Ek M 4	5.1	4.7	32.50	0.38	3.61
19	N7^o 27′ 28″ E5^o 33′ 19″	Ek M 5	4.8	5.0	31.90	0.39	3.73
20	N7^o 45′ 03″ E5^o 18′ 14″	Ek M 6	5.2	4.7	31.70	0.36	3.50
21	N7^o 41′ 29″ E5^o 24′ 21″	Ek M 7	4.8	5	34.60	0.43	3.98
22	N7^o 37′ 18″ E5^o 03′ 13″	Ek M 8	5.1	4.7	35.50	0.41	3.86

S/N	Coordinates	Notation	h (cm)	L (cm)	Q (cm^3)	Sat. Hyd. Cond (m/day)	Air Perm. (Ka) x 10^{-12} (m^2)
23	N7° 34′ 18″ E5° 09′ 33″	Ek M 9	4.9	4.7	35.10	0.42	3.89
24	N8° 55′ 33″ E4° 01′ 54″	Oy gg 1	4.8	5.1	73.21	0.91	7.23
25	N8° 30′ 19″ E3° 06′ 08″	Oy gg 2	4.7	5.1	55.39	0.69	5.85
26	N8° 45′ 09″ E4° 06′ 02″	Oy gg 3	5.3	4.7	67.92	0.77	6.33
27	N8° 08′ 28″ E3° 51′ 45″	Oy gg 4	4.9	4.6	38.60	0.45	4.15
28	N8° 47′ 09″ E4° 07′ 23″	Oy gg 5	5.0	4.8	66.92	8.79	6.47
29	N7° 18′ 08″ E4° 27′ 17″	Os gg 1	5.0	4.8	28.90	0.34	3.35
30	N7° 24′ 44″ E4° 30′ 53″	Os gg 2	4.7	5.1	32.80	0.41	3.87
31	N8° 00′ 03″ E4° 33′ 27″	Os gg 3	4.6	5.0	62.21	0.78	6.41
32	N7° 15′ 22″ E4° 40′ 56″	Os gg 4	4.9	4.7	26.60	0.32	3.12
33	N7° 26′ 09″ E4° 50′ 42″	Os gg 5	5.1	4.9	23.20	0.28	2.81
34	N7° 04′ 29″ E5° 20′ 31″	Od gg 1	4.8	5.0	17.40	0.22	2.31

S/N	Coordinates	Notation	h (cm)	L (cm)	Q (cm^3)	Sat. Hyd. Cond (m/day)	Air Perm. (Ka) x 10^{-12} (m^2)
35	N7^o 54′ 21″ E5^o 33′ 28″	Ek gg 1	5.0	4.8	25.70	0.31	3.05
36	N8^o 38′ 50″ E3^o 22′ 27″	Oy Sq 1	4.9	5.2	35.61	0.44	4.09
37	N9^o 04′ 54″ E3^o 53′ 24″	Oy Sq 2	5.1	5.0	25.48	0.31	3.05
38	N8^o 50′ 55″ E4^o 04′ 59″	Oy Sq 3	4.8	5.3	113.10	1.44	10.32
39	N8^o 44′ 05″ E3^o 43′ 21″	Oy Gb 1	5.3	4.9	40.80	0.48	4.32
40	N8^o 09′ 24″ E3^o 33′ 18″	Oy Gb 2	5.1	4.7	55.50	0.65	5.49
41	N7^o 24′ 56″ E3^o 10′ 48″	Oy Gb 3	4.8	5.2	45.50	0.57	5.01
42	N8^o 18′ 31″ E2^o 48′ 16″	Oy Gb 4	4.9	5.0	59.20	0.72	6.02
43	N7^o 36′ 28″ E4^o 44′ 42″	Os Gb 1	4.6	4.8	71.40	0.88	7.04
44	N7^o 35′ 13″ E4^o 23′ 12″	Os Gb 2	4.8	4.6	31.80	0.38	3.59
45	N7^o 48′ 12″ E4^o 50′ 10″	Os Gb 3	4.7	5.1	33.40	0.42	3.93
46	N8^o 00′ 29″ E4^o 40′ 57″	Os Gb 4	5.0	4.9	32.80	0.39	3.72

S/N	Coordinates	Notation	h (cm)	L (cm)	Q (cm^3)	Sat. Hyd. Cond (m/day)	Air Perm. (Ka) x 10^{-12} (m^2)
47	N6° 54′ 13″ E4° 48′ 07″	Od Gb 1	4.8	5.0	32.40	0.40	3.77
48	N7° 14′ 41″ E4° 47′ 30″	Od Gb 2	4.9	4.7	30.70	0.36	3.50
49	N8° 00′ 52″ E5° 05′ 10″	Ek Gb 1	4.8	5.0	26.50	0.33	3.22
50	N8° 01′ 24″ E3° 20′ 49″	Oy Su 1	5.2	4.9	39.80	0.47	4.27
51	N8° 01′ 04″ E3° 32′ 57″	Oy Su 2	5.0	4.7	28.60	0.34	3.28
52	N8° 32′ 42″ E3° 38′ 18″	Oy Su 3	5.1	4.9	34.80	0.41	3.86
53	N7° 30′ 22″ E4° 00′ 48″	Oy Su 4	4.9	5.0	44.30	0.54	4.79
54	N7° 51′ 02″ E3° 09′ 19″	Oy Su 5	4.7	5.2	48.40	0.62	5.29
55	N7° 42′ 27″ E4° 47′ 08″	Os Su 1	5.0	4.7	39.50	0.46	4.24
56	N7° 30′ 30″ E4° 34′ 19″	Os Su 2	4.9	4.6	42.99	0.50	4.53
57	N6° 57′ 32″ E4° 03′ 49″	Og Su 1	4.6	5.2	42.30	0.54	4.79
58	N7° 00′ 35″ E4° 07′ 58″	Og Su 2	4.9	4.8	34.50	0.41	3.87

S/N	Coordinates	Notation	h (cm)	L (cm)	Q (cm^3)	Sat. Hyd. Cond (m/day)	Air Perm. (Ka) x 10^{-12} (m^2)
59	N7^o 00′ 27″ E4^o 00′ 23″	Og Su 3	5.2	4.7	32.80	0.38	3.59
60	N6^o 57′ 47″ E3^o 58′ 32″	Og Su 4	5.0	4.9	38.60	0.46	4.23
61	N6^o 42′ 19″ E4^o 15′ 02″	Og Su 5	4.7	5.2	21.70	0.28	2.82
62	N7^o 08′ 39″ E5^o 41′ 07″	Od Su 1	5.1	4.8	12.90	0.09	1.17
63	N7^o 40′ 45″ E5^o 03′ 17″	Ek Su 1	5.0	4.8	116.74	1.39	10.03
64	N8^o 21′ 04″ E3^o 33′ 18″	Oy Sa 1	5.2	4.8	44.15	0.14	1.67
65	N8^o 06′ 22″ E3^o 27′ 18″	Oy Sa 2	5.0	4.7	4.80	0.02	0.29
66	N8^o 08′ 17″ E3^o 21′ 45″	Oy Sa 3	4.9	4.8	34.66	0.12	1.42
67	N7^o 26′ 34″ E3^o 16′ 39″	Oy Sa 4	4.7	5.1	13.10	0.05	0.68
68	N8^o 18′ 36″ E4^o 12′ 00″	Oy OGf 1	4.9	5.0	11.50	1.36	9.91
69	N8^o 18′ 05″ E4^o 18′ 03″	Oy OGf 2	5.1	4.8	20.80	0.25	2.56
70	N8^o 11′ 12″ E4^o 06′ 35″	Oy OGf 3	4.8	5.2	26.60	0.34	3.28

S/N	Coordinates	Notation	h (cm)	L (cm)	Q (cm^3)	Sat. Hyd. Cond (m/day)	Air Perm. (Ka) x 10^{-12} (m^2)
71	N7^o 29′ 58″ E4^o 15′ 55″	Os OGf 1	5.1	4.6	23.90	0.27	2.80
72	N7^o 32′ 52″ E4^o 12′ 29″	Os OGf 2	4.9	4.7	96.70	1.15	8.64
73	N7^o 03′ 13″ E4^o 17′ 22″	Og OGf 1	4.6	5.2	20.00	0.26	2.67
74	N6^o 45′ 06″ E4^o 46′ 19″	Od OGf 1	5.1	4.6	28.20	0.32	3.19
75	N6^o 51′ 09″ E4^o 50′ 21″	Od OGf 2	4.7	5.0	32.90	0.41	3.85
76	N8^o 36′ 14″ E3^o 00′ 29″	Oy OGm 1	5.4	4.7	45.60	0.51	4.59
77	N8^o 37′ 32″ E3^o 38′ 15″	Oy OGm 2	5.0	4.8	52.70	0.63	5.36
78	N8^o 38′ 00″ E3^o 35′ 40″	Oy OGm 3	4.7	5.0	9.40	0.06	0.83
79	N8^o 36′ 17″ E3^o 18′ 21″	Oy OGm 4	5.3	4.7	29.40	0.34	3.28
80	N7^o 12′ 14″ E4^o 54′ 28″	Od OGm 1	5.0	4.8	37.70	0.45	4.11
81	N8^o 19′ 35″ E4^o 06′ 38″	Oy OGp 1	4.9	4.8	18.70	0.23	2.39
82	N8^o 16′ 03″ E4^o 09′ 29″	Oy OGp 2	5.1	4.8	29.10	0.34	3.33

S/N	Coordinates	Notation	h (cm)	L (cm)	Q (cm^3)	Sat. Hyd. Cond (m/day)	Air Perm. (Ka) x 10^{-12} (m^2)
83	N8^o 12′ 06″ E3^o 24′ 09″	Oy OGp 3	4.7	5.1	32.70	0.41	3.86
84	N8^o 36′ 19″ E3^o 36′ 11″	Oy OGp 4	4.9	5.0	31.40	0.38	3.65
85	N7^o 21′ 08″ E5^o 15′ 16″	Od OGp 1	4.9	5.0	38.50	0.47	4.29
86	N6^o 50′ 12″ E4^o 42′ 27″	Od OGp 2	4.7	5.2	26.90	0.34	3.33
87	N7^o 04′ 15″ E5^o 05′ 41″	Od OGp 3	5.0	4.6	73.61	0.85	6.85
88	N7^o 00′ 47″ E5^o 09′ 39″	Od OGp 4	4.9	4.8	58.15	0.69	5.84
89	N7^o 28′ 15″ E5◦ 13′ 5″	Ek OGp 1	4.7	4.6	23.70	0.28	2.88
90	N8^o 47′ 22″ E3^o 24′ 35″	Oy OGp 5	5.1	4.8	39.50	0.46	4.24
91	N8^o 39′ 28″ E4^o 09′ 57″	Oy OGp 6	5.1	4.7	109.27	1.27	9.36
92	N8^o 30′ 09″ E4^o 03′ 27″	Oy OGp 7	4.8	5.0	34.50	0.43	3.97
93	N8^o 22′ 48″ E4^o 05′ 26″	Oy OGp 8	5.1	4.8	23.70	0.28	2.84
94	N7^o 12′ 40″ E4^o 33′ 00″	Os OGp 1	4.8	4.9	20.10	0.25	2.57

S/N	Coordinates	Notation	h (cm)	L (cm)	Q (cm^3)	Sat. Hyd. Cond (m/day)	Air Perm. (Ka) x 10^{-12} (m^2)
95	N7^o 05′ 52″ E4^o 30′ 32″	Os OGp 2	5.0	4.7	32.99	0.39	3.68
96	N6^o 51′ 45″ E4^o 08′ 31″	Og OGp 1	5.1	4.8	28.30	0.33	3.26
97	N7^o 56′ 23″ E3^o 15′ 45″	Oy OGb 1	5.3	4.7	42.70	0.49	4.39
98	N7^o 21′ 19″ E4^o 10′ 23″	Os P 1	4.9	5.0	72.30	0.89	7.05
99	N7^o 20′ 01″ E4^o 12′ 27″	Os P 2	4.7	4.9	52.30	0.65	5.49
100	N7^o 10′ 23″ E4^o 16′ 15″	Os P 3	5.2	4.6	45.90	0.52	4.65
101	N7^o 48′ 24″ E4^o 32′ 57″	Os P 4	4.8	4.7	39.50	0.47	4.31
102	N7^o 31′ 43″ E2^o 51′ 35″	Og OGGm 1	4.9	4.8	102.80	1.23	9.14
103	N8^o 00′ 57″ E5^o 00′ 09″	Os Qs 1	4.8	5.0	30.40	0.38	3.59
104	N7^o 24′ 26″ E4^o 52′ 52″	Os Qs 2	5.2	4.7	23.20	0.27	2.74
105	N7^o 43′ 56″ E4^o 59′ 29″	Ek Qs 1	5.0	4.7	38.10	0.45	4.12
106	N7^o 30′ 06″ E4^o 56′ 57″	Ek Qs 2	5.2	4.6	45.30	0.52	4.59

S/N	Coordinates	Notation	h (cm)	L (cm)	Q (cm^3)	Sat. Hyd. Cond (m/day)	Air Perm. (Ka) x 10^{-12} (m^2)
107	N7^o 46′ 34″ E4^o 28′ 15″	Os St 1	4.9	4.7	62.30	0.74	6.11
108	N7^o 12′ 19″ E4^o 27′ 18″	Os St 2	5.2	4.8	15.40	0.13	1.54
109	N7^o 26′ 35″ E4^o 27′ 21″	Os St 3	5.0	4.7	14.00	0.12	1.43
110	N7^o 32′ 57″ E4^o 28′ 00″	Os St 4	5.2	4.6	11.96	0.04	0.59
111	N7^o 42′ 05″ E4^o 38′ 41″	Os St 5	4.9	5.0	11.30	0.09	1.25
112	N7^o 42′ 16″ E4^o 33′ 41″	Os St 6	4.7	5.2	12.90	0.16	1.87
113	N7^o 35′ 13″ E4^o 27′ 12″	Os St 7	5.1	4.7	10.80	0.13	1.51
114	N6^o 55′ 28″ E3^o 09′ 02″	Og Fshl 1	4.7	5.2	52.52	0.67	5.65
115	N6^o 55′ 06″ E2^o 54′ 45″	Og Fshl 2	4.9	4.7	69.30	0.82	6.65
116	N6^o 51′ 08″ E3^o 23′ 48″	Og Fshl 3	5.1	4.9	50.96	0.61	5.22
117	N6^o 48′ 54″ E3^o 54′ 28″	Og Fshl 4	4.6	5.2	17.60	0.23	2.41
118	N7^o 05′ 19″ E2^o 44′ 54″	Og Fshl 5	5.0	4.8	28.50	0.34	3.29

S/N	Coordinates	Notation	h (cm)	L (cm)	Q (cm^3)	Sat. Hyd. Cond (m/day)	Air Perm. (Ka) x 10^{-12} (m^2)
119	N6^o 55′ 38″ E2^o 54′ 27″	Og Fshl 6	4.7	5.2	19.30	0.25	2.57
120	N6^o 46′ 08″ E3^o 20′ 17″	Og Fshl 7	4.8	5.1	37.00	0.46	4.23
121	N7^o 12′ 34″ E3^o 00′ 14″	Og Fshl 8	4.7	5.0	37.90	0.47	4.31
122	N7^o 11′ 05″ E3^o 06′ 26″	Og Asl 1	5.0	4.8	13.90	0.12	1.44
123	N7^o 05′ 58″ E3^o 10′ 57″	Og Asl 2	4.6	5.2	33.90	0.44	4.04
124	N7^o 00′ 19″ E3^o 28′ 52″	Og Asl 3	4.9	4.7	47.60	0.56	4.95
125	N6^o 54′ 06″ E3^o 41′ 36″	Og Asl 4	5.1	4.9	39.90	0.47	4.31
126	N6^o 45′ 26″ E3^o 59′ 20″	Og Asl 5	4.7	5.1	40.90	0.52	4.61
127	N6^o 48′ 42″ E3^o 42′ 18″	Og Asl 6	4.9	4.7	40.30	0.48	4.34
128	N6^o 53′ 45″ E3^o 32′ 59″	Og Asl 8	4.8	5.1	33.50	0.42	3.90

S/N	Coordinates	Notation	h (cm)	L (cm)	Q (cm^3)	Sat. Hyd. Cond (m/day)	Air Perm. (Ka) x 10^{-12} (m^2)
129	N8^o 31′ 42″ E3^o 18′ 45″	Oy Opg 2	5.1	4.9	20.80	0.25	2.58
130	N8^o 49′ 38″ E3^o 45′ 48″	Oy Opg 1	5.2	4.7	21.90	0.25	2.62
131	N6^o 19′ 31″ E4^o 50′ 02″	Od Rnst 1	4.8	5.1	13.10	0.07	0.94
132	N6^o 27′ 29″ E4^o 37′ 53″	Od Rnst 2	4.9	5.0	9.30	0.05	0.70
133	N6^o 38′ 05″ E3^o 17′ 01″	Lag Rnst 1	4.9	4.7	3.40	0.08	1.10
134	N6^o 38′ 36″ E3^o 33′ 23″	Lag Rnst 2	5.0	4.7	550.20	13.45	60.06
135	N6^o 37′ 56″ E3^o 39′ 05″	Lag Rnst 3	5.1	4.8	493.20	12.07	55.14
136	N6^o 30′ 29″ E3^o 48′ 02″	Lag Rnst 4	4.8	4.7	808.00	20.17	82.63
137	N6^o 45′ 38″ E2^o 22′ 52″	Og Rnst 1	4.9	5.1	74.80	1.93	12.99
138	N6^o 36′ 06″ E2^o 28′ 17″	Og Rnst 2	4.7	5.0	87.80	2.28	14.86
139	N6^o 38′ 03″ E3^o 08′ 14″	Og Rnst 3	4.8	4.9	49.40	1.26	9.29

S/N	Coordinates	Notation	h (cm)	L (cm)	Q (cm^3)	Sat. Hyd. Cond (m/day)	Air Perm. (Ka) x 10^{-12} (m^2)
140	N7^o 44′ 28″ E4^o 24′ 10″	Os OGCh 1	4.6	5.1	54.05	0.69	5.78
141	N7^o 43′ 54″ E4^o 21′ 08″	Os OGCh 2	4.8	4.7	74.87	0.89	7.12
142	N6^o 36′ 13″ E3^o 45′ 07″	Lag Csd 1	5.0	4.8	447.30	11.06	51.47
143	N6^o 27′ 47″ E2^o 26′ 48″	Lag Csd 2	5.1	4.8	738.90	18.08	75.79
144	N6^o 29′ 06″ E3^o 15′ 28″	Lag Csd 3	4.9	4.7	871.80	21.54	87.00
145	N6^o 30′ 19″ E3^o 23′ 34″	Lag Csd 4	4.8	4.9	758.40	19.33	79.91
146	N6^o 25′ 24″ E3^o 24′ 32″	Lag Csd 5	4.7	5.1	696.20	18.28	76.48
147	N6^o 39′ 19″ E3^o 47′ 24″	Lag Issh 1	4.6	4.9	386.10	10.05	47.74
148	N6^o 36′ 11″ E3^o 54′ 37″	Lag Issh 2	4.9	4.8	562.30	14.04	62.12
149	N6^o 27′ 15″ E4^o 03′ 38″	Lag Issh 3	5.0	4.8	771.70	19.07	79.06
150	N6^o 39′ 22″ E4^o 02′ 19″	Lag Issh 4	4.9	4.7	609.80	15.07	65.66

Appendix 1: Table 1A3: Geogenic Radon Potential (GRP) in 150 Sites over different Bedrocks in Southwest Nigeria

S/N	Coordinates ″	Notation	Geology	Air Perm. x 10^{-12} (m^2)	Radon Conc. (kBq/m^3)	GRP
1	N8^o 09′ 02″ E4^o 15′ 09″	OyM1	Migmatite	4.93	29.09	22.25
2	N8^o 20′ 55″ E4^o 11′ 25″	OyM2	Migmatite	5.17	2.16	1.68
3	N8^o 15′ 10″ E4^o 21′ 19″	OyM3	Migmatite	3.87	23.10	16.36
4	N7^o 28′ 10″ E3^o 44′ 49″	OyM4	Migmatite	4.45	2.26	1.68
5	N7^o 22′ 38″ E3^o 53′ 22″	OyM5	Migmatite	2.53	3.46	2.17
6	N7^o 53′ 02″ E4^o 14′ 28″	OsM1	Migmatite	4.38	3.26	2.40
7	N7^o 52′ 12″ E4^o 22′ 18″	OsM2	Migmatite	3.96	4.12	2.94
8	N7^o 15′ 01″ E3^o 39′ 22″	OgM1	Migmatite	3.28	2.43	1.63
9	N7^o 10′ 09″ E3^o 25′ 16″	OgM2	Migmatite	4.32	11.49	8.42
10	N6^o 56′ 32″ E3^o 55′ 17″	OgM3	Migmatite	3.51	3.34	2.29
11	N7^o 03′ 28″ E4^o 51′ 19″	OdM1	Migmatite	4.23	3.87	2.82
12	N7^o 18′ 19″ E5^o 08′ 23″	OdM2	Migmatite	10.41	35.02	35.64

S/N	Coordinates	Notation	Geology	Air Perm. x 10^{-12} (m^2)	Radon Conc. (kBq/m^3)	GRP
13	N7^o 16′ 25″ E5^o 30′ 07″	OdM3	Migmatite	1.54	23.48	12.95
14	N6^o 42′ 21″ E4^o 54′ 07″	OdM4	Migmatite	1.79	16.62	9.52
15	N7^o 35′ 42″ E5^o 12′ 15″	Ek M 1	Migmatite	12.45	2.89	3.19
16	N7^o 42′ 12″ E5^o 04′ 59″	Ek M 2	Migmatite	4.28	31.89	23.31
17	N7^o 36′ 35″ E5^o 24′ 27″	Ek M 3	Migmatite	4.80	3.49	2.65
18	N7^o 20′ 18″ E5^o 26′ 07″	Ek M 4	Migmatite	3.61	2.77	1.92
19	N7^o 27′ 28″ E5^o 33′ 19″	Ek M 5	Migmatite	3.73	3.53	2.47
20	N7^o 45′ 03″ E5^o 18′ 14″	Ek M 6	Migmatite	3.50	4.17	2.87
21	N7^o 41′ 29″ E5^o 24′ 21″	Ek M 7	Migmatite	3.98	3.49	2.49
22	N7^o 37′ 18″ E5^o 31′ 13″	Ek M 8	Migmatite	3.86	3.14	2.22
23	N7^o 34′ 18″ E5^o 09′ 33″	Ek M 9	Migmatite	3.89	4.55	3.23
24	N8^o 55′ 33″ E4^o 01′ 54″	Oy gg 1	Granite Gneiss	7.23	40.42	35.42

S/N	Coordinates	Notation	Geology	Air Perm. x 10^{-12} (m^2)	Radon Conc. (kBq/m^3)	GRP
25	N8^o 30′ 19″ E3^o 06′ 08″	Oy gg 2	Granite Gneiss	5.85	43.26	35.09
26	N8^o 45′ 09″ E4^o 06′ 02″	Oy gg 3	Granite Gneiss	6.33	44.89	37.46
27	N8^o 08′ 28″ E3^o 51′ 45″	Oy gg 4	Granite Gneiss	4.15	39.74	28.76
28	N8^o 47′ 09″ E4^o 07′ 23″	Oy gg 5	Granite Gneiss	6.47	41.96	35.28
29	N7^o 18′ 08″ E4^o 27′ 17″	Os gg 1	Granite Gneiss	3.35	11.43	7.75
30	N7^o 24′ 44″ E4^o 30′ 53″	Os gg 2	Granite Gneiss	3.87	9.65	6.83
31	N8^o 00′ 03″ E4^o 33′ 27″	Os gg 3	Granite Gneiss	6.41	42.06	35.25
32	N7^o 15′ 22″ E4^o 40′ 56″	Os gg 4	Granite Gneiss	3.12	8.99	5.98
33	N7^o 26′ 09″ E4^o 50′ 42″	Os gg 5	Granite Gneiss	2.81	13.48	8.69
34	N7^o 04′ 29″ E5^o 20′ 31″	Od gg 1	Granite Gneiss	2.31	18.74	11.46
35	N7^o 54′ 21″ E5^o 33′ 28″	Ek gg 1	Granite Gneiss	3.05	8.49	5.60
36	N8^o 38′ 50″ E3^o 22′ 27″	Oy Sq 1	Quartz Syenite	4.09	16.86	12.16

S/N	Coordinates	Notation	Geology	Air Perm. x 10^{-12} (m^2)	Radon Conc. (kBq/m^3)	GRP
37	N9^o 04′ 54″ E3^o 53′ 24″	Oy Sq 2	Quartz Syenite	3.05	34.54	22.79
38	N8^o 50′ 55″ E4^o 04′ 59″	Oy Sq 3	Quartz Syenite	10.32	35.73	36.23
39	N8^o 44′ 05″ E3^o 43′ 21″	Oy Gb 1	Banded Gneiss	4.32	5.82	4.26
40	N8^o 09′ 24″ E3^o 33′ 18″	Oy Gb 2	Banded Gneiss	5.49	8.43	6.69
41	N7^o 24′ 56″ E3^o 10′ 48″	Oy Gb 3	Banded Gneiss	5.01	7.84	6.03
42	N8^o 18′ 31″ E2^o 48′ 16″	Oy Gb 4	Banded Gneiss	6.02	9.43	7.72
43	N7^o 36′ 28″ E4^o 44′ 42″	Os Gb 1	Banded Gneiss	7.04	10.37	9.00
44	N7^o 35′ 13″ E4^o 23′ 12″	Os Gb 2	Banded Gneiss	3.59	7.36	5.09
45	N7^o 48′ 12″ E4^o 50′ 10″	Os Gb 3	Banded Gneiss	3.93	6.44	4.58
46	N8^o 00′ 29″ E4^o 40′ 57″	Os Gb 4	Banded Gneiss	3.72	5.37	3.75
47	N6^o 54′ 13″ E4^o 48′ 07″	Od Gb 1	Banded Gneiss	3.77	4.78	3.36
48	N7^o 14′ 41″ E4^o 47′ 30″	Od Gb 2	Banded Gneiss	3.50	2.76	1.89

S/N	Coordinates	Notation	Geology	Air Perm. x 10^{-12} (m^2)	Radon Conc. (kBq/m^3)	GRP
49	N8^o 00′ 52″ E5^o 05′ 10″	Ek Gb 1	Banded Gneiss	3.22	5.73	3.84
50	N8^o 01′ 24″ E3^o 20′ 49″	Oy Su 1	Undifferentiated schist	4.27	3.25	2.37
51	N8^o 01′ 04″ E3^o 32′ 57″	Oy Su 2	Undifferentiated schist	3.28	2.16	1.46
52	N8^o 32′ 42″ E3^o 38′ 18″	Oy Su 3	Undifferentiated schist	3.86	2.45	1.73
53	N7^o 30′ 22″ E4^o 00′ 48″	Oy Su 4	Undifferentiated schist	4.79	1.87	1.41
54	N7^o 51′ 02″ E3^o 09′ 19″	Oy Su 5	Undifferentiated schist	5.29	4.25	3.33
55	N7^o 42′ 27″ E4^o 47′ 08″	Os Su 1	Undifferentiated schist	4.24	2.47	1.79
56	N7^o 30′ 30″ E4^o 34′ 19″	Os Su 2	Undifferentiated schist	4.53	1.96	1.46
57	N6^o 57′ 32″ E4^o 03′ 49″	Og Su 1	Undifferentiated schist	4.79	4.13	3.13
58	N7^o 00′ 35″ E4^o 07′ 58″	Og Su 2	Undifferentiated schist	3.87	3.34	2.36
59	N7^o 00′ 27″ E4^o 00′ 23″	Og Su 3	Undifferentiated schist	3.59	2.49	1.73
60	N6^o 57′ 47″ E3^o 58′ 32″	Og Su 4	Undifferentiated schist	4.23	3.54	2.58

S/N	Coordinates	Notation	Geology	Air Perm. x 10^{-12} (m^2)	Radon Conc. (kBq/m^3)	GRP
61	N6° 42′ 19″ E4° 15′ 02″	Og Su 5	Undifferetiated Schist	2.82	3.04	1.96
62	N7° 08′ 39″ E5° 41′ 07″	Od Su 1	Undifferentiated schist	1.17	4.96	2.57
63	N7° 40′ 45″ E5° 03′ 17″	Ek Su 1	Undifferentiated schist	10.03	13.76	13.78
64	N8° 21′ 04″ E3° 33′ 18″	Oy Sa 1	Amphibole Schist & Amphibolite	1.67	13.56	7.64
65	N8° 06′ 22″ E3° 27′ 18″	Oy Sa 2	Amphibole Schist & Amphibolite	0.29	10.75	5.82
66	N8° 08′ 17″ E3° 21′ 45″	Oy Sa 3	Amphibole Schist & Amphibolite	1.42	10.75	5.81
67	N7° 26′ 34″ E3° 16′ 39″	Oy Sa 4	Amphibole Schist & Amphibolite	0.68	8.92	4.12
68	N8° 18′ 36″ E4° 12′ 00″	Oy OGf 1	Fine-grained Biotite granite	9.91	2.31	2.30
69	N8° 18′ 05″ E4° 18′ 03″	Oy OGf 2	Fine-grained Biotite granite	2.56	3.46	2.17
70	N8° 11′ 12″ E4° 06′ 35″	Oy OGf 3	Fine-grained Biotite granite	3.28	2.85	1.92
71	N7° 29′ 58″ E4° 15′ 55″	Os OGf 1	Fine-grained Biotite granite	2.80	3.22	2.08
72	N7° 32′ 52″ E4° 12′ 29″	Os OGf 2	Fine-grained Biotite granite	8.64	7.79	7.32

S/N	Coordinates	Notation	Geology	Air Perm. x 10^{-12} (m^2)	Radon Conc. (kBq/m^3)	GRP
73	N7° 03′ 13″ E4° 17′ 22″	Og OGf 1	Fine-grained Biotite granite	2.67	3.75	2.38
74	N6° 45′ 06″ E4° 46′ 19″	Od OGf 1	Fine-grained Biotite granite	3.19	3.59	2.39
75	N6° 51′ 09″ E4° 50′ 21″	Od OGf 2	Fine-grained Biotite granite	3.85	4.29	3.03
76	N8° 36′ 14″ E3° 00′ 29″	Oy OGm 1	M-CG Biotite & biotite hornblende granite	4.59	4.36	3.26
77	N8° 37′ 32″ E3° 38′ 15″	Oy OGm 2	M-CG Biotite & biotite hornblende granite	5.36	1.32	1.04
78	N8° 38′ 00″ E3° 35′ 40″	Oy OGm 3	M-CG Biotite & biotite hornblende granite	0.83	1.14	0.55
79	N8° 36′ 17″ E3° 18′ 21″	Oy OGm 4	M-CG Biotite & biotite hornblende granite	3.28	5.94	3.99
80	N7° 12′ 14″ E4° 54′ 28″	Od OGm 1	M-CG biotite & biotite hornblende granite	4.11	3.12	2.25
81	N8° 19′ 35″ E4° 06′ 38″	Oy OGp 1	CG Porphyritic biotite & biotite hornblende	2.39	3.56	2.19
82	N8° 16′ 03″ E4° 09′ 29″	Oy OGp 2	CG Porphyritic biotite & biotite hornblende	3.33	24.46	16.55
83	N8° 12′ 06″ E3° 24′ 09″	Oy OGp 3	CG Porphyritic biotite & biotite hornblende	3.86	5.49	3.89
84	N8° 36′ 19″ E3° 36′ 11″	Oy OGp 4	CG Porphyritic biotite & biotite hornblende	3.65	7.15	4.97

S/N	Coordinates	Notation	Geology	Air Perm. x 10^{-12} (m^2)	Radon Conc. (kBq/m^3)	GRP
85	N7^o 21′ 08″ E5^o 15′ 16″	Od OGp 1	CG Porphyritic biotite & biotite hornblende	4.29	23.67	17.31
86	N6^o 50′ 12″ E4^o 42′ 27″	Od OGp 2	CG Porphyritic biotite & biotite hornblende	3.33	2.88	1.95
87	N7^o 04′ 15″ E5^o 05′ 41″	Od OGp 3	CG Porphyritic biotite & biotite hornblende	6.85	45.62	39.19
88	N7^o 00′ 47″ E5^o 09′ 39″	Od OGp 4	CG Porphyritic biotite & biotite hornblende	5.84	47.59	38.58
89	N7^o 28′ 15″ E5^o 13′ 25″	Ek OGp 1	CG Porphyritic biotite & biotite hornblende	2.88	26.94	17.49
90	N8^o 47′ 22″ E3^o 24′ 35″	Oy OGp 5	CG Porphyritic biotite & biotite hornblende	4.24	5.67	4.13
91	N8^o 39′ 28″ E4^o 09′ 57″	Oy OGp 6	CG Porphyritic biotite & biotite hornblende	9.36	32.49	31.58
92	N8^o 30′ 09″ E4^o 03′ 27″	Oy OGp 7	CG Porphyritic biotite & biotite hornblende	3.97	3.47	2.47
93	N8^o 22′ 48″ E4^o 05′ 26″	Oy OGp 8	CG Porphyritic biotite & biotite hornblende	2.84	2.77	1.79
94	N7^o 12′ 40″ E4^o 33′ 00″	Os OGp 1	CG Porphyritic biotite & biotite hornblende	2.57	36.64	23.05
95	N7^o 05′ 52″ E4^o 30′ 32″	Os OGp 2	CG Porphyritic biotite & biotite hornblende	3.68	3.27	2.28
96	N6^o 51′ 45″ E4^o 08′ 31″	Og OGp 1	CG Porphyritic biotite & biotite hornblende	3.26	33.78	22.71

S/N	Coordinates	Notation	Geology	Air Perm. x 10^{-12} (m^2)	Radon Conc. (kBq/m^3)	GRP
97	N7° 56′ 23″ E3° 15′ 45″	Oy OGp 9	CG Porphyritic biotite & biotite hornblende	4.39	2.11	1.56
98	N7° 21′ 19″ E4° 10′ 23″	Os P 1	Pegmatite	7.05	4.12	3.57
99	N7° 20′ 01″ E4° 12′ 27″	Os P 2	Pegmatite	5.49	2.86	2.27
100	N7° 10′ 23″ E4° 16′ 15″	Os P 3	Pegmatite	4.65	5.42	4.06
101	N7° 48′ 24″ E4° 32′ 57″	Os P 4	Pegmatite	4.31	6.14	4.49
102	N7° 31′ 43″ E2° 51′ 35″	Og OGGm 1	Muscovite tourmaline granite gneiss	9.14	3.64	3.50
103	N8° 00′ 57″ E5° 00′ 09″	Os Qs 1	Flaggy quartzite & quartzite schist	3.59	6.37	4.41
104	N7° 24′ 26″ E4° 52′ 52″	Os Qs 2	Flaggy quartzite & quartzite schist	2.74	7.05	4.51
105	N7° 43′ 56″ E4° 59′ 29″	Ek Qs 1	Flaggy quartzite & quartzite schist	4.12	7.36	5.31
106	N7° 30′ 06″ E4° 56′ 07″	Ek Qs 2	Flaggy quartzite & quartzite schist	4.59	7.81	5.84
107	N7° 46′ 34″ E4° 28′ 15″	Os St 1	Talc Schist	6.11	7.83	6.45
108	N7° 12′ 19″ E4° 27′ 18″	Os St 2	Talc Schist	1.54	0.28	0.15

S/N	Coordinates	Notation	Geology	Air Perm. x 10^{-12} (m^2)	Radon Conc. (kBq/m^3)	GRP
109	N7° 26′ 35″ E4° 27′ 21″	Os St 3	Talc Schist	1.43	6.34	3.44
110	N7° 32′ 57″ E4° 28′ 00″	Os St 4	Talc Schist	0.59	4.74	2.12
111	N7° 42′ 05″ E4° 38′ 41″	Os St 5	Talc Schist	1.25	0.41	0.22
112	N7° 42′ 16″ E4° 33′ 41″	Os St 6	Talc Schist	1.87	5.84	3.38
113	N7° 35′ 13″ E4° 27′ 12″	Os St 7	Talc Schist	1.51	0.66	0.37
114	N6° 55′ 28″ E3° 09′ 02″	Og Fshl 1	Shale, Limestone & Siltstone	5.65	43.77	36.07
115	N6° 55′ 06″ E2° 54′ 45″	Og Fshl 2	Shale, Limestone & Siltstone	6.65	21.85	18.56
116	N6° 51′ 08″ E3° 23′ 48″	Og Fshl 3	Shale, Limestone & Siltstone	5.22	45.88	35.79
117	N6° 48′ 54″ E3° 54′ 28″	Og Fshl 4	Shale, Limestone & Siltstone	2.41	13.43	8.29
118	N7° 05′ 19″ E2° 44′ 54″	Og Fshl 5	Shale, Limestone & Siltstone	3.29	7.49	5.06
119	N6° 55′ 38″ E2° 54′ 27″	Og Fshl 6	Shale, Limestone & Siltstone	2.57	9.73	6.12
120	N6° 46′ 08″ E3° 20′ 17″	Og Fshl 7	Shale, Limestone & Siltstone	4.23	7.42	5.39

S/N	Coordinates	Notation	Geology	Air Perm. x 10^{-12} (m^2)	Radon Conc. (kBq/m^3)	GRP
121	N7° 12′ 34″ E3° 00′ 14″	Og Fshl 8	Shale, Limestone & Siltstone	4.31	9.77	7.16
122	N7° 11′ 05″ E3° 06′ 26″	Og Asl 1	Sandstone and Limestone	1.44	3.44	1.87
123	N7° 05′ 58″ E3° 10′ 57″	Og Asl 2	Sandstone and Limestone	4.04	4.25	3.05
124	N7° 00′ 19″ E3° 28′ 52″	Og Asl 3	Sandstone and Limestone	4.95	2.45	1.87
125	N6° 54′ 06″ E3° 41′ 36″	Og Asl 4	Sandstone and Limestone	4.31	4.89	3.58
126	N6° 45′ 26″ E3° 59′ 20″	Og Asl 5	Sandstone and Limestone	4.61	2.79	2.09
127	N6° 48′ 42″ E3° 42′ 18″	Og Asl 6	Sandstone and Limestone	4.34	1.89	1.39
128	N6° 53′ 45″ E3° 32′ 59″	Og Asl 7	Sandstone and Limestone	3.90	3.37	2.39
129	N8° 49′ 38″ E3° 45′ 48″	Oy Opg 1	Porphyroblastic gneiss	2.62	2.89	1.83
130	N8° 31′ 42″ E3° 18′ 45″	Oy Opg 2	Porphyroblastic gneiss	2.58	6.25	3.93
131	N6° 19′ 31″ E4° 50′ 02″	Od Bnst 1	Sand and Clay	0.94	0.76	0.37
132	N6° 27′ 29″ E4° 37′ 53″	Od Bnst 2	Sand and Clay	0.70	0.94	0.44

S/N	Coordinates	Notation	Geology	Air Perm. x 10^{-12} (m^2)	Radon Conc. (kBq/m^3)	GRP
133	N6° 38′ 05″ E3° 17′ 01″	Lag Bnst 1	Sand and Clay	1.10	0.33	0.17
134	N6° 38′ 36″ E3° 33′ 23″	Lag Bnst 2	Sand and Clay	60.06	0.91	4.09
135	N6° 37′ 56″ E3° 39′ 05″	Lag Bnst 3	Sand and Clay	55.14	2.64	10.22
136	N6° 30′ 29″ E3° 48′ 42″	Lag Bnst 4	Sand and Clay	82.63	0.84	10.13
137	N6° 45′ 38″ E2° 22′ 52″	Og Bnst 1	Sand and Clay	12.99	11.70	13.21
138	N6° 36′ 26″ E2° 28′ 17″	Og Bnst 2	Sand and Clay	14.86	12.78	15.44
139	N6° 38′ 03″ E3° 08′ 14″	Og Bnst 3	Sand and Clay	9.29	10.84	10.51
140	N7° 44′ 28″ E4° 24′ 10″	Os OGCh 1	Charnokite & Charnokitic rock	5.78	44.15	35.67
141	N7° 43′ 54″ E4° 21′ 08″	Os OGCh 2	Charnokite & Charnokitic rock	7.12	42.14	36.73
142	N6° 36′ 13″ E3° 45′ 07″	Lag Csd 1	Sand and Mash	51.47	0.34	1.17
143	N6° 27′ 47″ E2° 26′ 48″	Lag Csd 2	Sand and Mash	75.79	0.29	2.42
144	N6° 29′ 06″ E3° 15′ 28″	Lag Csd 3	Sand and Mash	87.00	0.33	5.52

S/N	Coordinates	Notation	Geology	Air Perm. x 10^{-12} (m^2)	Radon Conc. (kBq/m^3)	GRP
145	N6^o 30′ 19″ E3^o 23′ 34″	Lag Csd 4	Sand and Mash	79.91	0.977	10.03
146	N6^o 25′ 24″ E3^o 24′ 32″	Lag Csd 5	Sand and Mash	76.48	1.55	13.28
147	N6^o 39′ 19″ E3^o 47′ 24″	Lag Issh 1	Sand, Clay and Shale	47.74	0.69	2.13
148	N6^o 36′ 11″ E3^o 54′ 37″	Lag Issh 2	Sand, Clay and Shale	62.12	1.10	5.32
149	N6^o 27′ 15″ E4^o 03′ 38″	Lag Issh 3	Sand, Clay and Shale	79.06	1.69	16.65
150	N6^o 39′ 22″ E4^o 02′ 19″	Lag Issh 4	Sand, Clay and Shale	65.66	1.73	9.48

Appendix 1: Table 1A4: Values of $E_{I,i,j}$ and $F_{I,i,j}$ obtained from ANN Modelling of Soil-gas Radon Concentration

SN	E1	E2	E3	E4	E5	E6	E7	E8	F1	F2	F3	F4	F5	F6	F7	F8
1.	-4.19	-13.33	10.99	32.66	-29.36	-0.18	-0.76	17.10	-0.99	-1.00	1.00	1.00	-1.00	-0.18	-0.64	1.00
2.	-3.81	-13.27	11.48	32.42	-29.14	-0.11	-0.70	17.18	-0.99	-1.00	1.00	1.00	-1.00	-0.11	-0.61	1.00
3.	-5.88	-13.61	8.86	33.75	-30.35	-0.49	-0.99	16.76	-0.99	-1.00	1.00	1.00	-1.00	-0.46	-0.76	1.00
4.	-4.96	-13.46	10.02	33.16	-29.81	-0.32	-0.86	16.95	-0.99	-1.00	1.00	1.00	-1.00	-0.31	-0.69	1.00
5.	-8.04	-13.95	6.14	35.13	-31.61	-0.88	-1.28	16.33	-1.00	-1.00	0.99	1.00	-1.00	-0.71	-0.86	1.00
6.	-5.08	-13.48	9.87	33.23	-29.88	-0.35	-0.88	16.92	-0.99	-1.00	1.00	1.00	-1.00	-0.33	-0.71	1.00
7.	-5.75	-13.58	9.03	33.66	-30.27	-0.47	-0.97	16.79	-0.99	-1.00	1.00	1.00	-1.00	-0.44	-0.75	1.00
8.	-6.84	-13.76	7.65	34.36	-30.91	-0.67	-1.12	16.57	-1.00	-1.00	1.00	1.00	-1.00	-0.58	-0.81	1.00
9.	-5.17	-13.49	9.76	33.29	-29.93	-0.36	-0.89	16.91	-0.99	-1.00	1.00	1.00	-1.00	-0.35	-0.71	1.00
10.	-6.47	-13.69	8.12	34.12	-30.69	-0.59	-1.07	16.65	-1.00	-1.00	1.00	1.00	-1.00	-0.53	-0.79	1.00
11.	-5.32	-13.51	9.57	33.39	-30.02	-0.39	-0.91	16.87	-0.99	-1.00	1.00	1.00	-1.00	-0.37	-0.72	1.00
12.	-5.02	-13.47	9.94	33.19	-29.85	-0.34	-0.87	16.93	-0.99	-1.00	1.00	1.00	-1.00	-0.32	-0.70	1.00
13.	-9.63	-14.21	4.13	36.15	-32.54	-1.17	-1.51	16.01	-1.00	-1.00	0.99	1.00	-1.00	-0.83	-0.91	1.00
14.	-9.22	-14.14	4.65	35.89	-32.30	-1.09	-1.45	16.09	-1.00	-1.00	0.99	1.00	-1.00	-0.79	-0.89	1.00
15.	-4.96	-13.46	10.02	33.16	-29.81	-0.32	-0.86	16.95	-0.99	-1.00	1.00	1.00	-1.00	-0.31	-0.69	1.00

SN	E1	E2	E3	E4	E5	E6	E7	E8	F1	F2	F3	F4	F5	F6	F7	F8
16.	-5.23	-13.49	9.68	33.33	-29.97	-0.37	-0.89	16.89	-0.99	-1.00	1.00	1.00	-1.00	-0.36	-0.72	1.00
17.	-4.39	-13.37	10.74	32.79	-29.48	-0.22	-0.79	17.06	-0.99	-1.00	1.00	1.00	-1.00	-0.22	-0.66	1.00
18.	-6.31	-13.67	8.32	34.02	-30.60	-0.56	-1.05	16.68	-0.99	-1.00	1.00	1.00	-1.00	-0.52	-0.78	1.00
19.	-6.12	-13.64	8.56	33.89	-30.49	-0.53	-1.02	16.72	-0.99	-1.00	1.00	1.00	-1.00	-0.49	-0.77	1.00
20.	-6.48	-13.70	8.10	34.13	-30.70	-0.59	-1.07	16.64	-1.00	-1.00	1.00	1.00	-1.00	-0.54	-0.79	1.00
21.	-5.72	-13.58	9.07	33.64	-30.25	-0.46	-0.96	16.79	-0.99	-1.00	1.00	1.00	-1.00	-0.43	-0.75	1.00
22.	-5.91	-13.61	8.83	33.76	-30.36	-0.49	-0.99	16.76	-0.99	-1.00	1.00	1.00	-1.00	-0.46	-0.76	1.00
23.	-5.86	-13.60	8.89	33.73	-30.34	-0.49	-0.99	16.77	-0.99	-1.00	1.00	1.00	-1.00	-0.45	-0.76	1.00
24.	-0.54	-12.64	15.39	27.71	-24.87	-0.42	-0.77	15.52	-0.49	-1.00	1.00	1.00	-1.00	-0.39	-0.65	1.00
25.	-2.74	-12.99	12.61	29.12	-26.16	-0.82	-1.07	15.07	-0.99	-1.00	1.00	1.00	-1.00	-0.67	-0.79	1.00
26.	-1.97	-12.87	13.58	28.62	-25.71	-0.68	-0.97	15.23	-0.96	-1.00	1.00	1.00	-1.00	-0.59	-0.75	1.00
27.	-5.47	-13.43	9.17	30.87	-27.76	-1.31	-1.45	14.53	-0.99	-1.00	1.00	1.00	-1.00	-0.86	-0.89	1.00
28.	-1.75	-12.84	13.86	28.48	-25.58	-0.64	-0.94	15.27	-0.94	-1.00	1.00	1.00	-1.00	-0.56	-0.73	1.00
29.	-6.76	-13.64	7.54	31.69	-28.51	-1.55	-1.63	14.27	-1.00	-1.00	0.99	1.00	-1.00	-0.91	-0.93	1.00
30.	-5.92	-13.51	8.59	31.16	-28.02	-1.39	-1.52	14.44	-0.99	-1.00	1.00	1.00	-1.00	-0.88	-0.91	1.00

SN	E1	E2	E3	E4	E5	E6	E7	E8	F1	F2	F3	F4	F5	F6	F7	F8
31.	-1.85	-12.85	13.74	28.55	-25.64	-0.66	-0.95	15.25	-0.95	-1.00	1.00	1.00	-1.00	-0.57	-0.74	1.00
32.	-7.13	-13.70	7.08	31.92	-28.72	-1.61	-1.68	14.19	-1.00	-1.00	0.99	1.00	-1.00	-0.92	-0.93	1.00
33.	-7.63	-13.78	6.44	32.25	-29.02	-1.71	-1.75	14.09	-1.00	-1.00	0.99	1.00	-1.00	-0.94	-0.94	1.00
34.	-8.43	-13.91	5.44	32.76	-29.46	-1.85	-1.86	13.93	-1.00	-1.00	0.99	1.00	-1.00	-0.95	-0.95	1.00
35.	-7.25	-13.72	6.93	32.00	-28.79	-1.64	-1.69	14.17	-1.00	-1.00	0.99	1.00	-1.00	-0.93	-0.94	1.00
36.	-5.60	-13.35	8.79	28.33	-25.48	-2.23	-1.99	12.18	-0.99	-1.00	1.00	1.00	-1.00	-0.98	-0.96	1.00
37.	-7.28	-13.62	6.68	29.40	-26.46	-2.54	-2.22	11.85	-1.00	-1.00	0.99	1.00	-1.00	-0.99	-0.98	1.00
38.	4.39	-11.74	21.41	21.93	-19.64	-0.42	-0.61	14.19	0.99	-1.00	1.00	1.00	-1.00	-0.39	-0.54	1.00
39.	-5.28	-13.19	8.98	25.51	-22.94	-3.07	-2.46	9.93	-0.99	-1.00	1.00	1.00	-1.00	-0.99	-0.98	1.00
40.	-3.39	-12.89	11.37	24.29	-21.84	-2.73	-2.20	10.31	-0.99	-1.00	1.00	1.00	-1.00	-0.99	-0.97	1.00
41.	-4.17	-13.02	10.39	24.79	22.29	-2.87	-2.31	10.15	-0.99	-1.00	1.00	1.00	-1.00	-0.99	-0.98	1.00
42.	-2.55	-12.75	12.43	23.76	-21.34	-2.58	-2.09	10.48	-0.98	-1.00	1.00	1.00	-1.00	-0.98	-0.96	1.00
43.	-0.91	-12.49	14.49	22.71	-20.39	-2.28	-1.86	10.80	-0.72	-1.00	1.00	1.00	-1.00	-0.98	-0.95	1.00
44.	-6.44	-13.38	7.53	26.25	-23.62	-3.28	-2.62	9.69	-0.99	-1.00	0.99	1.00	-1.00	-0.99	-0.99	1.00
45.	-5.90	-13.29	8.21	25.90	-23.30	-3.18	-2.55	9.81	-0.99	-1.00	1.00	1.00	-1.00	-0.99	-0.98	1.00

SN	E1	E2	E3	E4	E5	E6	E7	E8	F1	F2	F3	F4	F5	F6	F7	F8
46.	-6.23	-13.35	7.79	26.12	-23.49	-3.25	-2.59	9.74	-0.99	-1.00	1.00	1.00	-1.00	-0.99	-0.99	1.00
47.	-6.15	-13.33	7.89	26.06	-23.45	-3.23	-2.58	9.75	-0.99	-1.00	1.00	1.00	-1.00	-0.99	-0.98	1.00
48.	-6.58	-13.40	7.34	26.34	-23.70	-3.31	-2.64	9.67	-1.00	-1.00	0.99	1.00	-1.00	-0.99	-0.98	1.00
49.	-7.04	-13.48	6.77	26.63	-23.97	-3.39	-2.71	9.57	-1.00	-1.00	0.99	1.00	-1.00	-0.99	-0.99	1.00
50.	-5.39	-13.11	8.64	22.96	-20.65	-3.99	-2.99	7.59	-0.99	-1.00	1.00	1.00	-1.00	-0.99	-0.99	0.99
51.	-6.97	-13.36	6.64	23.97	-21.58	-4.28	-3.22	7.27	-1.00	-1.00	0.99	1.00	-1.00	-0.99	-0.99	0.99
52.	-6.04	-13.21	7.82	23.37	-21.03	-4.11	-3.09	7.46	-0.99	-1.00	1.00	1.00	-1.00	-0.99	-0.99	1.00
53.	-4.56	-12.97	9.69	22.42	-20.16	-3.84	-2.88	7.76	-0.99	-1.00	1.00	1.00	-1.00	-0.99	-0.99	1.00
54.	-3.75	-12.84	10.71	21.91	-19.69	-3.69	-2.77	7.92	-0.99	-1.00	1.00	1.00	-1.00	-0.99	-0.99	1.00
55.	-5.45	-13.12	8.57	22.99	-20.68	-4.00	-3.00	7.58	-0.99	-1.00	1.00	1.00	-1.00	-0.99	-0.99	0.99
56.	-4.98	-13.04	9.16	22.69	-20.41	-3.92	-2.94	7.67	-0.99	-1.00	1.00	1.00	-1.00	-0.99	-0.99	1.00
57.	-4.54	-12.97	9.71	22.42	-20.16	-3.84	-2.88	7.76	-0.99	-1.00	1.00	1.00	-1.00	-0.99	-0.99	1.00
58.	-6.03	-13.21	7.84	23.37	-21.02	-4.11	-3.08	7.46	-0.99	-1.00	1.00	1.00	-1.00	-0.99	-0.99	0.99
59.	-6.47	-13.28	7.28	23.65	-21.28	-4.19	-3.15	7.37	-1.00	-1.00	0.99	1.00	-1.00	-0.99	-0.99	0.99
60.	-5.46	-13.12	8.56	23.00	-20.69	-4.00	-3.01	7.58	-0.99	-1.00	1.00	1.00	-1.00	-0.99	-0.99	0.99

SN	E1	E2	E3	E4	E5	E6	E7	E8	F1	F2	F3	F4	F5	F6	F7	F8
61.	-7.72	-13.48	5.70	24.45	-22.01	-4.41	-3.32	7.12	-1.00	-1.00	0.99	1.00	-1.00	-0.99	-0.99	0.99
62.	-4.16	-12.91	10.19	22.17	-19.93	-3.77	-2.83	7.84	-0.99	-100	1.00	1.00	-1.00	-0.99	-0.99	1.00
63.	-10.37	-13.91	2.36	26.15	-23.56	-4.89	-3.68	6.59	-1.00	-1.00	0.98	1.00	-1.00	-0.99	-0.99	0.99
64.	-9.59	-13.68	3.13	23.03	-20.75	-5.65	-4.09	4.43	-1.00	-1.00	0.99	1.00	-1.00	-0.99	-0.99	0.99
65.	-10.00	-13.74	2.62	23.29	-20.99	-5.72	-4.15	4.35	-1.00	-1.00	0.99	1.00	-1.00	-0.99	-0.99	0.99
66.	-10.55	-13.83	1.92	23.64	-21.31	-5.82	-4.23	4.24	-1.00	-1.00	0.96	1.00	-1.00	-0.99	-0.99	0.99
67.	-11.18	-13.93	1.12	24.05	-21.68	-5.94	-4.32	4.11	-1.00	-1.00	0.81	1.00	-1.00	-0.99	-0.99	0.99
68.	-4.91	-12.82	8.82	17.42	-15.67	-5.69	-3.97	3.05	-0.99	-1.00	1.00	1.00	-1.00	-0.99	-0.99	0.99
69.	-8.21	-13.35	4.67	19.53	-17.59	-6.29	-4.42	2.39	-1.00	-1.00	0.99	1.00	-1.00	-0.99	-0.99	0.98
70.	-7.06	-13.17	6.12	18.79	-16.92	-6.09	-4.26	2.62	-1.00	-1.00	0.99	1.00	-1.00	-0.99	-0.99	0.99
71.	-7.82	-13.29	5.16	19.28	-17.36	-6.22	-4.37	2.47	-1.00	-1.00	0.99	1.00	-1.00	-0.99	-0.99	0.99
72.	-4.91	-12.82	8.82	17.42	-15.66	-5.69	-3.97	3.05	-0.99	-1.00	1.00	1.00	-1.00	-0.99	-0.99	0.99
73.	-8.04	-13.32	4.88	19.42	-17.49	-6.26	-4.40	2.42	-1.00	-1.00	0.99	1.00	-1.00	-0.99	-0.99	0.98
74.	-7.19	-13.19	5.95	18.87	-16.99	-6.11	-4.28	2.59	-1.00	-1.00	0.99	1.00	-1.00	-0.99	-0.99	0.98
75.	-6.13	-13.02	7.28	18.19	-16.38	-5.92	-4.14	2.81	-0.99	-1.00	0.99	1.00	-1.00	-0.99	-0.99	0.99

SN	E1	E2	E3	E4	E5	E6	E7	E8	F1	F2	F3	F4	F5	F6	F7	F8
76.	-4.98	-12.73	8.53	14.84	-13.35	-6.61	-4.49	0.72	-0.99	-1.00	1.00	1.00	-1.00	-1.00	-0.99	0.62
77.	-3.76	-12.53	10.07	14.06	-12.64	-6.38	-4.33	0.96	-0.99	-1.00	1.00	1.00	-1.00	-0.99	-0.99	0.75
78.	-11.02	-13.69	0.91	18.71	-16.88	-7.70	-5.33	-0.49	-1.00	-1.00	0.72	1.00	-1.00	-1.00	-0.99	-0.45
79.	-7.09	-13.07	5.86	16.19	-14.59	-6.99	-4.79	0.29	-1.00	-1.00	0.99	1.00	-1.00	-1.00	-0.99	0.29
80.	-5.75	-12.85	7.56	15.34	-13.80	-6.75	-4.60	0.56	-0.99	-1.00	0.99	1.00	-1.00	-1.00	-0.99	0.51
81.	-8.55	-13.19	3.82	14.51	-13.08	-8.15	-5.51	-2.31	-1.00	-1.00	0.99	1.00	-1.00	-1.00	-0.99	-0.98
82.	-7.04	-12.95	5.72	13.55	-12.21	-7.88	-5.30	-2.01	-1.00	-1.00	0.99	1.00	-1.00	-1.00	-0.99	-0.96
83.	-6.19	-12.82	6.79	12.99	-11.70	-7.72	-5.18	-1.84	-0.99	-1.00	0.99	1.00	-1.00	-1.00	-0.99	-0.95
84.	-6.53	-12.87	6.37	13.21	-11.90	-7.78	-5.23	-1.91	-1.00	-1.00	0.99	1.00	-1.00	-1.00	-0.99	-0.96
85.	-5.51	-12.71	7.66	12.56	-11.31	-7.59	-5.09	-1.70	-0.99	-1.00	1.00	1.00	-1.00	-1.00	-0.99	-0.94
86.	-7.04	-12.95	5.72	13.54	-12.20	-7.87	-5.30	-2.01	-1.00	-1.00	0.99	1.00	-1.00	-1.00	-0.99	-0.96
87.	-6.20	-12.82	6.78	13.01	-11.71	-7.73	-5.18	-1.84	-0.99	-1.00	0.99	1.00	-1.00	-1.00	-0.99	-0.95
88.	-6.22	-12.82	6.76	13.02	-11.72	-7.73	-5.19	-1.85	-0.99	-1.00	0.99	1.00	-1.00	-1.00	-0.99	-0.95
89.	-7.77	-13.07	4.81	14.01	-12.63	-8.01	-5.40	-2.16	-1.00	-1.00	0.99	1.00	-1.00	-1.00	-0.99	-0.97
90.	-5.59	-12.72	7.55	12.62	-11.36	-7.61	-5.10	-1.72	-0.99	-1.00	0.99	1.00	-1.00	-1.00	-0.99	-0.94

SN	E1	E2	E3	E4	E5	E6	E7	E8	F1	F2	F3	F4	F5	F6	F7	F8
91.	-5.71	-12.74	7.39	12.69	-11.43	-7.64	-5.12	-1.75	-0.99	-1.00	0.99	1.00	-1.00	-1.00	-0.99	-0.94
92.	-6.02	-12.79	7.00	12.89	-11.61	-7.69	-5.16	-1.81	-0.99	-1.00	0.99	1.00	-1.00	-1.00	-0.99	-0.95
93.	-7.84	-13.08	4.72	14.05	-12.67	-8.02	-5.41	-2.17	-1.00	-1.00	0.99	1.00	-1.00	-1.00	-0.99	-0.97
94.	-8.26	-13.15	4.18	14.32	-12.91	-8.09	-5.47	-2.26	-1.00	-1.00	0.99	1.00	-1.00	-1.00	-0.99	-0.98
95.	-6.49	-12.86	6.42	13.19	-11.88	-7.77	-5.22	-1.90	-1.00	-1.00	0.99	1.00	-1.00	-1.00	-0.99	-0.96
96.	-7.16	-12.97	5.56	13.62	-12.28	-7.90	-5.32	-2.04	-1.00	-1.00	0.99	1.00	-1.00	-1.00	-0.99	-0.97
97.	-5.33	-12.68	7.88	12.45	-11.20	-7.57	-5.06	-1.67	-0.99	-1.00	1.00	1.00	-1.00	-1.00	-0.99	-0.93
98.	-1.12	-11.89	12.98	7.13	-6.39	-7.69	-5.00	-3.14	-0.81	-1.00	1.00	0.99	-0.99	-1.00	-0.99	-0.99
99.	-3.59	-12.29	9.85	8.72	-7.84	-8.15	-5.34	-3.64	-0.99	-1.00	1.00	1.00	-1.00	-1.00	-0.99	-0.99
100.	-4.97	-12.52	8.13	9.59	-8.64	-8.39	-5.53	-3.91	-0.99	-1.00	1.00	1.00	-1.00	-1.00	-0.99	-0.99
101.	-5.51	-12.60	7.44	9.95	-8.96	-8.49	-5.61	-4.02	-0.99	-1.00	0.99	1.00	-1.00	-1.00	-0.99	-0.99
102.	-6.71	-12.69	5.72	8.09	-7.30	-9.61	-6.29	-6.58	-1.00	-1.00	0.99	1.00	-1.00	-1.00	-0.99	-1.00
103.	-8.06	-12.91	4.01	8.96	-8.09	-9.86	-6.48	-6.85	-1.00	-1.00	0.99	1.00	-1.00	-1.00	-1.00	-1.00
104.	-5.85	-12.55	6.79	7.55	-6.80	-9.46	-6.17	-6.41	-0.99	-1.00	0.99	0.99	-1.00	-1.00	-0.99	-0.99
105.	-5.08	-12.43	7.78	7.05	-6.35	-9.32	-6.07	-6.25	-0.99	-1.00	1.00	0.99	-0.99	-1.00	-0.99	-0.99

SN	E1	E2	E3	E4	E5	E6	E7	E8	F1	F2	F3	F4	F5	F6	F7	F8
106.	-7.50	-12.71	4.51	5.98	-5.42	-10.65	-6.92	-9.06	-1.00	-1.00	0.99	0.99	-0.99	-1.00	-1.00	-1.00
107.	-10.03	-13.12	1.32	7.61	-6.89	-11.11	-7.27	-9.57	-1.00	-1.00	0.87	1.00	-1.00	-1.00	-1.00	-1.00
108.	-10.19	-13.15	1.11	7.71	-6.99	-11.14	-7.29	-9.59	-1.00	-1.00	0.81	1.00	-1.00	-1.00	-1.00	-1.00
109.	-9.95	-13.11	1.43	7.55	-6.84	-11.09	-7.26	-9.55	-1.00	-1.00	0.89	0.99	-1.00	-1.00	-1.00	-1.00
110.	-10.49	-13.19	0.74	7.89	-7.16	-11.19	-7.33	-9.66	-1.00	-1.00	0.63	1.00	-1.00	-1.00	-1.00	-1.00
111.	-9.49	-13.03	2.00	7.26	-6.58	-11.01	-7.19	-9.46	-1.00	-1.00	0.96	0.99	-1.00	-1.00	-1.00	-1.00
112.	-10.07	-13.13	1.27	7.63	-6.91	-11.12	-7.28	-9.57	-1.00	-1.00	0.85	1.00	-1.00	-1.00	-1.00	-1.00
113.	-3.47	-11.96	9.39	0.78	-0.70	-10.82	-6.88	-10.57	-0.99	-1.00	1.00	0.65	-0.61	-1.00	-1.00	-1.00
114.	-1.86	-11.70	11.41	-0.25	0.23	-10.53	-6.66	-10.25	-0.95	-1.00	1.00	-0.24	0.23	-1.00	-1.00	-1.00
115.	-4.14	-12.07	8.54	1.21	-1.09	-10.94	-6.98	-10.70	-0.99	-1.00	1.00	0.84	-0.79	-1.00	-1.00	-1.00
116.	-8.66	-12.79	2.83	4.11	-3.74	-11.76	-7.60	-11.61	-1.00	-1.00	0.99	0.99	-0.99	-1.00	-1.00	-1.00
117.	-7.24	-12.57	4.63	3.19	-2.91	-11.50	-7.40	-11.32	-1.00	-1.00	0.99	0.99	-0.99	-1.00	-1.00	-1.00
118.	-8.41	-12.75	3.16	3.95	-3.59	-11.71	-7.56	-11.56	-1.00	-1.00	0.99	0.99	-0.99	-1.00	-1.00	-1.00
119.	-5.75	-12.33	6.51	2.25	-2.04	-11.23	-7.19	-11.03	-0.99	-1.00	0.99	0.98	-0.97	-1.00	-1.00	-1.00
120.	-5.62	-12.31	6.68	2.16	-1.96	-11.21	-7.18	-10.99	-0.99	-1.00	0.99	0.97	-0.96	-1.00	-1.00	-1.00

SN	E1	E2	E3	E4	E5	E6	E7	E8	F1	F2	F3	F4	F5	F6	F7	F8
121.	-10.25	-12.95	0.62	2.51	-2.32	-12.95	-8.34	-14.25	-1.00	-1.00	0.55	0.99	-0.98	-1.00	-1.00	-1.00
122.	-6.09	-12.28	5.87	-0.16	0.12	-12.19	-7.76	-13.41	-0.99	-1.00	0.99	-0.16	0.12	-1.00	-1.00	-1.00
123.	-4.63	-12.04	7.71	-1.09	0.97	-11.93	-7.56	-13.12	-0.99	-1.00	1.00	-0.79	0.75	-1.00	-1.00	-1.00
124.	-5.66	-12.21	6.42	-0.43	0.37	-12.11	-7.70	-13.32	-0.99	-1.00	0.99	-0.41	0.35	-1.00	-1.00	-1.00
125.	-5.17	-12.13	7.03	-0.75	0.66	-12.02	-7.64	-13.23	-0.99	-1.00	0.99	-0.63	0.57	-1.00	-1.00	-1.00
126.	-5.60	-12.19	6.49	-0.47	0.40	-12.10	-7.69	-13.31	-0.99	-1.00	0.99	-0.44	0.38	-1.00	-1.00	-1.00
127.	-6.31	-12.31	5.59	-0.02	-0.01	-12.23	-7.79	-13.45	-0.99	-1.00	0.99	-0.02	-0.01	-1.00	-1.00	-1.00
128.	-8.39	-12.54	2.75	-1.29	1.12	-13.51	-8.60	-16.19	-1.00	-1.00	0.99	-0.86	0.81	-1.00	-1.00	-1.00
129.	-8.47	-12.55	2.66	-1.25	1.08	-13.52	-8.61	-16.21	-1.00	-1.00	0.99	-0.85	0.79	-1.00	-1.00	-1.00
130.	-3.36	-11.63	8.89	-7.14	6.42	-13.49	-8.42	-17.49	-0.99	-1.00	1.00	-1.00	0.99	-1.00	-1.00	-1.00
131.	-1.21	-11.28	11.61	-8.52	7.68	-13.09	-8.13	-17.07	-0.84	-1.00	1.00	-1.00	1.00	-1.00	-1.00	-1.00
132.	1.99	-10.66	15.44	-13.19	11.90	-13.41	-8.20	-18.74	0.96	-1.00	1.00	-1.00	1.00	-1.00	-1.00	-1.00
133.	-11.21	-12.68	-1.42	-7.35	6.54	-16.71	-10.55	-23.71	-1.00	-1.00	-0.89	-1.00	0.99	-1.00	-1.00	-1.00
134.	-11.58	-12.74	-1.89	-7.11	6.32	-16.78	-10.59	-23.78	-1.00	-1.00	-0.96	-1.00	0.99	-1.00	-1.00	-1.00
135.	29.67	-6.11	50.15	-33.54	30.43	-9.28	-4.90	-15.51	1.00	-0.99	1.00	-1.00	1.00	-1.00	-0.99	-1.00

SN	E1	E2	E3	E4	E5	E6	E7	E8	F1	F2	F3	F4	F5	F6	F7	F8
136.	29.67	-6.11	50.16	-33.54	30.43	-9.28	-4.90	-15.51	1.00	-0.99	1.00	-1.00	1.00	-1.00	-0.99	-1.00
137.	29.67	-6.11	50.15	-33.54	30.43	-9.28	-4.90	-15.51	1.00	-0.99	1.00	-1.00	1.00	-1.00	-0.99	-1.00
138.	-10.94	-12.64	-1.09	-7.52	6.69	-16.66	-10.51	-23.65	-1.00	-1.00	-0.79	-1.00	0.99	-1.00	-1.00	-1.00
139.	29.67	-6.11	50.16	-33.54	30.43	-9.28	-4.90	-15.51	1.00	-0.99	1.00	-1.00	1.00	-1.00	-0.99	-1.00
140.	29.67	-6.11	50.16	-33.54	30.43	-9.28	-4.90	-15.51	1.00	-0.99	1.00	-1.00	1.00	-1.00	-0.99	-1.00
141.	29.67	-6.11	50.16	-33.54	30.43	-9.28	-4.90	-15.51	1.00	-0.99	1.00	-1.00	1.00	-1.00	-0.99	-1.00
142.	-11.59	-12.64	-2.11	-9.73	8.67	-17.67	-11.12	-26.10	-1.00	-1.00	-0.97	-1.00	1.00	-1.00	-1.00	-1.00
143.	70.52	0.57	101.48	-62.33	56.66	-2.75	0.22	-9.64	1.00	0.51	1.00	-1.00	1.00	-0.99	0.22	-1.00
144.	70.52	0.57	101.48	-62.33	56.66	-2.75	0.22	-9.64	1.00	0.51	1.00	-1.00	1.00	-0.99	0.22	-1.00
145.	70.52	0.57	101.48	-62.33	56.66	-2.75	0.22	-9.64	1.00	0.51	1.00	-1.00	1.00	-0.99	0.22	-1.00
146.	-11.48	-12.52	-2.18	-12.42	11.09	-18.55	-11.62	-28.39	-1.00	-1.00	-0.98	-1.00	1.00	-1.00	-1.00	-1.00
147.	89.91	3.79	125.74	-77.37	70.35	-0.13	2.38	-8.07	1.00	0.99	1.00	-1.00	1.00	-0.13	0.98	-1.00
148.	89.91	3.79	125.74	-77.37	70.35	-0.13	2.38	-8.07	1.00	0.99	1.00	-1.00	1.00	-0.13	0.98	-1.00
149.	89.91	3.79	125.74	-77.37	70.35	-0.13	2.38	-8.07	1.00	0.99	1.00	-1.00	1.00	-0.13	0.98	-1.00
150.	39.11	-4.38	61.65	-44.82	40.66	-9.36	-4.63	-18.26	1.00	-0.99	1.00	-1.00	1.00	-1.00	-0.99	-1.00

Appendix 2: Flowchart for generated ANN model for soil-gas radon concentration in Southwest Nigeria

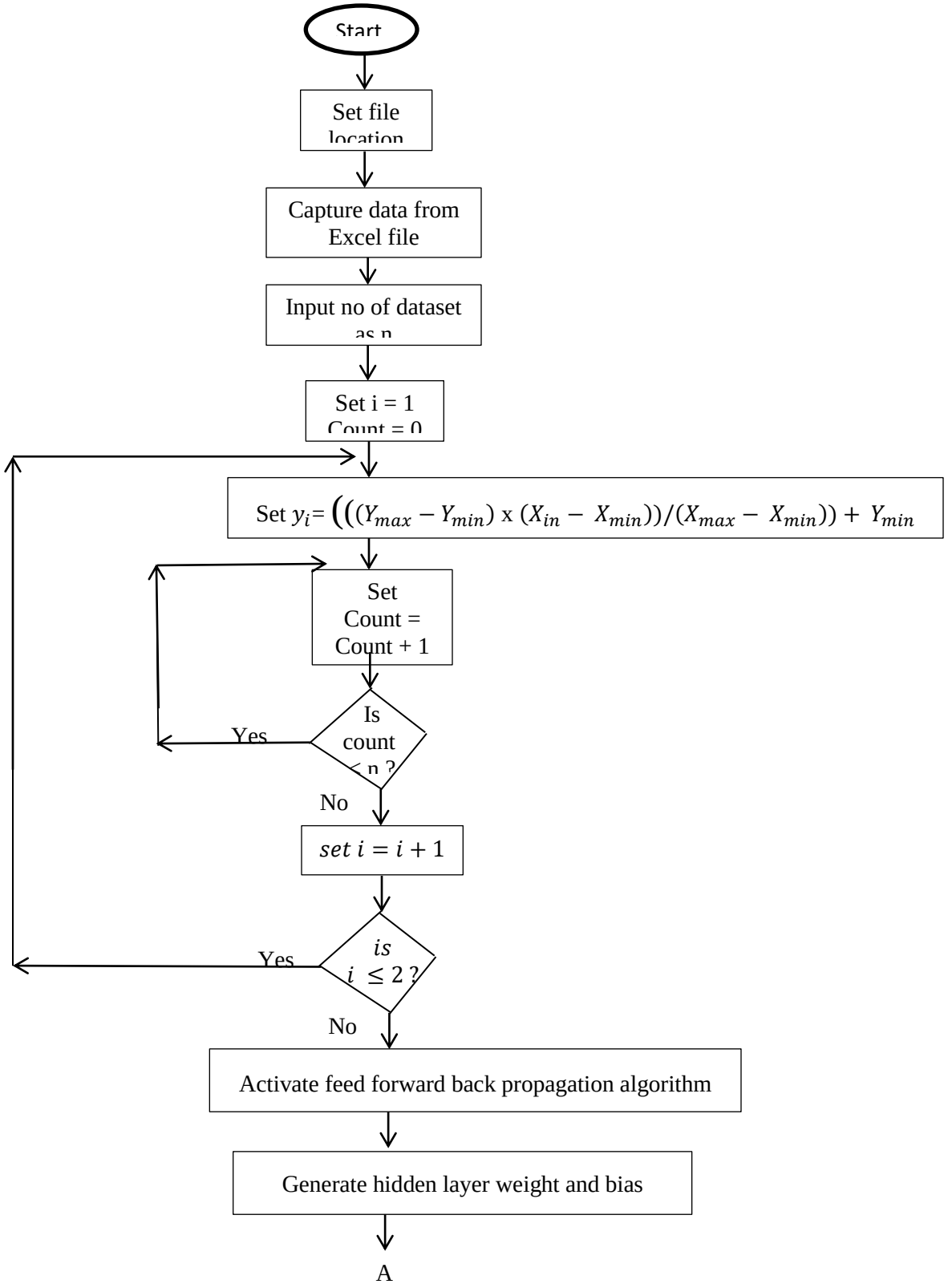

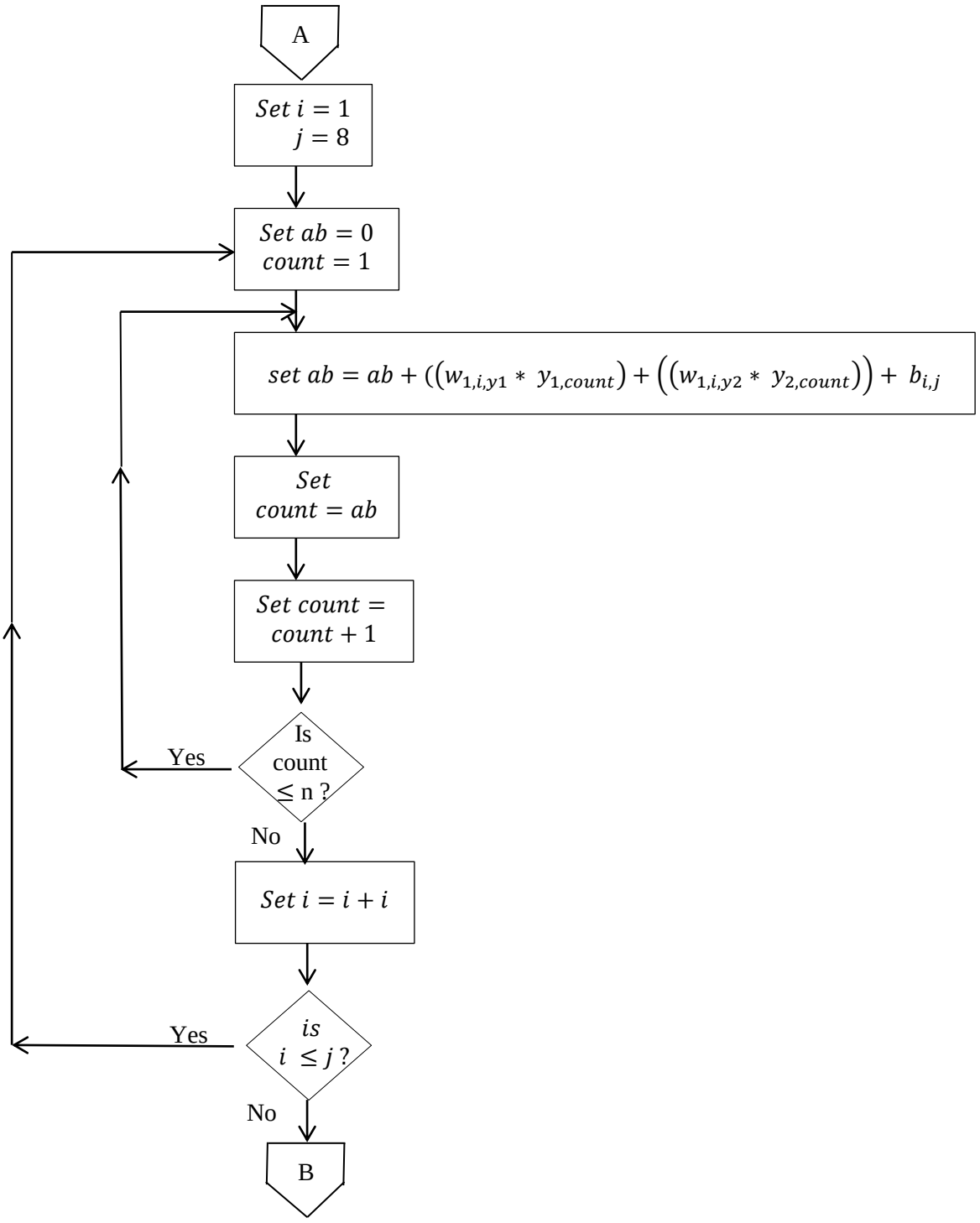
A
Set $i = 1$
$j = 8$
Set $ab = 0$
$count = 1$
$set\ ab = ab + ((w_{1,i,y1} * y_{1,count}) + ((w_{1,i,y2} * y_{2,count})) + b_{i,j}$
Set
$count = ab$
Set $count =$
$count + 1$
Is
count
≤ n ?
Yes
No
Set $i = i + i$
is
$i \leq j$?
Yes
No
B

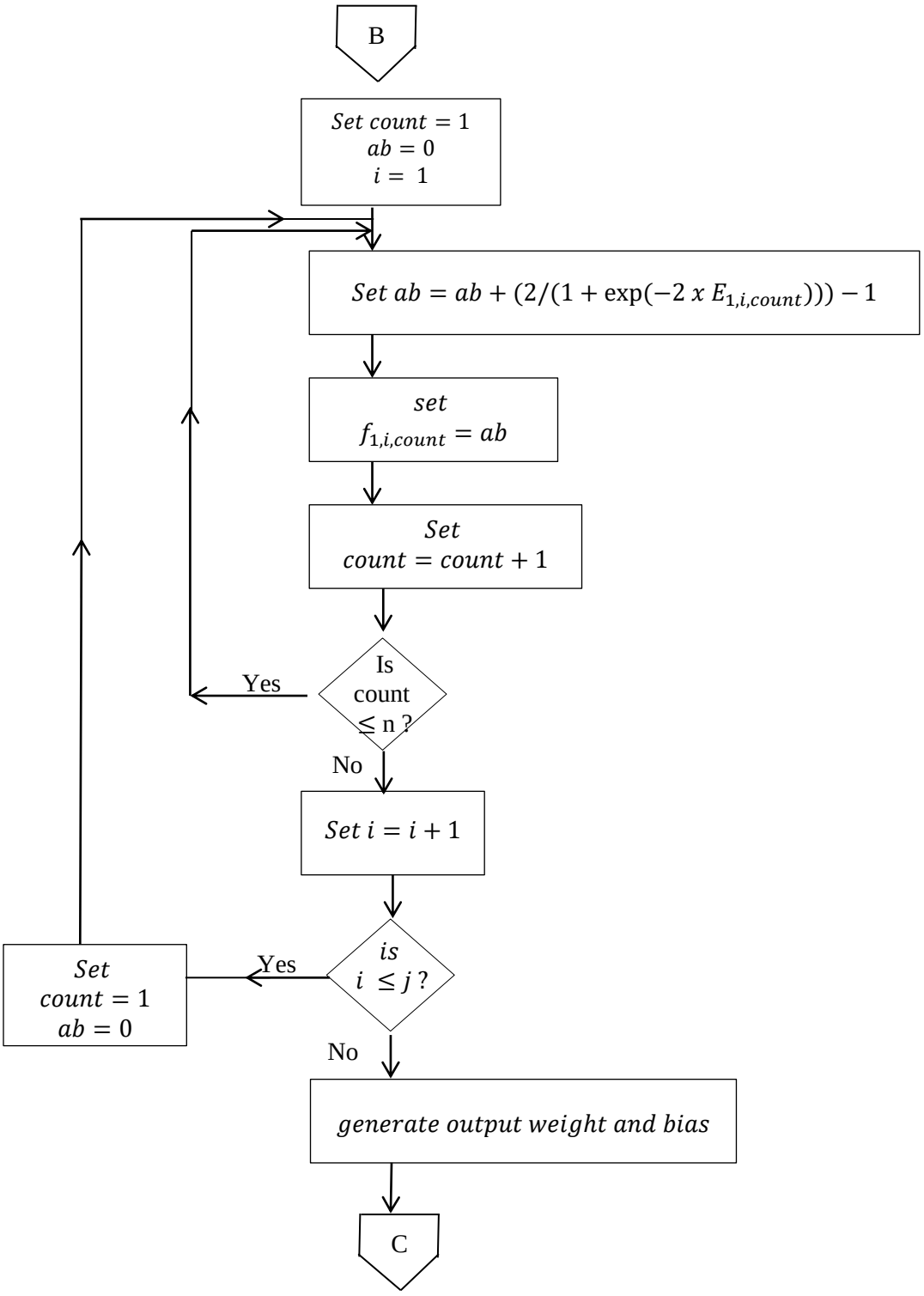
B
Set count = 1
ab = 0
i = 1
Set ab = ab + (2/(1 + exp(−2 x E1,i,count))) − 1
set
f1,i,count = ab
Set
count = count + 1
Is
count
≤ n ?
Yes
No
Set i = i + 1
is
i ≤ j ?
Yes
Set
count = 1
ab = 0
No
generate output weight and bias
C

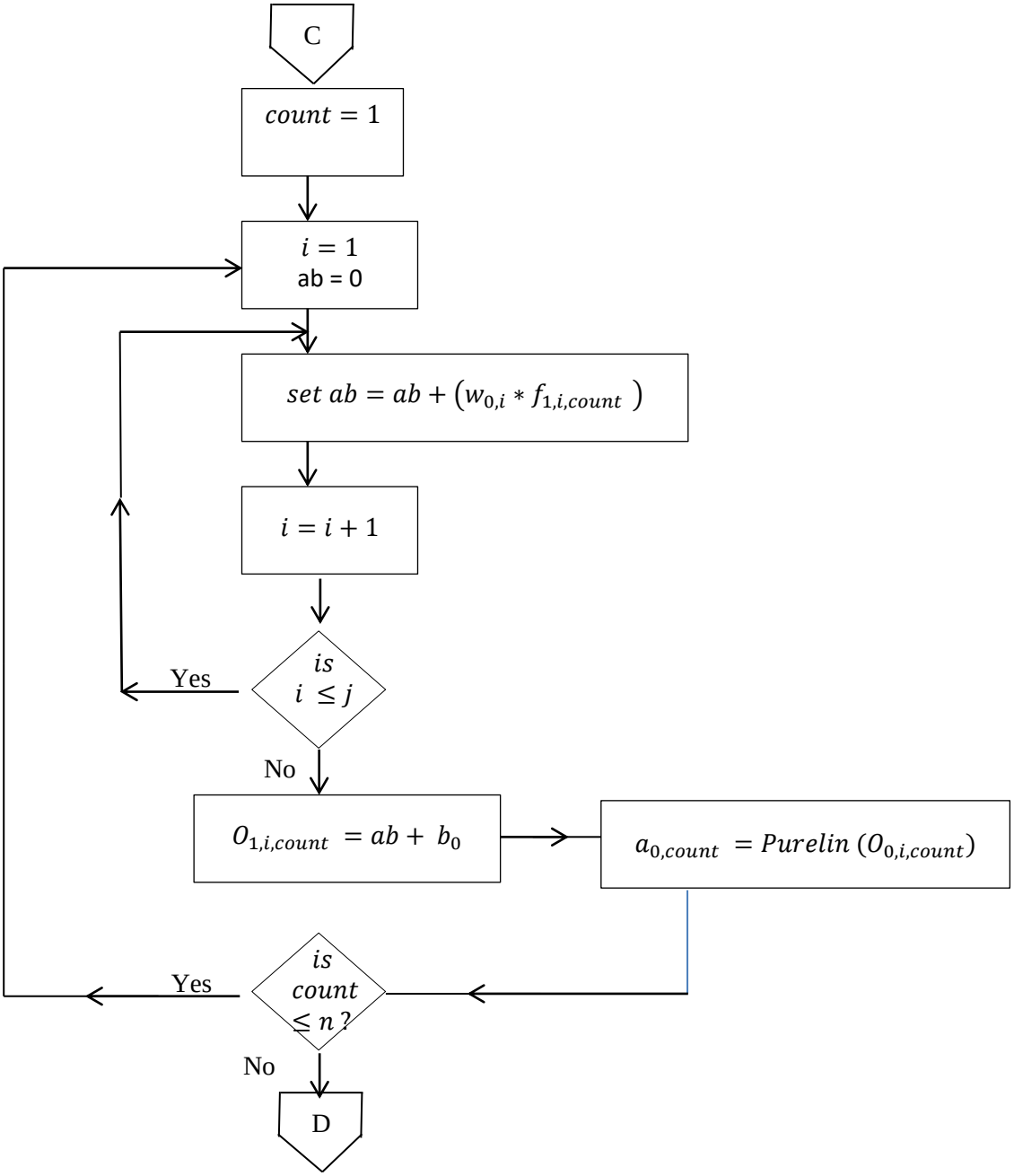
C
$count = 1$
$i = 1$
ab = 0
$set\ ab = ab + (w_{0,i} * f_{1,i,count})$
$i = i + 1$
$is\ i \leq j$
Yes
No
$O_{1,i,count} = ab + b_0$
$a_{0,count} = Purelin\ (O_{0,i,count})$
$is\ count \leq n\ ?$
Yes
No
D

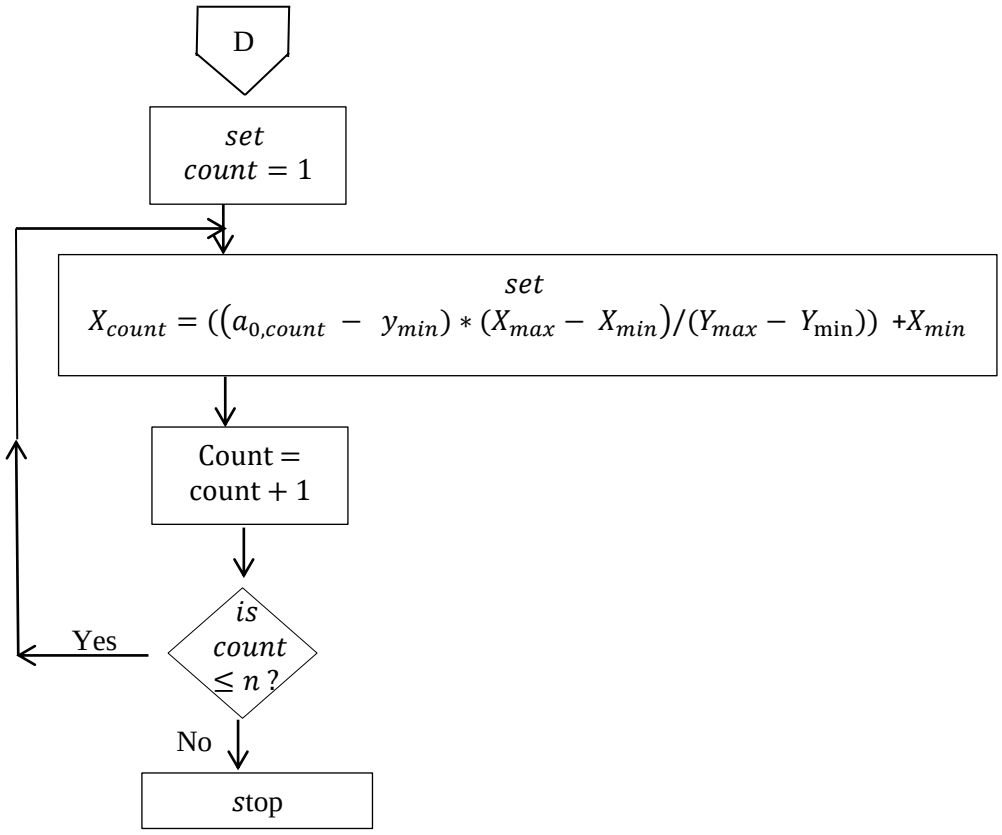
D
set
count = 1
set
$X_{count} = ((a_{0,count} - y_{min}) * (X_{max} - X_{min})/(Y_{max} - Y_{\min})) + X_{min}$
Count =
count + 1
is
count
≤ n ?
Yes
No
stop

Appendix 3: Mathlab Codes

Code 3A1: MathlabTraining Code for ANN Modelling

```
global targets inpno settar ninput ntarget
%nooftrain=input('Enter number of re-training = ');

filepath=[pwd,'\','dataset.xlsx'];
[data,text,datatext]=xlsread(filepath,'sheet1');
[row,col]=size(data);
inputs=data(:,1:2)';
targets=data(:,3)';

%arrayperc=[0.9 0.8 0.7 0.6];
%for i=1:length(arrayperc)

perctrain=1;
perctest=1-perctrain;

% Normalization MAP(MIN -MAX)
%=========================
%viewdata=data;
%ndata=(data-repmat(min(min(data,[],2)),row,col))./(repmat(max(max(data,[],2)),row,col)-
repmat(min(min(data,[],2)),row,col));
[ninput setin]=mapminmax(inputs);
[ntarget settar]=mapminmax(targets);

newfilename=[pwd,'\NEWresult.xlsx'];
xlswrite(newfilename,{'Input 1','Input 2','Output'},'normalized_input_output','A1');
xlswrite(newfilename,[ninput' ntarget'],'normalized_input_output','A2');

% inputn=ndata(:,1:5)';
 inpno=round(perctrain.*size(ninput,2));
 input=ninput(:,1:inpno);
%
ntargetn=ntarget;
target=ntarget(:,1:inpno);
%target=targets(:,1:inpno);

%% TRAINING
%epc=10:10:1000;

%for i=1:nooftrain

net=newff(minmax(input),target,[8],{'tansig','purelin'},'trainlm');
net.LW{1,2}=net.LW{1,2}*0.01;
net.b{2}=net.b{2}*0.01;

[dat,tex,datatex]=xlsread(filepath,'Sheet2');
```

```
net.IW{1,1}=dat(:,1:2);
inputlayer=net.IW{1,1};
net.b{1}=dat(:,3);
bias=net.b{1};
xlswrite(newfilename,{'W(1)','W(2)','Bias'},'inputweight_and_bias','A1');
xlswrite(newfilename,[inputlayer bias],'inputweight_and_bias','A2');

[dat,tex,datatex]=xlsread(filepath,'Sheet3');
net.LW{2,1}=dat(1,1:8);
outputlayer=net.LW{2,1};
net.b{2}=dat(1,9);
outputbia=net.b{2};
xlswrite(newfilename,{'W(1)','W(2)','W(3)','W(4)','W(5)','W(6)','W(7)','W(8)','Bias'},'outputweight
_and_bias','A1');
xlswrite(newfilename,[outputlayer outputbia],'outputweight_and_bias','A2');

net.performFCN='mse';
net.trainParam.lr=0.05;
net.trainParam.mc=0.95;
net.trainParam.show=20;
net.trainParam.epochs=1000;

[net,tr]=train(net,input,target);
save trainnet.mat net;

%kfoldloss
%plotconfusion
%accuracy = 1 - kfoldloss

% x = testinput;
% xx=input;
% %[rox cox]=size(x);
%  ttr = ntarget(1,1:inpno);
%  tte = ntarget(1,inpno+1:end);
%  [rot cot]=size(ttr');
%  yhat = classify(x',xx',ttr');
%  [royhat colyat]=size(yhat);
%  [cm,order] = confusionmat(tte',yhat)
%  acc=((cm(1,1)+cm(2,2))/((cm(1,1)+cm(1,2)+cm(2,1)+cm(2,2))))*100
%
%  tpr=(cm(1,1)/(cm(1,1)+cm(2,1)))*100
%  fpr=(cm(1,2)/(cm(1,2)+cm(2,2)))*100
%
%  figure
%  plotroc(tte,x)
%  ax = gca;
% h = findobj(gca,'Type','line');
% x = h.XData;
% y = h.YData;
%
```

```
% figure,
% plot(x,y,'r-*')

%end

%viewx=x

% % Denormalization
%
% depredict=(predict.*(repmat(max(predict),roww,coll)-repmat(min(predict),roww,coll))+...
%     repmat(min(predict),roww,coll));
%
% mse=sum((target-predict).^2)./numel(target);

% figure,
% plotregression(predict,target)
% hold on
%
% end
% hold off
```

Appendix 3: Matlab Codes
Code 3A2: Mathlab Code used to generate Measures of Performance for the Model

```
%% TESTING
global targets inpno settar ninput ntarget
newfilename=[pwd,'\NEWresult.xlsx'];
if inpno==numel(targets)
   testinput=ninput(:,1:inpno);
else
testinput=ninput(:,inpno+1:end);
end

load trainnet.mat
predict=sim(net,testinput);
% Denomization;
dpredict=mapminmax.reverse(predict,settar);
nnp=size(dpredict);
nnt=size(targets);

if inpno==numel(targets)
  obs = ntarget(1,1:inpno);
else
obs = ntarget(1,inpno+1:end);
end
obspred=obs-dpredict;
absobspred=abs(obs-dpredict);
obspredpow=(obs-dpredict).^2;
% Average validation Error
avg_valid_error=(1/numel(targets)).*sum(abs((dpredict'-targets')./(max(targets)-
min(targets))))
% Nash-Sutcliffe efficiency coefficient
%NS=1-(sum((dpredict'-mean(targets)).^2)./sum((targets'-mean(targets)).^2));
MAE=sum(abs(targets'-dpredict')/numel(targets));
% mean absolute percentage error
MAPE=((1/numel(targets)).*(abs((mean(targets)-mean(dpredict))/mean(targets))))*100;
% mean square error
MSE=(sum(targets'-dpredict').^2)/numel(targets);
% root mean square error
RMSE=sqrt(MSE);
%Goodness of prediction(G)
G=(1-(sum((targets'-dpredict').^2)./sum((targets'-mean(target)).^2)))*100;
xlswrite(newfilename,{'Normalized','Denormalized','Target'},'output','A1');
xlswrite(newfilename,[predict' dpredict' targets'],'output','A2');
xlswrite(newfilename,{'Eavg','G','MAE','MSE','RMSE','MAPE'},'METRICS','A1');
xlswrite(newfilename,[avg_valid_error G MAE MSE RMSE MAPE],'METRICS','A2');
msgbox('Executed and Saved Successfully As NEWRESULT');
```

Appendix 4: Results of model-predicted validation

Table 4A1: Result of the 20 Measured and Model-predicted Soil-gas Radon Concentration

S/N	Bedrock	Latitude	Longitude	Air Perm. x 10^{-12} (m^2)	Measured CR_n (kBq/m^3)	Predicted CR_n (kBq/m^3)
1.	Migmatite	$7^0\ 11^1\ 00^{11}$	$3^0\ 51^1\ 00^{11}$	0.88	8.83	9.48
2.	Undifferentiated Schist	$7^0\ 30^1\ 22^{11}$	$4^0\ 00^1\ 58^{11}$	0.68	9.89	10.65
3.	CG Porphyrictic biotite & Biotite Hornblende Granite	$7^0\ 15^1\ 2^{11}$	$5^0\ 12^1\ 36^{11}$	0.15	7.75	7.45
4.	Undifferentiated Schist	$7^0\ 27^1\ 34^{11}$	$3^0\ 57^1\ 58^{11}$	0.19	5.15	4.53
5.	Migmatite	$7^0\ 22^1\ 40.44^{11}$	$3^0\ 48^1\ 25^{11}$	1.53	21.11	19.10
6.	Talc Schist	$7^0\ 24^1\ 00^{11}$	$4^0\ 26^1\ 51^{11}$	0.62	5.96	5.02
7.	Banded Gneiss	$7^0\ 21^1\ 05^{11}$	$3^0\ 09^1\ 52^{11}$	1.98	8.67	6.09
8.	Banded Gneiss	$8^0\ 24^1\ 07^{11}$	$3^0\ 48^1\ 39^{11}$	0.84	6.48	5.19
9.	Flaggy Quartzite and Quartzite Schist	$7^0\ 24^1\ 35^{11}$	$3^0\ 20^1\ 07^{11}$	0.70	9.27	10.95
10.	Migmatite	$7^0\ 06^1\ 00^{11}$	$5^0\ 02^1\ 00^{11}$	0.23	7.58	7.57
11.	Migmatite	$7^0\ 18^1\ 00^{11}$	$5^0\ 20^1\ 00^{11}$	0.19	8.72	7.56
12.	Quartzite Schist	$7^0\ 05^1\ 04^{11}$	$3^0\ 54^1\ 31^{11}$	0.19	5.43	5.11
13.	Banded Gneiss	$8^0\ 24^1\ 55^{11}$	$3^0\ 18^1\ 45^{11}$	0.90	10.22	5.19

S/N	Bedrock	Latitude	Longitude	Air Perm. x 10^{-12} (m^2)	Measured CR_n (kBq/m^3)	Predicted CR_n (kBq/m^3)
14.	CG Porphyrictic biotite & Biotite Hornblende Granite	$7^0\ 22^1\ 51^{11}$	$4^0\ 05^1\ 51^{11}$	1.21	8.37	7.44
15.	Quartz Schist	$7^0\ 39^1\ 16^{11}$	$4^0\ 57^1\ 25^{11}$	1.78	6.43	6.09
16.	Quartz Syenite	$7^0\ 43^1\ 20^{11}$	$4^0\ 10^1\ 14^{11}$	1.89	21.46	21.63
17.	Quartzite Schist	$7^0\ 42^1\ 21^{11}$	$4^0\ 57^1\ 26^{11}$	1.77	7.62	6.09
18.	Quartzite Schist	$7^0\ 42^1\ 21^{11}$	$3^0\ 45^1\ 30^{11}$	0.19	5.78	5.01
19.	Quartzite Schist	$7^0\ 43^1\ 21^{11}$	$3^0\ 48^1\ 32^{11}$	1.46	6.63	6.12
20.	Talc Schist	$7^0\ 33^1\ 00^{11}$	$4^0\ 30^1\ 00^{11}$	2.30	3.53	6.09

Appendix 4: Table 4A2: Result of the 20 Measured and Model-predicted Geogenic Radon Potential

S/N	Bedrock	Latitude	Longitude	Air Perm. x 10^{-12} (m^2)	Measured GRP	Predicted GRP
1.	Migmatite	7^0 11^1 00^{11}	3^0 51^1 00^{11}	0.88	4.29	4.61
2.	Undifferentiated Schist	7^0 30^1 22^{11}	4^0 00^1 58^{11}	0.68	4.57	4.91
3.	CG Porphyrictic biotite & Biotite Hornblende Granite	7^0 15^1 2^{11}	5^0 12^1 36^{11}	0.15	2.75	2.65
4.	Undifferentiated Schist	7^0 27^1 34^{11}	3^0 57^1 58^{11}	0.19	1.90	1.68
5.	Migmatite	7^0 22^1 40.44^{11}	3^0 48^1 25^{11}	1.53	11.63	10.52
6.	Talc Schist	7^0 24^1 00^{11}	4^0 26^1 51^{11}	0.62	2.69	2.27
7.	Banded Gneiss	7^0 21^1 05^{11}	3^0 09^1 52^{11}	1.98	5.09	3.57
8.	Banded Gneiss	8^0 24^1 07^{11}	3^0 48^1 39^{11}	0.84	3.13	2.50
9.	Flaggy Quartzite and Quartzite Schist	7^0 24^1 35^{11}	3^0 20^1 07^{11}	0.70	4.31	5.09
10.	Migmatite	7^0 06^1 00^{11}	5^0 02^1 00^{11}	0.23	2.87	2.87
11.	Migmatite	7^0 18^1 00^{11}	5^0 20^1 00^{11}	0.19	3.21	2.78
12.	Quartzite Schist	7^0 05^1 04^{11}	3^0 54^1 31^{11}	0.19	1.99	1.88
13.	Banded Gneiss	8^0 24^1 55^{11}	3^0 18^1 45^{11}	0.90	4.99	2.54

S/N	Bedrock	Latitude	Longitude	Air Perm. x 10^{-12} (m^2)	Measured GRP	Predicted GRP
14.	CG Porphyrictic biotite & Biotite Hornblende Granite	$7^0\ 22^1\ 51^{11}$	$4^0\ 05^1\ 51^{11}$	1.21	4.37	3.88
15.	Quartz Schist	$7^0\ 39^1\ 16^{11}$	$4^0\ 57^1\ 25^{11}$	1.78	3.67	3.47
16.	Quartz Syenite	$7^0\ 43^1\ 20^{11}$	$4^0\ 10^1\ 14^{11}$	1.89	12.45	12.55
17.	Quartzite Schist	$7^0\ 42^1\ 21^{11}$	$4^0\ 57^1\ 26^{11}$	1.77	4.35	3.48
18.	Quartzite Schist	$7^0\ 42^1\ 21^{11}$	$3^0\ 45^1\ 30^{11}$	0.19	2.12	1.84
19.	Quartzite Schist	$7^0\ 43^1\ 21^{11}$	$3^0\ 48^1\ 32^{11}$	1.46	3.47	3.34
20.	Talc Schist	$7^0\ 33^1\ 00^{11}$	$4^0\ 30^1\ 00^{11}$	2.30	2.16	3.72